Numerical Modelling of Hydrodynamics and Sedimentation in Upland Lakes and Implications for Sediment Focusing

Luis Alejandro Morales Marín

Coastal and Estuarine Research Unit
Department of Geography

University College London

A thesis submitted for the degree of

Doctor of Philosophy

April 2013

To my wonderful wife Eliana, and my beautiful daughter Juliana, to whom I owe this effort.

Declaration

I, *Luis Alejandro Morales Marín*, declare that this thesis entitled *Numerical Modelling of Hydrodynamics and Sedimentation in Upland Lakes and Implications for Focusing Hypothesis* is the result of my own research. Where information has been derived from other sources, I confirm that this has been indicated in the thesis.

Signature _____

Name _____

Date _____

Acknowledgements

I would like to acknowledge to the Department of Geography UCL for the awarded scholarship to pursue my PhD; without this it would had been impossible to carry out this research. My sincerely gratitude to my first supervisor Prof. Jon French whose expertise and understanding guided me through the difficulties of the PhD. He always was very willing to explain and resolve any difficulties with great patience and enthusiasm. I'd also like to thank my co-supervisor Dr. Helene Burningham for her advice and contribution, and all the support given since the beginning.

I acknowledge the CEH Bangor for the provided data of Llyn Conwy catchment which constituted valuable information within the development of this research. I acknowledge also the Coastal and Estuarine Research Unit (CERU) to provide the equipment and training during the field campaigns realised at Llyn Conwy. A special thanks to Ian Patmore for his commitment and useful lessons about field and laboratory works. A special thank also to Prof. Rick Battarbee for the information provided about Llyn Conwy and the interesting insights that helped to guide this research.

A special thank to my wife for her love and care. She was able to bear the difficulties during these years and sacrifice all for this dream. To the most beautiful gift that God gave us, my daughter Juliana, who always made me happy and gave more sense to my life.

Lastly, I would like to thank to parents in my beloved Colombia, my dad Luis and my mother Marlene, my brothers Jorge and Camilo, all them that always encouraged me and gave the love needed during this long way. To my parents-in-law, Julio and Liney for all their support and care. To my brothers- and sisters-in-law, Adrian, Liney, Julio, Maria and Mateo, who contributed to the realisation of this dream. To my friends at UCL, Mandy, Richard, Miriam, Temitope, Nahid, Aikaterini, Lizzie, Darryl, Mohammed, Andrew and Charlotte, thank you indeed.

Abstract

Despite the increasing resolution and precision of palaeolimnological studies these are often founded on assumptions regarding the distribution and completeness of lake deposits that are not always justified. In particular, the assumption that focusing of suspended sediments leads to preferential deposition in the deepest part of a lake is not always supported by observations, especially in upland lakes subject to energetic wind forcing. Surprisingly, very few studies have investigated the hydrodynamic controls on sediment accumulation. This thesis approaches this problem through physically-based numerical modelling of a small oligotrophic upland lake (Llyn Conwy, north Wales, UK). First, a new one-dimensional model is developed to characterise seasonal variation of lake thermal structure and its interaction with meteorological factors. Second, a three-dimensional model, *FVCOM*, is used to investigate the wind-driven circulation. The existing *FVCOM* model code is enhanced through provision of a new graphical user interface and a semi-empirical wind wave model. Simulations are performed for varied meteorological conditions and evaluated with respect to observations. Modelled variations in the bottom stress due to currents and wind waves are compared with the observed distribution of bottom sediments. Contrary to the "sediment focusing" hypothesis, some of the deepest waters are devoid of recent sediment accumulation and this can be directly attributed to intermittent wind-driven currents that are competent to resuspend material. The processes determining sediment accumulation are investigated further through simulations of suspended sediment dynamics for a set of idealised lake bed configurations and realistic meteorological forcing. Whilst the magnitude and frequency of such resuspension events is a function of the imposed wind climate, their spatial distribution and that of sedimentation within the lake, appears to be strongly influenced by the shape of the basin. Further work is required to extend this analysis to a wider range of upland lake contexts and geometries.

Contents

List of Figures

List of Tables

Chapter 1

Introduction

Resume

This chapter presents an overview of physical processes in lakes, and the principal hydrodynamic processes that control the fate of suspended materials and the accumulation of bottom sediments. The importance of understanding spatial variation in sedimentation for environmental reconstructions based on the interpretation of lake sediment cores is explored. The potential of physically-based numerical modelling as a basis for extending the results of previous empirical studies and for predicting the distribution and completeness of lake sediment sequences is highlighted. Finally, the aims and objectives of the research are presented.

1.1 Occurrence and Physical Characteristics of Lakes

Lakes are standing bodies of fresh or salt water surrounded by land. From a geomorphological perspective, they comprise both a contributing basin and a receiving water body. Hydrologically, they are distinguished from connected riverine systems by virtue of their width and depth (Kuusisto & Hyvarinen, 2000). They are also distinguished from ponds, which are considered to be temporary bodies of water associated with artificial lakes (e.g. fish pond, farm ponds, etc.), where rooted macrophytes usually emerge to the water surface (Welch, 1963; Timms, 1992; O'Sullivan & Reynolds, 2005).

Lakes are numerous in mountainous areas, rift zones and areas with ongoing or recent glaciation, where the primary sources of water are melting ice and snow, runoff

from the land surface and precipitation. During the Pleistocene (about 2.588 Ma until 11,600 Ka BP), most of the world's present lake basins came into existence within the areas of continental glaciation at least 40% of them in Canada George, 2010). In addition, many older lake basins became reshaped, although very little is known about their extent during the interglacials. This is evidenced by most of the present Alpine piedmont lakes. At the end of each glaciation, large proglacial lakes developed at the ice fronts. After the most recent glaciation, the Laurentian Ice Lake (with an area of more than 300×10^3 km^2), the Baltic Ice Lake and the West Siberian Ice Lake, expanded along the line of withdrawal of the Northern Hemisphere continental glaciers. In contrast to the first two, which left behind the Great Lakes and the Baltic Sea, the West Siberian Ice Lake, as well as Lake Agassiz in North America, disappeared completely. In addition, at this time, many volcanic lakes came into existence; the crater lakes Lago di Monterosi (formed about 26×10^3 yr BP) and Lago di Monticchio (about 75×10^3 yr BT) in Italy are some examples of these (O'Sullivan & Reynolds, 2005).

The total volume of water presently located in natural and artificial lakes amounts to at least 229×10^3 km^3 (Margalef, 1994), although some other estimates are as high as 280×10^3 km^3 (Herdendorf, 1990). A large fraction of this volume, including that of the Caspian Sea (78.7×10^3 km^3), is saline. The catastrophic decline of several large lakes (e.g. the Aral Sea from 69×10^3 km^2 during the 1960s to less than 30×10^3 km^2 at present, Lake Chad from 25×10^3 km^2 during the 1970s to about 1000 km^2), is easily compensated for by the rapidly increasing number of reservoirs (e.g. Lake Volta about 8000 km^2 and each of the two dams, Lake Kariba and the Aswan Lake, with about 5000 km^2) and artificial ponds (O'Sullivan & Reynolds, 2005). Although total global lake volume amounts to only 0.017% of the total global water volume, lakes contain about 98% of the surface freshwater available for human use (George, 2010).

Recent studies of the occurrence and size distribution of surface freshwater bodies have highlighted the importance of small lakes, especially those smaller than 1 km^2. Based on analysis of high-resolution digital map datasets, Downing *et al.*, 2006 estimated the global lake inventory to be 304 million lakes totaling 4.2×10^6 km^2 in area. This areal estimate is twice as large as earlier estimates (e.g. Meybeck, 1995) due to the inclusion of millions of previously overlooked small water bodies. Small lakes have disproportionately high hydrological and nutrient processing rates (Smith *et al.*,

2002) and their sheer number means that they are a significant contributor to global geochemical cycles and elemental budgets (Hanson *et al.*, 2007).

Various authors have attempted to classify lakes according to their origin and in relation to the geomorphological characteristics of their basins. One of the most widely used genetic classification schemes is that devised by Hutchinson, 1957 (Table 1.1), who also related various morphometric parameters to lake physical characteristics. Likewise, in a Scandinavian context, Håkanson & Karlsson, 1984 have linked lake morphometry to basin geomorphology at a regional scale. The ability to generalise and predict morphometric characteristics such as area, volume and depth is important since these, in turn, determine many of the important hydrological, sedimentological and ecological aspects of lakes (Wetzel, 1975; Håkanson & Karlsson, 1984).

Compared with rivers and estuaries, distinctive characteristics of lakes include: relatively low flow velocities, relatively low inflows and outflows, intermittent development of vertical stratification, and their function as particularly efficient sinks for nutrients, sediments and toxins (Imberger, 1998; Tsanis *et al.*, 2007; Ji, 2008; Mohanty, 2008). As a consequence of velocity differences, the fast-flowing nature of rivers often results in well-mixed profiles in the vertical and lateral directions and rapid downstream transport, whereas the deeper and slower-moving water in lakes tends to have stratified vertical profiles and lateral variations in the degree of mixing (Imberger & Hamblin, 1982). Additionally, lakes tend to store water over seasons and years, making internal chemical and biological processes significant in the lake water column and the sediment bed; these processes tend to be less important in rapid-flowing rivers. Lakes are also distinguished from estuaries that interact directly with the ocean and are subject to tidal exchanges (of both water and salt) and periodic variations in surface level (Ji, 2008).

Lakes interact with all three major components of the hydrological system: atmospheric water, surface water and groundwater. Potential sources of water to lakes include: (i) direct precipitation, (ii) inflowing streams, and (iii) groundwater. Losses occur to (iv) evaporation, (v) streams, (vi) groundwater and (vii) extraction of lake water for human use. Inflows contribute to the mixing of lake water and serve as a primary source of sediments and nutrients. Together, inflows and outflows determine lake water balance, which, in turn, defines variation in the water surface elevation, surface area, and lake volume (Winter, 1981; Winter & Woo, 1990; Ji, 2008).

Table 1.1: Genetic classification of lakes (after Hutchinson, 1957).

Type	**Description**	**Examples**
Tectonic	Formed by movements of the deeper part of the earth's crust.	*Caspian Sea*, Asia, and *Victoria Lake*, Africa
Volcanic	Formed by volcanic damming.	*Snag Lake*, USA
Landslide	Held by rockslides, mudflows and screes; often ephemeral.	
Glacial	Produced by glacial activity; dominate landscape in northern Europe and America.	*English Lake District*, UK, and *Lake Geneva*, Switzerland
Solution	Formed by the percolation of water in soluble material (limestone, gypsum).	*Karst area* at the Dalmatian coast
Fluvial	Produced by the activity of running water, such as: water falls or rapids, deltas, flood plains.	*The Rhone Delta*, Switzerland, and *The Danube Delta*, Romania
Aeolian	Formed by wind action, mainly in arid regions.	
Shoreline	Formed by damming of material transported by longshore currents.	*Laurentian Lakes*, USA
Organic	Formed by blocking vegetation and beaver dams.	
Anthropogenic	Formed by human activity.	*Bratskoye Dam*, Russia; *Aswan Dam*, Egypt
Meteorite	Created catastrophically through meteorite impact.	*Chubb Lake*, Canada

One way to evaluate the relative effects of hydrological fluxes in a lake is to calculate the water residence time. This is the time taken for the water in a lake to be replaced, assuming that fluxes are uniformly replacing the lake volume. Residence time is most commonly calculated by dividing lake volume by the rate of outflows, but is also calculated by dividing volume by the rate of inflows (Winter, 1981). Water residence time is typically short (days to months) for open lakes located in mountainous, riverine or glacial terrain because large amounts of water can be lost by means of surface stream outflow. In contrast, water residence time for lakes whose main water losses are via evaporation and by groundwater is generally much longer (potentially measured in years) because these two processes operate much more slowly than open channel flow (Winter & Woo, 1990).

Water-balance can provide the basis for classifying lakes. Szesztay, 1974 defined inflow and outflow factors, IF and OF, as:

$$IF = \frac{I}{I+P} \tag{1.1}$$

$$OF = \frac{O}{O+E} \tag{1.2}$$

where I = inflow, O = outflow, P = precipitation input and E = evaporative loss. In lakes dominated by throughflow OF approaches 100%, while in closed lakes OF tends towards 0%. Values of IF are lowest for very large lakes.

From a physical perspective, lakes are dominated essentially by three sets of external forcings: heat flux exchanges and thermal forcings, inflows and outflows, and wind forcing (Figure 1.1). The vertical profile of a lake water column typically varies quite markedly with season. At the end of winter, a lake is often well mixed from top to bottom as the result of winter meteorological conditions (e.g., cold air temperature, strong wind, and weak solar radiation). In spring and summer, buoyancy confines the warmed waters near the surface layer, resulting in the development of a stratified temperature profile formed by three identifiable layers: 1) epilimnion, 2) thermocline (metalimnion), and 3) hypolimnion (Figure 1.1). Surface water temperature decreases towards the end of the summer through the winter, and eventually the lake temperature profile becomes homogenous in winter (Dake & Harleman, 1969; Riley & Stefan, 1988; Hondzo & Stefan, 1993).

Lake thermal structure is strongly dependent on the environmental conditions that prevail. Accordingly, lakes can also be classified on the basis of their thermal structure

(Hutchinson & Löffler, 1956; Hutchinson, 1957; Dake & Harleman, 1969; Lindell, 1980; Table 1.2).

From a mass balance perspective, inflows to lakes and reservoirs include river flows, watershed runoff, groundwater inflow, and discharges from wastewater treatment plants. An inflow displaces the standing lake water after entering a lake (Winter, 1981; Winter & Woo, 1990). If there is no density difference between the inflow water and the lake water, the inflow will mix with the lake water rapidly. If there are density differences, turbulent mixing in the lake will be affected, and the inflow will move as a density current in the form of overflow, interflow, or underflow (Imberger & Hamblin, 1982; Imberger, 1998). Inflows contribute to lake mixing and also serve as a primary source of sediments and nutrients (Hondzo & Stefan, 1993).

Lake outflows include natural discharges as well as releases via reservoir dams, water abstractions (e.g. pumping systems) and other control structures. When water is released from a reservoir, potential energy is converted into kinetic energy. Mixing is a result of this conversion of energy, and the degree of mixing varies with the location of the discharge outlets within the water column. Bottom discharge increases vertical mixing and the potential for resuspension of bottom materials, whereas the surface discharge has a minimal impact on the bottom materials (Imberger, 1998).

Wind forcing is a key factor determining the pattern of water circulation and also constitutes a major energy source for vertical mixing. Wind energy is converted into turbulence in the surface layer and is then transferred to the lower parts of the epilimnion by turbulent diffusion, until the thermal gradient dissipates the energy (Spigel & Imberger, 1980). Turbulent mixing in a lake has a layered vertical structure, because the water motion is largely confined to the epilimnion and currents in the hypolimnion are weak (Bailey & Hamilton, 1997; Cózar *et al.*, 2005). In shallow lakes, wind-induced turbulence may occur at all depths, and therefore can significantly enhance nutrient entrainment from the sediment bed as well as intermittently resuspending bottom sediments (Imberger, 1998; Jin & Ji, 2004).

1.2 Lake Sediment Dynamics

Because of their location in the landscape, lakes tend to function as very effective sinks for sediments introduced through catchment erosion and runoff, or produced within

Table 1.2: Thermal classification of lakes. *Dotted lines:* winter and/or summer stratification; *dashed lines:* circulation temperature; and *shaded area:* ice cover (after Lindell, 1980)

Type	Description	Thermal Structure
Amictic lakes	Never circulate and always frozen.	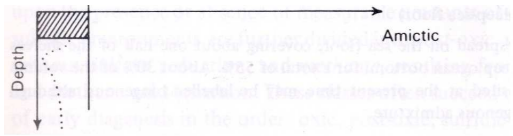
Cold monomictic lakes	Temperature never $> 4^oC$; circulate in summer.	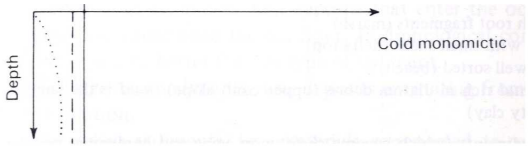
Dimictic lakes	Circulate twice a year in Spring and Autumn.	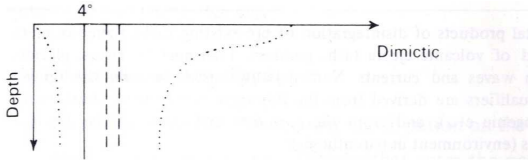
Warm monomictic lakes	Temperature never $< 4^oC$; circulate once a year.	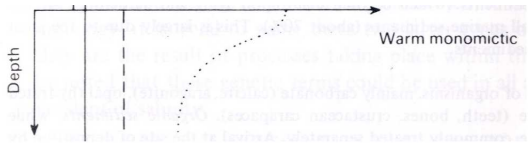
Polymictic lakes	Have frequent circulation. Exist in regions with rapidly changing weather conditions.	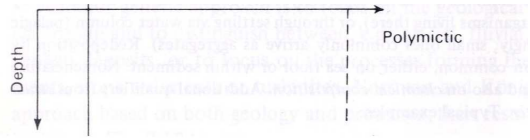
Oligomictic lakes	Found in tropical zone. Have irregular circulations.	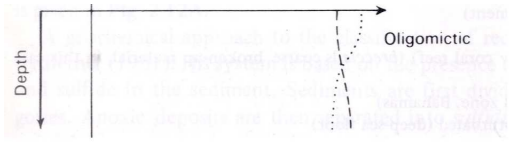

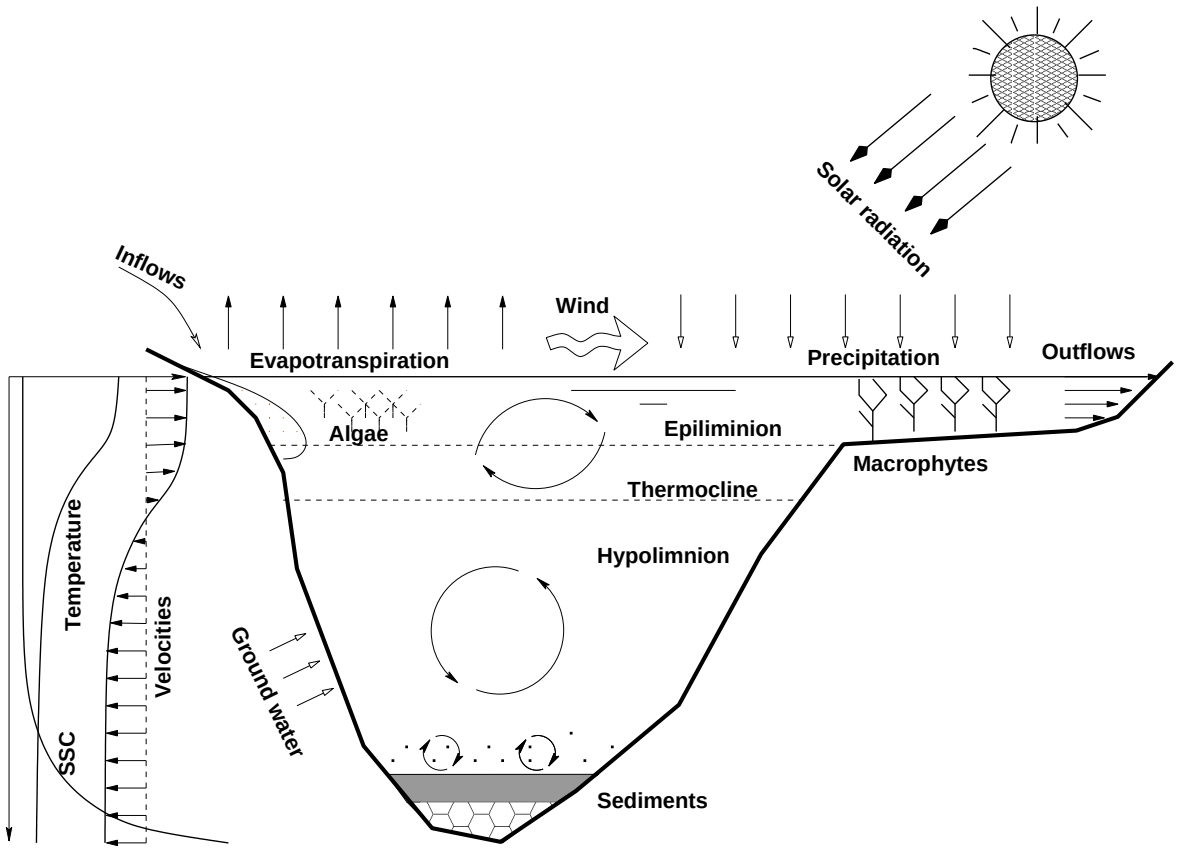

Figure 1.1: Schematic representation of physical processes in lakes.

the lake water column as a result of biological activity. Although lakes are generally considered to be less complex than many other sedimentary environments (e.g. Håkanson, 1981; Leeder, 1982; Margalef, 1994), recent years have seen an increased interest in the physical and biological controls on lake sedimentation and the importance of sedimentary processes for contemporary water quality (e.g. Chao *et al.*, 2009, Fukushima *et al.*, 2010). Work has also focused on the elucidation of past environmental conditions based on the analysis of bottom sediment sequences (e.g. Håkanson, 1984; Stumm, 1985; Imberger, 1998; Brönmark & Hansson, 2005).

Lake sediments vary in origin, the primary distinction is that between allochthonous sediments transported into the lake as a result of the weathering and erosion within the catchment, and autochthonous sediments produced in situ by biological activity (Imberger, 1998). Particulate material of allochthonous origin is mainly derived from bedrock and soils and thus its composition is dominated by clastic inorganic minerals.

The geology of the catchment, and the human activities (e.g. agriculture) within it, are therefore of crucial importance with respect to allochtonous input, both of solutes and of particulate matter (Bloesch, 1982; Hatfield & Maher, 2009; Zaharescu *et al.*, 2009). The main point of sources of allochthonous particle input are rivers. In many lakes, riverine inputs give rise to a distinctive clastic sedimentology characterised by well-developed delta sediment bodies. Classic examples include the Laitaure Delta in Swedish Lapland (Andrén, 1994), Lake Geneva and the inflow of the River Rhone (Lambert & Giovanoli, 1988) and inflow of the River Rhine into Lake Constance (Lambert, 1982). Under natural conditions, gravel and sand would be sorted in subsurface delta areas (Sturm & Matter, 1978). In developed regions, however, most natural braided delta structures have been canalised and/or substantially destroyed as a result of the exploitation of their sand and gravel resources (Zhiliang, 1986).

Although allochonthous inputs are often dominated by inorganic clastic sediments, particulate organic matter (POM) is closely associated with suspended mineral particles, (e.g. adsorbed on to iron oxide surfaces), and is thus transported in this form into lakes (Gu *et al.*, 1996). In Hallwilersee, Switzerland, up to 43% of the total phosphorus input was attributed to nine small streams from the surrounding agricultural catchment (Bloesch *et al.*, 1997). Lakes also tend to accumulate contaminants such as heavy metals, and these elements interact strongly with sediment characteristics such as mineralogy, grain-size, organic matter, carbonate content, acidity, salinity and pH (Krauskopf, 1979; Langmuir, 1997; Last *et al.*, 2001). Research by Kazancı *et al.*, 2010 in Lake Ulubat, a freshwater shallow lake located in northwest Anatolia, Turkey, reported that, in the last 50 years, the mean sedimentation rate increased from 0.37 $mm\ yr^{-1}$ to 1.6 $mm\ yr^{-1}$ due to the establishment of two boron mines and three lignite industries in the catchment. These establishments represented an important source of sediments and contaminants, especially heavy metals such as Al, Fe and Ba (Kazancı *et al.*, 2004). Moreover, a heterogeneous distribution of heavy metals around the lake was attributed to wind intensity and a short water residence time (Blom *et al.*, 1992; Kazancı *et al.*, 2010), and high heavy metals concentrations were found at the lake outlets as a consequence of rapid flushing of the lake water (Algan *et al.*, 2004).

Lakes situated in more remote forested areas may receive significant quantities of organic material such as plant and wood debris. Such inputs can be significant in lakes whose area is small compared with that of their catchments (e.g. Mirror Lake in New Hampshire, USA, of Hubbard Brook Valley; Likens, 1985). Large woody debris may

alter the aquatic ecosystem and hydrological processes by increasing the amount of biomass transported and altering the water balance of a lake (Triska & Cromack Jr, 1980; Harmon & Hua, 1991; Christensen *et al.*, 1996).

In contrast to the above inputs, direct airborne deposition of particulate material is normally insignificant in terms of its contribution to total suspended particulate material (SPM) loadings and to subsequent bottom sedimentation. However, airborne deposition may represent a significant source of specific contaminants. For instance, airborne chlorinated compounds have been found in high concentrations in the Canadian Great Lakes (Eisenreich *et al.*, 1981) and in Swiss mountain lakes (Czuczwa *et al.*, 1985), reflecting the importance of long-distance inputs from industrial areas (Czuczwa & Hites, 1986; Rose, 2002).

In many lakes, SPM largely comprises autochthonous sediment produced by in-lake biological and chemical processes. POM is formed by primary production by phytoplankton and in the subsequent food chain by grazers (zooplankton) and decomposers (bacterial)(Bloesch *et al.*, 1977; Stumm, 1985; Brönmark & Hansson, 2005; Elliott *et al.*, 2007). When the littoral zone (shallow zones where 1% of surface sunlight reaches the bottom) covers a significant amount of the lake area (e.g. as in Lake Okeechobee, Florida; Jin & Ji, 2004), plant debris from littoral macrophytes may also be an important source of SPM. Chemical and physical processes also contribute significantly to production of autochthonous SPM. Biogenic calcite precipitation is a major source of particulate inorganic matter (PIM) in lakes of the temperate zone (Bloesch *et al.*, 1977; Kelts & Hsü, 1978).

Sediment dynamics describes the processes by which sediments are eroded, transported and deposited within geophysical flows. In lakes, sediments introduced to or produced within the water column participate in a variety of processes that influence vertical settling (and therefore the rate of sedimentation) as well as the entrainment (or resuspension) of sediments (and therefore the behaviour of the lake bed). As Håkanson & Jansson, 1983 have argued, lake sediment dynamics are influenced by the nature and origin of the sedimentary materials and by the hydrological and hydrodynamic characteristics of the lake. These, in turn, are controlled by a combination of geological, climatic and anthropogenic factors. All of this results in geographical variation in lake sediment regimes and in the nature, distribution and rate of sediment accummulation (see Figure 1.2).

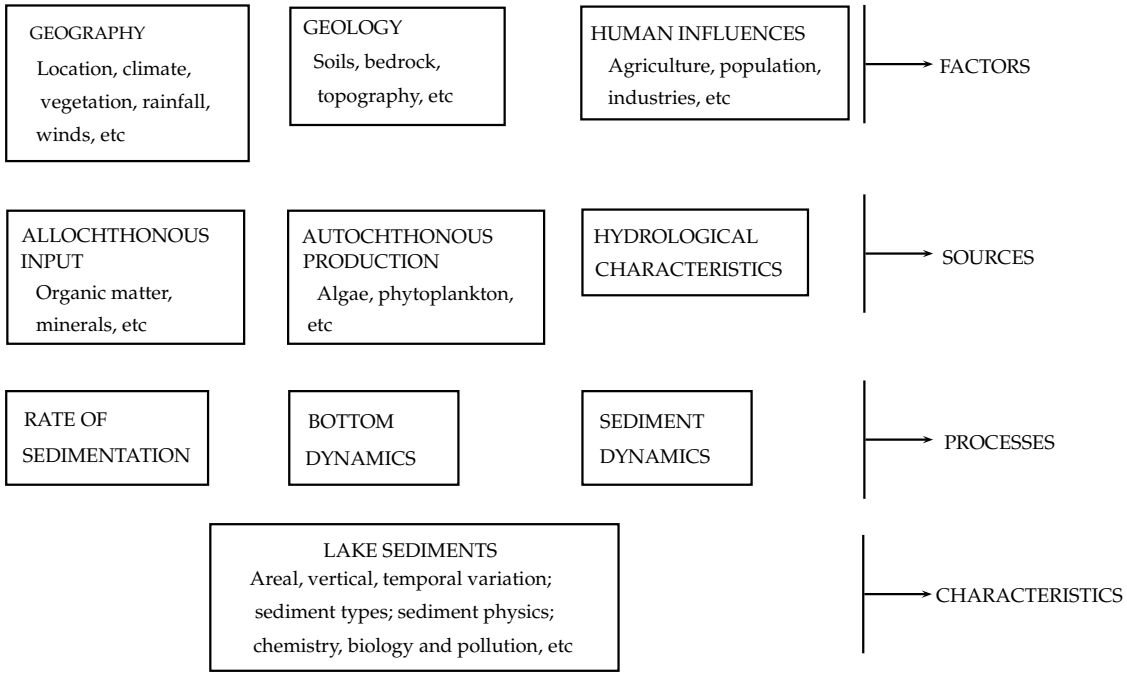

Figure 1.2: Factors that influence sediment supply, processes of deposition and resuspension, and the characteristics of the resulting sedimentary deposits (modified from Håkanson & Jansson, 1983).

A more detailed representation of the main physical processes governing the dynamics of particulate sediments in lakes is presented in Figure 1.3. The influence of the key processes depicted in this scheme on the concentration of sediment particles within the water column and exchanges of material with the bed can be expressed mathematically by the advection-diffusion equation (1.3) (Fischer, 1979; Imberger, 1998; Ji, 2008):

$$\underbrace{\frac{\partial C}{\partial t}}_{\substack{\text{Net change of}\\ \text{concentration}}} = -\underbrace{\mathbf{U}\frac{\partial C}{\partial \mathbf{x}}}_{\substack{\text{Advection}\\ \text{term}}} + \underbrace{\frac{\partial}{\nabla\cdot}(\mathbf{D}\frac{\partial C}{\partial \mathbf{x}})}_{\substack{\text{Diffusion}\\ \text{term}}} + \underbrace{S}_{\substack{\text{Deposition \&}\\ \text{Erosion}}} + \underbrace{R}_{\substack{\text{Reactivity}}} + \underbrace{Q}_{\substack{\text{External}\\ \text{Load}}} \tag{1.3}$$

where C = sediment concentration, t = time, $\mathbf{U} = \begin{pmatrix} \vec{u} \\ \vec{v} \\ \vec{w} \end{pmatrix}$, are the velocity components; $\mathbf{x} = \begin{pmatrix} \vec{x} \\ \vec{y} \\ \vec{z} \end{pmatrix}$ is the position; $\mathbf{D} = \begin{pmatrix} K_h \\ K_v \end{pmatrix}$ are the horizontal and vertical diffusivity coefficients respectively; S = sources and sinks due to deposition and erosion; R = reactivity of chemical and biological processes; and Q = external loadings from point and non-point sources.

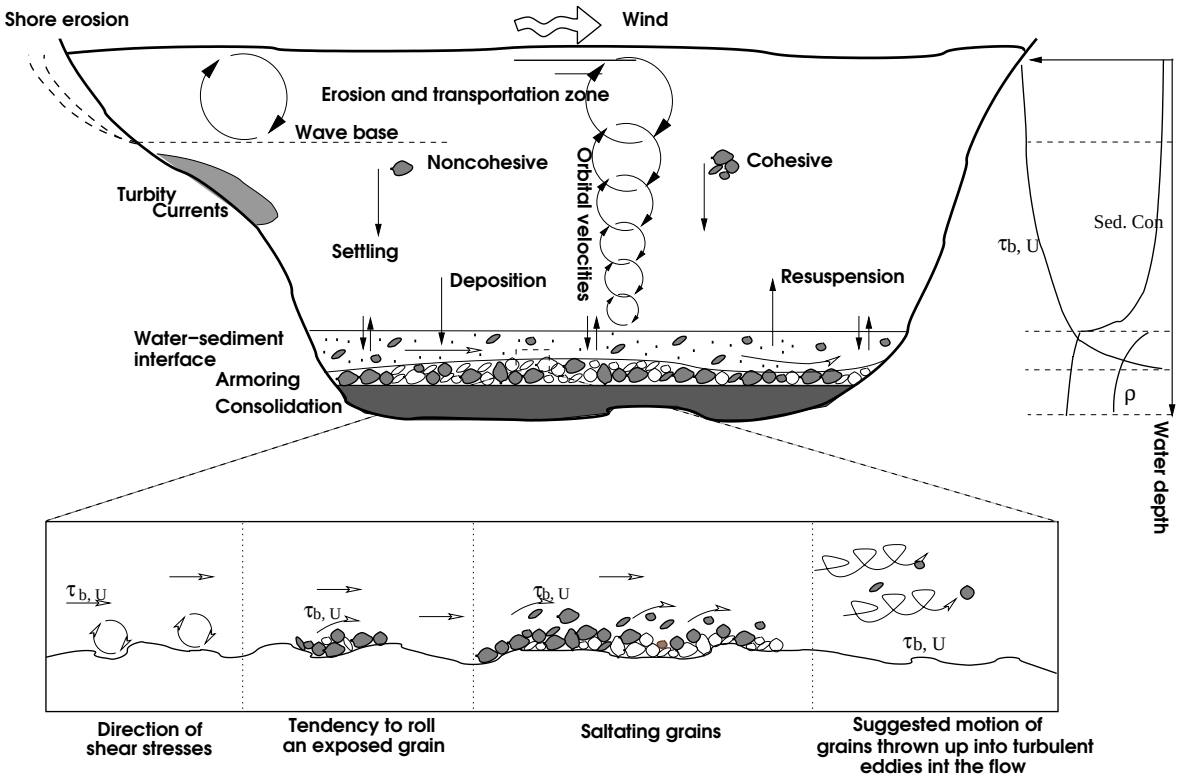

Figure 1.3: Schematic representation of sediment dynamics in lakes.

Although the external load term may be the dominant source of suspended material in many lakes (e.g. Filstrup & Lind, 2010), exchanges between the water column and the bed are also important, particularly in shallow lakes (Sheng & Lick, 1979; Luettich Jr *et al.*, 1990; Hamilton & Mitchell, 1996). Erosion of sediment from the bed occurs when the stresses exerted by the combined effect of currents and wind-waves are greater than the resisting stresses. In some lakes, bed erosion may be the dominant process that maintains high levels of turbidity within the water column. The magnitude of this process in relation to losses, such as sedimentation, outflow, grazing, and bacterial degradation, determines water turbidity and concentration of suspended solids in the water (Horppila & Niemisto, 2008). With the erosion of sediments, nutrients and pollutants are resuspended too, and these sometimes constitute approximately 80% to 90% of the total amount of particulate material (Cózar *et al.*, 2005).

In shallow lakes, wind-waves are the most important factor controlling the erosion or resuspension of bottom sediments (e.g. Chung *et al.*, 2009). Wind exerts stresses on the water surface, creating waves that grow towards the shoreline in the direction

of the fetch (Young & Verhagen, 1996a; Young & Verhagen, 1996b; Young *et al.*, 1996; Fagherazzi & Wiberg, 2009). The impact of wave-induced stresses on the stability of bed sediments is greatest in shallow zones (water depth less than half of the wave length; Luettich Jr *et al.*, 1990; Brydsten, 1992; Kazancı *et al.*, 2010). The extent (and relative of importance) of resuspension, is thus a function of the energy imparted to the system by wind-waves, and the lake size and hyposometry (Gabrielson & Lukatelich, 1985; Bloesch, 1994; Lövstedt & Bengtsson, 2008).

Wind blowing over a lake exerts a stress on the water surface that causes waves to form, break and transfer momentum to the water. The wave motion, especially when waves are breaking, produces turbulence in the upper layers. This turbulence then interacts with the mean shear in the upper few metres to produce further turbulent kinetic energy. Often this interaction produces a secondary motion as well as mean windward drift. Such secondary motions are called Langmuir cells and they are distinguishable to an observer by the characteristic slick pattern associated with regions of convergence (Csanady, 1978; McWilliams *et al.*, 1997). The net turbulent kinetic energy produced in these upper few metres is then exported to lower parts of the epilimnion by turbulence diffusion or by the advective motion associated with the Langmuir circulation (Fischer, 1979; Imberger, 1998).

Additionally, the wind stress initiates motion of the water in the epilimnion in the direction of the wind. If the water surface is to remain nearly horizontal, as it does, then the water in the hypolimnion must counter this flow and move in the reverse direction. A shear will develop across the thermocline, which will increase with time until the thermocline has tilted sufficiently to set up a hydrostatic pressure gradient that just balances the surface stress (Pan *et al.*, 2002; Schwab & Beletsky, 2003; Laval *et al.*, 2003). At this stage the motion changes from a whole basin circulation to two closed gyres, one each in the epilimnion and the hypolimnion and the shear at the interface will decrease to a very small value. All the work done by the wind is then either dissipated internally or used to deepen the epilimnion (Stocker & Imberger, 2003).

Different combinations of wind regime, thermal structure and lake morphology result in varying circulation patterns. For example, Lake Kinneret in Israel is highly temperature stratified and strongly forced by a daily sea breeze. The mean surface layer circulation is directly driven by wind stress curl and topological moment, which are of similar magnitude and of the same sign. However, the spatially varying wind

field and the complex topography has suggested the need for further studies to understand the variation of surface circulation (Stocker & Imberger, 2003; Laval *et al.*, 2003). In Lake Geneva during summer time, a steady cyclonic gyre with a mean speed of $4cms^{-1}$ is found in the central portion of the deep lake basin where the main circulation characteristics are: steady currents with means close to instantaneous speeds, constant current directions, movement in the epilimnion and the thermocline layers in the same direction and internal waves with small amplitudes. Hence, the formation of gyres produces water mass displacements different from the lake-basin end-to end transports envisioned under homogeneous wind field forcing (Strub & Powell, 1986; Lemmin & D'Adamo, 1997).

Deposition of particulate matter is governed by particle size, shape and density, and by water temperature, viscosity and density. For spherical particles, Stokes theoretical formula gives for the settling velocity (v_s) as (Julien, 1998):

$$v_s = 2gr^2(\rho' - \rho)/9\eta \tag{1.4}$$

where g is the gravitational acceleration ($m\ s^{-2}$), η is the coefficient of viscosity of the fluid medium ($kg\ ms^{-1}$), ρ is its density and ρ' is the density of the particle ($kg\ m^{-3}$) and r is its radius (m). Various adaptions of this formula have been proposed for non-spherical particles (Komar & Reimers, 1978; Baba & Komar, 1981). The Stokes settling law neglects the effects of fluid motion and assumes stagnant waters and particle Reynolds numbers in the laminar range. The settling behaviour of fine particles in natural water bodies is more complex. Since the vertical sinking velocity of settling particles in the range of $1 - 40\mu\,m$ is generally one to six orders of magnitude less than that of horizontal water currents, we must dismiss the common concept of a steady downward flux of detritus or phytoplankton cells (Bloesch, 1982). Particles do not sink vertically, or even at a certain angle, but tend to be carried passively in turbulent eddies (Bloesch *et al.*, 1977).

Sediment traps deployed at mid-lake stations can be used to measure settling flux (Gabrielson & Lukatelich, 1985; Bengtsson *et al.*, 1990). The flux determined is then extrapolated to the whole (or partial) lake area. Vertical sediment-flux differences in deep lakes, for example between traps located just below the thermocline (epi-traps) and those deployed above lake bottom (hypo-traps), when compared with horizontal

and temporal difference, are rather low (Håkanson *et al.*, 1989). Hypo-traps are expected to collect less of the primary flux than epi-traps, since decomposition of organic material within the water column will diminish the amount of sediment reaching the bed (Bloesch & Uehlinger, 1986). Such vertical differences are more distinct in shallow lakes subject to wind fetch and intensive resuspension and, during periods of stratification, may considerably exceed horizontal variations (Weyhenmeyer *et al.*, 1997; Terasmaa & Punning, 2006).

Temporal variation in sediment flux is mainly governed by the seasonal dynamics of primary production. The settling flux in temperate lakes may, in summer, exceed that of winter by more than an order of magnitude, and usually also exhibits one or two peaks in spring and late summer, respectively (Bloesch *et al.*, 1977). In a small dimictic lake in northern Estonia, sediment influxes into the traps increased continuously from April until July and peaked during July-September (lower trap) and July-August (upper trap). Subsequent sedimentation decreased rapidly to minimum values by winter (unstratified period). In addition, the influx into the lower traps exceeded that of the upper traps by up to 2.7 times during the summer and 1.1 to 1.3 times at other times (Bloesch, 1982).

In the long term, sediment dynamics influences the evolution of lake morphology. Erosion and resuspension processes may be associated with large fluxes of material, mainly in the shallow zones of the lake (Sly, 1978; Håkanson, 1981). Smaller transfers of material occur from higher energy zones of resuspension to lower energy zones of deposition. Nevertheless these processes take a long time to affect the lake morphology significantly, and also these depend of the magnitude and frequency of sediment input, lake morphology, and the extent of anthrophogenic activities such as deforestation.

Sedimentary processes also influence lake ecosystems through changes in the levels of productivity and the quantity of nutrients within the water column (Gabrielson & Lukatelich, 1985). An increase in suspended sediment concentration modifies the light provided by solar radiation within the epilimnion and therefore the levels of phytoplankton productivity (Scheffer, 1998; Elliott *et al.*, 2007). Temporal and spatial variation in the distribution of the sediments on the lake bottom due to the variation of current and wave-generated bottom stress also influences the distribution of the aquatic vegetation around the lake (Jeppesen, 1998). New deposits of sediments will allow the growth of macrophytes in shallow zones, which are then able to inhibit resuspension and promobe deposition by damping wave activity. This, in turn can help maintain

the transparency of the water and allow transmission of incident light through the water column (James *et al.*, 2004). Also and as a consequence of the presence of macrophytes, the levels of phytoplankton are maintained in shallow eutrophic lakes (Horppila & Nurminen, 2003). In addition, the ability of macrophytes to protect the lake bottom against erosion can reduce the transport of fine sediment to deeper zones (Herb & Stefan, 2005).

Water quality conditions are often affected by anoxia, which is a potential issue in lakes with a well-developed hypoliminion layer (Nürnberg, 1995; Quinlan *et al.*, 1998; Carpenter *et al.*, 1999). These phenomenon allow the release of nutrients and hazardous elements from the lake bottom to the overlaying water. Understanding of sediment resuspension processes and their distribution in lakes thus helps to identify sites where anoxia has developed to take the needed control actions and reduce the impacts on the lake ecosystem (Likens, 1985).

From a engineering point of view, high concentrations of sediments in lakes, reservoirs, ponds and estuaries introduce several problems relating to the construction and operation of hydraulic structures. Non-cohesive particles flowing at high velocities may abrade spillways, pipes and turbines (Julien, 1998; Novak *et al.*, 2007). Also, rapid accumulation of cohesive sediments in slack water zones around dams can cause emergency and drainage gates to become inoperative (Morris & Fan, 1998). Maintenance of structures that are lateral to the flow such as gates, culverts and weirs, requires knowledge of sediment dynamics in order that spatial variation in suspended sediment concentration, and the erosion and sedimentation zones, can be predicted in order to prolong structure operation and reduce the cost of sediment stripping from water intakes (Novak *et al.*, 2007). Researchers have attempted to control the entry of sediments by implementing lateral dams and dikes tested in physical scale models, finding in some cases that these structures produce either a remarkable deposition problem or significant erosion near the foundation (Udall, 1968). One of the most important issues associated with the presence of sediments is the loss of reservoir capacity (McMahon & Mein, 1978; Morris & Fan, 1998; White, 2001). The rate of sediment infilling clearly depends on the load of sediments discharged by streams and/or by superficial runoff into the lake. Extreme events such as strong storms and landslides speed up this process. Additionally, the loss of capacity in lakes and reservoirs involve the loss of navigability, and dredging works may be necessary.

1.3 Sediment Dynamics for Environmental Reconstruction

Sediment accumulation in lakes is driven by a variety of physical, geochemical and biological processes. Lake sediment sequences have the potential, therefore, to record important information on changing environmental conditions within the lake (Battarbee, 1978), within their catchments (Davis, 1969; Oldfield, 1977; Davis, 1982; Foster I.D., 1988; Smol, 1992) as well as broader scale changes in climate (Battarbee, 2000; Solovieva *et al.*, 2005; Wang *et al.*, 2008). Sedimentation rates are often quite rapid, often of the order of a few $mm\ yr^{-1}$. Moreover, the preservation potential of lake sedimentary features is high compared to many other sedimentary environments (Leeder, 1982), thereby allowing more-or-less continuous reconstruction of environmental changes at decadal resolution or better (e.g Stern *et al.*, 2005). Many glacial lakes are characterised by annually-laminated or varved sediments, that reflect seasonal variation in meltwater and clastic sediment input (and by implication temperature; Itkonen & Salonen, 1994), and which provide an absolute incremental chronology (O'Sullivan, 1983; Gajewski *et al.*, 1997). More typically, lake sediments tend to be highly organic and to contain a rich sub-fossil record that can provide the basis for information about the nature of the atmosphere, the catchment, and physical and ecological characteristics of the lake waters (Battarbee, 2000).

At the heart of palaeolimnological research is the acquisition of representative sediment cores and the sub-sampling of cores for analyses of standard sedimentological parameters (e.g. bulk density, loss on ignition, grainsize) and an increasing variety of geochemical and biological proxy measures, ranging from mineral magnetics (Dearing *et al.*, 1981; Flower *et al.*, 1984) and stable isotopes (Talbot, 1990) to fossil pollen, diatoms and chironomid assemblages (Smol *et al.*, 1991; Stoermer & Smol, 2001). Multi-proxy approaches are increasingly favoured (Brooks & Birks, 2000; Battarbee, 2000) as a means of not investigating just past changes in environmental forcing, but also lake ecosystem responses to climate change (Battarbee *et al.*, 2012).

Sedimentological studies include analyses of the time-variation in seasonal sediment influx recorded by varve laminations (Nuhfer & Anderson, 1984; Zhai *et al.*, 2006) and sedimentary cycles inferred from upward-shoaling sequences associated with variations in lake water depth over much longer geological timescales (e.g. Trauth *et al.*, 2001). At Holocene timescales, analyses have focused on reconstruction of factors influencing

the radiation balance and/or the water balance. Radiation balance determines the availability of light and also influences lake water temperature regimes, which are also mediated by winter ice, snow cover and by wind. Progressive trends in the radiation balance lead to changes in the nature and intensity of thermal stratification, with consequences for a wide range of geochemical and ecosystem processes.

Investigations of temperature changes are usually based on the analysis of deep-water cores. The deeper zones of freshwater lakes are considered to be foci of sediment deposition. These usually contain a continuous biologically rich and diverse fossil record that can be potentially used to reconstruct surface water temperature, a variable that is strongly correlated with air temperature (Livingstone & Lotter, 1998. Palaeolimnological techniques such as stable isotopes and biological transfer functions have been used to reconstruct temperature. Stable isotopes studies have focused on carbonate sources, either bulk authigenic material (Stuiver, 1970; Eicher & Siegenthaler, 1976) or on ostracod or mollusc calcite (Grafenstein *et al.*, 1994). Biological transfer function approaches for direct temperature reconstruction include the analysis of chironomids (Walker *et al.*, 1991; Walker *et al.*, 1997) that are also indicators of hypolimnetic oxygen conditions and lake trophic status.

Overall water balance is most obviously reflected in variation in lake water level (Street-Perrott & Harrison, 1985) and residence time. Closed basin lakes with minimal surface or ground water outflows and moisture losses dominated by evaporation are especially sensitive to changes in precipitation. Quite small changes in moisture availability (i.e. the balance between precipitation and evaporation) can result in large level and salinity variations that often produce a geochemical or biological signal within the lake sedimentary record (Fritz, 1990; O'Reilly *et al.*, 2003; Wünnemann *et al.*, 2006). Most freshwater lakes function as open systems, however, and an excess of precipitation over evaporation is balanced by surface water or groundwater outflows. Lakes with fixed surface outlet threshold elevations may be insensitive to changes in moisture availability, whereas lakes formed in more permeable basins in which groundwater fluxes are significant may experience large shifts in shoreline position in response to changes in water balance. In this type of lake system, level changes may affect the structure of marginal habitats, and can lead to the redistribution of previously deposited bottom sediments (Dearing, 1997; Punning *et al.*, 2005). These changes can be recognised from the characteristics of marginal sediments analysed using lithostratigraphic and biostratigraphic techniques (Digerfeldt, 1988). Changes in the water

residence time affect the availability of nutrients as well as the ionic composition of lake water (Anderson *et al.*, 1996; Schindler *et al.*, 1996).

Quantitative analysis of the rate of sediment accumulation is made difficult by the tendency of deposited sediments to be resuspended within shallow marginal areas and transported progressively to deeper areas. Gross sedimentation rates, as measured by short-term sediment trap studies, are typically higher in shallow areas as a result of resuspension by waves and currents (Evans, 1994). Deeper areas, especially in stratified lakes, are not directly influenced by wave-induced bottom stresses and typically experience less powerful currents (Håkanson, 1977b). As a result, bottom sediment sequences in the deepest parts of a lake tend to be less disturbed and to show higher net accumulation rates (Davis, 1969). Likens & Davis, 1975 coined the term 'sediment focusing' to describe this set of processes.

Sediment focusing has important implications for palaeolimnological studies based on the analysis of bottom sediment core samples. The assumption that sediment focusing is an important mechanism controlling the distribution, thickness and completeness of bottom sediment sequences often guides the selection of core sampling locations (Dearing, 1986; Gilbert, 2003). Moreover, it is often assumed that time-variation in the rate of accumulation inferred from core depth-age profiles can be directly related to influx of material from the surrounding catchment. As a consequence, various studies have been undertaken to investigate these processes in more detail. Lehman, 1975 presented simple models of sediment accumulation rate for different idealised lake basin morphologies, and showed that in lakes approximated by a conical geometry, large discrepancies can occur between the rate of deposition at the centre of the lake and catchment sediment flux.

Detailed empirical studies show that the linkages between lake morphology and sedimentation rate are often much more complex. Davis, 1982 investigated sediment focusing processes in Mirror Lake, New Hampshire, based on multiple cores dated using ^{14}C dating and cross-core pollen analysis. The results indicated complex changes in the pattern of accumulation over the last 11,000 years, attributed to circulation patterns affected by water volume variability causing intermittent resuspension of inorganic material deposited initially in littoral zones. The resulting distribution of sedimentation appeared to be better approximated by the hyperboloide or sinusoide model of Lehman, 1975, but due to the complex bathymetry, this simple model does not describe the pattern exactly. Gilbert, 2003 used sub-bottom acoustic surveys to reveal

the distribution of sedimentary facies in a morphologically complex lake in southern Ontario, Canada. At this site, both the extent and thickness of facies vary under the influence of changing process regimes. Crucially, they found only a weak relationship between sediment thickness and water depth. Schiefer, 2006 documents spatially varied rates of sedimentation in a montane lake in British Columbia, and presents evidence to show changes in the pattern of deposition between moderate and extreme sediment delivery events. Larsen *et al.*, 2010 analysed 22 cores from lake and marine sites along the Norwegian and Svalbard coast as part of a project to investigate historical accumulation of polycyclic aromatic hydrocarbons. At these sites, deposition rates are low due to the resistant geology and low biological productivity of the contributing catchments. Whilst some sites appear to show continuous deposition influenced by sediment focusing, others showed irregular deposition with episodic inputs attributable to slump events.

Short-term sediment trap studies have contributed additional information on the fundamental processes governing the dynamics of sediments and associated nutrients and contaminants in lake systems (Bloesch & Uehlinger, 1986; Wieland *et al.*, 2001). The work of Hilton, 1985 and Hilton *et al.*, 1986a has been especially valuable in providing a conceptual framework for understanding sedimentation regimes of small lakes based on multiple cores and data from sediment traps. Hilton *et al.*, 1986a identified at least ten distinct mechanisms for sediment dispersal in small lakes.

Riverine delta formation: When river flow enters a lake, its energy is dissipated by the interaction between the standing lake water and the riverine jet. Coarse particles are deposited, forming a fan that, in some cases, can cover a third of the lake bottom (Pickrill & Irwin, 1983).

River plume sedimentation: Some fine sediments remain in suspension after larger particles settle to form the fan. These particles are transported by thermal convection and Coriolis effects that favour movement of suspended particles towards the right-hand shore line. Sediments are deposited when the energy of the plume diminishes (Pharo & Carmack, 1979).

Continuous complete mixing: Where suspended sediments are continuously mixed such that a more-or-less spatially constant flux of particles enters the bottom layer above the bed. This is consistent with studies showing similar fluxes in sediment traps deployed in deep and shallow water (e.g. Pennington & Tutin, 1974).

Intermittent complete mixing: A potential mechanism for the resuspension of sediments throughout the lake is the 'stress-drop-jet' (Bunge & Bryson, 1956), which occurs when the wind stress driving the circulation suddenly drops. The result is a rapid current reversal and increase in velocity at the thermocline. Since the settling flux that follows such a mixing is proportional to the mass of the sediment contained within the water column (which is well mixed), sedimentation rate will increase linearly with depth (Pennington & Tutin, 1974).

Intermittent epilimnetic complete mixing: Studies with *Lycopodium* powder in stratified experiments by Reynolds, 1979 showed deposition of sediments in proportion to the water depth in the epilimnion, and a constant flux of sediments settling below the thermocline.

Peripheral wave attack: Turbulence created by waves that strike the shoreline is sufficient to resuspend sediment, some proportion of which will be transported into deeper water, where it will settle out of the influence of future wave action and strong resuspension of sediment. Where this process is significant (e.g. Lake Vanern, Sweden (Håkanson, 1977b)), accumulation rate increases linearly with depth but with well-defined zones of accumulation and transport.

Random redistribution of sediments: Davis, 1973 and Davis & Brubaker, 1973 used pollen tracers recorded in sediment traps to demonstrate that resuspension occurred all the year. In this case, wind-waves caused constant resuspension of sediments, which was corroborated by the fact that the lake did not show periods of stratification. The dependence of sedimentation on water depth in this situation is weak.

Current erosion/deposition: Gould & Budinger, 1958 attributed a low amplitude ridge of sediment along the centre of Lake Washington to high velocity convection currents originating from water cooling processes in shallow bays. These currents erode material from the steep side slopes and then redeposit it within the central part of the lake, resulting in a distinctive 'W' cross-sectional profile.

Slumping and sliding on slopes: Håkanson, 1977b suggested that accumulation is negligible for slopes $> 14\%$ and that on slopes $> 4\%$ but $< 14\%$ less sediments accumulate than in horizontal zones. The processes that cause this difference are a combination of sliding (movement of the material parallel to the slope) and

slumping (a movement started by a rotational failure of the sediments). Evidence of this process has come from the analysis of deposited material in which the most superficial layer of sediment has an older ^{14}C date than the sediments below (Wetzel & Manny, 1978).

Organic degradation: During periods of rapid algal decomposition, organic particulate matter is deposited in shallow oxic zones. However, other studies in deep anoxic zones have found greater accumulation of sediment than in shallow places (Deevey, 1955).

Only four of the above processes are readily associated with sediment focusing: intermittent complete mixing; peripheral wave attack; slumping and sliding on slopes; and organic degradation (Hilton, 1985). Based on an intensive multi-core study of Esthwaite Water, a small eutrophic lake in the English Lake District, Hilton *et al.*, 1986a concluded that processes associated with sediment focusing accounted for 59% of the variance in sediment accumulation rate. Peripheral wave action and intermittent complete mixing appear to be the most important of the above mechanisms, with riverine plume and turbidity current effects being locally important.

Complex variability in the spatial and temporal distribution of sedimentation means that multiple sediment cores may be necessary to draw reliable inferences concerning past environmental changes (Bloesch & Uehlinger, 1986; Schiefer, 2006; Wang *et al.*, 2009). The sampling effort in such studies is influenced mainly by logistical considerations (equipment available, water depth, remoteness of the lake, etc) and the complexity of the intended analysis (Chambers & Cameron, 2001; Gilbert, 2003). Although the selection of core locations is often intuitive, following the hypothesis of sediment focusing, where cores taken from the deepest part are considered representative of the whole basin, several studies have evaluated alternative bases for determining the number and location of cores for environmental reconstruction (e.g. Håkanson & Jansson, 1983; Håkanson, 1984; Håkanson, 1992). Håkanson, 1984 proposed an empirically-derived sampling formula based on lake area and shoreline morphology. This formula recognises the tendency of larger lakes with more complex morphologies to have greater spatial variablity in sedimentation (Carpenter, 1983). Evans & Rigler, 1983 proposed simple depth regression equations to predict mean sedimentation rate from depth in order to account for the effects of sediment focusing, although such correlations are often weak (e.g. Cornett *et al.*, 1984).

Other work has started to explore more directly the connections between the pattern of sedimentation and hydrodynamic processes. Rowan *et al.*, 1995, for example, present a sampling framework for ^{210}Pb dating based on the mud deposition boundary depth ($mudDBD$) theory (Rowan *et al.*, 1992). This interprets lake bathymetry to identify erosional, depositional and transitional zones according to the influence of wave resuspension. Zones are determined empirically via simple functions of exposure, E, or a combination of exposure and bottom slope, S. The mud deposition boundary is thus given by:

$$mudDBD = 2.685E^{0.305} \quad \text{(no inclusion of bed slope)} \tag{1.5}$$

$$mudDBD = 1.327E^{0.370}10^{0.0526}S \quad \text{(with inclusion of bed slope)} \tag{1.6}$$

Mud deposition is assumed to occur for depth $> 1.34\, mudDBD$. Lakes that are everywhere shallower than the $mudDBD$ are subject to disturbance of bottom sediments over their entire area. Data for large Canadian lakes suggest that $mudDBD$ theory is useful for predicting sediment distribution and extrapolating core data (Rowan *et al.*, 1992).

Sediment accumulation patterns in lakes are often complex and, for any given lake morphology, are clearly related to hydrodynamic processes, as well as to meteorological forcing. Empirical studies of the kind reviewed above are useful, but tend to lack generality. One way of extending the understanding obtained from the numerous previous field studies is to undertake numerical modelling of the main hydrodynamic factors implicated in lake sedimentation and their dependence on both lake morphology and external forcing.

1.4 Numerical Modelling of Lake Hydrodynamics and Sediment Dynamics

Given the complexities of lake sedimentary processes, numerical modelling approaches are becoming increasingly popular as a means of characterising the circulation, mixing and stratification processes that control the transport and deposition of sediments (Rueda *et al.*, 2003; Lee *et al.*, 2007; Chao *et al.*, 2008; Chao *et al.*, 2009). For studies of vertical thermal structure and density stratification, especially in small lakes, one-dimensional (1D) models have been used with some predictive success, and also coupled with biogeochemical and ecosystem models (Svensson, 1998; Blenckner *et al.*,

2002; Elliott *et al.*, 2007; Saloranta & Andersen, 2007). Two-dimensional (2D) (vertically averaged) schemes have been used in a few cases, where depth-variation in velocity or temperature is not significant. This is usually the case only in very shallow water bodies (Fragoso *et al.*, 2008) and this approach is thus not very common in the limnological literature. In most lakes, especially in which wind-driven currents dominate the water circulation, 2D models are inappropriate and three-dimensional (3D) schemes are required. In most cases, models that assume a hydrostatic pressure distribution are employed (e.g. Stansby, 1997; Jin & Ji, 2005).

A variety of numerical schemes are available for fluid dynamics problems (Ji, 2008). The most popular are based on finite difference, finite element or finite volume methods. Finite difference methods (*FDM*) are the most straightforward to implement. These use either an orthogonal or non-orthogonal curvilinear grids (Blumberg *et al.*, 1987; Tan, 1992; Lin & Chandler-Wilde, 1996). Finite differences are sometimes considered to have advantages over finite element methods (*FEM*) in terms of the accuracy and efficiency of the solution. However, improvements in *FEM* (Reed & Hill, 1973; Maday & Patera, 1989; Cockburn *et al.*, 1990) have made *FEM* the most common approach, especially on account of their better ability to represent very irregular domain boundaries. More recently, finite volume methods (*FVM*) have been used in numerical computations of fluid dynamics (Versteeg & Malalasekera, 1995). *FVM* resolve the governing equations expressed in the integral form, ensuring the conservation of mass, momentum and energy by the flux calculation in every single unit volume (LeVeque, 2002). The finite volume method thus combines the best attributes of finite-differences (e.g. simple discrete computational efficiency) and finite-elements (geometric flexibility) (Chen *et al.*, 2003).

In terms of their representation of time and space, numerical models can be categorised as: 1) steady state or time dependent (dynamic) and 2) zero, one- (1D), two- (2D) or three-dimensional (3D) respectively. Steady state models are useful when the input data and boundary conditions are constant in time and the governing equations are thus a function only of space. On the other hand, time-dependent models include the time derivatives in the governing equations, so the output is affected by changes in the forcing and boundary conditions (Abbott, 1991; Tsanis *et al.*, 2007).

Model selection must necessarily be guided by the requirement of the project, including the resources available and the research questions to be addressed. Choice of a particular model may also be influenced by the level of technical support available,

the quality of supporting documentation and the professional recognition of its performance. The range of hydrodynamic and related (e.g. water quality or sedimentary) processes will also feature in the choice between a simple and a complex model, and its resolution in space and over time (Hearn, 2008; Ji, 2008).

Comprehensive models are often preferred over simple models for large and complex water systems, since they provide not only predictive output but also aid the understanding of the underlying hydrodynamic, water quality and sediment transport processes in the system. 3D models offer the closest approximation to reality by simulating gradients along all three spatial dimensions. Since the 1990s, such models have improved greatly in their capability and the enormous developments in computing mean that models that would once have required a super-computer can now be run on the desktop. A wide variety of 3D models is available, including commercially-developed packages such as *DELFT3D* (Lesser *et al.*, 2004) and open-source community models (e.g. *POM*, Blumberg & Mellor, 1987; *FVCOM*, Chen *et al.*, 2003). Although all essentially solve the same 3D Navier-Stokes equations, they differ in terms of their approach to turbulence closure, numerical solution method, discretization in space (grid or mesh type) and treatment of boundary conditions. It must also be remembered that although 3D numerical models represent one extreme of the complexity spectrum, they still do not include all the processes and mechanisms that may govern the behaviour of an aquatic system. Also, despite their physically-complete representation of the real world, they still incorporate empirical coefficients that must be calibrated by reference to observations. All such models also remain highly dependent upon the quality of the data used to calibrate and force them (Jin & Ji, 2004; Cea & French, 2012).

In limnology, 3D numerical models have mainly been applied in the context of water or sediment quality problems (Park, 1995; Rajar & Cetina, 1997; Taguchi & Nakata, 1998). In the case of Oaks Arm basin of Clear Lake, California, a 3D numerical model was employed to understand the implications of hydrodynamic circulation for the dispersion of mine-derived mercury in the water body. Numerical simulation showed that the cyclonic baroclinic circulation is driven by stratification, periodic and uniform winds, and Coriolis effects that, in turn, influence the transport and redistribution of mercury (Rueda *et al.*, 2003). Sediment resuspension in upland lakes can impact the physical and chemical environment of the water column (Kristensen *et al.*, 1992; Mehta, 1996). Increased suspended sediments can reduce light availability, which then impacts algal and aquatic vegetation growth (Blom *et al.*, 1994) and also can affect

the cycling of nutrients by absorption and desorption of dissolved nutrients from the water column (Cerco & Cole, 1994).

Numerical modelling of hydrodynamics and sediment transport can be used to evaluate the response of a ecosystem to changes of sediment concentration in the water column. A well-known case is Lake Okeechobee, a large shallow multi-functional lake in south Florida, USA. The water quality of Lake Okeechobee has been affected dramatically in the last century as a result of nutrient input from agriculture and other human activities (Havens *et al.*, 1996). 3D numerical modelling has been undertaken with the aim of evaluating the impacts of sediment resuspension on the lake water quality (Jin & Ji, 2005). Model results indicate that wind waves and water currents drive sediment resuspension/deposition in the water column, affecting the water quality via the elevation of phosphorus concetration in shallower zones that are rich in fish populations.

Although hitherto primarily used in larger lowland lakes, 3D numerical hydrodynamic modelling clearly has considerable potential as a means of evaluating the factors controlling spatial patterns of sediment accumulation in smaller upland lakes. The present study uses numerical modelling to evaluate the influence of meteorological forcing on the hydrodynamics of an upland oligotrophic lake. Modelled circulation patterns and variations in the bottom stress due to currents and surface wind waves are compared with the observed distribution of bottom sediments with a view to evaluating the applicability of the sediment focusing model in similar systems subject to strong wind forcing.

1.5 Aims and Objectives

This thesis aims to advance the understanding of hydrodynamics and patterns of sediment accumulation in upland lakes through physically-based numerical modelling. Specifically, a numerical hydrodynamic model is used to investigate the sensitivity of water circulation and the distribution of bottom stress in upland lakes to meteorological forcing. Inferences are then made concerning the linkages between hydrodynamics and the distribution of bottom sediments.

This broad aim is addressed through a number of specific objectives:

1. Development of a new 1D model with which to characterize lake vertical structure as affected by meteorological forcing and to provide a context for higher dimensional modelling.

2. Adaptation of an existing open source 3D finite volume hydrodynamic model (*FVCOM*; Chen *et al.*, 2004a) for application to upland lake problems, including the development of a new fetch-limited wave module.

3. Development of a Graphical User Interface (GUI) for the enhanced *FVCOM* code, including pre- and post-processing tools specifically designed for lake modelling problems.

4. Implementation and validation of the modified *FVCOM* code to a case study lake (Llyn Conwy, North Wales, UK) and investigation of the sensitivity of its circulation to meterological forcing at hourly to annual timescales.

5. Investigation of the relations between modelled hydrodynamics and the observed distribution of bottom sediments, with a view to testing the applicability of sediment focusing hypothesis in Llyn Conwy basin.

Chapter 2

Research Design

Resume

This chapter outlines the scientific approach for this study. UCLAKE*, a new 1D lake dynamic model, is described and its use to characterise lake behaviour prior to the deployment of higher dimension models is outlined. The selection of the 3D* FVCOM *model, is then justified in more detail. The formulation and capabilities of* FVCOM *are summarised, together with some of its limitations. A case is made for the development of a pre- and post-processing interface to facilitate application of* FVCOM *to the problem of meteorological forcing of lake hydrodynamics and sedimentation. Finally, the case study location, Llyn Conwy, is described along with details of existing datasets and the data acquisition campaigns undertaken as part of this research.*

2.1 Computational Modelling Approach

Computational modelling (Te Chow *et al.*, 1988; Abbott, 1991; Versteeg & Malalasekera, 1995) has been widely used to tackle a wide variety of hydrodynamic problems relating to transport processes, buoyant jets and plumes, density stratified flows in natural environments, and sedimentation and erosion of particulate matter (Fischer, 1979; Imberger, 1998; Ji, 2008; Mohanty, 2008). In the context of lakes, 1D schemes have been widely applied to the representation of vertical variability in temperature, water quality, suspended sediment concentration and biological processes in lakes (Imberger *et al.*, 1978; Riley & Stefan, 1988; Hamilton & Schladow, 1997). 1D models have low

CPU and memory usage requirements by modern standards and their computational efficiency makes them particularly suited to the simulation of longer-term behaviour, including resolution of both seasonal and interannual variability in hydrodynamic and associated physical and biological processes (Hamilton & Schladow, 1997). For example, Bell *et al.*, 2006 used a 1D model to simulate seasonal variations in the temperature and oxygen depth profiles of Bassenthwaite Lake in the English Lake District. Another 1D model used to simulate vertical temperature variation and ice thickness in two small lakes, Thrush Lake (Minnesota) and Little Rock Lake (Wisconsin), showed standard errors of 0.48 and 0.68 °C respectively in modelled mean winter water temperatures (Fang & Stefan, 1996). 1D models have been applied mainly in small to medium-sized lakes, where the assumption of minimal spatial variability in the water mass is reasonable and justifies the emphasis on vertical variation. However, such an assumption is much less reasonable in larger lakes, or in small lakes that are subject to strong wind forcing and/or where density currents are known to be important (Fischer, 1979).

Increases in computing power have meant that 2D depth-integrated hydrodynamic models have become widely used to model systems that can be considered vertically well-mixed but which exhibit large horizontal variability. Such schemes are well suited to problems involving rivers and floodplains (Gee *et al.*, 1990; Nicholas & Walling, 1997; Horritt & Bates, 2002), and well-mixed estuarine and coastal waters (Ji *et al.*, 2001; Cea *et al.*, 2006). They have also been applied to wetlands and very shallow lakes (Moustafa & Hamrick, 2000; Lam *et al.*, 2004; Fragoso *et al.*, 2008). These models allow better approximation of physical processes that show a strong spatial variability (Blom *et al.*, 1992). In their research on Lake Ketel, a shallow Dutch lake, Blom & Toet, 1993 used a 2D model to simulate the erosion of polluted bottom sediments. More generally, the inability of 2D depth-averaged models to resolve vertical stratification of the water column means that their applicability to lake problems is extremely limited.

The earliest implementations of 3D models were mainly concerned with ocean hydrodynamic problems (Blumberg & Mellor, 1987), and even when implemented at coarse spatial resolution, incurred high computational overhead. However, the combination of rapid advances in computer power and the development of more efficient numerical algorithms to solve the three-dimensional form of the equations of fluid motion have made the implementation of such models a much more practical proposition. 3D models are increasingly implemented using unstructured meshes and typically comprise modules to represent a wide range of physical processes (Chen *et al.*, 2003; Lesser

et al., 2004; Chao *et al.*, 2008).

In limnology, 3D models have been more commonly applied to the understanding of hydrodynamic processes in large lakes. They are well suited to resolving complex circulation patterns and processes influencing water quality (Jin *et al.*, 2000; Chen *et al.*, 2004c; León *et al.*, 2007). However, the implementation of such models in small upland lakes has been very limited. This is probably because 1D models have usually been considered to be adequate for studies concerned primarily with the thermal structure of lakes at seasonal and longer timescales (Ford & Stefan, 1980). Studies in which sediment resuspension has been of interest have usually resorted to empirical formulations (Hamilton & Mitchell, 1996). Even in small lakes, however, 3D models offer clear advantages in their ability to resolve the full complexity of water circulation and the interaction between sediments and the water column. In fact, as the review of lake hydrodynamics in the previous chapter has shown, a 3D scheme is necessary to realistically simulate hydrodynamic and sediment transport processes in lakes subject to strong wind forcing.

Despite this, 1D models retain a role in lake modelling on account of their computational efficiency, which makes them particularly sited to the simulation of longer-term lake behaviour. It is often useful to gain preliminary insights into the behaviour of a system using a simple model before progressing to models of greater complexity and computational cost. Accordingly, a 1D model (*UCLAKE*) was first developed in order to understand more fully the physical behaviour of the case study lake. This model was validated against existing temperature profile data (see below), and the resulting understanding assisted with the implementation of a 3D model that was used for the main part of the study.

An ocean model, *FVCOM* (Chen *et al.*, 2003; Chen *et al.*, 2004a), was chosen for the 3D modelling. *FVCOM* is the product of a community modelling effort and is fully open source. A significant limitation is the lack of any graphical interface to support model implementation and visualisation of results, and the development of such an interface is an important component of this study. In addition to wind-driven circulation, surface wind waves are an important factor influencing the dynamics of bottom sediments. The generation and propagation of wind waves was therefore investigated using a newly-developed semi-empirical wave model, *UCL-SWM*. The *UCL-SWM* model was benchmarked against the widely-used but more computationally-intensive *SWAN* 3rd generation spectral model (Booij *et al.*, 1996; Booij *et al.*, 1999; Jin & Ji, 2001). Both

the *FVCOM* and *UCL-SWM* models were validated against observations drawn from existing datasets as well as from additional datasets acquired during the course of this study.

The *UCLAKE*, *FVCOM* and *UCL-SWM* simulations are then used to investigate the nature of water circulation within a case study lake. Llyn Conwy, an upland lake in the North Wales, UK, was chosen for this purpose (see Section 2.8). This work investigates the sensitivity of the modelled velocity field to wind speed and direction. Variations in bottom stress due to the combined effects of wind-driven circulation and surface wind waves are investigated, along with their likely influence on the accumulation of bottom sediments.

2.2 Model Calibration and Validation

Calibration involves adjusting certain empirical parameters of a model with the aim of fitting the model output to real data. This process succeeds if the model is able to reproduce observed variability in the processes of interest to an acceptable level of accuracy (Moriasi *et al.*, 2007). The calibration is usually carried out for a specific time period taken from a portion of a longer historical sequence of real data, from which is also extracted an additional portion of data against which to perform a separate model validation (Power, 1993). Such calibration and validation periods must span a representative time interval that exhibits the sufficient variability in the processes of interest. However, the choice of such periods is often restricted by the availability of data. In the event of low data availability the calibration period should be selected to subject the model to the most challenging tests.

Model calibration also requires a sensitivity analysis of the model parameters with the aim of establishing their sensible ranges. Such analysis also aids the identification of those parameters that cause major changes in the model output, which makes it easier to achieve the calibration of complex multi-parameter models. Many difficulties arise during model calibration and most of them are related to availability and quality of the real data. Uncertainty is introduced during the acquisition of field data because of the precision of the measurement devices and inaccuracies in their calibration (French, 2010; Cea & French, 2012). It is thus important to pre-analyse the information with the aim of 'cleaning up' the time series before using it as model input or during calibration (Sutherland *et al.*, 2004).

Calibration should evaluate the model performance both qualitatively and quantitatively. The qualitative evaluation is made on the correctness and plausibility of the physical model behaviour and requires expert knowledge to judge. On the other hand, the quantitative evaluation should also be made with reference to one or more objective performance functions (Sutherland *et al.*, 2004; Moriasi *et al.*, 2007). Standard regression techniques are commonly used to evaluate the linear relationship between modelled data and observed information by calculating the slope (m) and the correlation coefficient (ρ) (e.g. Santhi *et al.*, 2001).

Dimensionless model performance formulations include the Nash-Sucliffe efficiency (NSE) (Equation 2.1) that relates the relative magnitude of the residual variance ('noise') and the measured data variance, establishing how well the model output fits the observed values (Nash & Sutcliffe, 1970; Legates & McCabe, 1999). An efficiency < 0 indicate that the residual variance exceeds the data variance (i.e the mean of the observed data is a better predictor than the model). Values close to 1 are preferred. Henriksen *et al.*, 2003 present a qualitative classification of NSE values ranging from 'very poor' ($NSE < 0.2$) to 'exellent' ($NSE > 0.85$), although this kind of classification reflects judgements that will likely depend on exactly what is being modelled.

$$NSE = 1 - \frac{\sum_{i=1}^{n}(Y_i^o - Y_i^s)^2}{\sum_{i=1}^{n}(Y_i^o - Y^o)^2} \qquad -\infty \leq \text{NSE} \leq 1. \tag{2.1}$$

Error index goal functions include the following (Singh *et al.*, 2005; French, 2010):

- Mean absolute error (MAE)

$$MAE = \frac{1}{N}\sum_{i=1}^{N}|Y_i^o - Y_i^s| \qquad 0 \leq \text{MAE} \leq \infty. \tag{2.2}$$

- Relative mean absolute error (RMAE)

$$RMAE = \frac{1}{N}\sum_{i=1}^{N}\left|\frac{Y_i^o - Y_i^s}{Y_i^o}\right| \qquad 0 \leq \text{RMAE} \leq \infty. \tag{2.3}$$

- Root mean square error (RMSE)

$$RMSE = \frac{1}{N}\sqrt{\sum_{i=1}^{N}(Y_i^o - Y_i^s)^2} \qquad 0 \leq \text{RMSE} \leq \infty. \tag{2.4}$$

Values near to 0 for MAE, RMAE and RMSE indicate very small model errors. These metrics indices are valuable because they are expressed in the original units of the variable of interest.

The calibration and validation of the computational models implemented and utilized in the present research utilises NSE as a measure of overall model performance, supported where appropriate by one or more of the absolute error metrics.

2.3 One-dimensional Lake Dynamic Model, *UCLAKE*

Although higher dimension models offer the best approach to simulate physical processes in lakes, these are still computationally expensive, which restricts their use, especially in exploratory modelling. Certainly, for initial modelling to get a feel for lake behaviour and the characterisation of vertical structure, 1D models remain a valuable tool (Holland *et al.*, 1982; Henderson-Sellers, 1984).

Several 1D lake models have been developed in the last 20 years. These are usually classified as either eddy diffusivity models, such as: MINLAKE (Riley & Stefan, 1988) and QUALAKE-DOT (Antonopoulos & Gianniou, 2003), or energy budget models, such as DYSREM (Imberger & Patterson, 1981). Eddy diffusivity models describe vertical transport using the advection-diffusion partial differential equation. In contrast with energy budget models, eddy diffusivity models assume a homogeneous distribution in the epilimnion and estimate the turbulent diffusion coefficient using either an analytical (Henderson-Sellers, 1984) or empirical (Orlob & Selna, 1970) approach. The latter are based on turbulence closure schemes in which vertical transport is related to the turbulent kinetic energy induced by surface wind stresses.

As a first approach to understand the most significant physical processes in lakes and provide insights into lake behaviour at seasonal interannual scales, a new 1D eddy diffusivity model (*UCLAKE*) (Morales *et al.*, 2011-Unpublished) has been developed. This simulates the vertical temperature structure in spatially homogeneous lakes and reservoirs. *UCLAKE* resolves the 1D advection-diffusion equation through the water column using an implicit finite difference scheme. The model includes groundwater inflows, river inflows and water withdrawals, such as the water outlets in a reservoir dam. River inflows are treated as density currents on the basis that inflowing water often differs in density from the lake surface water. The density current model in *UCLAKE* is based on the methodology described by Akiyama & Stefan, 1984, which predicts the vertical layer within which the inflowing current becomes mixed.

One of the advantages of 1D lake dynamic models is that they do not require spinning-up to achieve realistic initial conditions for a simulation. 2D and 3D models require previous model runs to reach a steady-state condition with respect to the hydrodynamics. 1D models do not because the spatial variation of the field velocities is not involved, and convective forces are mapped by the turbulent diffusion coefficient,

which is usually adjusted to improve the model performance. Therefore the initial conditions for a 1D simulation are usually taken from observations.

In contrast with models such as MINLAKE (Riley & Stefan, 1988), QUALAKE-DOT (Antonopoulos & Gianniou, 2003) and TEMIX (Bell *et al.*, 2006) that perform the computation on a daily time step, *UCLAKE* provides hourly resolution. This permits the representation of diurnal variations of lake temperature, including the effects of the small scale changes in meteorological forcings on the temperature structure. This was considered important given the later focus on modelling such forcing in 3D. Although the model is numerically stable on account of the use of a implicit finite differences scheme, there is a risk of excessive numerical diffusion. To deal with this, an algorithm is included to adapt the time-step as a function of the turbulent diffusion coefficient, in order to control the numerical diffusion and to damp spurious behaviour of the time series.

UCLAKE has been programmed in C and offers very good computational efficiency. Thus, for a year of simulations using 25 vertical layers, the program takes approximately 8 min to run on a Sun Ultra 24 workstation with 3 GHz Intel Xeon quad-core processor. It is thus particularly suitable for multi-annual analyses of lake behaviour. The subsections below explain briefly, the theory behind the model, its algorithmic structure and the input information required. A more detailed description is provided by the *UCLAKE* User Manual (Morales *et al.*, 2011-Unpublished).

2.3.1 Model approach

UCLAKE calculates the water temperature profile using several homogeneous layers (Figure 2.1). This approximation is valid for most lakes in which tilting of the epilimnion by the action of wind stresses on the water surface is negligible. The model resolves the advection-diffusion equation (Equation 2.5):

$$\frac{\partial T(z,t)}{\partial t} = \frac{1}{A(z)}\frac{\partial}{\partial z}\left(A(z)Kz(z,t)\frac{\partial T(z,t)}{\partial z}\right) - \frac{1}{\rho C_p A(z)}\frac{\partial (A(z)q(z,t))}{\partial z} \qquad (2.5)$$

where z is the water depth (m) measured downward from water surface ($z = 0$) to the bottom ($z = h$); t is the time (s), $T(z,t)$ is the water temperature (^oC), $A(z)$ is the transverse area (m^2) of the middle of a layer (see Ala_i in Figure 2.1); $Kz(z,t)$ is the turbulent diffusion coefficient ($m^2\ s^{-1}$) and $q(z,t)$ is the net rate of heat ($W\ m^{-2}$)

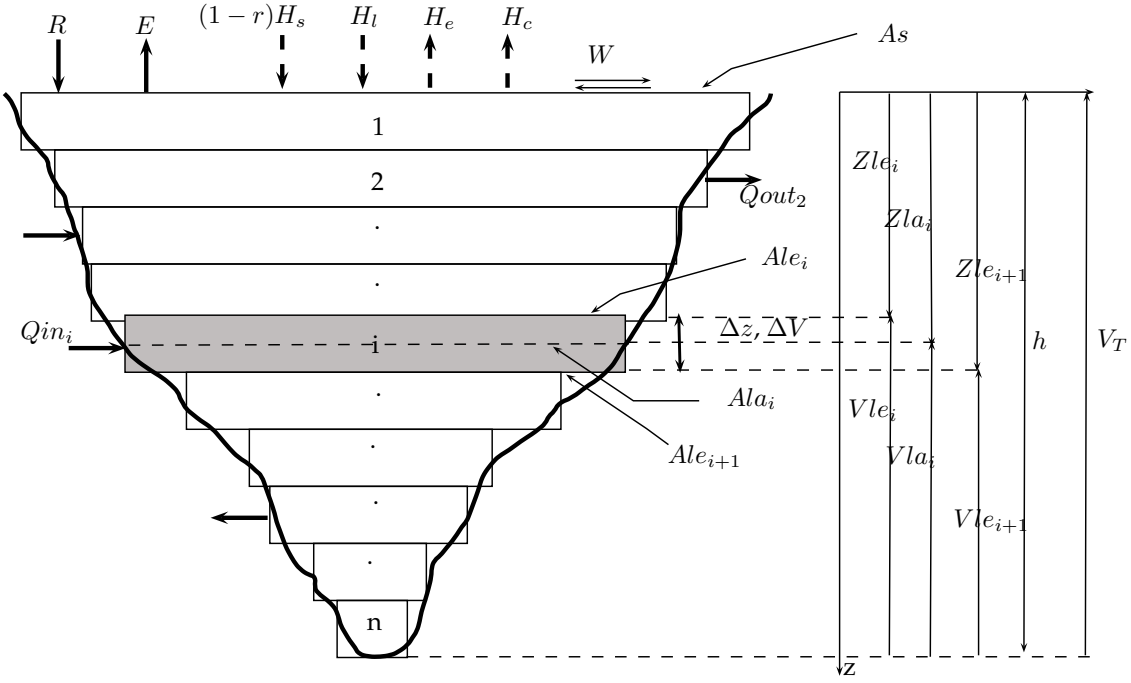

Figure 2.1: Computational discretization of a lake domain in *UCLAKE*.

generated per unit of area absorbed from the top to the bottom layer.

Water surface boundary conditions

The boundary conditions at the water surface are the main driving mechanism of the physical conditions in a lake. These comprise the net heat flux at the water surface and the shear stresses exerted by the wind. The net heat budget, represented as $q(z,t)$ in Equation 2.5, is computed as follows:

$$q(z) = \begin{cases} Hn = (1-r)Hs + Hl - He - Hc & \text{if } z = 0 \text{ (Top layer)} \\ (1-\beta_s)Hn\exp(-\eta z) & \text{if } z > 0 \text{ (Lower layers)} \end{cases} \tag{2.6}$$

where Hn is the net heat flux at the water surface ($W\ m^{-2}$); Hs is the short-wave irradiation measured at the water surface ($W\ m^{-2}$); Hl is the long-wave radiation ($W\ m^{-2}$); He is the evaporated heat flux, Hc is the sensible heat ($W\ m^{-2}$), r is the short-wave reflectivity and β_s is the the short-wave irradiation fraction absorbed at the surface of the lake.

The fluxes described above are evaluated using the following expressions:

- The long-wave radiation (Hl) is the net heat flux between the radiation emitted by the water surface (Hl_{ro}) and the net radiation received from the atmosphere and the clouds (Hl_{ra}) (Henderson-Sellers, 1984).

$$Hl = Hl_{ra} - Hl_{ro} \tag{2.7}$$

Hl_{ro} is estimated as $Hl_{ro} = \varepsilon_w \sigma T_w^4$ where T_w is the water surface temperature in ^oK, σ is the Stefan-Boltzmann constant $= 5.67 \times 10^{-8}$ and ε_w is emissivity ~ 0.97 for water. Hl_{ra} is estimated as $Hl_{ra} = Hl_{ri}(1 - A_L)$, where A_L is the long wave reflectivity constant equal to 0.03. The incoming radiation from the atmosphere and clouds is given by $Hl_{ri} = \varepsilon_a \sigma T_a^4$ where T_a is the air temperature in ^oK and the emissivity ε_a is:

$$\varepsilon_a = \begin{cases} 0.87 - \frac{n}{D}(0.175 - 29.92 \times 10^{-6}\psi e_{sa}) + 2.693 \times 10^{-5} & \text{if } \frac{n}{D} \leq 0.4 \\ 0.84 - \frac{n}{D}(0.100 - 9.973 \times 10^{-6}\psi e_{sa}) + 3.491 \times 10^{-5} & \text{if } \frac{n}{D} \geq 0.4. \end{cases}$$

In the expressions for ε_a, $\frac{n}{D}$ is the sunshine duration, ψ is the relative humidity given as

$$\psi = \frac{\text{actual vapour pressure}}{\text{saturated vapour pressure}}$$

and the saturated vapour pressure is given by the empirical equation (Glanz *et al.*, 1973) $e_s = 2.171 \times 10^{10} \exp^{-4157/(T-33.41)}$ $(N\ m^{-2})$ where T is the temperature of water or air.

- The evaporated heat flux (He) represents the heat energy loss due to water evaporation; it is estimated as:

$$He = L_v \rho E; \tag{2.8}$$

where the latent heat of vaporisation is given as $L_v = 1000[2500.9 - 2.365(T_w - 273)]$ $(J\ kg^{-1})$, ρ is the water density $(kg\ m^{-3})$ (Huber & Harleman, 1968) give as $\rho = 1000[1.0 - 6.63 \times 10^{-6}(T - 277)^2]$ and E is the evaporation flux $(m\ s^{-1})$ given as $E = f(W)(e_{sw} - e_a)$ where $f(W) = a + bW$ is a function of wind velocity (W), and a and b are constant. *UCLAKE* implements five different formulations (Penman, Meyer, MacMillan, USGS and Sill; Henderson-Sellers, 1984; Morales *et al.*, 2011-Unpublished) to estimate E. One of the most popular is the Penman function $E = 0.44 \times 10^{-10}(1 + 0.437u_2)(e_{sw} - e_a)$, where e_{sw} is the saturated vapour pressure at the water temperature and e_a is the actual vapour pressure at the temperature of the air.

- The sensible heat flux (Hc) is related to He through the Bowen ratio (β)(Henderson-Sellers, 1984) as:

$$Hc = 0.61 \times 10^{-3} pHe \left(\frac{T_w - T_a}{e_{sw} - e_a} \right) \tag{2.9}$$

  where p is the atmosphere pressure ($mbar$).

Additionally turbulent kinetic energy (E_k) is supplied by wind shear and it is available for possible entrainment from the mixed layer to the hypolimnion layers (Ford & Stefan, 1980):

$$E_k = \int_{A_s} C\hat{w}\tau dA_s \tag{2.10}$$

where C is the wind sheltering coefficient, A_s is the water surface area (m^2) and $\hat{w} = \tau/\rho$ is the friction velocity ($m\ s^{-1}$). $\tau = \rho_a C_D w^2$ is the shear stress, where ρ_a is air density ($kg\ m^{-3}$), C_D is the drag coefficient and w is the wind velocity ($m\ s^{-1}$). The drag coefficient is a function of altitude and multiple formulations exist. In *UCLAKE*, C_D is calculated using the following expression originally derived for oceans but also applicable to lakes (Wu, 1982);

$$C_D = \begin{cases} 1.25 w^{-0.5} \times 10^{-3} & w \leq 1.\text{ms}^{-1} \\ 0.5 w^{0.5} \times 10^{-3} & 1. < w < 15.\text{ms}^{-1} \\ 2.6 \times 10^{-3} & w \geq 15.\text{ms}^{-1} \end{cases} \tag{2.11}$$

Water mass balance

Water balance calculation is very important for the understanding of lake hydrodynamics. Low water levels reduce the water depth and enhance the ability of wind to deepen the mixed layer and to re-suspend sediments from the bottom. Inflows such as streams and rivers can modify the basin shape, contribute to the sedimentation and indirectly, affect the lake thermal structure by the modification of the turbidity levels (Håkanson, 1984).

The following water fluxes are included in *UCLAKE*:

- Rainfall and evaporation: Rainfall R ($m\ h^{-1}$) is a measured quantity usually obtained from a meteorological station. The evaporation E ($m\ h^{-1}$) is calculated using the Penman equation (Henderson-Sellers, 1984).

  Both quantities only affect the water balance of the uppermost layer and are considered homogeneously distributed across the water surface. Thus, the balance

at the first layer can be expressed as:

$$\frac{V_1^{t+1} - V_1^t}{\Delta t} = +(R - E)Ala_1^t; \tag{2.12}$$

where V_1 is the volume (m^3) of the first layer.

- Inflows: These are considered to include groundwater flows, river discharges and/or surface runoff. Groundwater flows derive from aquifers that seep into the basin and reach a level conducive to mixing. Rivers and surface runoff are treated as density currents because of the differences with the water density of the lake. Such currents enter the basin, usually with higher density, and move through the stagnant water until reaching the plunge point. The current then slides down the basin bottom until it reaches the layer with similar density, where mixing finally occurs.

- Outflows: These are considered as water withdrawals at the water surface, via streams, artificial channels, or underground pipes. Although the turbulence created by outflows might potentially affect the physical characteristics of the lake such as temperature and turbidity, outflows are only considered in terms of their effect on the water mass balance.

2.3.2 Turbulent diffusion coefficient

The vertical diffusion coefficient ($Kz(z,t)$) is the rate at which the energy available in the system is dissipated through time, at different water depths. Such energy originates from heat energy due to surface heat balance and kinematic energy input by the wind action. So in the event of a calm day with wind velocity close to zero, the energy dissipation is due to the interaction among water molecules at a rate known as the molecular diffusion coefficient (Kz_m), which depends on the water temperature and is approximately equal to $Kz_m \approx 1.2 \times 10^{-7}$ ($m\ s^{-2}$) (Henderson-Sellers, 1984, Bonnet *et al.*, 2000). Thus Kz is a function of time (t) and water-depth (z). Multiple formulations have been deduced from an analytical point of view (Jassby & Powell, 1975) and from empirical analysis (Walters *et al.*, 1978; Simons, 1980; Henderson-Sellers, 1984; Hondzo & Stefan, 1993).

The computation of Kz is performed for the mixed layer (h_{mix}) and for the subsequent layers using the following equations (Henderson-Sellers, 1985):

- Kz at the mixed layer is calculated as follows:

$$Kz_0 = \frac{\hat{w}^2}{uk^*} \exp(-zk^*) \quad 0 \leq z \leq h_{mix} \tag{2.13}$$

where $k^* = 4.7(f/\hat{w})$ is the decay constant of $\hat{w}$, f is the Coriolis coefficient and $u = 22.6\hat{w}w^{-0.1}/\sin(lat)$ is related to wind velocity ($m\ s^{-1}$), and the latitude (lat).

- Kz in the layers below is calculated as follows (Munk & Anderson, 1948):

$$Kz = Kz_0(1 + \alpha R_i^{\gamma})^{-\beta} \quad h_{mix} < z \leq h \tag{2.14}$$

where α, γ and β are constant and usually take values of 37, 2 and 1 respectively (Henderson-Sellers, 1985). R_i is the Richardson number:

$$R_i = \frac{-1 + \sqrt{1 + \frac{40N^2\kappa^2z^2}{\hat{w}^2 \exp -2k^*z}}}{20}$$

where $\kappa = 0.4$ is the Von Karman constant and $N^2 = -(g/\rho)(\partial\rho/\partial z)$ is the Brunt-Vaisala frequency.

Due to the fact that the above expressions are an approximation of the variation of Kz behaviour through the water column, it is necessary to fit Kz at the layers below the mixed layer by limiting it to a maximum diffusion coefficient that must be obtained through calibration.

2.3.3 General model structure

The *UCLAKE* code is structured into different routines that read the input files, perform the computation of the different variables, and write out the results in ascii text format (Figure 2.2). A brief description of the input file contents is given below:

- `casename_run.dat`: This defines run time information such as start time, number of iterations and time step. Various constants and parameters are also defined here.

- `casename_inf.dat`: Inflow information such as: discharge ($m^3\ s^{-1}$), temperature (^oC) and salinity (ppm) for specific water depths and times.

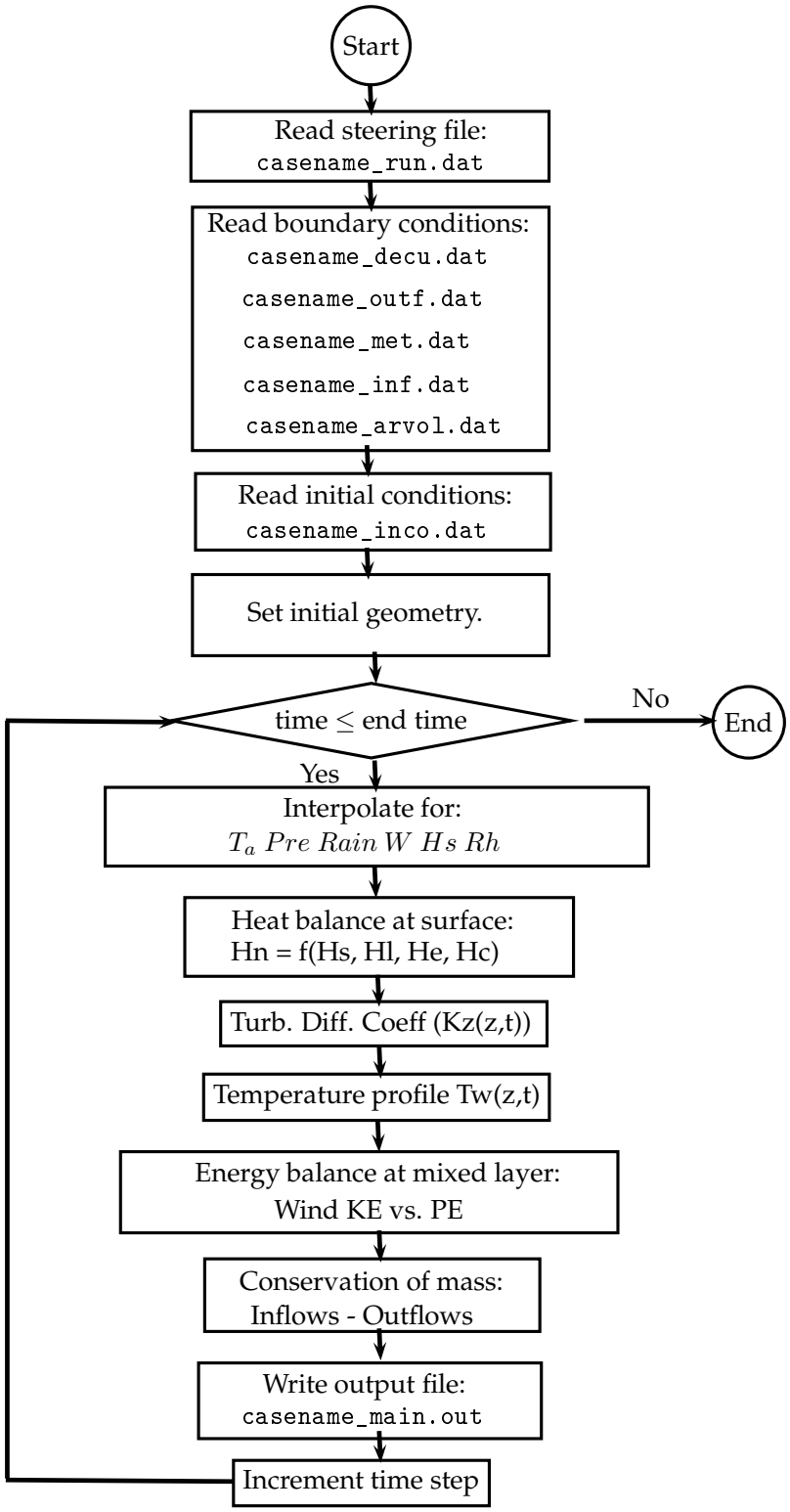

Figure 2.2: *UCLAKE* program structure.

- `casename_arvol.dat:` Relationships of water level against lake area and, water level against lake volume.
- `casename_met.dat:` Meteorological information such as air temperature (^oC), relative humidity (%), air pressure ($mbar$), precipitation (m), wind velocity ($m\ s^{-1}$) and short-wave irradiation ($W\ m^{-2}$).
- `casename_outf.dat:` Time series of outflows at specific water depths.
- `casename_inco.dat:` Water temperature profile at the beginning of the simulation.
- `casename_decu.dat:` Density current information for multiple inflow channels such as channel roughness coefficient, width (m) and slope, and time series for water discharge ($m^3\ s^{-1}$) and water temperature (^oC).

2.4 *FVCOM* Model

FVCOM is a prognostic, unstructured-grid, finite-volume, free-surface, three-dimensional primitive equation ocean model developed originally by Chen *et al.*, 2004a. It has been designed to simulate time-dependent variation in water levels, currents, temperature, salinity, tracers, cohesive and non-cohesive sediments and waves in a variety of marine and freshwater systems. *FVCOM* includes the following capabilities:

1. runtime computed (internal) and pre-computed (external) hydrodynamics,
2. cohesive and non-cohesive sediment transport,
3. sediment-bound tracer transport (conservative or first-order decay),
4. dissolved tracer transport (conservative or first-order decay),
5. neutrally-buoyant particle tracking and
6. inclusion of wind-wave effects on hydrodynamics and sediment transport.

In contrast with other 3D models such as *ECOMsi* (Blumberg, 1991) and *POM* (Mellor *et al.*, 1993), where the equation resolution is performed on orthogonal and non-orthogonal mesh coordinate transformation, *FVCOM* offers the capability of dealing

with irregular geometries using a triangular unstructured mesh (Chen *et al.*, 2003). This makes it well suited to the representation of complex geometries, such as lake basins with highly irregular shorelines. *FVCOM* is programmed in Fortran 90 (see Figure 2.3). Its modular structure allows a user to customise the model with just those routines required for a particular application. It can optionally be compiled using the parallel library *Message Parallel Interface (MPI)* (Cowles, 2008), with the aim of running a model on multiple machines connected through a network or in a cluster.

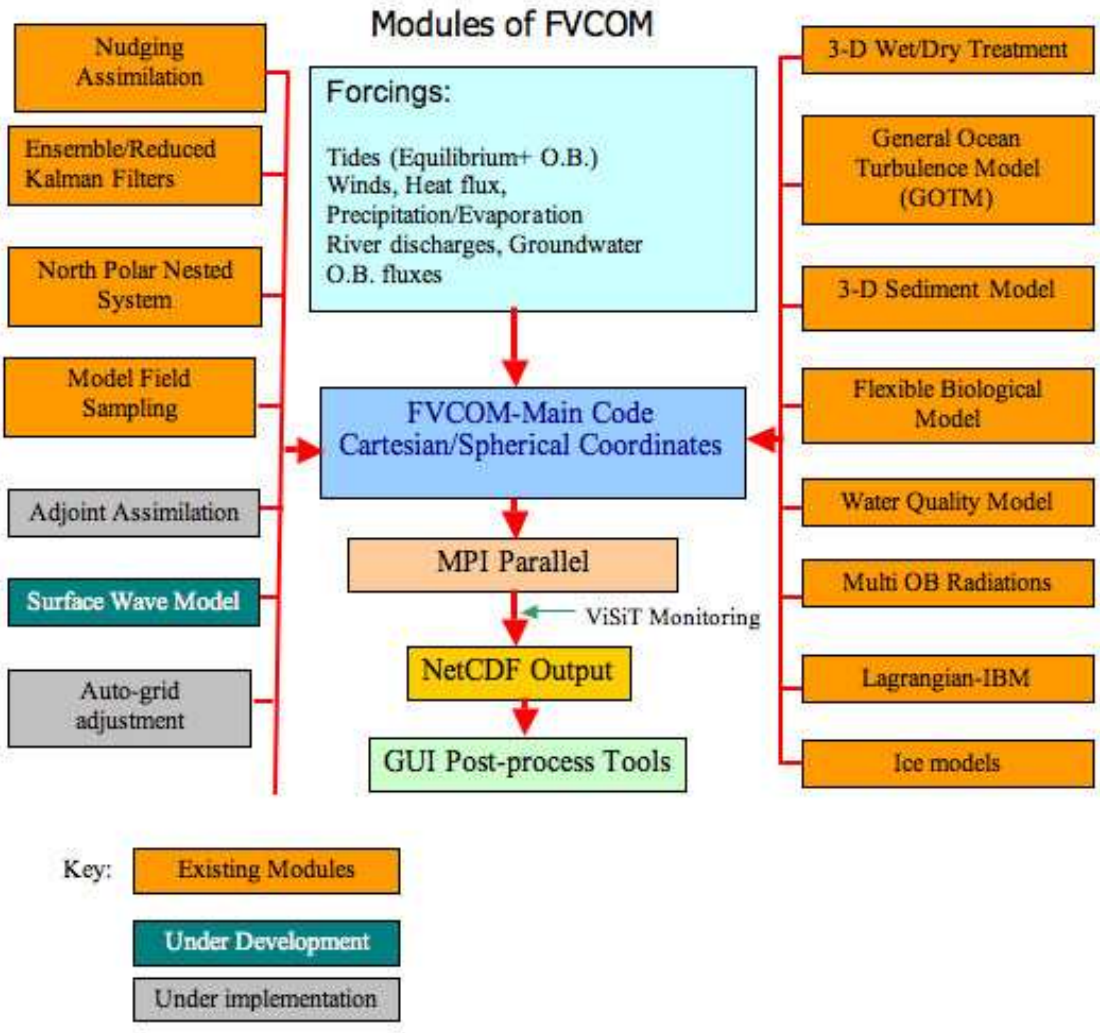

Figure 2.3: *FVCOM* program module structure (from Chen *et al.*, 2004a).

Although originally developed as an ocean model, *FVCOM* has been applied to a number of lakes, including a study of hydrodynamics and thermal structure in Lake Superior, and an examination of the influences of biological matter and sediment transport in the ecosystem of Lake Michigan (Chen *et al.*, 2004b).

2.4.1 Hydrodynamic module

The basic equations in *FVCOM* are cast in a bottom following sigma coordinate system, which is illustrated in Figure 2.4 (Blumberg & Mellor, 1987). The sigma level scheme is based on the transformation of the Cartesian coordinate z, and gives a smooth representation of the bathymetry,

$$\sigma = \frac{z - \zeta}{H - \zeta} \tag{2.15}$$

where $D = H + \zeta$ is water depth, $H(x, y)$ is the bottom topography and $\zeta(x, y, t)$ is the surface elevation. Thus, σ ranges from $\sigma = 0$ at $z = \zeta$ to $\sigma = -1$ at $z = H$.

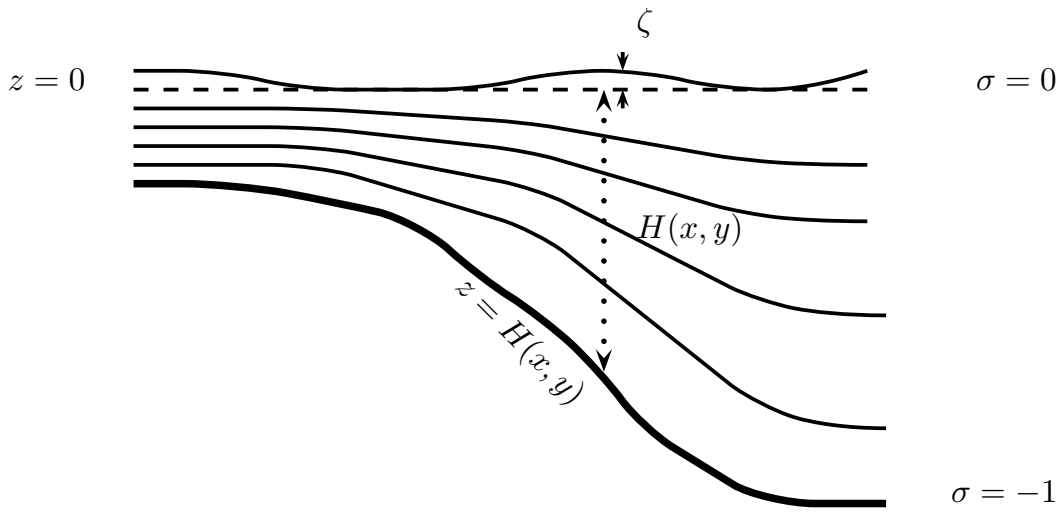

Figure 2.4: The sigma coordinate system used in *FVCOM* .

The equations of mass, momentum and temperature conservation in σ-coordinates are given below:

$$\frac{\partial \zeta}{\partial t} + \frac{\partial Du}{\partial x} + \frac{\partial Dv}{\partial y} + \frac{\partial \omega}{\partial \sigma} = 0 \tag{2.16}$$

$$\frac{\partial uD}{\partial t} + \frac{\partial u^2 D}{\partial x} + \frac{\partial uvD}{\partial y} + \frac{\partial u\omega D}{\partial \sigma} - fvD = -gD\frac{\partial \zeta}{\partial x} - \frac{gD}{\rho_o}\Big[\frac{\partial}{\partial x}\Big(D\int_\sigma^0 \rho\, d\sigma'\Big) + \sigma\rho\frac{\partial D}{\partial x}\Big] + \frac{1}{D}\frac{\partial}{\partial \sigma}\Big(K_m\frac{\partial u}{\partial \sigma}\Big) + DF_x \tag{2.17}$$

$$\frac{\partial vD}{\partial t} + \frac{\partial uvD}{\partial x} + \frac{\partial v^2 D}{\partial y} + \frac{\partial v\omega D}{\partial \sigma} - fuD = -gD\frac{\partial \zeta}{\partial y} - \frac{gD}{\rho_o}\Big[\frac{\partial}{\partial y}\Big(D\int_\sigma^0 \rho\, d\sigma'\Big) + \sigma\rho\frac{\partial D}{\partial y}\Big] + \frac{1}{D}\frac{\partial}{\partial \sigma}\Big(K_m\frac{\partial v}{\partial \sigma}\Big) + DF_y \tag{2.18}$$

$$\frac{\partial TD}{\partial t} + \frac{\partial Tu D}{\partial x} + \frac{\partial TvD}{\partial y} + \frac{\partial T\omega D}{\partial =} \frac{1}{D}\frac{\partial}{\partial \sigma}\Big(K_h\frac{\partial T}{\partial \sigma}\Big) + D\hat{H} + DF_T \tag{2.19}$$

$$\rho = \rho(T) \tag{2.20}$$

wherein the horizontal diffusion terms are defined as:

$$DF_x \approx \frac{\partial}{\partial x}\Big[2A_m H\frac{\partial u}{\partial x}\Big] + \frac{\partial}{\partial y}\Big[A_m H\Big(\frac{\partial u}{\partial x} + \frac{\partial v}{\partial y}\Big)\Big] \tag{2.21}$$

$$DF_y \approx \frac{\partial}{\partial x}\Big[A_m H\Big(\frac{\partial u}{\partial y} + \frac{\partial v}{\partial x}\Big)\Big] + \frac{\partial}{\partial y}\Big[2A_m H\frac{\partial v}{\partial y}\Big] \tag{2.22}$$

$$DF_T \approx \frac{\partial}{\partial x}\Big(A_h H\frac{\partial T}{\partial x}\Big) + \frac{\partial}{\partial y}\Big(A_h H\frac{\partial T}{\partial y}\Big) \tag{2.23}$$

where u, v and ω are the velocity components in x, y and σ directions respectively; T is the water temperature; ρ is the density; f is the Coriolis parameter; K_m is the vertical eddy viscosity coefficient; K_h is the thermal vertical eddy diffusion coefficient; A_m and A_h are the horizontal eddy and thermal diffusion coefficients, respectively. K_m and K_h are parameterized using Mellor & Yamada, 1982 level 2.5 (MY2.5) turbulence closure scheme, as modified by Galperin *et al.*, 1988. On the other hand, A_m and A_h can be used as constant values or using Smagorinsky parameterization method (Smagorinsky, 1963).

The boundary conditions for u, v, ω and T at the water surface ($\sigma = 0$) are defined as:

$$\Big(\frac{\partial u}{\partial \sigma}, \frac{\partial v}{\partial \sigma}\Big) = \frac{D}{\rho_o K_m}(\tau_{sx}, \tau_{sy}); \omega = \frac{\hat{E} - \hat{P}}{\rho} \tag{2.24}$$

$$\frac{\partial T}{\partial \sigma} = \frac{D}{\rho c_p K_h}\Big(Q_n(x,y,t) - SW(x,y,0,t)\Big) \tag{2.25}$$

and at the bottom ($\sigma = -1$) as:

$$\Big(\frac{\partial u}{\partial \sigma}, \frac{\partial v}{\partial \sigma}\Big) = \frac{D}{\rho_o K_m}(\tau_{bx}, \tau_{by}); \omega = \frac{Q_b}{\Omega} \tag{2.26}$$

$$\frac{\partial T}{\partial \sigma} = \frac{A_h D tan\alpha}{K_h - A_h tan^2\alpha}\frac{\partial T}{\partial n} \tag{2.27}$$

where $\hat{P}$ and $\hat{E}$ are the precipitation and evaporation rates, respectively; the $Q_n = Q_s + Q_l + Q_e + Q_c$ is the surface net heat flux, which consists of four components: downward shortwave radiation (Q_n), longwave radiation (Q_l), sensible heat (Q_e), and latent fluxes (Q_c); $SW(x,y,0,t)$ is the shortwave flux incident at the water surface; Q_b is the groundwater volume flux at the bottom and Ω is the area of the groundwater source; c_p is the specific heat of water, α is the slope of the bottom bathymetry and n is a horizontal axis. The downward flux SW is approximated by:

$$SW(x,y,z,t) = SW(x,y,0,t)\left[Re^{z/a} + (1-R)e^{z/b}\right] \tag{2.28}$$

where a and b are attenuation lengths for longer and shorter (blue-green) wavelength components of the shortwave irradiance, and R is the percent of the total flux associated with the longer wavelength irradiance (Simpson & Dickey, 1981).

The shear stresses at the water surface are expressed as:

$$\begin{pmatrix}\tau_{sx}\\ \tau_{sy}\end{pmatrix} = \rho_a C_{dw}\begin{pmatrix}w_x\\ w_y\end{pmatrix}\sqrt{w_y^2 + w_y^2} \tag{2.29}$$

where w_x, w_y are the wind velocity components in x and y respectively, ρ_a is the air density, and C_{dw} is the drag coefficient defined in the model.

Similarly, the shear stresses at the bottom due to flow currents are expressed as:

$$\begin{pmatrix}\tau_{cx}\\ \tau_{cy}\end{pmatrix} = \rho C_d\begin{pmatrix}u\\ v\end{pmatrix}\sqrt{u^2 + v^2} \tag{2.30}$$

where C_d is the drag coefficient determined by matching a logarithmic bottom layer to the model at a height z_{ab} above the bottom; that is:

$$C_d = \max\left[\frac{\kappa^2}{\ln\left(\frac{z_{ab}}{z_o}\right)^2}, 0.0025\right] \tag{2.31}$$

where $\kappa = 0.4$ is the Von Karman constant and z_o is the bottom roughness parameter.

2.4.2 Sediment transport module

The *FVCOM* sediment transport module models the transport of suspended sediments for unlimited number of user-defined size classes of cohesive and non-cohesive sediments. Each class has fixed attributes of grain diameter, density, settling velocity, critical shear stress for erosion and erodability constant. These properties are used to determine the bulk properties of each bed layer (Chen *et al.*, 2004a; Warner *et al.*, 2008).

The suspended load model is represented by the diffusion-advection equation:

$$\frac{\partial C_i}{\partial t} + \frac{\partial uC_i}{\partial x} + \frac{\partial vC_i}{\partial y} + \frac{\partial C_i(w - w_i)}{\partial z} = \frac{\partial}{\partial x}\left(A_h \frac{\partial C_i}{\partial x}\right) + \frac{\partial}{\partial y}\left(A_h \frac{\partial C_i}{\partial y}\right) + \frac{\partial}{\partial z}\left(K_h \frac{\partial C_i}{\partial z}\right) \tag{2.32}$$

where x, y and z are the Cartesian coordinates; the sub-indices i represent the sediment class; w_i the settling velocity; and C_i the sediment concentration.

The boundary condition at the water surface is:

$$K_h \frac{\partial C_i}{\partial z} = 0 \tag{2.33}$$

and at the bottom is:

$$K_h \frac{\partial C_i}{\partial z} = E_i - D_i \tag{2.34}$$

where D_i the depositional flux and the erosion rate (E_i) is calculated as:

$$E_i = \delta t Q_i (1 - P_b) f_{bi} \left(\frac{\tau_b}{\tau_c i} - 1\right) \tag{2.35}$$

where Q_i is the erosive flux, P_b is the bottom porosity, f_{bi} is the fraction of sediment i in the bottom, τ_b is the bottom shear stress for erosion, and τ_{ci} is the critical shear stress of sediment class i.

Sediment is entrained when the local bottom shear stress reaches a critical user-defined value and is removed at a rate defined by the user. The resulting concentration profile depends on the net balance between advection, vertical diffusion, introduction of new material through erosion, and loss of material from the water column through settling (Chen *et al.*, 2004a). The sediment bed is represented by three-dimensional arrays

with a fixed number of layers beneath each horizontal model cell (see Figure 2.5). Each cell of each layer in the bed is initialised with a thickness, sediment-class distribution, porosity, and age. The mass of each sediment class in each cell can be determined from these values and the grain density. The bed framework also includes two-dimensional arrays that describe the evolving properties of the seabed, including bulk properties of the surface layer (active layer thickness, mean grain diameter, mean density, mean settling velocity, mean critical stress for erosion). The bottom stresses are then used by the sediment routines to determine resuspension and transport, providing a feedback from the sediment dynamics to the hydrodynamics (Warner *et al.*, 2008).

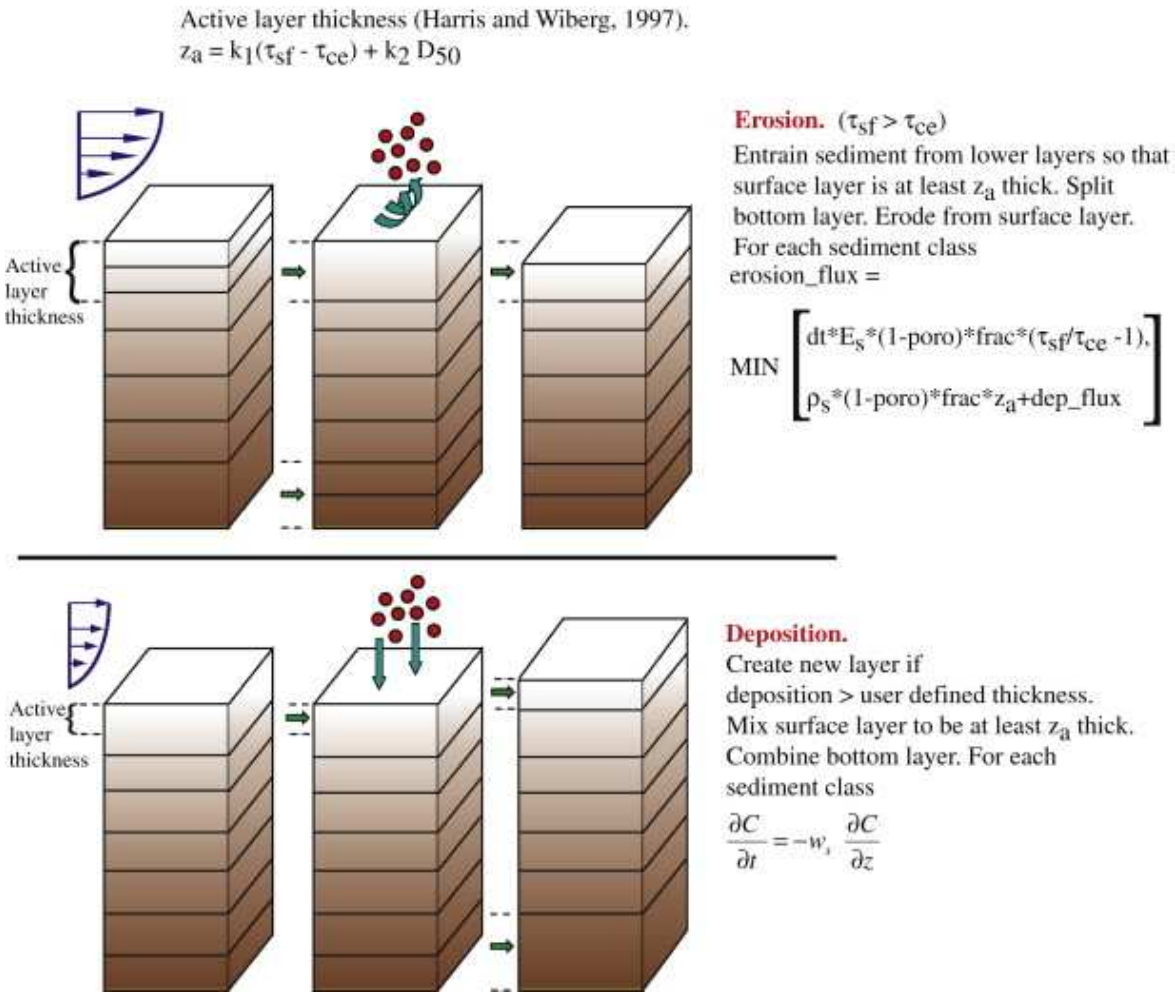

Figure 2.5: Erosion and sedimentation algorithm in *FVCOM* .

The bed layers are modified at each time step to account for erosion and deposition.

At the beginning of each time step, an active layer thickness z_a is calculated based on the relation of Harris & Wiberg, 1997,

$$z_a = \max\left[k_1\left(\tau_b - \overline{\tau_{ci}}\right)\rho_0, 0\right] + k_2 D_{50} \tag{2.36}$$

where τ_b is the bottom skin-friction stress due to current interaction; $\bar{\tau}_{ci}$ the averaged critical stress for erosion over all sediment classes; D_{50} is the median grain diameter of surface sediment and k_1 and k_2 are empirical constants set to 0.007 and 6.0 respectively.

The top bed layer has a minimum thickness equivalent to z_a. If the top layer is thicker than z_a, no action is required. If the top layer is less than z_a thickness, then its thickness is increased by the entering sediment mass in the deeper layers, until the top layer thickness equals z_a. If sediment from deeper layers than the second layer is mixed into the top layer, the bottom layer is split to enforce a constant number of layers and conservation of sediment mass.

2.4.3 Numerical scheme

FVCOM discretizes the horizontal numerical computational domain as a set of non-overlapping unstructured triangular cells, which are comprised of three nodes, a centroid, and three sides. The vertical discretization is integrated over multiple layers from the water surface ($\sigma = 0$) to the bottom ($\sigma = -1$). This scheme is summarised in Figure 2.6.

The model has two calculation modes, an external mode and an internal mode, for each time step, Δt. The external mode resolves the conservation equations integrated vertically, using the modified fourth-order Runge-Kutta time stepping scheme (Kobayashi *et al.*, 1999) for the surface elevation ($D = H + \zeta$) and the vertical averaged velocities, u_a and v_a. The spatial discretization integrates the advective and diffusive fluxes through the element boundary for each bidimensional element.

Assuming that everything is known at t^{n-1} and t^n, the integrals involving the baroclinic forcing and the advective terms are supplied to the external mode along with the bottom stress (feedback process, see Figure 2.7) by the internal mode, whose values are held constant from t^n to t^{n+1}. The external mode uses a Leap Frog discretization scheme (Blumberg, 1991) in the time step Δt_E to get the vertical and time average velocities and water level, utf, vtf and etb at the time t and utb, vtb and etf for a previous time. These values are passed to the internal mode where the 3D equations

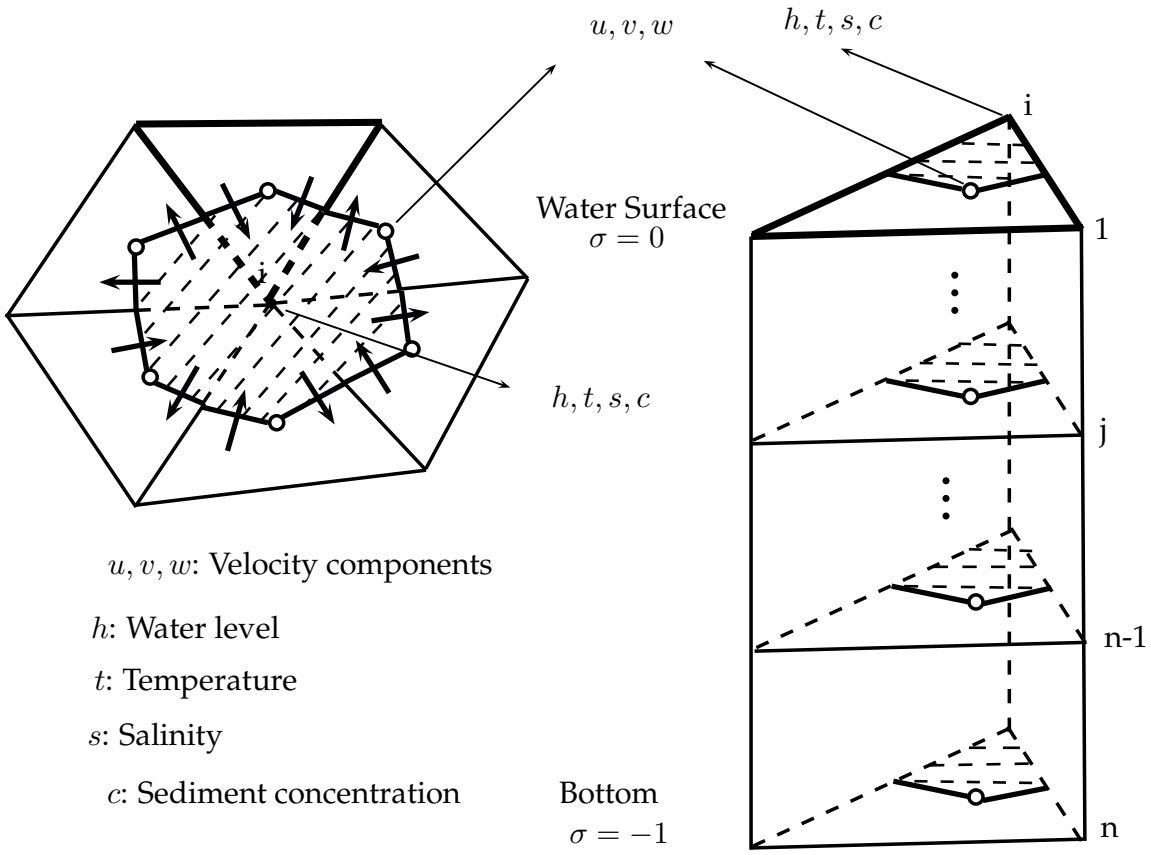

Figure 2.6: Ilustration of *FVCOM* unstructured triangular grid and the locations of the variables.

(described in Section 2.4.1) are solved numerically for a time step Δt_I using a simple combined explicit and implicit scheme in which the local change of the currents is integrated using the first-order upwind scheme.

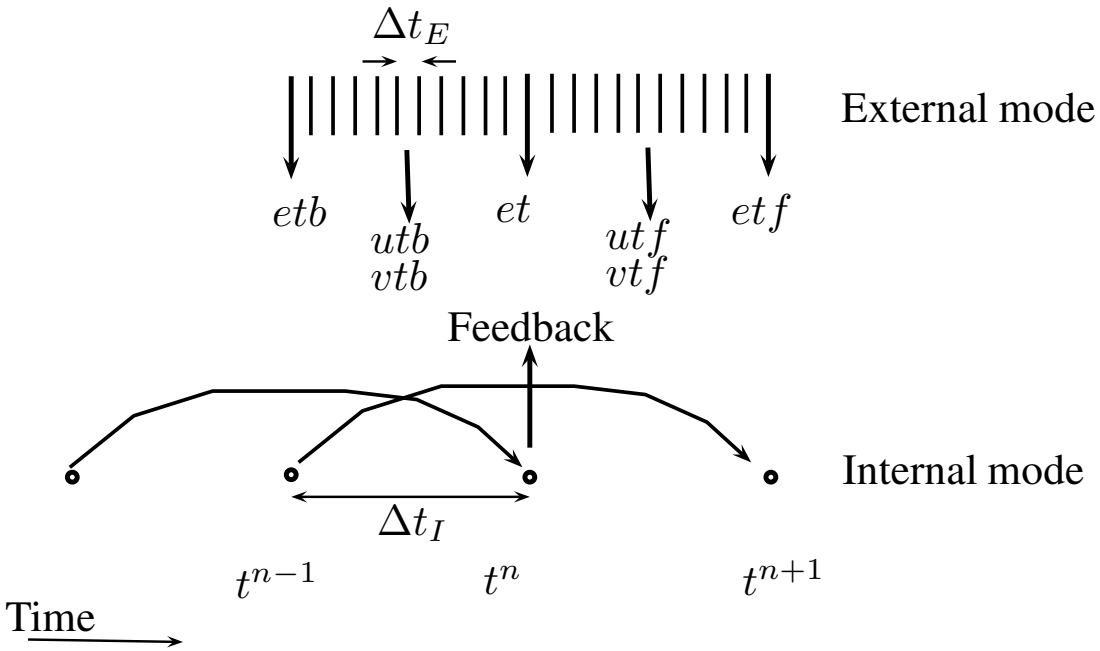

Figure 2.7: Illustration of the interaction of the *FVCOM* external and internal modes.

The numerical solutions of the equations in both internal and external mode, must satisfy the Courant-Friedrich Levy (CFL) stability criterion. This requires that the ratio between the celerity of a gravity wave and the numerical scheme speed must be ≤ 1, so that:

$$\Delta t_E \leq \frac{\Delta L}{U + \sqrt{gD}} \tag{2.37}$$

where Δt_E is the time step of the external mode, ΔL is the computational length scale represented by the shortest edge of the triangular grid elements, U is the magnitude of the horizontal velocity, and D is the local depth. This criterion is derived from the surface gravity wave lineal equation, where advective and diffusive effects are ignored. In the same manner, the time step for the internal mode is restricted by:

$$\Delta_I \leq \frac{\Delta L}{C_1} \tag{2.38}$$

where C_1 is the maximum phase speed of internal gravity waves. Since C_I is usually smaller than $C_E = \sqrt{gD}$, it is desirable that $\Delta t_I \leq 10\Delta t_E$.

2.4.4 Limitations of *FVCOM*

FVCOM is a powerful tool for the simulation of 3D hydrodynamics and its underlying algorithms and numerical scheme have been applied with success in a variety of situations. One of its main limitations, however, is the lack of any graphical interface to support pre-processing of model runs and/or visualisation of the solution files. An early task of the present study therefore was the development of a flexible and friendly graphical user interface, *FVCOM-GUI*, to assist with the compilation of the large number of input files required by *FVCOM* and to analyse and visualise its output files.

The generation of a computational mesh is also a fundamental component of any spatially-distributed hydrodynamic modelling effort. Various proprietary and open source mesh generators are available. Environmental hydrodynamic problems typically involve complex model domains, which may involve highly irregular boundaries and spatial variation in flow depths or surface characteristics (e.g. bottom roughness) that need to be reflected in the model mesh. One of the most capable mesh generators is that provided within the Surfacewater Modeling System (*SMS*) package. Although this is commercial software (marketed by *ems-i* in the USA), it offers features not commonly available in open source alternatives, notably support for a variety of mesh generation algorithms. *SMS* was therefore selected as the primary tool for the generation of meshes in the present study, and the *FVCOM-GUI* thus allows generic SMS-generated meshes to be read directly.

Another limitation of *FVCOM* that is especially important for upland lake problems is the lack of a surface wave model. As noted in Chapter 1 (Section 1.2), wave action is an important aspect of the interaction between hydrodynamics and sedimentation, especially in shallow zones. There is a strong correlation between sediment resuspension and the occurrence of waves because the bottom stresses exerted by waves in the shallower zones usually greatly exceed those induced by currents. The partial dependence of wave characteristics on surface circulation means that coupled wave and current models are often preferred (Zhang & Li, 1997; Warner *et al.*, 2008). However, where

currents are weak, de-coupled calculation of wave generation, propagation, and bottom stress may be sufficient. The requirement to understand spatial variation in wave characteristics and their influence on bottom stress and zones of sediment resuspension and deposition is met here by development of a semi-empirical model, *UCL-SWM*, based on linear wave theory and wave growth as limited by fetch. This simplified, and computationally efficient, model is calibrated and validated against wave observations at multiple locations around the lake shoreline. It is also compared with simulations using the more capable but computationally-intensive *SWAN* model (Booij *et al.*, 1996; Booij *et al.*, 1999).

Like many 3D hydrodynamic schemes, *FVCOM* uses a hydrostatic approximation in place of the vertical momentum equation. In other words, the pressure at any point within the vertical is a function only of the depth. In a lake setting, this hydrostatic assumption is not considered to be a major limitation, since the dynamic pressure effects are likely to be negligible relative to the hydrostatic pressure gradient. However, the modelling of lake hydrodynamics using a non-hydrostatic model is an area worthy of future research.

The active layer bed model (Harris & Wiberg, 1997) used to represent the bottom sediment dynamics in *FVCOM* (and also other models such as *ROMS* (Moore *et al.*, 2004) and *ECOMsi*) does not take account sediment consolidation and the distributions of multiple sediment classes in a cell. The effects of sediment autocompaction are not especially relevant to studies of short-term sediment dynamics (sub-annual scales for which computationally-intensive models such as *FVCOM* are most appropriate), but may be significant at historical and longer timescales.

2.5 Pre-processing and Post-processing

The computational modelling of hydrodynamics and transport processes in lakes and hydrosystems can be thought of as a multi-stage process, the key elements of which are summarised in Figure 2.8. The pre-processing effort usually accounts for a significant proportion of the time taken to complete a modelling study. It includes conceptualising the problem, selecting an appropriate modelling methodology and model, and assembling all the required input data and generating the computational geometry (grid or mesh).

Most modelling systems, including *FVCOM*, comprise several modules (see Figure 2.3) that can be selected and/or customised according to particular requirements. Such customisation may or may not require changes to the model source code and re-compilation to produce an executable binary file. During the compilation the user must set up the links between non-standard libraries and the source code, with the aim of adding the external functions. *FVCOM* also supports execution in parallel across a cpu cluster. Specification of the external *METIS* library that supports parallel processing by dividing the computational domain into a set of zones is therefore an optional part of the compilation process for *FVCOM* (Figure 2.9).

Preparation of the input information usually begins with the specification of the physical boundary of the model domain and its discretization into a computational grid or mesh. As noted above, *FVCOM* uses an unstructured triangular mesh that is generated by an external utility program (in this study, *SMS*). An externally-generated computational mesh must be imported and stored in the required format that defines the spatial co-ordinates of its nodes and the interconnections between them. Bathymetry data must then be assembled and interpolated onto the mesh. The principal run control parameters must then be specified. These generally reside in one or more steering files and include the simulation start and end times, time step, number of iterations, and additional information on the vertical discretization, turbulence coefficients, and output information format. In *FVCOM*, all this input information is stored in ascii files that separately handle the computational mesh, meteorological data, bathymetry, boundary conditions, inflows and outflows, and initial conditions. The meteorological information includes time series for variables such as air temperature, wind direction, wind velocity and solar radiation.

Post-processing encompasses the visualisation and analysis of the results produced by the model. Key tasks at this stage include calibration and validation of the model against observational data, sensitivity analysis to understand the dynamics of the system being modelled, and application of the model in the context of the research questions.

2.6 A Linear Wind-Wave Model for *FVCOM*

Wind-waves exert a major influence on the deposition and resuspension of sediments in lakes (Bengtsson & Hellström, 1992; Bailey & Hamilton, 1997; Jin & Ji, 2004; Cózar

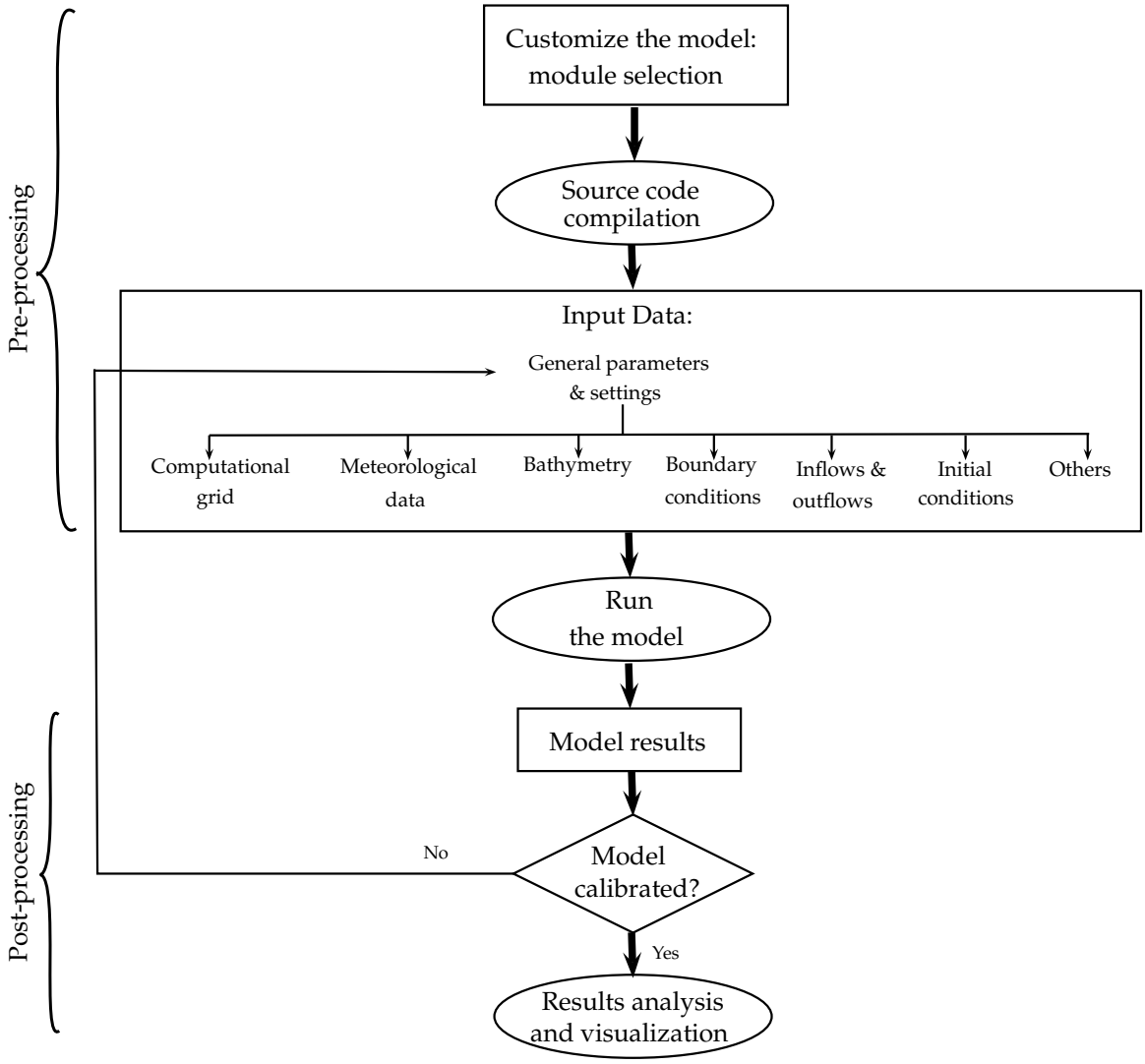

Figure 2.8: General representation of computational modelling in hydrodynamics and transport models.

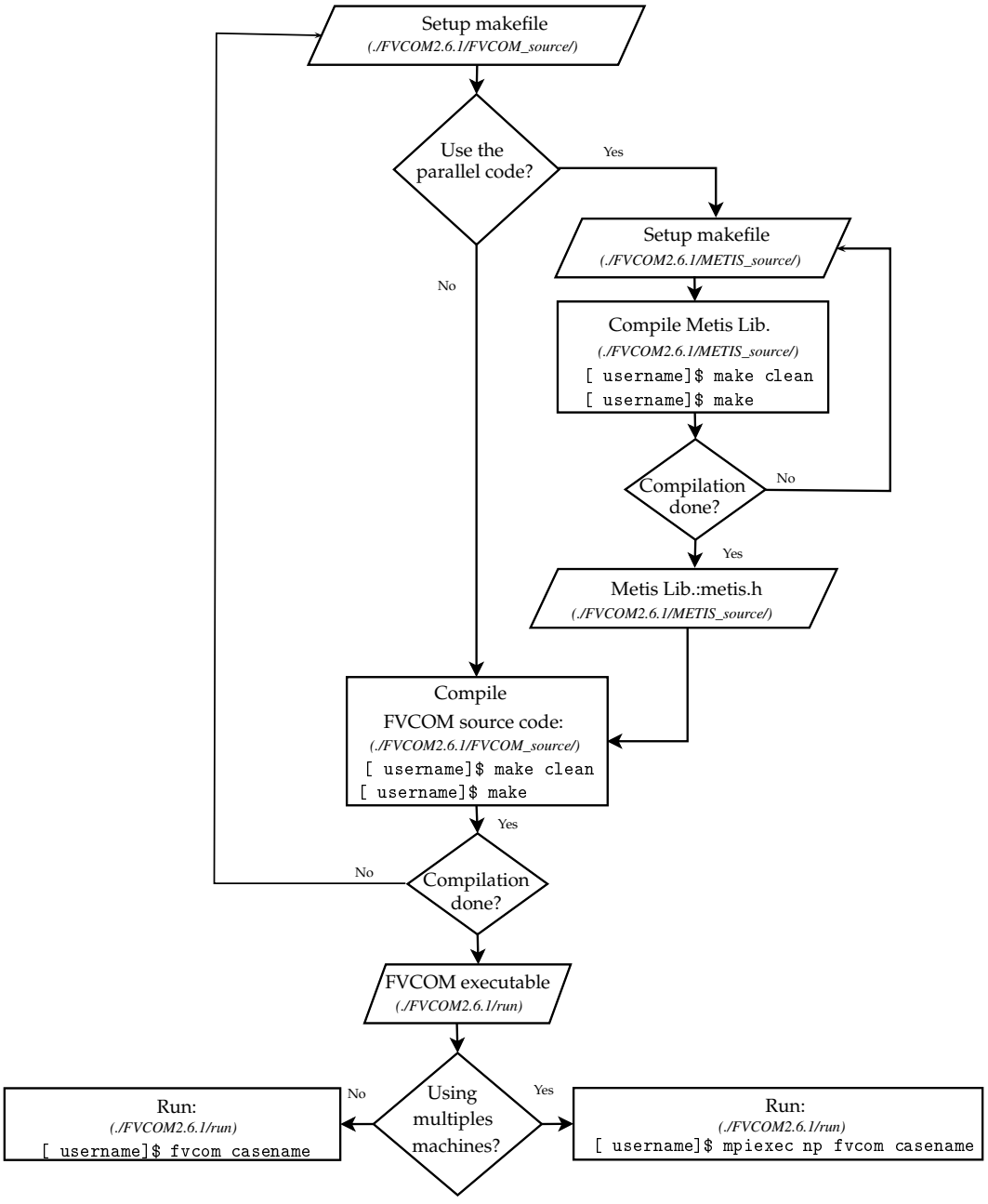

Figure 2.9: Compilation and execution of *FVCOM* .

et al., 2005). When the wind blows over sufficiently large surface water areas, stresses are transfered creating waves of a magnitude that depends on the wind velocity, fetch and water depth (Håkanson, 1977b; Rueda *et al.*, 2005; Fagherazzi & Wiberg, 2009), and also the persistence of the wind (Lövstedt & Bengtsson, 2008).

To address the lack of a wave model in *FVCOM* a linear wave model, *UCL-SWM*, was developed, based on linear wave theory and empirical relationships between the wave properties, physical forcings and the properties of the water body. *UCL-SWM* features include estimation of wave parameters such significant wave height, period, and frequency, and computation of the bottom shear stresses due to waves. With the addition of *UCL-SWM*, *FVCOM* is better able to quantify the sediment resuspended and to identify potential areas of erosion. Among the advantages of *UCL-SWM* in contrast to a more sophisticated wave model such as *SWAN* (Booij *et al.*, 1999) are higher computational efficiency and simplicity of the input information required.

2.6.1 *UCL-SWM* model approach

Sverdrup & Munk, 1947 developed some of the earliest empirical relationships to estimate ocean wave characteristics based on weather conditions. Based on field data from Lake Okeechobee and the Gulf of Mexico, Bretschneider, 1957 developed graphical relations between wave height, wave period, water depth and wind fetch. These where then were translated to empirical formulations, thereby extending the Sverdrup & Munk, 1947 model. This became known as the SMB (Sverdrup, Munk and Bretschneider) model. The *SMB* model was replaced by Hasselmann, 1973, who studied fetch-limited wave growth in deep water. Their *JONSWAP* model was then included in the US Army Corps Of Engineers Shore Protection Manual (Corps & Center, 1984).

The *JONSWAP* model provides good prediction of wave evolution in deep water. However, limitations arise in shallow areas. To address this, Young & Verhagen, 1996a undertook experiments in Lake George, Australia, a shallow ($\approx$ 2 m maximum depth) lake, to study the wave evolution in fetch-limited areas. They derived new empirical formulations in which the non-dimensional wave energy $\epsilon = g^2E/U_{10}^4$ and non-dimensional peak frequency $\nu = fU_{10}/g$ are related to the non-dimensional fetch $\chi = gx/U_{10}^2$ and the non-dimensional water depth $\delta = g\bar{d}/U_{10}^2$ through the expressions:

$$\epsilon = \alpha_1 \left[\tanh A_1 \tanh \left(\frac{B_1}{\tanh A_1} \right) \right]^{\gamma_1} \tag{2.39}$$

and

$$\nu = \alpha_2 \left[\tanh A_2 \tanh \left(\frac{B_2}{\tanh A_2} \right) \right]^{\gamma_2} \tag{2.40}$$

where g is the gravitational acceleration, E is wave energy, f is wave frequency, U_{10} is the wave wind velocity at an elevation of 10 m given by the expression $\frac{U_{10}}{U} = \frac{10}{z}^{1/7}$, x is fetch described as the distance between the point of computation and the upwind shoreline, $A_1 = 0.493\delta^0.75$, $B_1 = 3.13 \times 10^{-3}\chi^0.57$, $A_2 = 0.331\delta^1.01$, $B_2 = 5.215 \times 10^{-4}\chi^0.73$ and the following calibration constants: $\alpha_1 = 3.64 \times 10^{-3}$, $\gamma_1 = 1.74$, $\alpha_2 = 0.133$ $\gamma_2 = -0.37$. The value of $\bar{d}$ is calculated as the mean of the water depth along fetch as:

$$\bar{d} = \frac{1}{x} \int_0^x d(x) dx \tag{2.41}$$

Significant wave height (H) is calculated from wave energy using the expression $E = \rho g H^2/8$ and wave period (T) uses $T = U/(g\nu)$.

The computation of sediment resuspension requires estimation of the bottom shear stress due to waves $(\vec{\tau_w})$ given by (Dyer, 1986):

$$\begin{pmatrix} \tau_{wx} \\ \tau_{cy} \end{pmatrix} = \frac{1}{2} \rho f_w \begin{pmatrix} u_{bx} \\ u_{by} \end{pmatrix} \sqrt{u_{bx}^2 + u_{by}^2} \tag{2.42}$$

where f_w is the friction factor estimated as:

$$f_w = 2(Re_w)^{-1/2} \tag{2.43}$$

where $Re_w = \frac{U_b A_b}{\nu}$ is the wave Reynolds Number. The wave orbital velocity (U_b) and wave orbital amplitude (A_b) are estimated using the equations below (Luettich Jr *et al.*, 1990; Ji, 2008):

$$U_b = \frac{2\pi H}{T \sinh(k\bar{d})} \tag{2.44}$$

$$A_b = \frac{U_b T}{2\pi} \tag{2.45}$$

where k is the wave number obtained resolving the following implicit equation:

$$\frac{2\pi}{T} = \sqrt{gk \tanh(kd)}. \tag{2.46}$$

2.6.2 *UCL-SWM* structure

UCL-SWM is programmed in a structured way using *Fortran 90*. Figure 2.10 shows the program structure. The model starts by reading the `casename_run.dat`, which is a configuration file to set the model parameters and to enable/disable additional computations. The mandatory files consist of the x, y and z node coordinates (`casename_xyz.dat`), the connectivity of the triangular elements (`casename_cnod.dat`) that form the unstructured triangular mesh, the water level as a function of time (`casename_lev.dat`), the wind velocity and the wind direction as function of time (`casename_met.dat`), x and y flow velocity components as a function of space and time (`casename_vel.dat`) and bottom roughness coefficient as a function of space (`casename_rou.dat`). An optional file (`casename_sed.dat`) is required to run a sediment module, which identifies potential areas and rates of sediment resuspension.

The computation in *UCL-SWM* begins with the interpolation of the time-dependent variables such as wind velocity, wind direction and water level. Then, according to the water level value, any wet elements (triangles) are identified. This is followed by calculation of the fetch and the mean water depth $\bar{d}$, using the following algorithm:

1. Extraction of the triangle edges belonging to the main basin shoreline and island shorelines.

2. As the fetch and $\bar{d}$ are calculated in each node of the mesh, the following is the procedure used for a node `i`:

   (a) Identify whether the node `i` is on the shoreline. If it is, it is necessary to know the distance from node `i` to the closest shoreline following the upwind direction of the wind (go to next step). If by following such direction, the search algorithm finds itself outside the mesh, the fetch is zero and $\bar{d}$ is equal to water depth in `i` (start calculation for the next node).

   (b) Identify nodes that are in the quadrant opposite to the wind direction.

   (c) Find the element edges that intersect the straight line along the wind direction from node `i`. Element edges that are parallel to the line are ignored during the search.

   (d) If more than one shoreline is encountered, the nearest to `i` is chosen.

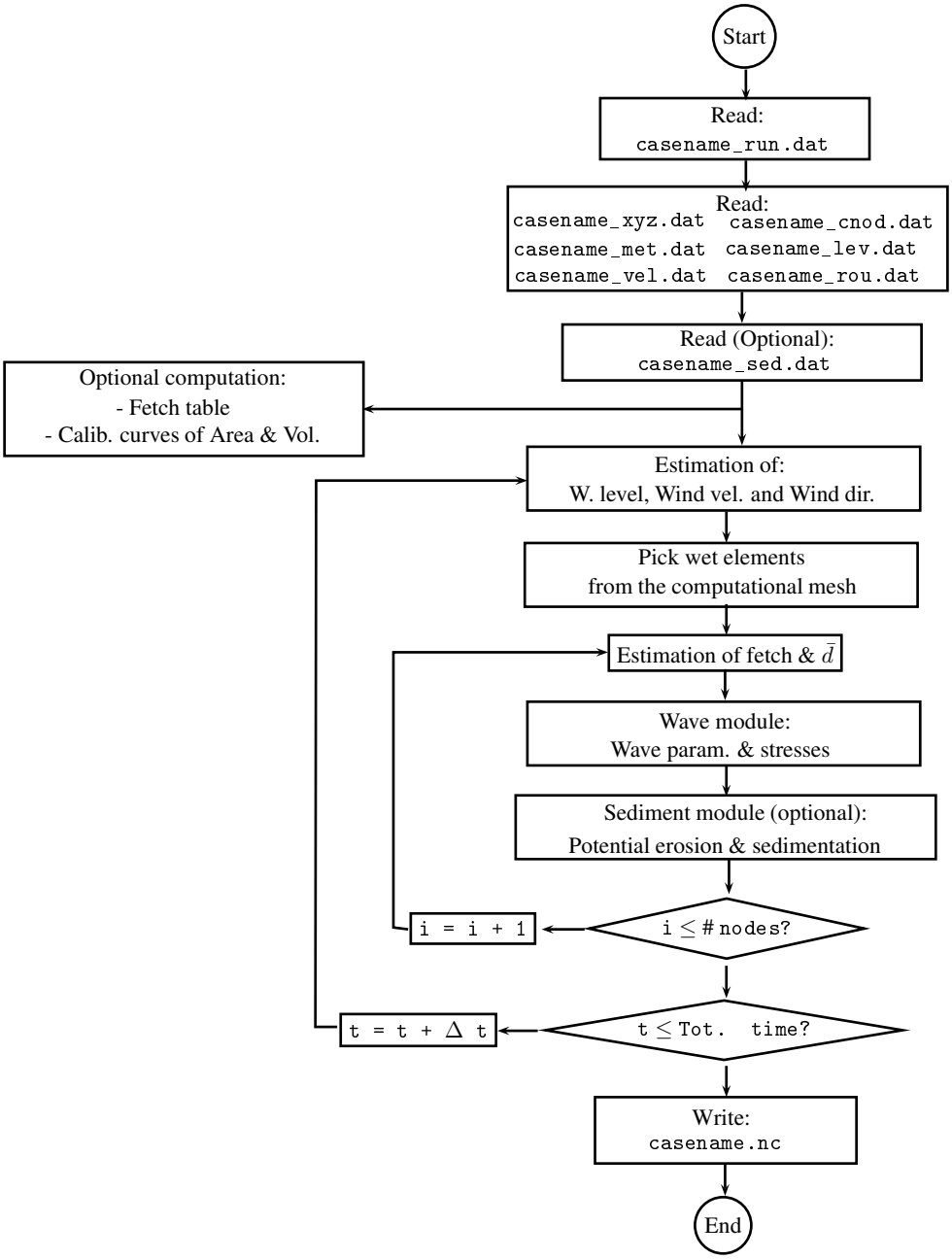

Figure 2.10: *UCL-SWM* program structure.

(e) Calculate the fetch as the distance between the intersection point and the point `i`. Calculate $\bar{d}$ by the Equation 2.41 using the closest points to the fetch line.

Once the fetch and $\bar{d}$ has been estimated, *UCL-SWM* calculates the wave parameters and the bottom stresses using the equations described above.

Information such as fetch, wave parameters, wind stresses and sedimentation information are written in (`casename.nc`), using the *NetCDF* library (Rew & Davis, 2002), which provides a compact and structured way to store large datasets. *UCL-SWM* offers the option of computing key information as a look-up fetch table and calibration curves for lake area and volume. The fetch table is computed for multiple values of wind directions (columns) and water levels (rows), both dimensions uniformly distributed. Calibration curves for the lake area and volume are estimated as a function of the water depth.

2.7 Oscillatory Motions

Oscillatory motions or seiches are a fundamental aspect of the hydrodynamics of closed basins. Such motions are caused when wind acting on the water surface pushes the fluid downwind tilting the surface and leading to vertical circulations in the mixed layer (Imberger & Hamblin, 1982). The tilting of the mixed layer is balanced by a counter-flow circulation in the lowest layers causing the tilting of the pynocline (hypothetical layer that distinguish the mixed layer from the lowest layers) in the opposite direction. When the wind ceases or changes its direction, free back-and-forth oscillatory motions of the lake water surface (Csanady, 1975; Ji & Jin, 2006) commence.

The occurrence of seiches can trigger more complex motions such as Kelvin and Poincare waves. The former are triggered along the shores as consequences of the periodic oscillation of the lake. Kelvin waves also rotate counter-clockwise around the lake and decay exponentially toward the interior, and look similar to a spinning coin just before it falls flat (Csanady, 1967; Hodges *et al.*, 2000). Poincare waves look similar to Kelvin waves but combine the gravitational effects of Earth's rotation and posses transverse velocity components.

Seiches are parametrized by the estimation of the vertical displacement ($\Delta\zeta$) at the downwind end, and the period (T_1) at which seiches oscillate. Assumming that the lake basin can be represented by a closed rectangular channel with vertical walls and

uniform depth, from the 1D motion equation the vertical displacement is calculated using the following espression (Ji, 2008):

$$\Delta\zeta = \frac{\tau_s L}{\rho g H} = \frac{C_D \rho_a w^2 L}{\rho g H} \tag{2.47}$$

where C_D is the wind drag coefficient, w is the wind velocity, L is the horizontal distance, H is the mean water depth, ρ is the water density and ρ_a is the air density. Similarly, the the longest seiche period (T_1) for free oscillations in a lake basin is given by:

$$T_1 = \frac{2L}{\sqrt{gH}}. \tag{2.48}$$

Seiches are potentially an important feature of lake hydrodynamics, not least because they can influence sediment transport and the distribution of bottom sediments (Gloor *et al.*, 1994). Seiches usually interact with the bathymetry at different levels with varying consequences for sediment dynamics. Oscillatory motions of the mixed layer resuspend sediments in shallow areas and enhance the transport by the action of Kelvin and Poincare waves. On the other hand, within layers below the mixed layer, seiches interact with the benthic turbulent layer to resuspend sediments and enhance the transport of matter between the sediments and the water body.

2.8 Case Study Design

2.8.1 Llyn Conwy

Llyn Conwy (Lake Conwy), a small upland lake in North Wales, UK, was chosen for an intensive case study for the various modelling approaches developed in this thesis. Llyn Conwy is situated at an altitude of 450 m above mean sea-level at the head of the Conwy catchment (Figure 2.11, Figure 2.12a). The surrounding catchment is small (96 ha compared to a lake area of 40 ha) and its moderate relief has a maximum elevation of 526 m, only 75 m above the lake surface (Patrick & Stevenson, 1986). Catchment geology is a mixture of Ordovician and Silurian mudstones and shales, with occasional outcrops of Ordovician volcanics (Patrick & Stevenson, 1986). Soils are predominantly blanket peats, with some ditching dating from the 1930s to 1960s; these have since been blocked as part of a project to restore the peat upland habitat. The peatland's dominant vegetation is *Calluna vulgaris*, *Erophorum vaginatum*, *Cladonia* spp and *Sphagnum* spp. Two small streams enter the lake from the northeast (Figure 2.12b)

and southeast but inflow is largely distributed around the shoreline and occurs by seepage and surface runoff from the blanket peat. A single outflow drains from the southern end of the lake into the River Conwy. Mean and maximum water depth are approximately 7.7 and 22.0 m respectively, and the bathymetry is characterised by a central basin flanked by shallower bays to the south and east.

The lake provides a secondary source of drinking water to the upper Conwy Valley and its level is controlled by an artificial sill (Figure 2.12c). Lake water level may fall below this level in the summer or due to water supply abstraction. Since the level changes due to abstraction are small (estimated at < 1 m) and given the relatively small inflows and outflows, these are neglected in the present model application.

Mean annual precipitation is approximately 2300 mm, and mean annual temperature is 8^oC (Austnes *et al.*, 2010). The lake is exposed to strong wind forcing in the form of predominantly westerly to southwesterly winds. A Centre for Ecology and Hydrology (CEH) automatic weather station installed within the catchment between 2006 and 2008 recorded mean annual wind speeds of $\sim$10 $m\ s^{-1}$, with peak hourly wind speeds exceeding 30 $m\ s^{-1}$ on several occasions.

2.8.2 Data acquisition

The primary datasets required for the Llyn Conwy modelling study include bathymetry, time-series of various meteorological forcing variables, time-series of vertical thermal structure, and observations of surface water circulation, vertical velocity structure, and surface wave characteristics, and information on the nature and distribution of the bottom sediments.

One of the main factors influencing the selection of Llyn Conwy as a case study was the availability of data from an instrumented buoy deployment by CEH Bangor. These data were collected as part of a broader programme to monitor upland lakes throughout the UK, and include time series of water temperature variation with depth measured with a thermistor string in the deepest part of the lake (see Figure 2.13). The thermistor string was equipped with 10 platinum resistance thermometers (PRTs) deployed at 2 m intervals in the vertical. The CEH monitoring programme also included acquisition of meteorological data at two automatic weather stations, one located on the buoy and the other sited close to the lake shoreline (see Figure 2.13). Table 2.1 summarizes the extent of these data.

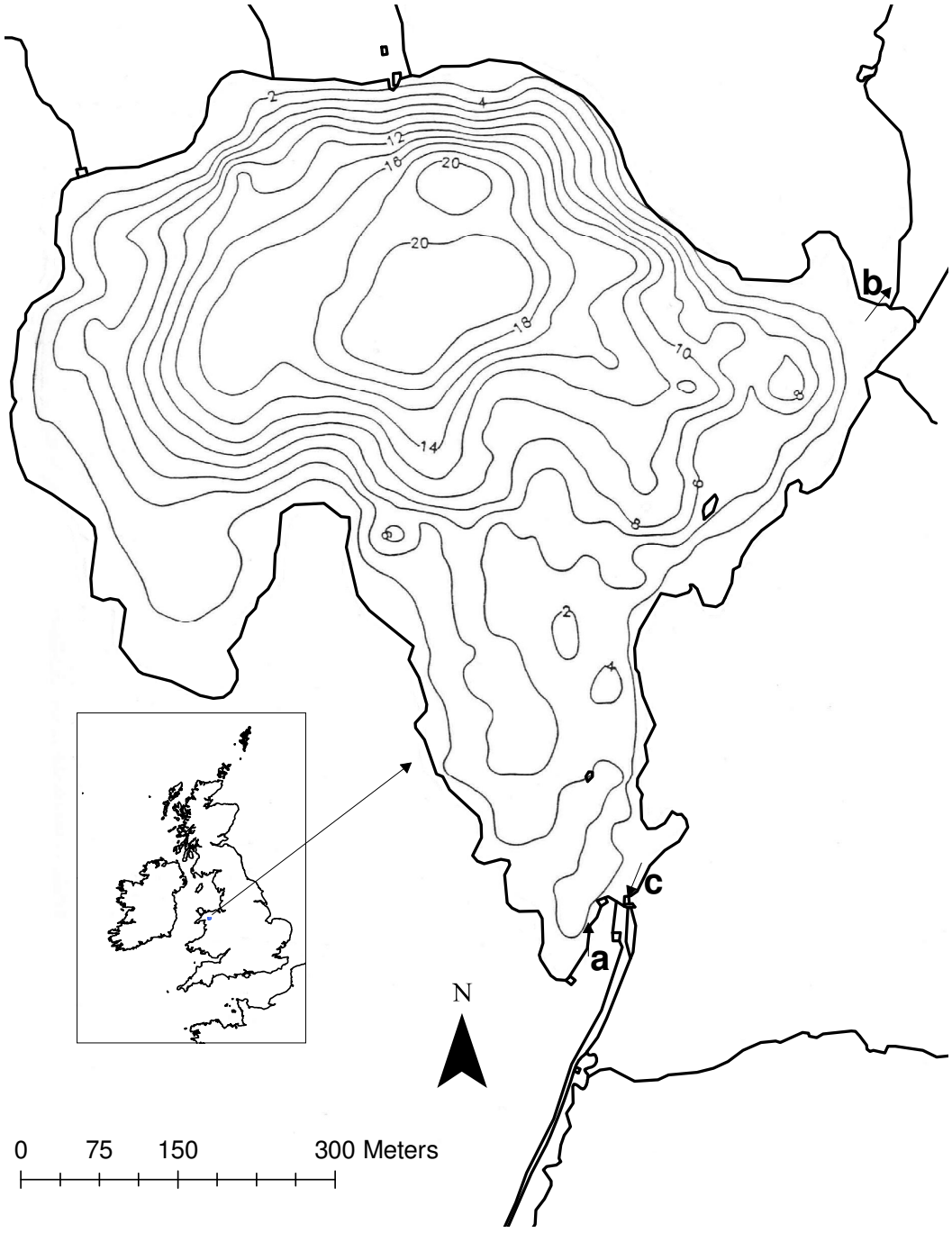

Figure 2.11: Llyn Conwy general location and bathymetry (depth contours in m). *a, b, c* refer to location of photographs in Figure 2.12. Bathymetry is sourced from Patrick & Stevenson, 1986.

(a) Northerly view.

(b) Inflow on northeastern shore.

Figure 2.12: Photographs of Llyn Conwy in July 2010.

(c) Outflow showing evidence of minor fluctuations in lake level (arrows).

Figure 2.12: (Continued).

Table 2.1: Summary of meteorological and limnological data collected by CEH at Llyn Conwy.

	Buoy Station	Weather Station
Latitude	53.001555^o	52.993484^o
Longitude	-3.8200267^o	-3.814053^o
Elevation	450 m (a.s.l)	460 m (a.s.l)
Start Date	02/11/2006	01/11/2006
End Date	15/12/2008	17/07/2007
$\Delta time$	1 Hour	1 Day
Measured Data	wt ws wd at ap sr	rh ws wd at st ra sr
Completeness %	$\approx$ 89.6 %	$\approx$ 11.0 %

wt: Water temperature (C^o); at: Air temperature (C^o);
sr: Solar radiation ($W\ m^{-2}$); ap: Air pressure ($mBar$);
ws: Wind speed ($m\ s^{-1}$); wd: Wind direction (Deg);
st: Soil temperature (C^o); ra: Rainfall (mm);
rh: Relative humidity (%)

Table 2.2: Summary of data available from UK Met. office station 1171 at Capel Curig.

Latitude	53.0939^o
Longitude	-3.94016^o
Elevation	216 m (a.s.l)
Start Date	01/01/2005
End Date	01/01/2010
$\Delta time$	1 Hour or 1 Day
Measured Data	atm_d atM_d at_h ws_h ra_h wd_h
Completeness %	$\approx$ 98.5 %

atm_d: Daily min air temperature (C^o)
atM_d: Daily max air temperature (C^o)
at_h: Hourly air temperature (C^o)
ws_h: Hourly wind speed ($m\ s^{-1}$)
wd_h: Hourly wind direction (Deg)
ra_h: Hourly rainfall ($mm\ h^{-1}$)
Note: The ra_h serie ends in 04/11/2009.

The information recorded by CEH Bangor contains significant gaps, and an attempt was made to fill these using UK Met Office MIDAS station data. Station 1171 (Capel Curig No. 3; see Table 2.2) was particularly useful for this purpose given its proximity to Llyn Conwy and the completeness of its data.

Two field campaigns were undertaken in order to acquire the additional data needed for calibrate the 3D hydrodynamic model (including the wave sub-model) together with information on the nature and distribution of the lake bottom sediments. Data acquired in these campaigns are summarised in Tables 2.3 and 2.4. The first campaign (July 2010) included reconnaissance survey of the lake, preliminary data on variation in wind waves with fetch and wind speed and direction, measurements of surface circulation and core sampling of the bottom sediments. Sampling locations are shown in Figure 2.13. The second campaign (April 2011) concentrated on the acquisition of extended wind wave data and more intensive measurements of the vertical velocity field at two locations within the lake. Systematic mapping and sampling of bottom sediment characteristics was also undertaken at this time. Measurement and sampling locations for this campaign are shown in Figure 2.14.

Meteorological data were obtained using a Davis Automatic Weather Station (AWS)

equipped with sensors for wind speed (±3% accuracy), direction (±7 degree accuracy), temperature (accuracy ±1 °C), pressure (accuracy ±1 mB) and relative humidity (accuracy ±3%). The AWS was installed on a small island off the eastern shore of the lake (Figure 2.13 summarises this and other measurement locations), with the sensors approximately 2 m above the water level.

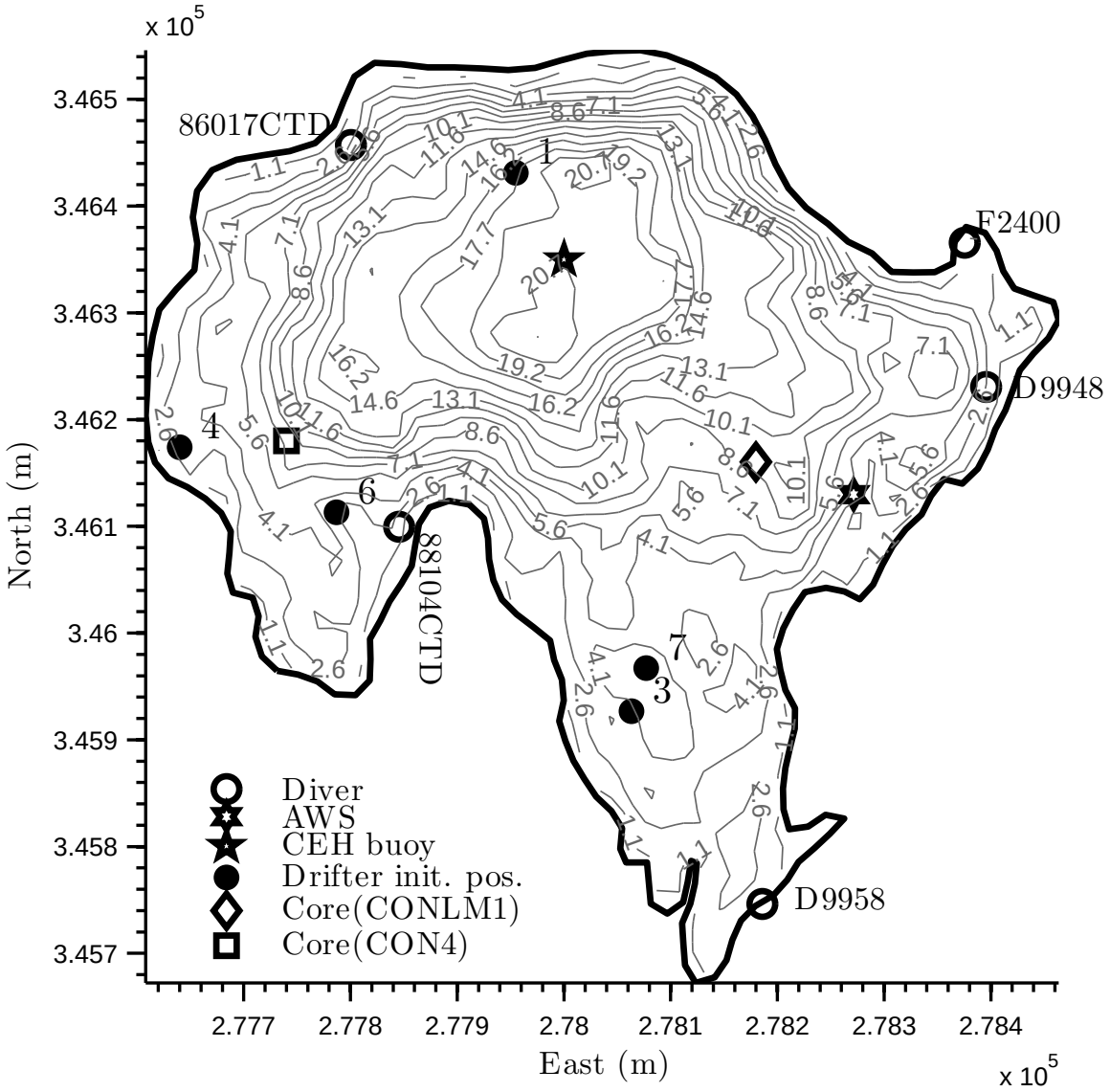

Figure 2.13: Locations of the CEH data buoy, and measurements made in the July 2010 field campaign. Location of 1987 (CON4) and 2010 (CONLM1) cores also shown.

Wind wave measurements were undertaken at 6 locations around the lake shore

Table 2.3: Summary of data acquired during field campaign 1 (5-9 July 2010). AWS = Automatic Weather Station.

Measurement	**Device**	**Duration**	**Purpose**
Meteorology (wind speed and direction, air temperature, pressure and relative humidity)	Davis AWS	6-8 July	Forcing for wave and hydrodynamic models
Wind waves	Druck PTX1830 pressure sensor and Campbell CR10 data recorder systems (6 units)	6-8 July	Validation of *UCL-SWM* wave model
Water level fluctuations	Cera-Diver self recording pressure sensors (5 units)	6-8 July	Analysis of seiching
Water temperature hydrodynamics	Cera-Diver self recording pressure sensors (5 units)	6-8 July	Validation of FVCOM
Surface circulation patterns hydrodynamics	GPS drifters (5 units)	7 July	Validation of FVCOM
Secchi depth	Secchi disc	8 July	Parameterisation of 1D UCLAKE model
Sediment coring	Rodless piston corer (Chambers & Cameron, 2001)	8 July	Estimation of sediment accumulation rate

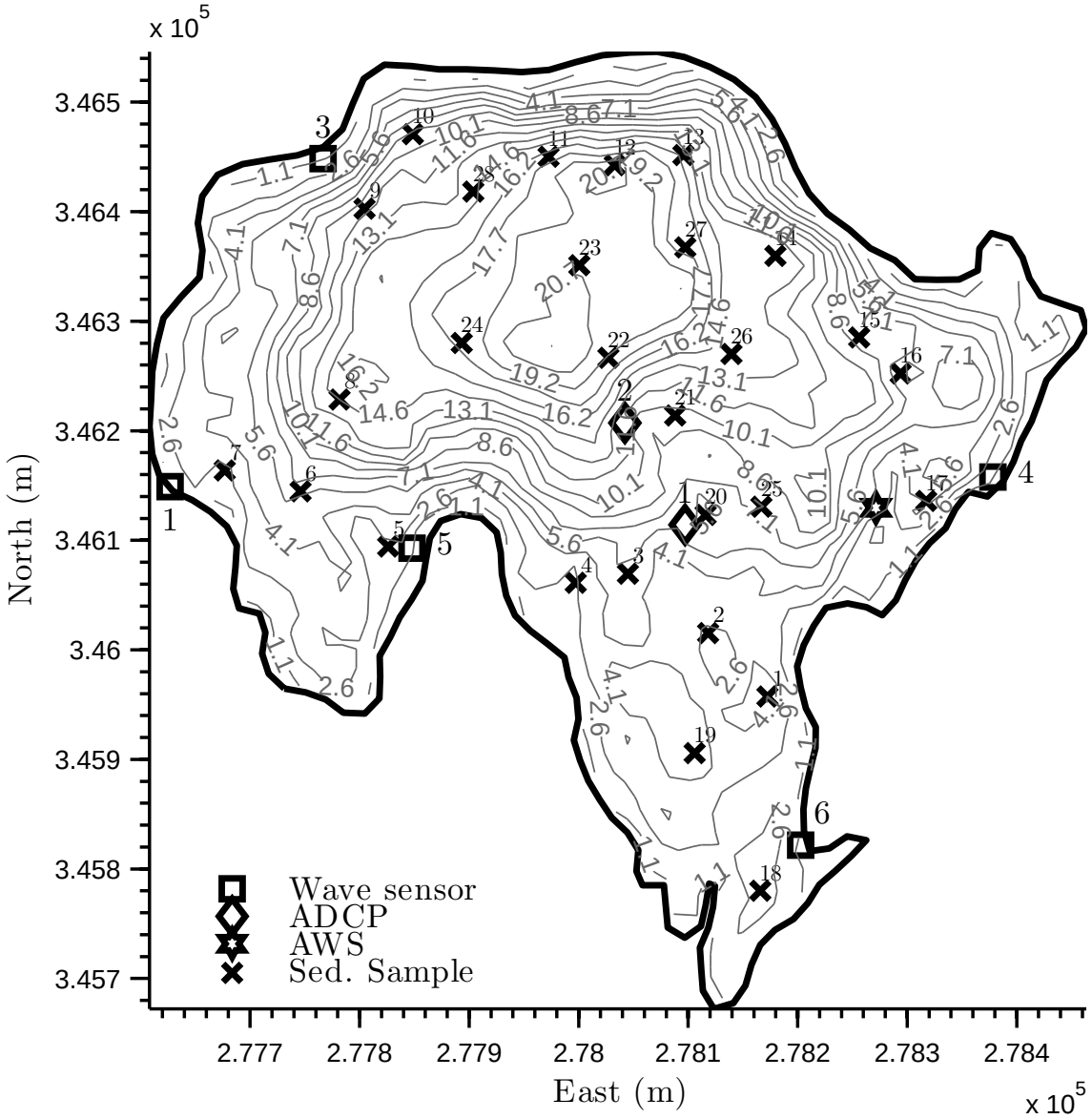

Figure 2.14: Locations of the measurements and sampling in April 2011 field campaign.

Table 2.4: Summary of data acquired during field campaign 2 (3-8 April 2011).

Measurement	**Devise**	**Duration**	**Purpose**
Meteorology (wind speed and direction, air temperature, pressure and relative humidity)	Davis AWS	3-8 April	Forcing for wave and hydrodynamic models
Wind waves	Druck PTX1830 pressure sensor and Campbell CR10 data recorder systems (6 units)	3-8 April	Validation of UCL-SWM wave model
Vertical velocity profiles	ADCP (RDI Workhorse 1200KHz)	4-6 and 6-7 April	Validation of FVCOM hydrodynamics
Bathymetry	Echosounder equipped with dGPS pressure sensors (5 units)	various	Update of existing bathymetric chart of Patrick & Stevenson, 1986
Bottom sediment sampling	Ekman grab	various	Characterisation of bottom sediments

using Druck PTX1830 pressure sensors, connected via atmospherically-vented cables and sampled at 8Hz using Campbell CR10 data recorders located on shore. Pressure sensors were secured to steel rods driven into the lake bed about 1 m below the water surface. 4096 value sequences of near-bed pressure were used to construct wave height parameters at the free surface using the method of Lee & Wang, 1984. A separate set of Cera-Diver self-recording pressure recorders were co-deployed at the same locations to investigate short-term oscillations in water level due to seiching.

Surface water circulation patterns were investigated using GPS-equipped tracking drifters. These were constructed of polyurethane foam, with a weighted anchor line to limit movement driven purely by the wind. Tracking was accomplished using eTRex H GPS units (rms accuracy ± 3 m) enclosed within waterproof bags. Drifters were released at 5 locations along the eastern and southern shore and recovered by boat.

A major element of the second field campaign was the deployment of an acoustic Doppler current profiler (ADCP) at two locations within the lake to determine time variation in vertical velocity profiles in response to wind forcing. The ADCP (RDI 1200KHz Workhorse Sentinel) was deployed in upward looking mode on a bottom frame. The instrument was set to record 3D velocities at a vertical interval of 0.5 m, using ensembles of 150 pings to give a precision (standard deviation) of ± 0.057 $m\ s^{-1}$.

Sediment coring utilised a modified rod-less version of the piston corer designed by Chambers & Cameron, 2001, equipped with a 7 cm diameter core tube. A single 1.18 m core (UCL-CONLM1) was recovered from a depth of approximately 9 m within the eastern part of the lake. The core was sliced on-site at 1 cm intervals, with samples being stored in individual bags prior to laboratory analysis. This included standard determinations of bulk density, grainsize and loss-on-ignition. Additional bottom sediment samples were obtained at 28 locations using an Ekman grab. These were similarly analysed for grainsize and for loss-on-ignition.

Dried sediment samples from the CONLM1 core were analysed for ^{210}Pb, ^{226}Ra, ^{137}Cs and ^{241}Am by direct gamma assay in the Bloomsbury Environmental Isotope Facility (BEIF) at University College London (UCL), by Dr Handong Yang. Analysis was carried out using an ORTEC HPGe GWL series well-type coaxial low background intrinsic germanium detector. ^{210}Pb was determined via its gamma emissions at 46.5keV, and ^{226}Ra by the 295keV and 352keV gamma rays emitted by its daughter isotope ^{214}Pb following 3 weeks storage in sealed containers to allow radioactive equilibration. ^{137}Cs and ^{241}Am were measured by their emissions at 662keV and 59.5keV (Appleby

et al., 1986). The absolute efficiencies of the detector were determined using calibrated sources and sediment samples of known activity. Corrections were made for the effect of self absorption of low energy gamma rays within the sample (Appleby *et al.*, 1992).

The quality of the bathymetric data exerts a critical influence on the results obtained using computational hydrodynamic models (Hodges *et al.*, 2000; Cea & French, 2012). In the case of Llyn Conwy, the only existing bathymetric data were those obtained by Patrick & Stevenson, 1986. As shown in Figure 2.15a, this survey lacks detail in the shallow water marginal areas and also indicates a rather smooth-floored depression in the deepest part of the lake. To increase the resolution for modelling purposes, additional data were obtained with a Raytheon echo sounding system interfaced to a dGPS, along multiple intersecting transects. Data were merged with the earlier dataset to create a bathymetry that better represented the shallow marginal areas in particular. The revised composite bathymetry (Figure 2.15b) reveals the deepest part of the lake to have a slightly more complex topography, as well as highlighting the irregular morphology of the margins (notably on the eastern and southeastern shores). Differences between the two datasets are shown in Figure 2.15c, and indicate the potentially large errors within the earlier survey. Figure 2.16 further compares the surveys along selected transects.

A timeline for the various datasets used in this study is provided in Figure 2.17. This includes the historic Meteorological Office data for station at nearby Capel Curig, the data buoy and AWS deployments carried out by CEH bangor, and the two field campaigns conducted by the author in 2010 and 2011.

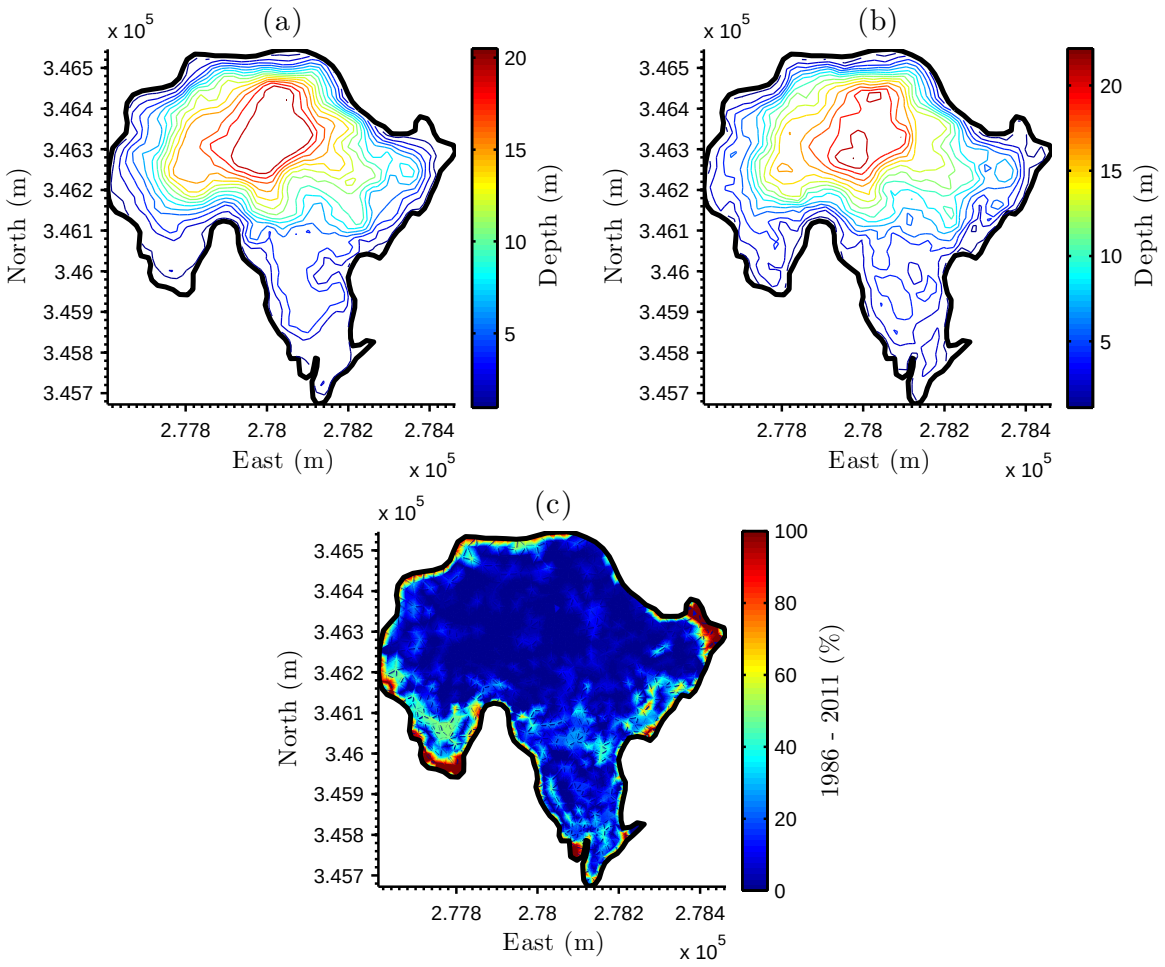

Figure 2.15: Comparison between the bathymetry of Patrick & Stevenson, 1986 and the composite bathymetry of 2011. a) 1986 survey b) composite 1986 and 2011 data c) difference between bathymetries.

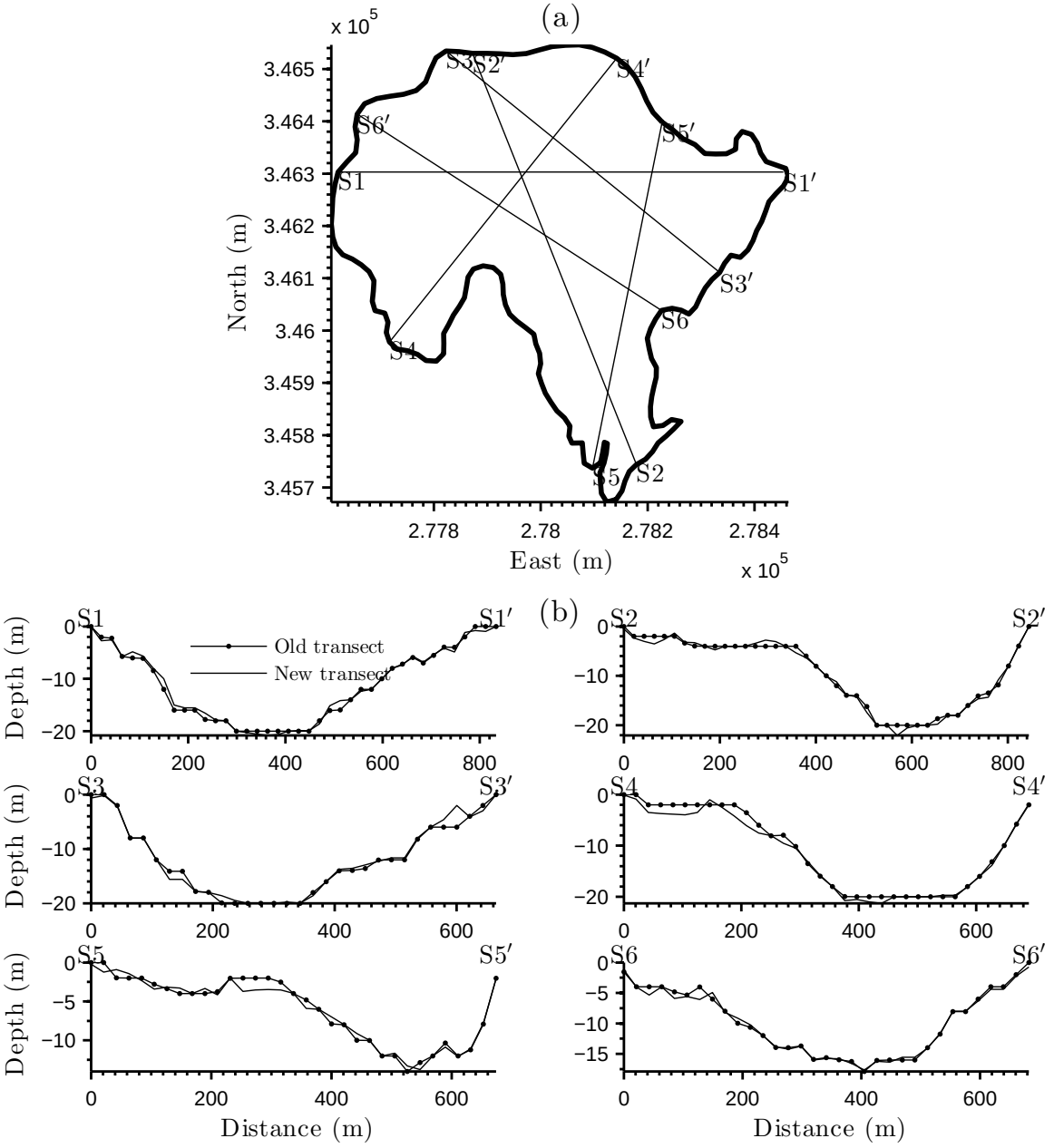

Figure 2.16: 1986 and new composite bathymetry. a) Transect locations b) old and new survey data.

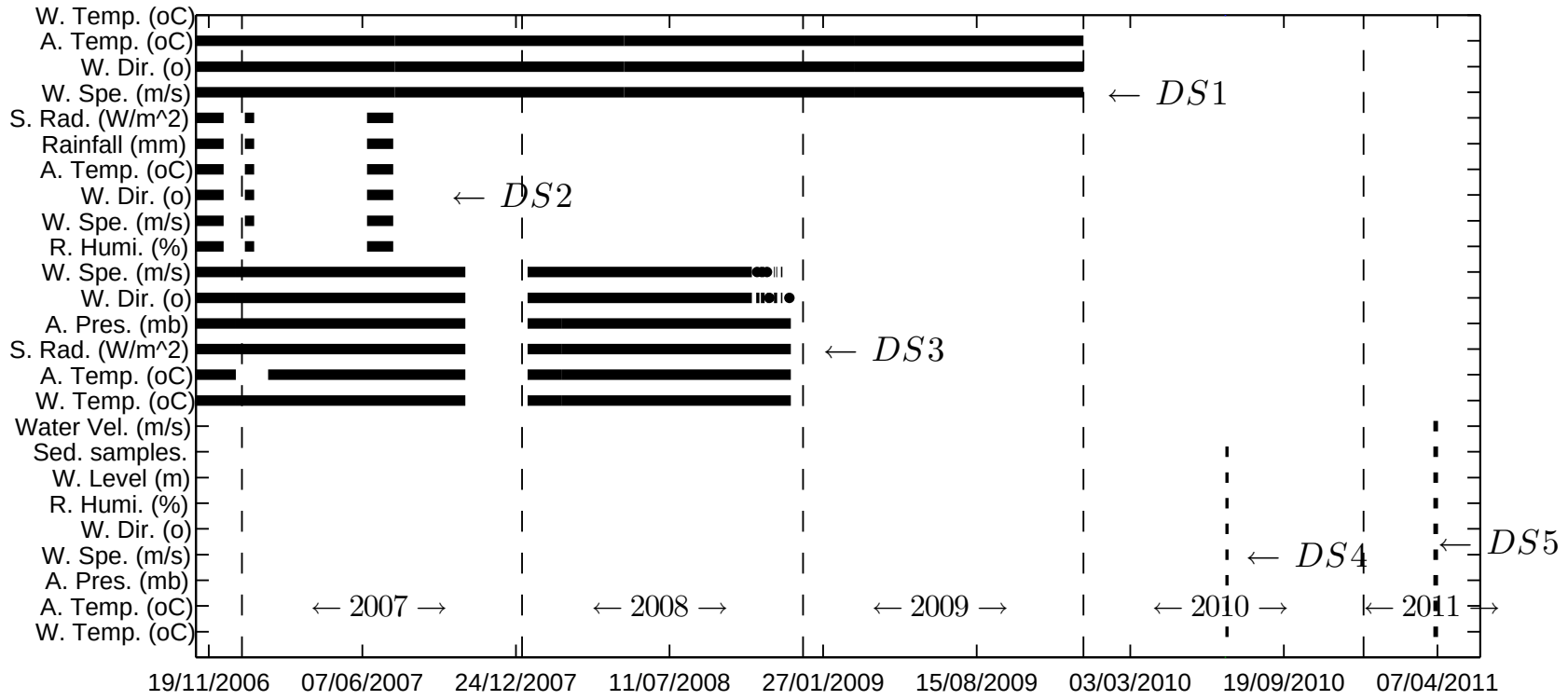

Figure 2.17: Time line for datasets used in this study. *DS1* = Capel Curig St. 1171; *DS2* = CEH AWS; *DS3* = CEH data buoy; *DS4* = field campaign 1; *DS5* = field campaign 2.

2.9 Modelling Tasks

The objectives of this study are delivered through a series of more-or-less self-contained modelling tasks.

1. Calibration and validation of *UCLAKE* model against temperature profile data for Llyn Conwy to give insights into the seasonal variability of thermal structure in the lake and identify periods with stratification. Also, *UCLAKE* will help to identify sensible parameter values for the thermal model in *FVCOM*.

2. Adaptation of the *FVCOM* model, which was originally developed for ocean modelling applications, to problems involving small lakes. Provision of a GUI to support pre- and post-processing of model runs is an important element of this task.

3. Validation of the *FVCOM* hydrodynamic model against field measurements of the surface circulation and vertical velocity structure in Llyn Conwy.

4. Validation of a surface wave generation and propagation model (*UCL-SWM*) based on the widely used *SWAN* model, against wave measurements around Llyn Conwy.

5. Analysis of lake hydrodynamics modelled using *FVCOM* and estimates of the wave base obtained from a *SWAN*-based wave model in order to determine likely zones of sediment erosion, resuspension and deposition in Llyn Conwy. These analyses are supported by sampling of the distribution of bottom sediments.

Chapter 3

Implementation and Validation of A One-dimensional Lake Dynamic Model

Resume

This chapter summarises the implementation, calibration and validation of the 1D model, UCLAKE. *The model is calibrated against the Llyn Conwy thermistor chain data for a one-year period (November 2006 to October 2007) and validated using a separate one-year dataset for 2008. The validation period is used to characterise the seasonal evolution of the vertical thermal structure and to identify the timing and extent of stratification and overturn. The response of the lake to high-frequency (hourly) variability in meteorological forcing is also considered.*

3.1 Introduction

As a prelude to higher dimensional (3D) modelling of the hydrodynamic regime of Llyn Conwy and its response to meteorological forcing, a 1D model (*UCLAKE*, see Section 2.3) has been developed to provide insights into the vertical structure of the lake at annual timescales. The main requirement here is to understand how the thermal structure of the lake evolves seasonally, especially in order that the importance of stratification can be judged prior to the application of the more computationally

intensive 3D model.

This chapter describes the calibration of *UCLAKE* against observations for the period from 3 November 2006 to 20 October 2007. Calibration was achieved through adjustment of three key empirical parameters: the maximum turbulent diffusion coefficient at the hypolimnion (Kz_{max}), the wind sheltering or wind efficiency (C) and the extinction coefficient (η) (Hondzo & Stefan, 1993; Bonnet *et al.*, 2000; Gal *et al.*, 2003). The last part of the chapter describes the validation of the model against data for 20 January 2008 to 13 December 2008, using the optimal parameters obtained from the calibration stage. The validation includes an analysis of the thermal structure by the identification of the overturn and stratified periods. The behaviour of the mixed layer is also analysed, along with the wind velocity variation. Additionally, short periods of strong meteorological forcing are examined, with the aim of understanding the response of the lake thermal regime over short (hourly) timescales. The chapter concludes with a comparison between the kinematic energy imposed by wind forcing and the potential energy through the vertical temperature structure, and with an analisis of the energy balance as a proxy of the lake stratification.

3.2 General Model Setup

The relationship between the bathymetry and the water depth can be summarised through the construction of the hypsographic curve (horizontal lake areas vs. water depths) (Figure 3.1 a)) and the volumetric curve (accumulated volumes vs. water depth) (Figure 3.1 b)). The hypsographic curves exhibit a slightly convex form, which has been corroborated by obtaining the inverse of the lake form factor ($V_d^{-1} = 0.93$) Håkanson, 1977a. Based on this, the morphology of Llyn Conwy can be classified as linear but very close to slightly convex, which is a common characteristic of small lakes with an area $\leq 1km^2$. In terms of V_d^{-1}, Llyn Conwy is characterised as a lake with a intermediate extent of shallow areas (half of the lake bottom is classified as shallow). This clearly has implications for the degree of sediment resuspension by wind-generated waves given the exposure of the lake to strong winds.

Figure 3.1 shows fitted curves (second order polynomial ($f(x) = a_2x^2 + a_1x + a_0$) functions) for both area ($A = f(h)$) and volume ($V = f(h)$).

Llyn Conwy experiences relatively little variation of water level ($\approx \pm 1\ m$) throughout a typical year. This is less than 5% of the annual-mean maximum water depth ($\approx$

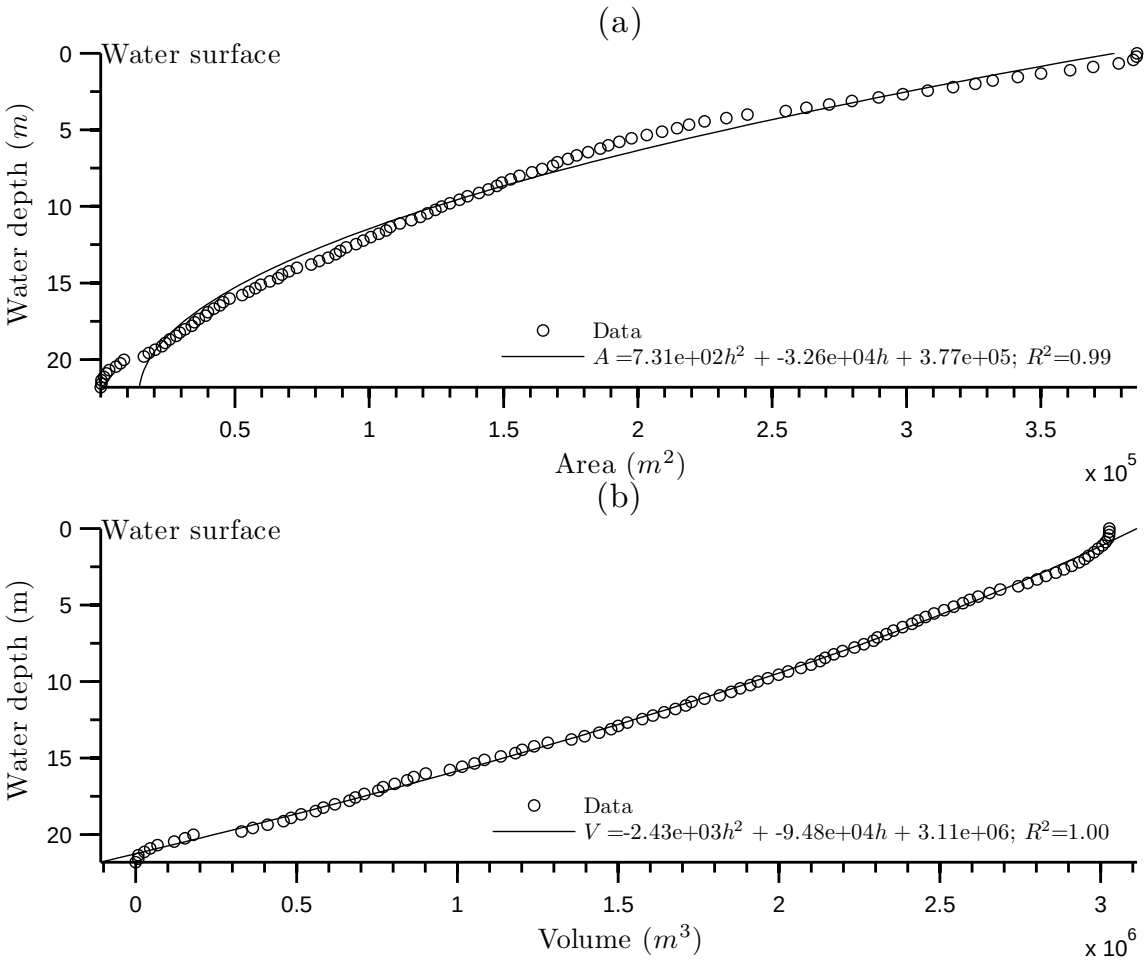

Figure 3.1: a) Hypsographic curve (area vs. water depth), and b) volumetric curve (volume vs. water depth) for Llyn Conwy.

21 m), which implies that the inflows and outflows can be considered negligible for the purposes of the present analysis. Therefore, only the incoming rainfall and the outgoing evaporation through the water surface are included in the water balance calculations. However, to guarantee the mean water depth throughout the periods of calibration and validation, a fixed outflow of $3.8{\times}10^{-2}$ m^3 s^{-1} was needed to account for the excess of rainfall over evaporation. This outflow was estimated from computation of the water balance based on rainfall and evaporation at the water surface layer. The very low value of this term is not unexpected given the small size and ephemeral nature of the outlet stream and small scale of water abstraction.

The parameters used during the calibration and validation are summarised in Ta-

Table 3.1: Parameters values used in *UCLAKE*. Parameters in bold are adjusted as part of the model calibration process.

Parameter	Symbol	Values	Units	Literature Source
Max. layer thickness	δ_{max}	1.5	m	[5]
Min. layer thickness	δ_{min}	0.5	m	[5]
Max. hypolim. turb. diff. coeff.	Kz_{max}	See Table 3.2	m^2s^{-1}	–
Long-wave albedo	α	0.04	–	[4]
Short-wave reflectivity	r	0.08	–	[1]
Wind sheltering coefficient	C	See Table 3.2	–	–
Emissivity of water	ϵ	0.972	–	[2]
Solar rad. fract. absor. in first layer	β_s	0.5	–	[6]
Extinction coefficient	η	See Table 3.2	m^{-1}	–
Constant in Equation 2.14	α	37	–	[3]
Constant in Equation 2.14	β	1	–	[3]
Constant in Equation 2.14	γ	2	–	[3]
Molecular diffusion coefficient	Kz_{mol}	1.2×10^{-7}	m^2s^{-1}	[6]
Latitude	Lat	53	^{o}	–
Initial number of layers	n_{lay0}	25	–	–
Initial water surface level	Lev_{ws}	0.0	m	–
Bottom depth	Lev_{bot}	21.0	m	–

[1] Patten *et al.*, 1975; [2] Imberger & Patterson, 1981; [3] Henderson-Sellers, 1985; [4] Nakamura & Hayakawa, 1991; [5] Hondzo & Stefan, 1993; [6] Bonnet *et al.*, 2000

ble 3.1. It worth noting that some of these parameters could potentially be estimated using locally determined empirical relationships. Such relationships have been used to estimate: short-wave reflectivity, solar radiation fraction absorbed in the first layer, extinction coefficient (Henderson-Sellers, 1984) and wind sheltering coefficient (Hondzo & Stefan, 1993). However, given that such relationships were obtained under certain climate conditions, lake turbidity levels and morphometric characteristics, their use is generally limited to lakes that have similar conditions.

3.3 Model Calibration

The *UCLAKE* model was calibrated using data spanning a period of nearly one year from 3 November 2006 to 20 October 2007. Hourly meteorological information for this period is shown in Figure 3.2.

The period between November and January is characterised by intermittently high

wind speeds that on occasion exceed 25 $m\ s^{-1}$. Air temperature is fairly uniform at around 9 $°C$ whilst rainfall intensities are high but irregular. It is also observed that, in late December and early February, air temperature are lowest and air pressures highest ($\approx$ 1080 $mbar$). These dry periods coincide with the lowest wind speeds.

Spring and summer are characterised by gradually increasing of solar irradiation, which exceeds 1000 $W\ m^{-2}$ in early June and July. Air temperatures increase to 23 $°C$ at the end of June. Seasonality is very evident in the solar irradiation series, but much less so for the air temperature. This is not unexpected given the sensitivity of temperature to wind speed, precipitation, and to the local effects such as high humidity in the vicinity of the lake.

For calibration purposes, fixed values for most of the model paramenters were used, with reference to appropriate literature sources (Table 3.1). Three parameters were adjusted in order to calibrate model output against observed data: maximum turbulent diffusion coefficient in the hypolimnion (Kz_{max}), the wind sheltering or wind efficiency coefficient (C), and the extinction coefficient (η). The ranges for each calibration parameter and literature sources are listed in Table 3.2.

Table 3.2: Summary of calibration parameter ranges.

Parameter	Range of Values	Units	Literature Source
Kz_{max}	9.95e-7 - 1.00e-4	m^2s^{-1}	Lewis Jr, 1983
C	0.1 - 1.0	m^{-1}	Hondzo & Stefan, 1993
η	0.1 - 2.0	–	Henderson-Sellers, 1984

Calibration was accomplished using 80 different sets of parameter values. Sampling of parameters was carried out using a Monte-Carlo approach (Beven & Freer, 2001), whereby each parameter was picked randomly from its range with the assumption that values were uniformly distributed. The model was evaluated following three objective functions (see Section 2.2), with particular emphasis on maximisation of the Nash-Sucliffe coefficient (NSE).

The first step was to compare the simulated and observed water temperature based on the analysis of NSE at three different levels within the water column: the water surface; mid depth; and the bottom of the lake. The results from this stage are shown in the Figures 3.3, 3.4 and 3.5 respectively. At the water surface (Figure 3.3) the results show that for 95% of the parameters, the model performs very well. NSE values are all

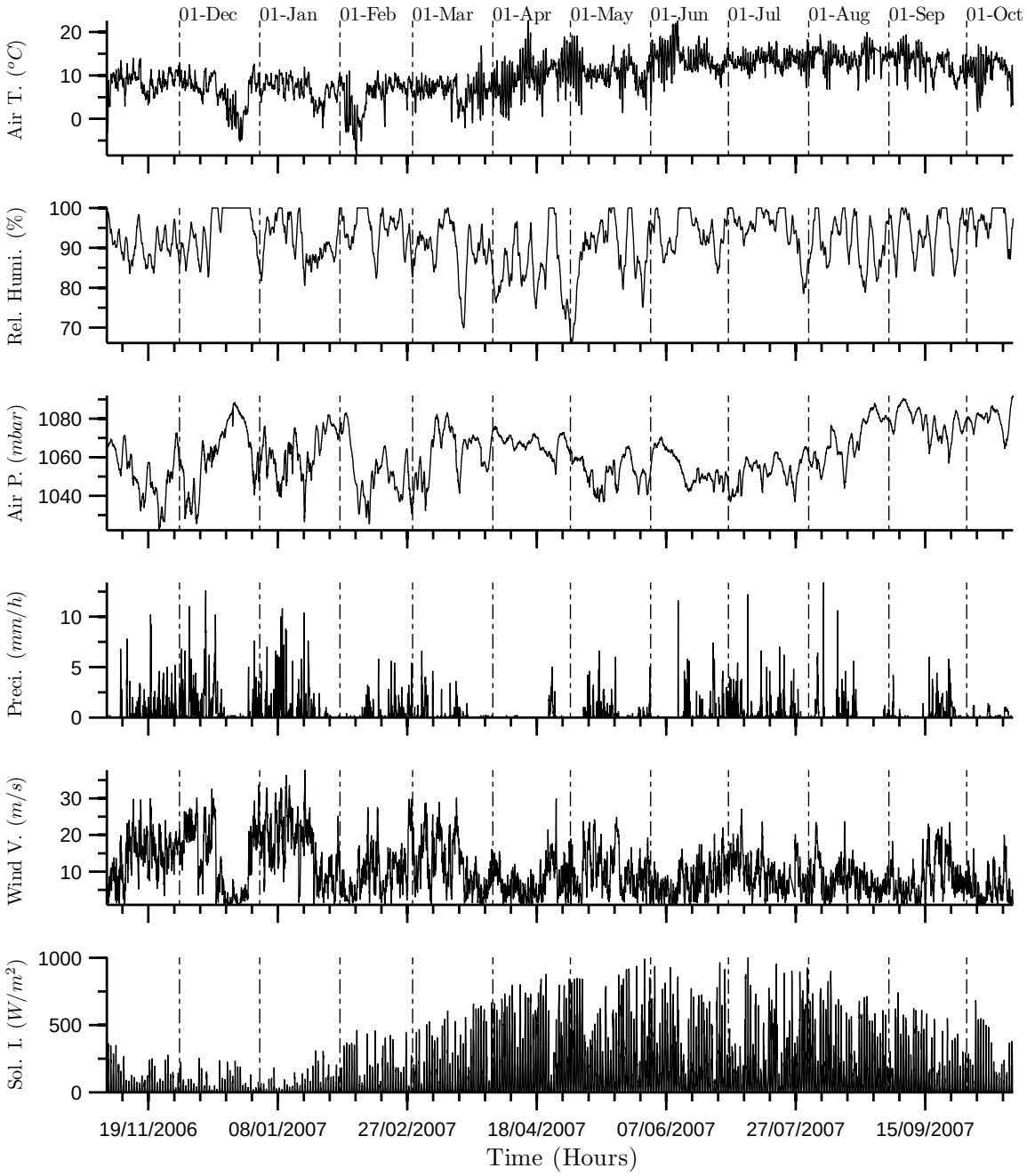

Figure 3.2: Hourly averaged meteorological variables between 03/11/2006 and 20/10/2007 used during the calibration of *UCLAKE*.

above 0.94. In contrast, the model performance simulating temperature is weaker at mid-depth (Figures 3.4) and at the bottom (Figures 3.5). Even here, however, values of NSE are still good with about 95% of the parameter value combinations yielding NSE between 0.5 and 1.

The spread of the model performance at half of the water depth and at the bottom (about $-1.5 < NSE < 1.0$) is larger than that at the water surface (about $0.88 < NSE < 1.0$). This implies that greater efforts have to be made to calibrate the model at those levels below the mixed layer. Table 3.3 shows the best parameter set values at each water depth.

A clear pattern is observed in the mid- and bottom layers (Figures 3.4 and 3.5, respectively), where the worst model performance arises for those parameter sets that include values of Kz_{max} under $1.5{\times}10^{-5}$. This pattern is explained by the fact that the energy dissipation carried out by the model at the rate specified by Kz_{max} below the mixed layer is overestimated for those periods where there is stratification.

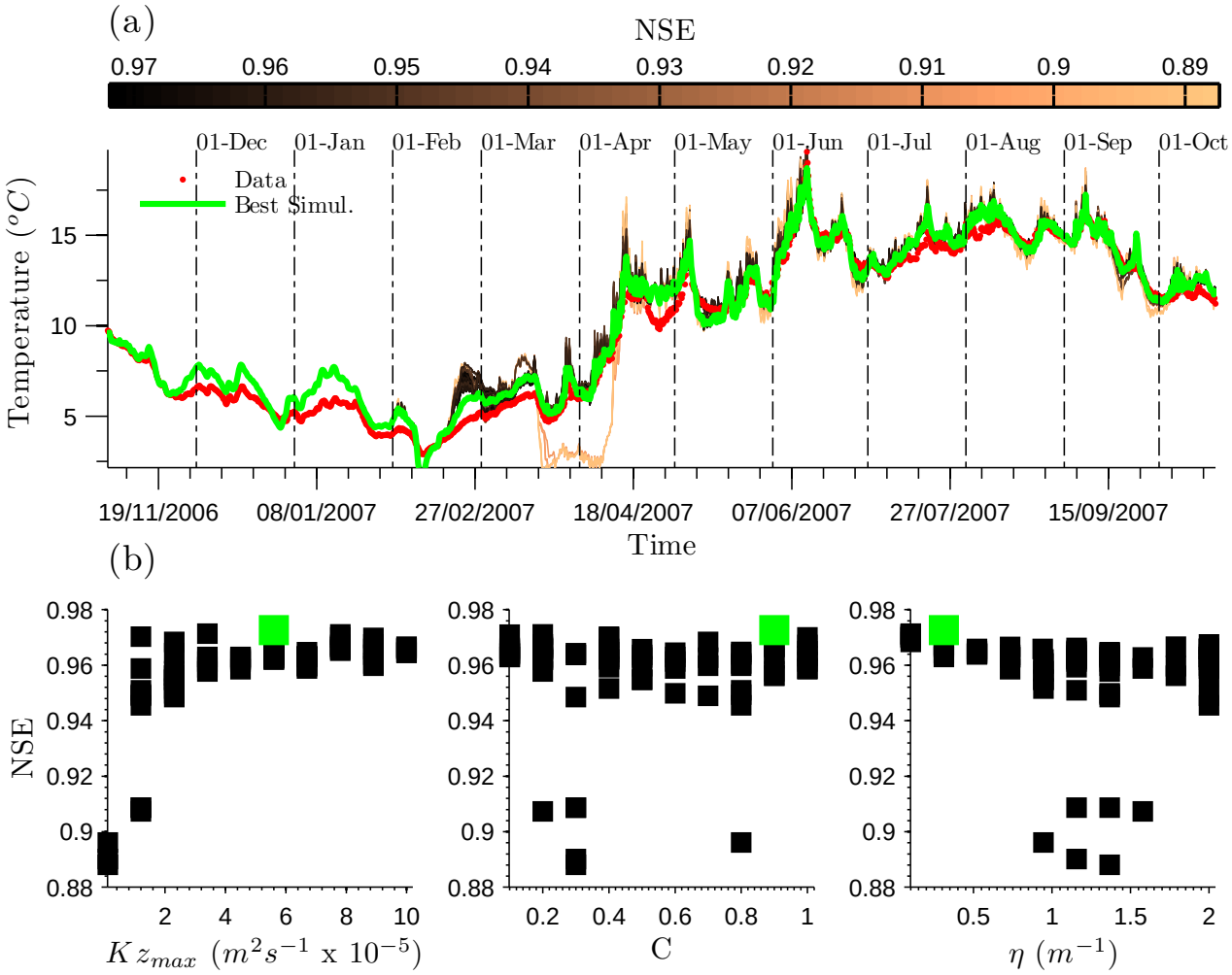

Figure 3.3: (a): Comparison between the observed data (red dots), the model simulations for different parameter sets (degraded lines base on NSE), and the best model simulation (green line) at 0% of the water depth (Surface). (b): NSE vs. Kz_max, C and η; the green squares match the best parameter set.

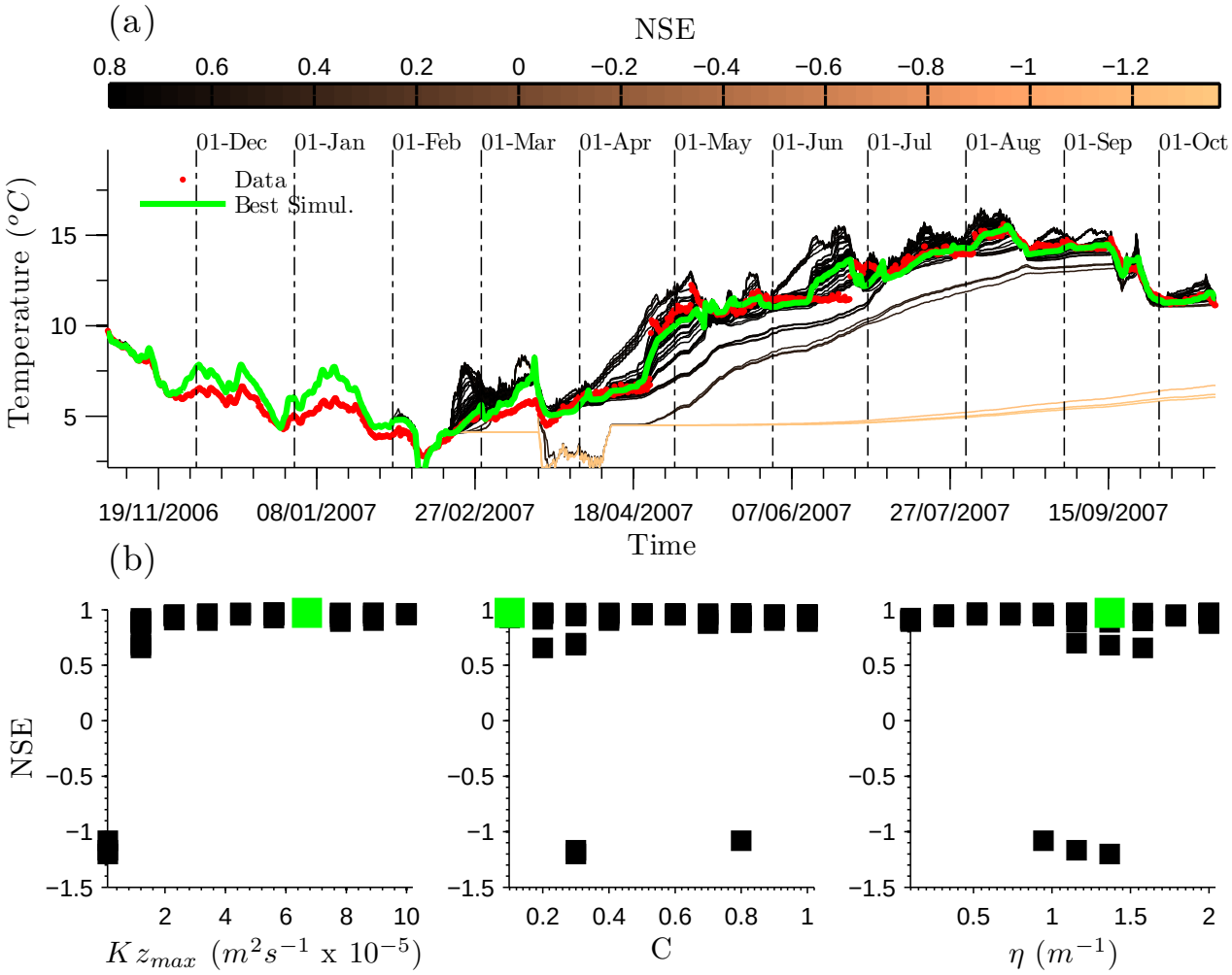

Figure 3.4: (a): Comparison between the observed data (red dots), the model simulations for different parameter sets (degraded lines base on NSE), and the best model simulation (green line) at 50% of the water depth (mid-layer). (b): NSE vs. Kz_max, C and η; the green squares match the best parameter set.

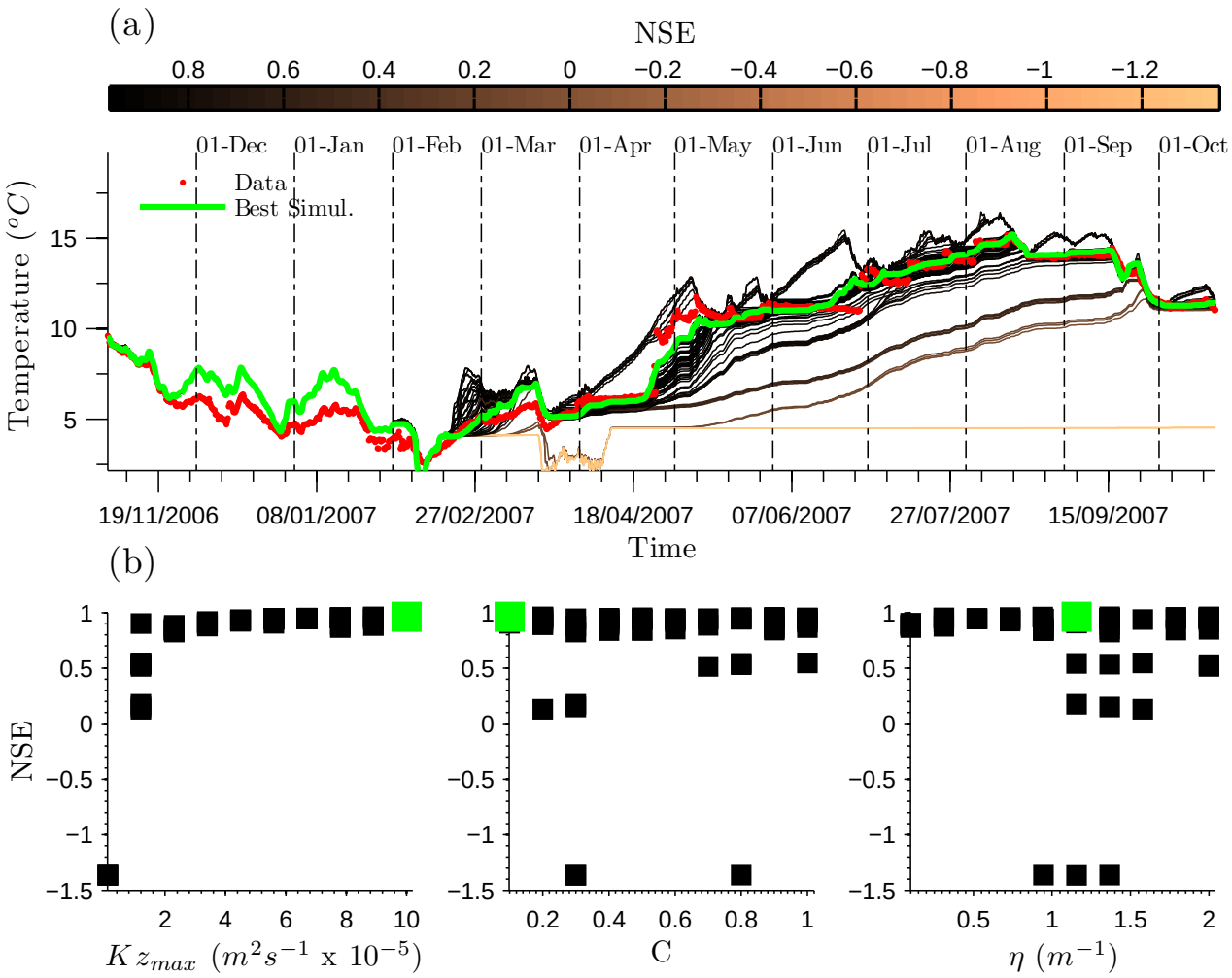

Figure 3.5: (a): Comparison between the observed data (red dots), the model simulations for different parameter sets (degraded lines base on NSE), and the best model simulation (green line) at 100% of the water depth (bottom). (b): NSE vs. Kz_max, C and η; the green squares match the best parameter set.

Table 3.3: The best parameter set for three different water depths based on the minimum value of NSE.

h/H	RMSE	RMAE	NSE	Kz_{max}	C	η
0	0.6884	0.0760	0.9726	5.60e-05	0.9000	0.3111
0.5	0.6565	0.0698	0.9707	6.70e-05	0.1000	1.3667
1.0	0.7317	0.0853	0.9626	1.00e-04	0.1000	1.1556

It is clear from Table 3.3 that the optimum parameter values vary as a function of the water depth. It is thus necessary to obtain a single set that provides the best overall performance over the water column as a whole. To do this, a comparison of the geometry means (Equation 3.1) of the simulated and observed water temperature profile was carried out. The top five parameter sets are shown in Table 3.4.

$$\bar{Te}(t) = \frac{1}{Nlayers} \sum_{i=1}^{Nlayers} Te_i \tag{3.1}$$

Hondzo & Stefan, 1993 implemented a formulation similar to Equation 3.1, in which the water temperature at each layer is subjected to a weight, in this case the layer volume, and the cumulative sum is divided by the total lake volume. Several attempts to calibrate the model were made using this approach. However, it was found that this approximation places too much weight on the upper layers and much less on the lower ones because of the distribution of the water volume (Figure 3.1 b)). Choosing the optimum data set values using this approach yields good performance for the weighted vertical water temperature average but significant discrepancies still occur in the temperature at lower levels.

Figure 3.6 compares the simulated temperature series (degraded lines) using the best parameter set ($Kz_{max} = 8.90\times10^{-5}$, $C = 0.20$ and $\eta = 2.00$) against the observed temperature values (red lines) at five different fractions (h/H) of the water depth (H) from 0.0 (water surface) to 1.0 (bottom lake) at intervals of $h/H = 0.25$. Model performance is very good with a value of NSE =0.9785.

Examination of the objective model performance function (Table 3.4) shows that the model performance is very good for all the top five model runs. However, it is notable that all the values for Kz_{max} are above 5.0×10^{-5}, close to its upper bound, and the values of C are ≤ 0.2. With regard to Kz_{max}, the high levels of water turbulence

imposed by the wind forcing necessitates increase in the value of Kz_{max}, with the aim of controlling the energy diffusion through the water column correctly.

With regard to C, work by Hondzo & Stefan, 1993 on small lakes has established that C is function of the lake area (or more specifically, of the maximun fetch). Consideration of the Llyn Conwy's surface area suggests a value of $C = 0.11$, which coincides with the results reported in Table 3.4. On the other hand, due to the fact that the wind velocities were measured on a buoy on Llyn Conwy located more than halfway along the fetch for the dominant southwesterly winds, an overestimation of the wind velocity values is implicit in the measurement, because wind velocity typically increases with the fetch (Young & Verhagen, 1996a). This means that the further the wind measurement is made along the fetch, the smaller the value of C.

Multiple relationships of the form $\eta = az_{sd}^{-b}$, where z_{sd} is the sechi disk depth in metres, and a and b are constant $\approx$ to 1.5 and 1.0 respectively, were derived to estimate the value of η (Henderson-Sellers, 1984; Hondzo & Stefan, 1993). Such formulations vary markedly from site to site, such that they are probably not readily transferable. Using a mean value of $z_{sd} = 1.8$ measured during the first field campaign at Llyn Conwy, a value of $\eta = 1.1$ (m^{-1}) is computed using formulation proposed by Henderson-Sellers, 1984. This differs considerably from the optimal value ($\eta = 2.0$ (m^{-1}) but is similar to the second and third best parameter sets (Table 3.4).

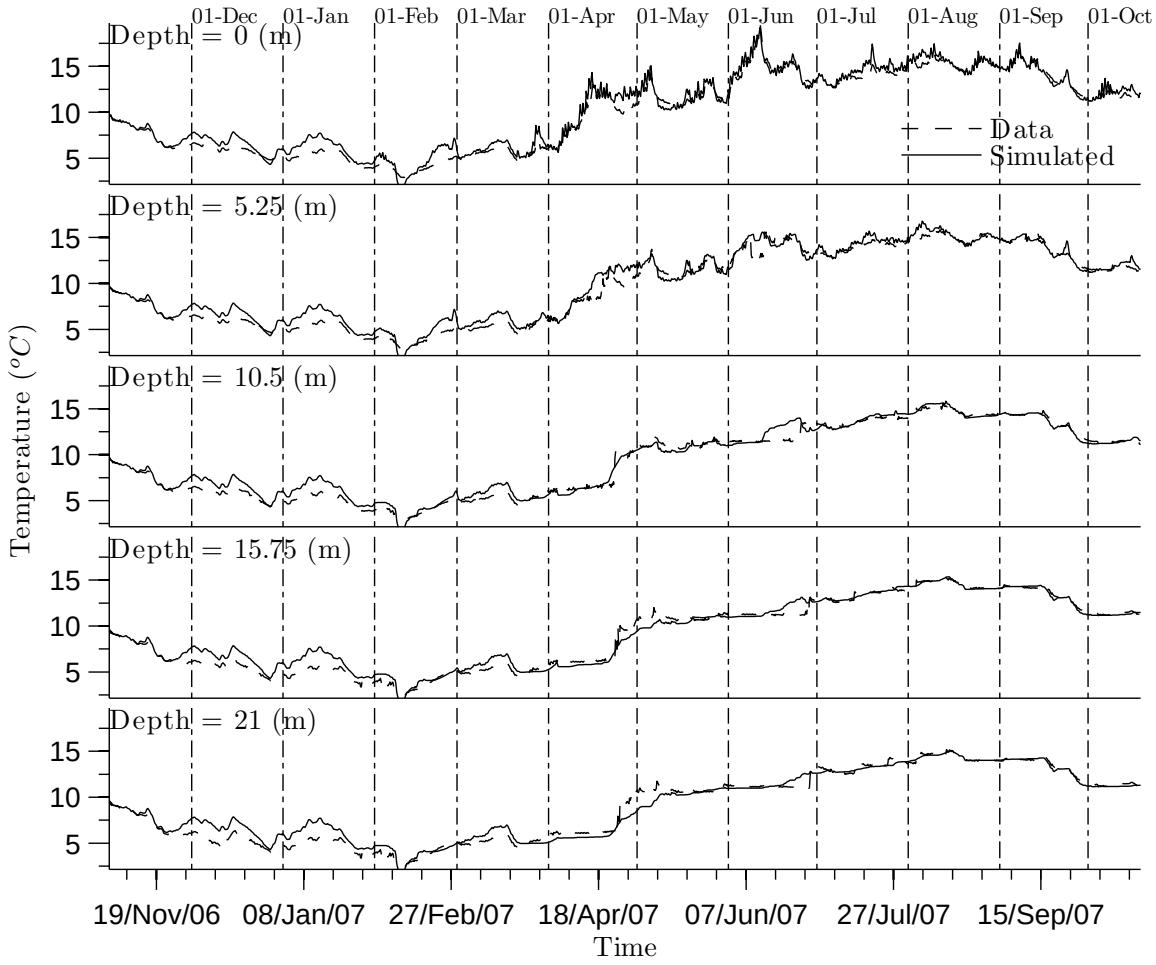

Figure 3.6: Comparison between the best simulated temperature and the observed temperature at five water depths (every 20% of the water depth from the water surface to the bottom), for the best parameter set (see first row in Table 3.4).

Table 3.4: Best five parameter sets for depth-averaged model performance. Bold values indicate the best parameter values.

Run	RMSE	RMAE	NSE	Kz_{max}	C	η
54	**0.7092**	**0.0648**	**0.9785**	**8.90e-05**	**0.2000**	**2.0000**
11	0.7160	0.0651	0.9782	7.80e-05	0.1000	1.1556
46	0.7196	0.0651	0.9776	8.90e-05	0.1000	0.9400
55	0.7311	0.0653	0.9775	7.80e-05	0.2000	0.7333
30	0.7396	0.0656	0.9775	6.70e-05	0.1000	1.3667

An alternative method to compare the results of simulated and observed data is by computing the determination coefficient (R^2) between observed and modelled values. Encouragingly, Figure 3.7 shows a clear linear relationship between the best simulated and the measured temperature at the top, middle and bottom levels. Values of R^2 are around 0.98 in all cases.

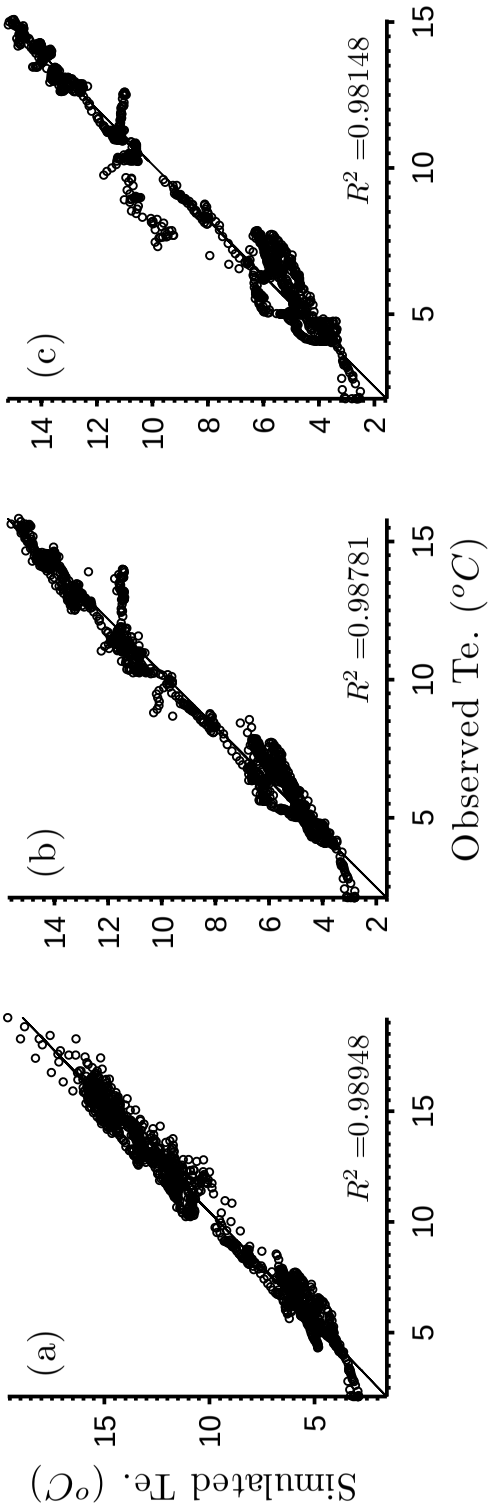

Figure 3.7: Linear correlation between the best simulated and observed temperature series at different levels: a) water surface, b) mid-depth and c) bottom.

3.4 Sensitivity Analysis

A sensitivity analysis provides further insights into how water temperature responds to variation in the model parameters. To do this, a time-dependent sensitivity quantity (S_i) was computed for each parameter as:

$$S_i = \frac{|Te_i^{up} - Te_i^{lo}|}{Te_i^{best}} \tag{3.2}$$

where the subscript i indicates a time instant, Te_i^{up} is the temperature simulated with the upper bound value of the parameter, Te_i^{lo} is the simulated temperature with the lower bound value of the parameter and Te_i^{best} is the simulated temperature with the best set of parameters. The higher the values of (S_i) the more sensitive the water temperature is to any change in the parameter.

Figures 3.8 and 3.9 show the results of the sensitivity analysis for the temperature at the water surface and at mid-depth. Comparing the results at both water levels (see Table 3.5) the water temperature at mid-depth is very sensitive to changes in the parameters, especially in spring and summer. The main reason for this is that the uppermost layers are more sensitive to changing weather conditions, such that temperature variations are driven most of the time by the heat flux (Hn) at the water surface. The quality of the temperature prediction at the epilimnion thus depends strongly on the quality of the meteorological data.

On the other hand, the temperatures in the layers below the mixed layer are strongly influenced by how the turbulent energy, represented by Kz, and the downward distribution of the remaining incoming solar radiation (Hs) are parametrised. This is demonstrated in Figures 3.9a and 3.9c, which show that the model results are very sensitive to Kz_{max} and η and that model uncertainty is greatest at lower levels in the water column.

Additionally, the model is practically insensitive to any changes of the parameters from mid-autumn to late-winter. This period is characterised by low incoming heat energy and high wind velocities, triggering a constant convective circulation. This produces high values and a homogeneous distribution of Kz, which guarantees constant mixing throughout the water depth. It follows that, the water temperature structure in these periods is exclusively sensitive to changes in weather conditions, and the accuracy of the simulations again depends on the quality of the weather data.

Table 3.5: The average sensitivity (S_i) for each calibrated parameter at the water surface and 50 % of the water depth.

	Sensitivity index (%) for		
% W. Depth	Kz_{max}	C	η
0	5.8748	1.3498	6.7857
50	46.9890	2.8394	52.5188

Water temperature has a low sensitivity to changes in C most of the time, with relatively high values of S_i for both water depths between mid-February to late-March. These high values coincide with the beginning of the rise of Hs, and with a slight decrease in the wind velocity with respect to the periods before. This is therefore a transition period between a state dominated by wind action with poor stratification to another where the heat fluxes play a significant role in allowing stratification. As the kinematic energy transferred from the wind is affected by C, such transitions increase the uncertainty in the chosen of a value for C. This also causes difficulties in the way that the model estimates the temperature, which is readily observable in the difference between the simulated and the measured values in the top graphs in Figures 3.8b and 3.9b.

3.5 Validation

Following calibration, *UCLAKE* was validated for a separate period between 8 January 2008 and 16 December 2008. To achieve this, the model was run using the same fixed parameter values and information described in Section 3.2, and the final overall best calibrated parameter values determined in Section 3.3.

The validation period is characterised by highly variable weather (Figure 3.10). Air temperature exceeds 20 $°C$ in the first half of May and June, and in late July, which coincides with the highest values of incoming solar radiation (up to 1000 Wm^{-2}). Air temperatures decrease to -10 $°C$ in mid-February and in early-December, with low values of incoming solar radiation under 100 Wm^{-2}. Wind speed is characterised by high values in winter and early spring, reaching 35 $m\ s^{-1}$ on 01 of February. Spring is much calmer, with mean wind speed around 8 ms^{-1}. In summer, speeds of nearly 30 $m\ s^{-1}$ are reached during a few days at the end of June and August. The month

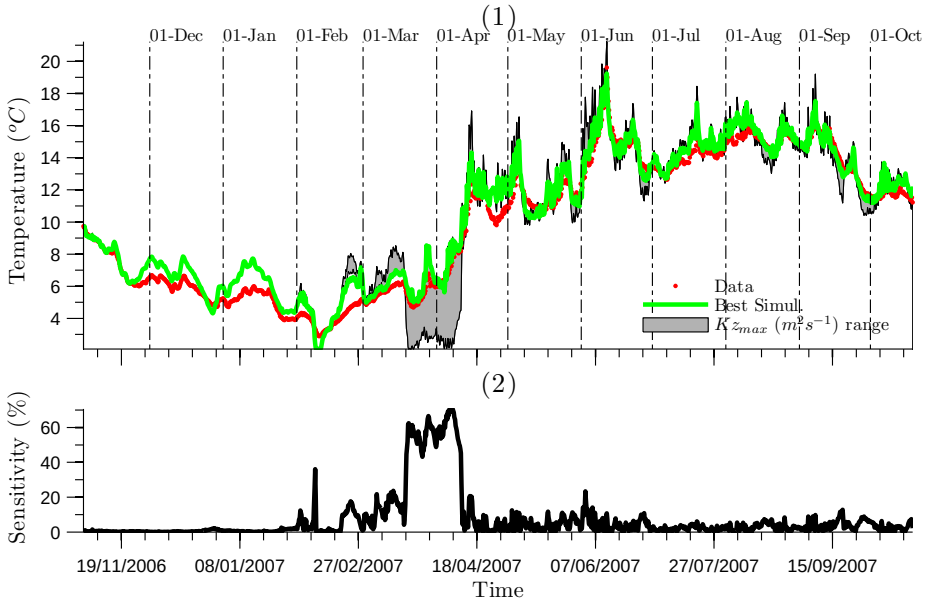

(a) Kz

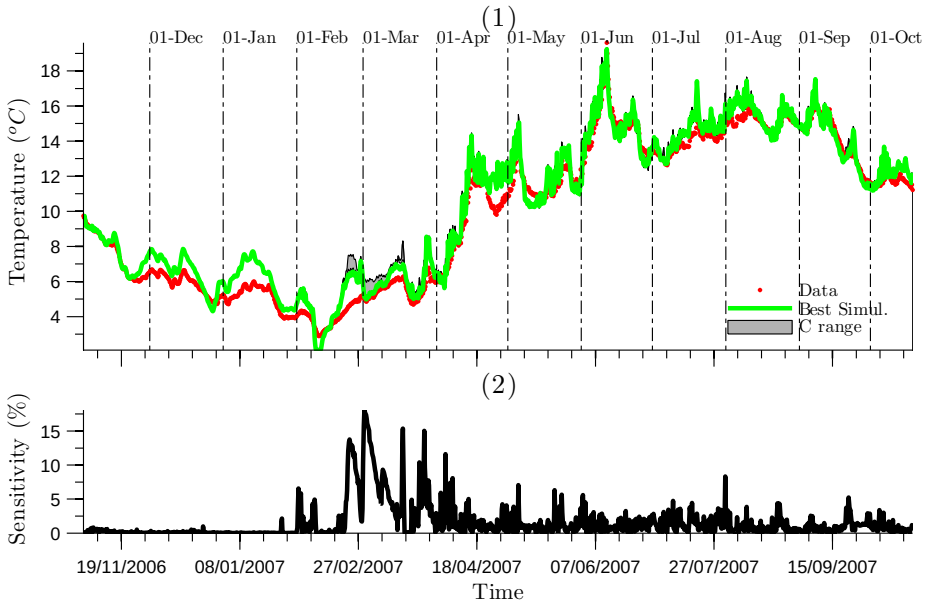

(b) C

Figure 3.8: Sensitivity analysis of water temperatures at the water surface. 1) Comparison of observed data, the best model simulation, and the range of model simulations for the upper and the lower parameter limits. 2) Sensitivity index (S_i) estimated using Equation 3.2.

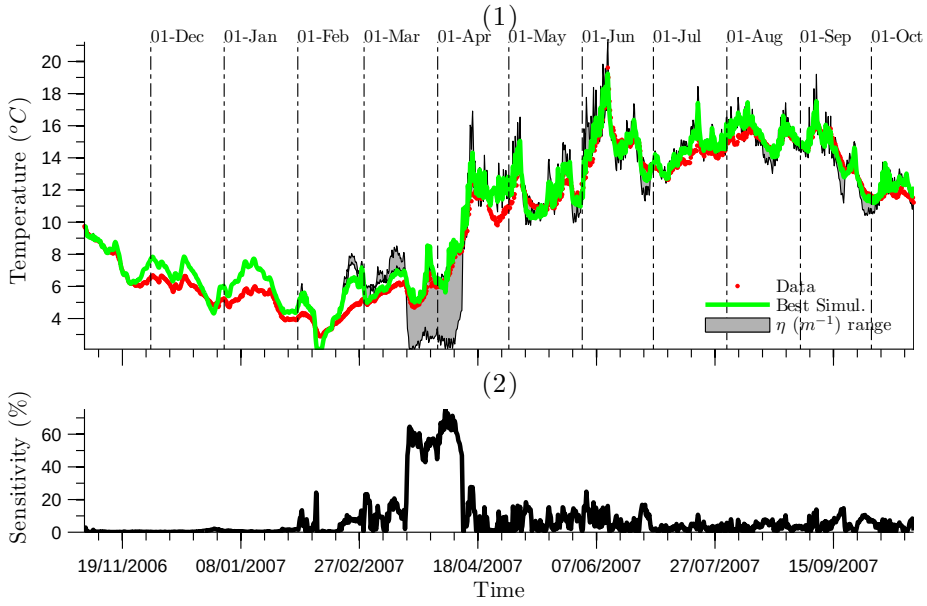

(c) η

Figure 3.8: Continued.

of February exhibits conditions similar to these encountered in the calibration period. The air temperature decreases to -10 $°C$, wind speeds drop below 5 $m\ s^{-1}$, and very little rainfall occurs.

During the calibration of *UCLAKE*, parameter set values were established based on the optimisation of the NSE statistics. Such values shown also in Table 3.4 were used in the validation of *UCLAKE*. These parameter set values were: $Kz_{max} = 8.90{\times}10^{-5}$, $C = 0.2$ and $\eta = 2.0$.

Figure 3.11 shows a good agreement between the observed and the simulated temperature, with NSE values of 0.9510, 0.9718 and 0.9725 at the water surface, mid-depth and at the bottom respectively. Similarly, the temperature profiles at different times (Figure 3.12), demonstrate the ability of the model to represent the temperature profile at any time during the year. A maximum difference of 3.9 $°C$ during the first half of February is registered and the mean $RMAE$ is 8.1% for the 24 profiles plotted. Numerical analysis of the vertical temperature structure throughout the validation period, shows that $RMAE$ is below 10% for 77% of the time. This confirms that the model is able to simulate the whole vertical structure within the water column.

The main differences between simulated and observed series occur during the months

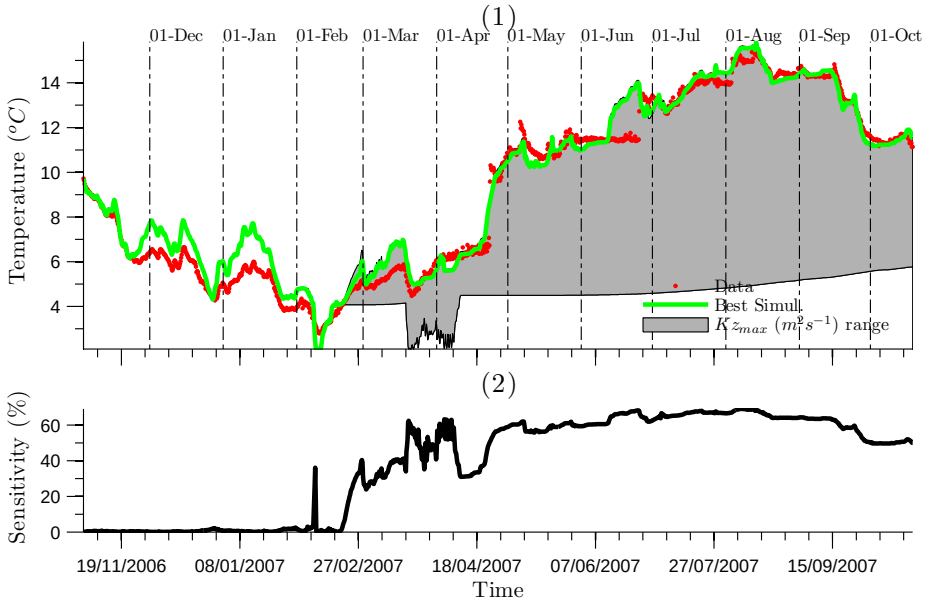

(a) Kz

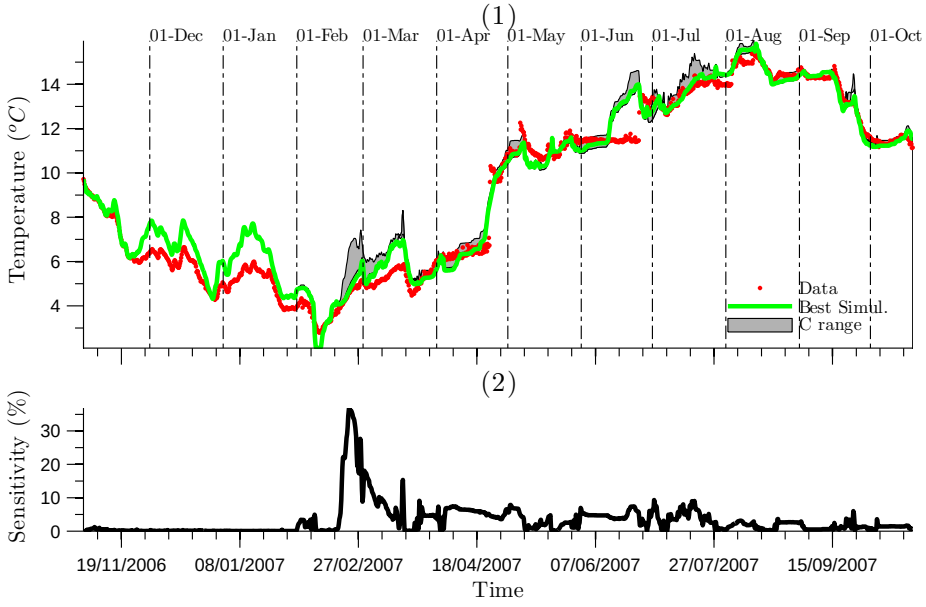

(b) C

Figure 3.9: Sensitivity analysis of water temperatures at 50% of the water depth. 1) Comparison of observed data, the best model simulation, and the range of model simulations for the upper and the lower parameter limits. 2) Sensitivity index (S_i) estimated using Equation 3.2.

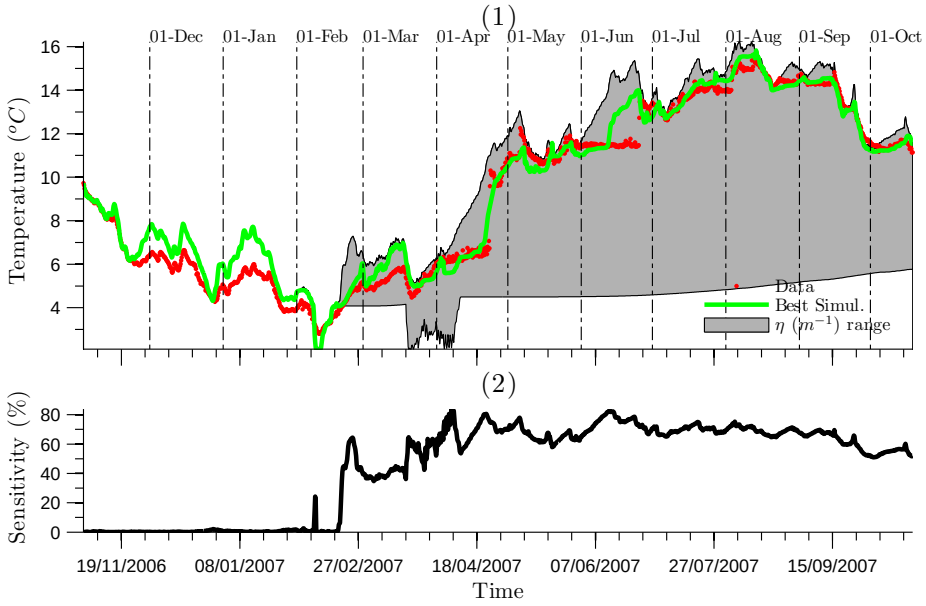

(c) η

Figure 3.9: Continued.

of February and March, where errors reach 50%. These discrepancies are caused mainly by the time scale at which the model is implemented. Sub-daily changes in the meteorological forcings are only weakly coupled to changes in the thermal structure because the latter are gradual and usually lag the longer term weather conditions.

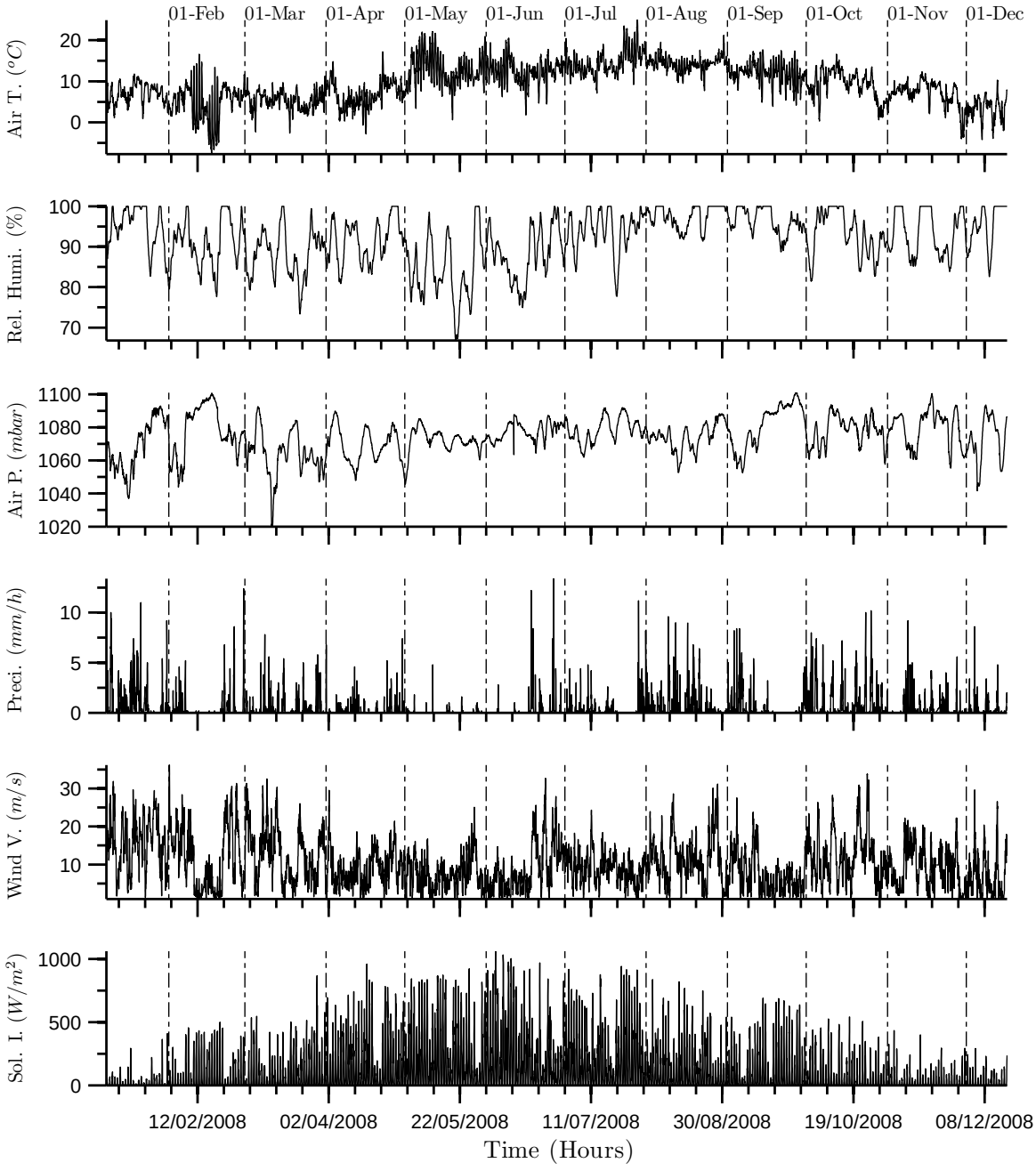

Figure 3.10: Hourly meteorological variables between 08/01/2008 and 16/12/2008 used during the validation of *UCLAKE*.

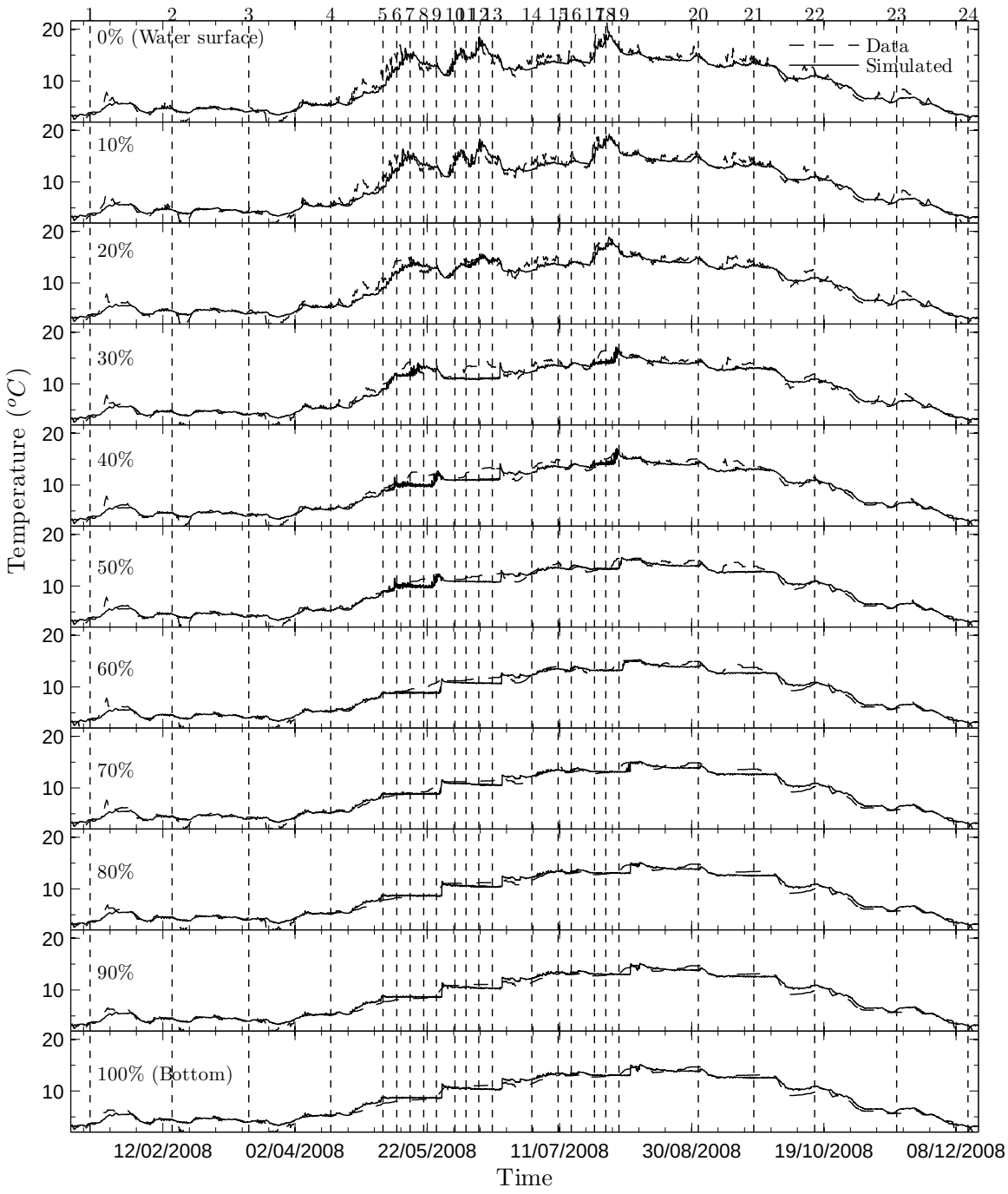

Figure 3.11: Comparison between the best simulated temperature (continuous line) and the observed temperature (dashed line) at multiple water levels (every 20% of the water depth from the water surface to the bottom). The vertical dashed lines indicate the times of the profiles plotted in Figure 3.12.

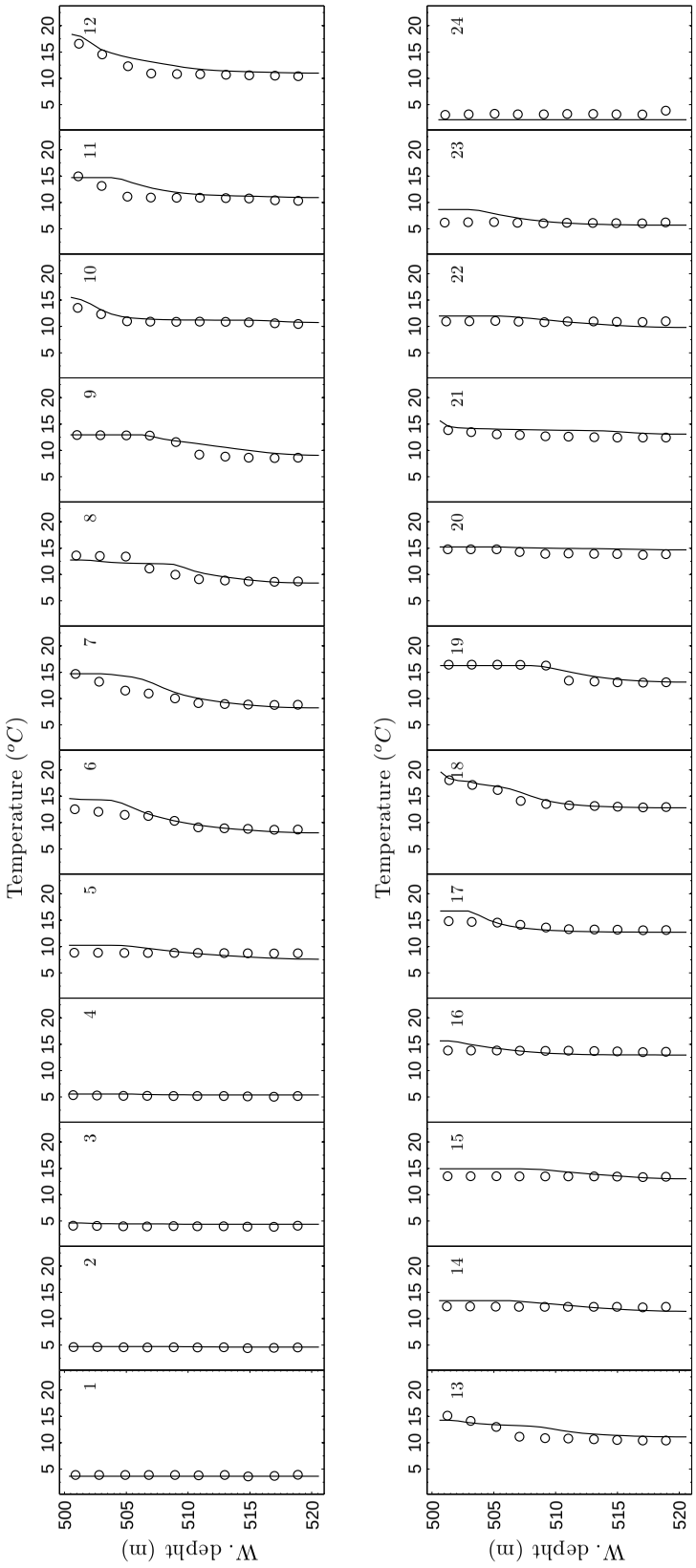

Figure 3.12: Observed (empty circles) and simulated (continuous line) water temperature profiles at different times indicated in the Figure 3.11 (see numbers on the top right).

With the aim of testing the timestep scale issues, *UCLAKE* was set up using daily averaged meteorological data, except for the solar irradiation where a single value corresponding to the midday value was taken. The analysis shows that the maximum temperature differences between observed and simulated decrease to 1.7 $^{\circ}C$ (50% less than in the analysis made using sub-daily time step data) with a decrease in the $RMAE$ to 6.1%. Although the analysis demonstrates that model performance improves significantly when a daily timestep is used, the sub-daily details of the lake stratification is not modelled and information on lake response to sub-daily variability is lost.

Other sources of error are related to the uncertainty of the meteorological information. Small changes in air temperature affect the temperature structure, especially the mixed layer. Likewise, changes in wind forcing trigger changes in the flux of heat by evaporation, and therefore changes in the net heat balance at the water surface. Incremental increase in wind speed can cause a misleading deepening of the mixed layer and therefore changes in the temperature structure at the hypolimnion.

The high variability of the meteorological conditions at subdaily scales, where for example wind speed varys from 0 to 40 $m\ s^{-1}$ over the winter months, represents a challenge to the modelling of the thermal structure in lakes at such scales, since the numerical stability of the model is constantly affected. The condition of stability of 1D advection-diffusion models establishes that numerical calculations will be stable if $\frac{\delta}{2Kz\Delta t} \leq 1$ (Ryan & Harleman, 1973). Since Kz varies continuously, an adaption of Δt was required with the aim of guaranteeing numerical stability. Figure 3.13(a) shows that Δt usually varies between $0 < \Delta t < 1405.5\ s$, and for some periods between $0 < \Delta t < 3600\ s$. The analysis of frequency (see Figure 3.13 (b)) shows a two-mode probability distribution function. The first mode indicates that values of Δt close to 0 s are the most frequent (∼50% of the whole period), and correspond to the wind speeds $> 10\ m\ s^{-1}$. The second mode indicates that Δt around 1405.5 s are the second most frequent and correspond to periods of thermal overturn. On the other hand, $\Delta t = 3600$ s corresponds to wind speeds $< 5\ m\ s^{-1}$.

The relationship between wind speed and Δt (see Figure 3.14) is inversely proportional, so when wind speed increases the value of Δt will decrease. A little dispersion is shown in Figure 3.14. However, it is noticeable that $\Delta t = 1405.5\ s$ is set independently of the wind speeds when Kz_{max} reaches the threshold value 8.9 $\times 10^{-5}\ m^2\ s^{-1}$ which corresponds to periods of thermal overturn. Since it is quite unusual in the literature to

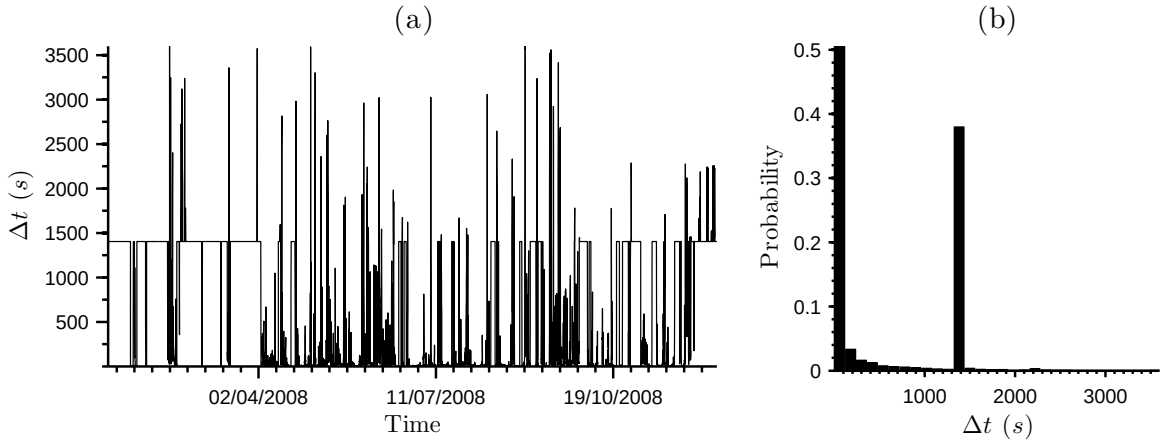

Figure 3.13: Analysis of the timestep (Δt) calculated by *UCLAKE* between 08/01/2008 and 16/12/2008 (validation period). a) Δt against time; b) probability density function of Δt.

find lake dynamic models driven by wind speeds $> 15\ m\ s^{-1}$, the adaptive Δt is a very useful feature that makes *UCLAKE* extremely well suited to modelling the long-term thermal structure of lakes subjected to strong wind forcing conditions. The adaptation of Δt in *UCLAKE* not only guarantees its numerical estability but also improves the model performance.

3.6 Analysis of the Mixed Layer

Meteorological forcings are clearly the main factor driving the hydrodynamics of Llyn Conwy. The wind velocity field interacts with the water body, triggering a near constant stirring of the water column through the year (Figure 3.15 (c)). On the other hand, increasing heat energy, especially in May, June and July, ensures certain periods of continuous stratification (Figure 3.15 (b)), which are intermittently interrupted by the occurrence of high wind speeds.

In winter and autumn, the lake is well mixed around 67.5 % of the time (Figure 3.16). The mean low incoming solar radiation and high wind velocities (mean 12.7 $m\ s^{-1}$) ensure that the water column remains totally mixed. During early spring, the lower average wind velocity of 11 $m\ s^{-1}$ allows the lake to stratify for 44 % of the time (Figure 3.16). The low temperatures and the high wind velocities, especially in the first

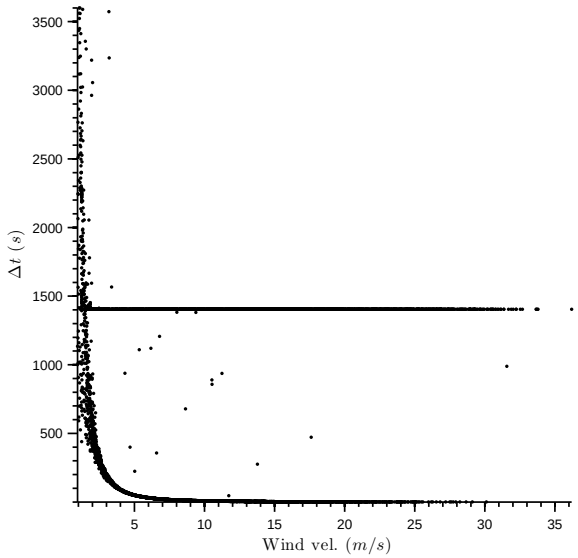

Figure 3.14: Relationship between wind speed and timestep (Δt) for the period 08/01/2008 to 16/12/2008.

half of March, guarantee a mixed layer through the whole month, with very episodic overturns in the middle of the month. April is characterised by intermittent overturns of the thermal structure due to the chaotic variance of the wind speed and the onset of a more sustained air temperature rise. Through late April and May, the lake becomes stratified with an apparently constant mixed layer depth of 2.5 m. This lasts through the first half of May until an increase in wind speed above 12 $m\ s^{-1}$ deepens the mixed layer to 15 m.

As expected, the lake is stratified for about 80% of the time in summer (Figure 3.15 (b) and Figure 3.16). The mixed layer is held constant at 2 m and reaches the bottom in the second half of June; stratification returns at the end of the month when the wind forcing decreases from 30 ms^{-1} to below 10 ms^{-1}. Periods of stratification occur again in May and June, and episodic mixing due to wind forcing in late May, late June, through July and August (Figure 3.15 (c)). The first half of July is characterised by intermittent periods of stratification. However, the reduction in the wind speed and the rise in air temperature over 22 $°C$ stimulates a rapid stratification that lasts until the first week of August. Intermittent water mixing events through August are matched by highly variable wind forcing that enhances mixing as the heat energy sources begin to decrease.

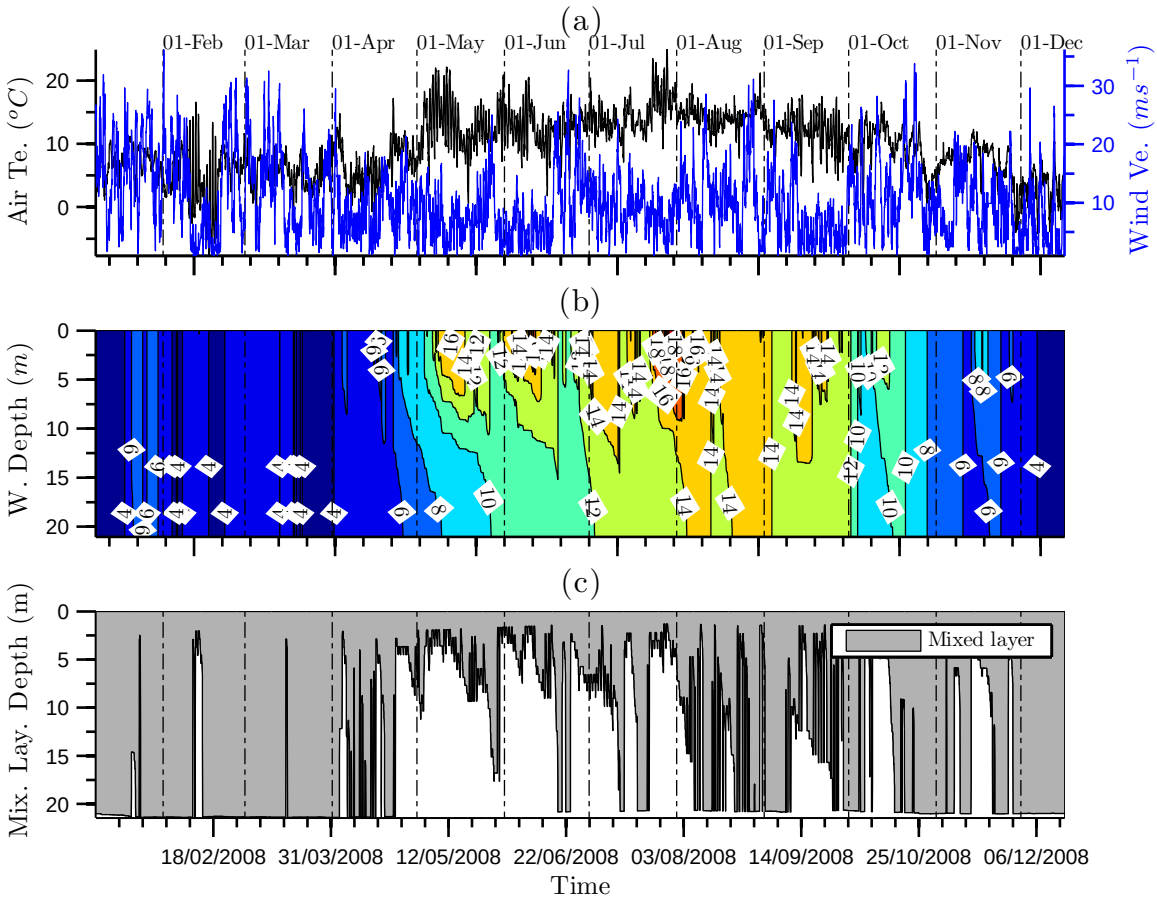

Figure 3.15: a) Time series for dominant meteorological forcing variables air temperature (black) and wind velocity (blue); b) simulated water temperature contours; c) simulated mixed layer depth.

Figure 3.17 shows a complementary analysis of the lake stratification based on an analysis of the energy balance. During the months of January, February and March, the balance of energy at the water column is dominated by the wind kinematic energy where no resisting forces, represented by the stratification gradient, appear to damp the wind effects. Thus the whole range of wind magnitudes guarantee the homogeneous temperature structure in the lake. Between the months of April and September, an increase in incoming heat energy ensures stratification, raising the potential energy in the lake and impeding wind stirring of the water column. It is also notable that, for these months, wind velocities under 10 ms^{-1} (Figure 3.17 (b)) guarantee the existence of the thermocline and the multiple mixing events are due to the gradual increase

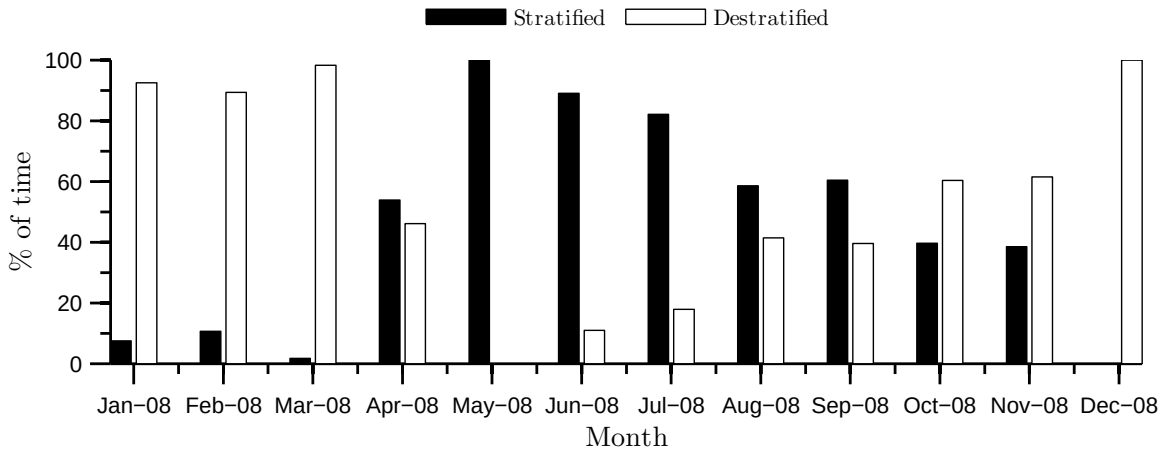

Figure 3.16: Relative duration of thermal stratification and destratification by month.

of the wind velocity over this threshold and the deepening of the mixed layer. In winter, overturn of the water column is the predominant state. Stratification occurs during short periods when wind speed falls below 5 ms^{-1} and the incoming solar radiation provides sufficient heat energy to the uppermost layers. Winter is therefore characterized by homothermal conditions controlled by high wind speeds that also presumably serve to enhance turbidity by sediment resuspension.

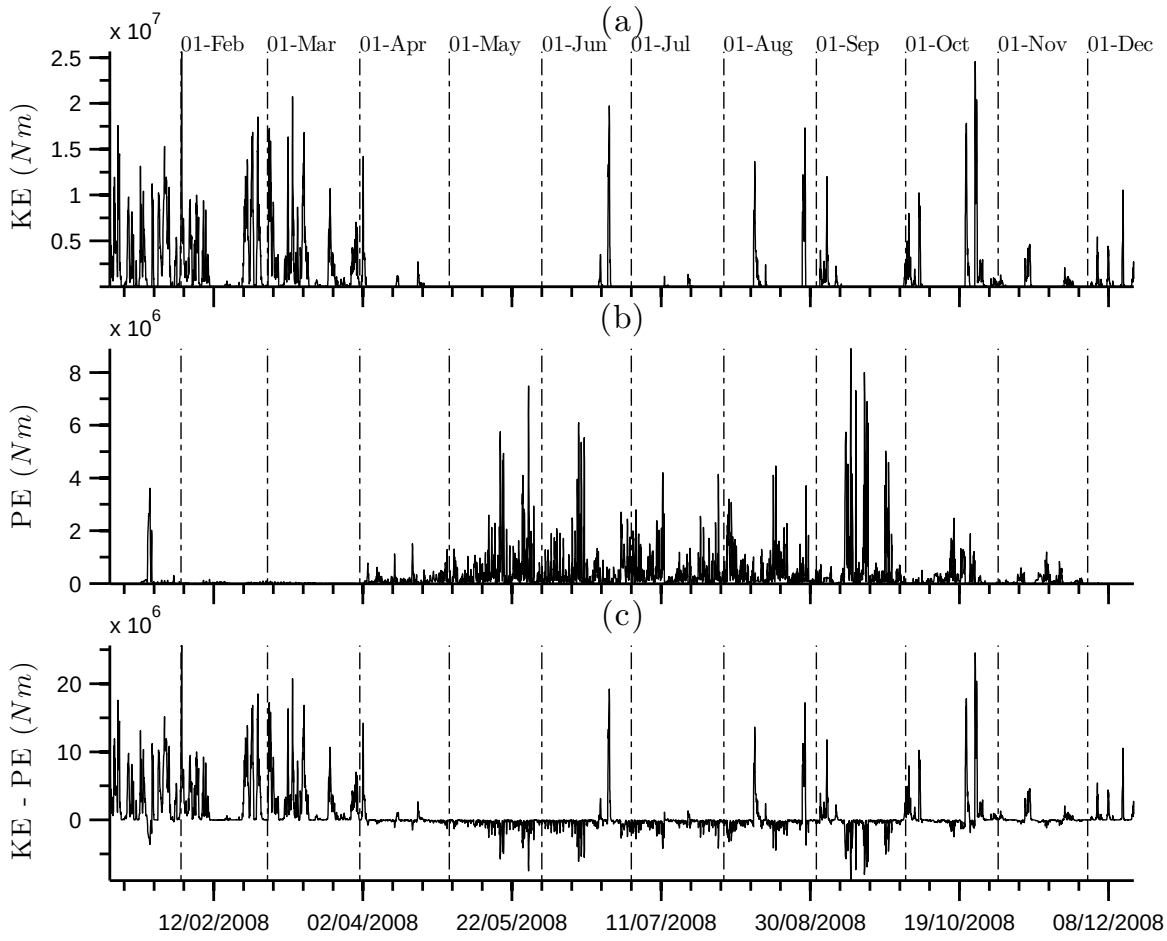

Figure 3.17: (a) Wind kinematic energy (KE). (b) Mixed layer potential energy (PE). (c) Net energy (KE - PE) available to stir the water column.

Chapter 4

FVCOM Graphical User Interface (GUI) Development

Resume

A Graphical User Interface (GUI) to pre-process and post-process FVCOM *information has been designed and programmed. The GUI is used to create the input files required by* FVCOM *for different setups and to analyse and visualize the results produced. It is specially configured for lake modelling problems. This chapter begins with a description of the* FVCOM *input file configuration and a brief explanation of the different functions that these perform. The architecture of the pre- and post-processing interface is explained with the aim of giving an idea of its capabilities and some areas for future development. In order to demonstrate the use of the GUI, an illustrative case study of Llyn Cowlyd, North Wales, is set up using* FVCOM-GUI.

4.1 Design Requirements of a GUI for *FVCOM*

4.1.1 Overview

Computational modelling requires interfaces to manipulate the model information in an optimal and versatile manner. This is particularly the case for spatially-distributed hydrodynamic models applied to environmental problems involving complex domain boundaries (French & Clifford, 2000; Covelli *et al.*, 2002). Most numerical model

codes require multiple data files that specify the computational mesh, bathymetry, and boundary conditions. Additionally, one or more steering files are commonly required to control aspects of model execution, including timestep, values for model constants, and numerical solver parameter values. Dynamic simulations performed at high spatial and temporal resolution generate large solution files and effective visualisation tools are also required. Powerful pre- and post-processing software thus not only facilities and simplifies the modelling process, but also allows the modeller to obtain greater insight into the environmental problem being studied (Garcia-Martinez & Rodriguez-Molina, 1998).

Graphical User Interfaces (GUI) are increasingly provided as an integral part of hydraulic and hydrological model codes. Commercial models such as the *Mike series* (Havnø *et al.*, 1995; Thompson *et al.*, 2004) and *Delft3D* are packaged with GUIs that offer comprehensive pre- and post-processing functionality. Other standalone software packages, such as the *Surface Water Modeling System* (SMS, Zundel, 2005) offer similar functionality in a generic format such that a broad suite of different model codes are supported. Proprietary GUI software is typically programmed using a low level language, often one with object oriented facilities such as *Visual Basic*, *C++* and *Java*. Such GUI software is often tied to a particular computer operating system, even though many model codes are open source and capable of installation and compilation across multiple platforms. However, such packages usually provide very powerful visualisation features, such as the ability to overlay hydrodynamic solutions on base maps or to generate animations.

Open source model codes originating from the research community tend to have less well developed pre- and post-processing software. Sometimes, such GUI functionality is provided in the forms of libraries of routines developed using scripting languages such as *Matlab* or *Python*. For example, Rusu *et al.*, 2008 describe the implementation of a Matlab-based GUI for the *SWAN* shallow water wave model. From a research perspective, development of GUIs using scripting languages offers greater flexibility since the underlying code can be readily modified to suit particular user needs, even where the scripting language itself is part of a proprietary package (such as *Matlab* or *IDL*). Indeed, commercial packages such as *Matlab* are quite attractive for GUI development on account of their in-built features that support specialised data storage formats used within the modelling community (e.g. *NetCDF*; Rew *et al.*, 1997, Rew & Davis, 2002), and tools for GUI programming (such as the *GUIDE* toolbox included

with *Matlab*). They also allow development of plotting, data extraction and video animation capabilities to match any commercial package. Of course, the use of such GUIs requires the user to have access to the scripting language, which generally requires the purchase of the appropriate licence.

The *FVCOM* hydrodynamic code selected for the present study is not equipped with a dedicated general purpose GUI. Accordingly, a major component of the study has been the development of a GUI to provide a flexible and fast tool for the management of *FVCOM* modelling tasks. As shown in Figure 4.1, the GUI includes both pre- and post-processing tools. The pre-processing interface allows the user to set up the input files that contain the model bathymetry, boundary conditions, initial conditions and meteorological forcing data. The post-processing interface has been designed to visualise and selectively analyse the solution files resulting from *FVCOM* model runs. In particular, time series and vertical profiles can be derived for multiple variables at a specific mesh node, and 2D plots can be produced for levels within the water column or along a user-defined section. In addition, the post-processing interface includes an option to produce and save animations to show the time evolution of any given variable.

FVCOM-GUI has been developed in *Matlab*. *Matlab* was selected as a development platform for several reasons. First, it provides a powerful fourth-generation programming language that incorporates a large set of built-in mathematical and data manipulation functions. Second, it has excellent graphical and visualisation capabilities. Third, it includes a set of GUI design environment (*GUIDE*) tools that allow interactive creation of complex GUI templates. Fourth, specialised toolboxes are available to perform functions that are crucial to supporting numerical hydrodynamic modelling applications. Of particular importance, it the availability of a *NetCDF* toolbox that greatly simplifies handling of the large (> 1Gb) model solution files produced by *FVCOM*. Fifth, it is supported under most major operating systems (Linux, Mac OS X, Windows). Finally, although it is proprietary product, *Matlab* is widely used within the hydrodynamic modelling community and generally available within universities and research institutes.

4.1.2 Structure of *FVCOM* Input and Result files

FVCOM requires a set of input files that vary according to the application. These are all ascii text files. The model may write files in ascii format but the *netCDF* (Network Common Data Form) format is more commonly specified for practical applications.

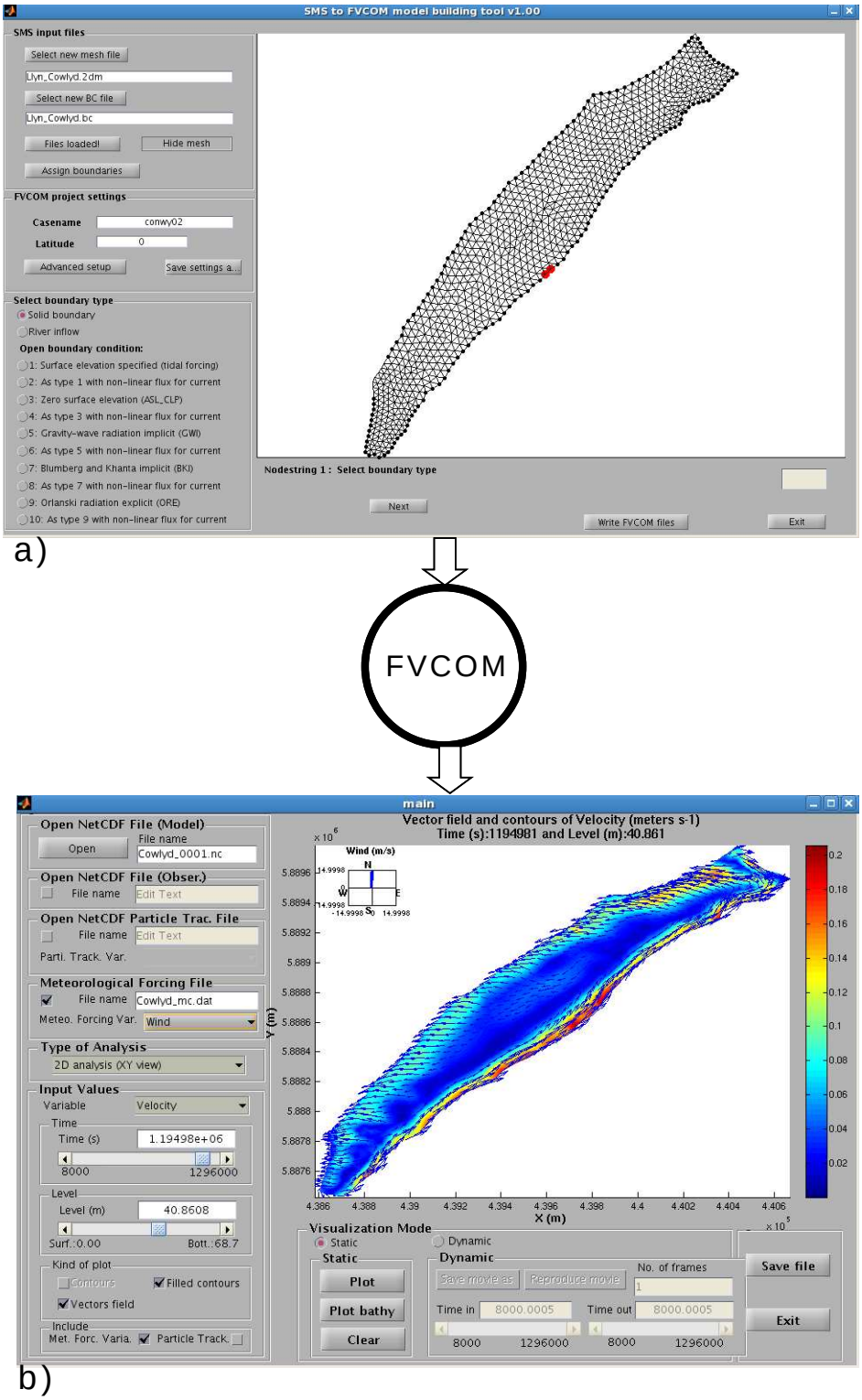

Figure 4.1: Schematic representation of the interaction of a) *FVCOM-GUI* pre-processing and, b) post-processing with *FVCOM*.

NetCDF is distributed as a machine-independent software library that provides multiple functions to create, access and share scientific information. Its implementation provides a format for representing scientific data in a compact and organised manner (Rew & Davis, 2002). The *netCDF* format is widely used in climatology, oceanography and GIS applications and offers an efficient means of storing and interrogating very large multivariate data sets.

Overall execution of *FVCOM* is controlled by the `casename_run.dat` file. This includes information on the simulation duration and timestep, parameters that control input and output (including format of the data fields), and certain global parameters relating to diffusivity, baroclinic pressure gradient terms, and atmospheric and/or tidal forcing. Other aspects of the computation, such as the representation of wetting and drying, are governed by settings contained in this file. In addition to the run control file, *FVCOM* requires a variable set of input files, which can be broadly classified according to their function (Figure 4.2). These file groups include:

- *INPUT FILES REQUIRED FOR ALL SETUPS*: This is a group of mandatory files that contain essential information relating to the computational mesh, bathymetry and boundary conditions.

- *STARTUP DEPENDENT FILES*: This group includes the files that define the initial conditions depending on the `RESTART` option set in `casename_run.dat` file. A model can be cold-started from unknown initial conditions and spun-up until it reaches a steady-state condition. Alternatively, a hot-start option is available to enable the model to be restarted from a file containing all the model variables saved from a previous simulation. This last option is useful for very long simulations where, in some cases, it is necessary to stop and restart the model.

- *METEOROLOGICAL FORCING DEPENDENT FILES*: This file group contains information on meteorological forcings. These can be spatially uniform across the model domain and either time-varying or constant, or else can be spatially varied (controlled by settings contained in the `casename_run.dat` steering file). Whilst many climate forcings are appropriately defined as time series distributed uniformly in space, there may be certain cases where spatially distributed forcings may be required.

- *OPEN BOUNDARY CONDITIONS SPECIFICATION FILES*: This group of files is used to define the open boundary conditions, including inflow and/or outflow discharges and also, if required, water temperature and salinity.

- *OPEN BOUNDARY SURFACE ELEVATION SPECIFICATION FILES*: This group of files is used to define time-dependent forcing of water surface elevation. Although not relevant to lake simulations, various options are available to specify tidal forcings.

- *LAGRANGIAN TRACKING DEPENDENT FILES*: This group includes only one file that is used to specify the starting locations of particles tracked using *FVCOM's* Lagrangian tracking module.

- *SEDIMENT MODELLING DEPENDENT FILES*: These files are used to define the physical characteristics of sediments and the structure and composition of the bed, which can be represented as a series of layers. The sediment model may optionally be forced by imposed suspended sediment concentrations at a set of open boundary nodes or as point sources at river boundary nodes.

The outputs arising from an *FVCOM* model run can be obtained directly from the screen during run-time execution. In practice, however, they are retrieved from one or more *NetCDF* output files. The file `casename_0001.nc`, contains the mesh configuration, bathymetry, and the values of the variables (previously specified in the `casename_run.dat` file) at every mesh node (or, for some variables, at the element centres) for each time step.

The file `casename_ave_0001.nc` contains the mean value of the selected variables at specific time intervals. The file `casename_lag.nc` is optionally used to save the x, y and z coordinates of each particle followed by the Langrangian tracking module through time. It is also possible to append the values of variables (e.g. velocity and temperature) to each particle at every position.

It is evident from this brief overview of *FVCOM* input and output files that a considerable effort is required to assemble and format the required information and to organise the file set. This task also requires low-level understanding of *FVCOM* file structures, source code organisation, and output formats - especially the *NetCDF* file structure. This stage of the modelling process is therefore a prime candidate for simplification by use of a GUI.

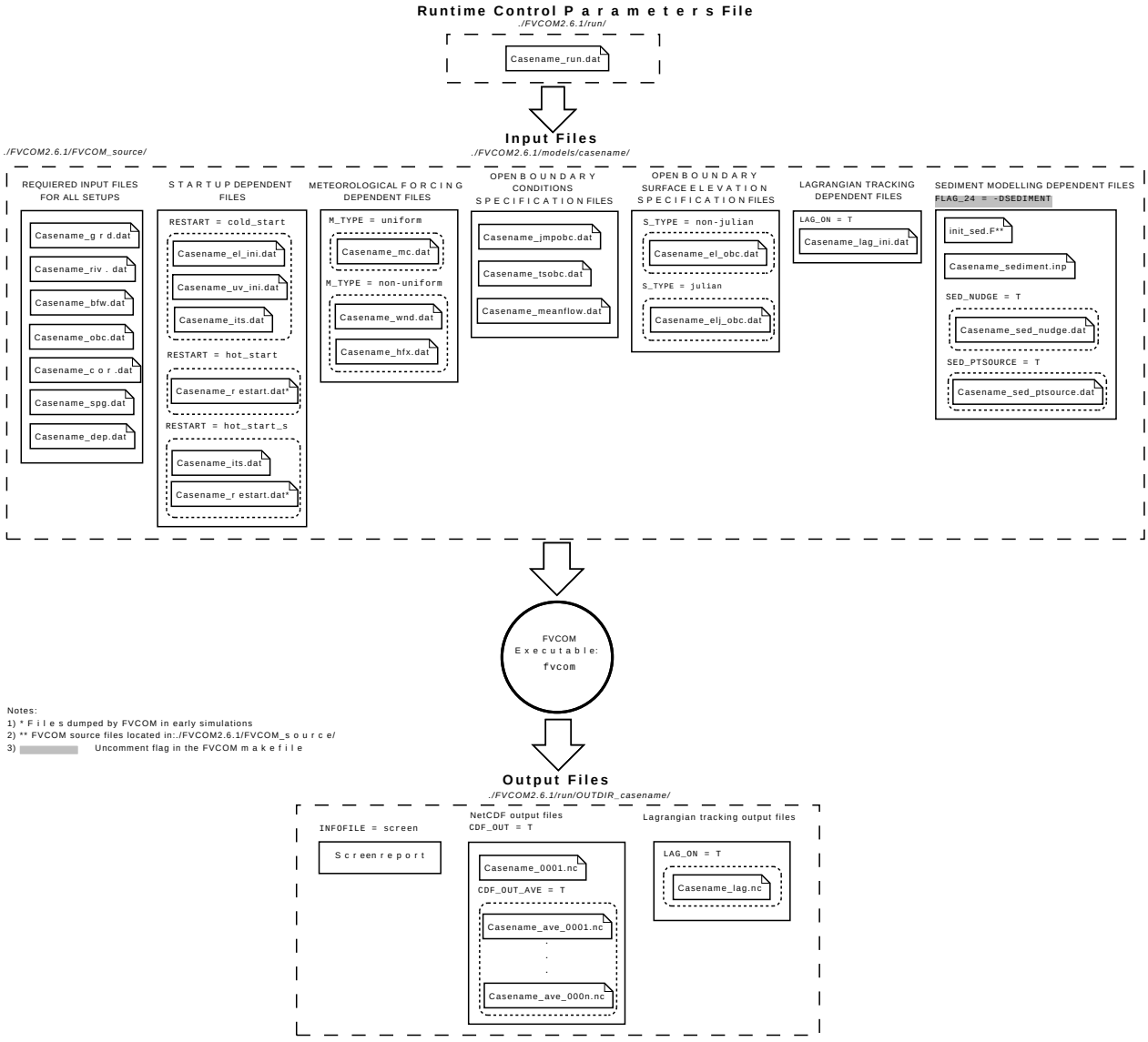

Figure 4.2: Structure of input and output files in *FVCOM*.

4.2 GUI Architecture

The overall GUI architecture is summarised in Figure 4.3. The GUI starts by executing a *Matlab* script `fvcom_gui.m`, which calls the two main program modules, `sms2fvcom.m` and `main.m`, that manage the pre-processing and post-processing interfaces respectively.

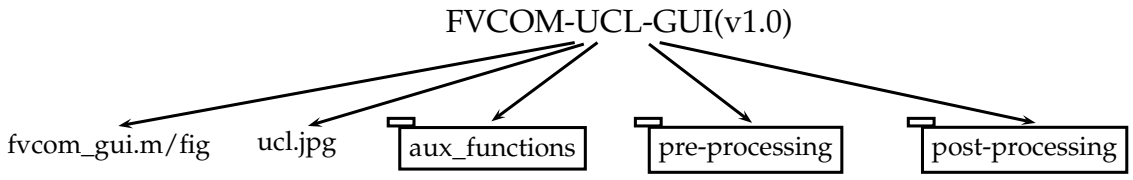

Figure 4.3: *FVCOM-GUI* file and directory structure.

The pre-processing functionality is provided by a set of *Matlab* script files contained in the pre-processing directory. These are invoked as required by the managing script `sms2fvcom.m` , as shown in Figure 4.4. The pre-processing is described by the flow chart represented in Figure 4.5. Pre-processing starts with the reading of two files that contain the x and y coordinates of the computational mesh, and the x and y coordinates of the boundary nodes. Generation of the computational mesh is thus handled externally (the Surfacewater Modeling System, SMS, has been used to generate all the mesh files used in this study) and this functionality is not presently built into the GUI. Once these files have been read, the mesh can be displayed.

The GUI then allows the user to set three kinds of boundary conditions (BCs): solid boundaries, specified inflows and outflows, and open boundary conditions (OBC). At solid boundaries it is assumed that there is no flow through the boundary and this is the default boundary type within *FVCOM*. Alternatively, inflows can be defined as point sources where discharge, temperature and/or salinity can be set for a specific mesh boundary point and elevation for groundwater inflows, or else distributed through the water depth in the case of river inflows. Outflows are specified in the same way but signed as negative values. The OBC option, includes ten distinct types of open boundary conditions used to model forcing by time-varying water surface elevations. These include a range of tidal options and are not fully implemented in the present version of the GUI (they are not immediately relevant to lake modelling problems).

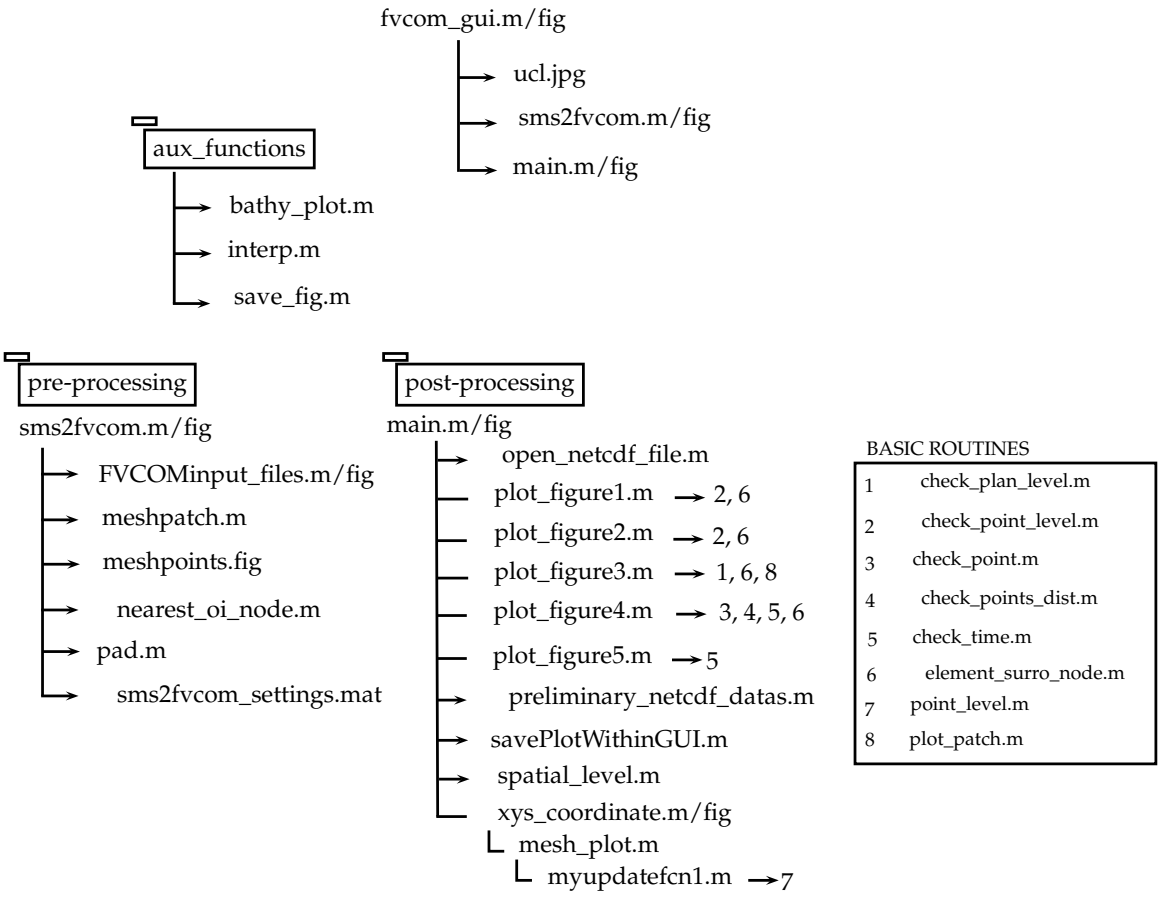

Figure 4.4: *FVCOM-GUI* script file dependencies. The *BASIC ROUTINES* are scripts called on multiple occasions by the post-processing routines.

BC assignment is handled interactively. The user first specifies a BC type and then selects the associated boundary points on screen. For each node selected in this way, the GUI records, the type of BC, the node number and its x and y coordinates. Multiple BC types can be set for a study case, by repeating the selection of BC, the points chosen and the saving of the information.

The GUI is presently configured to generate the various categories of *FVCOM* input file as described in Section 4.1.2. At the present time, however, generation of the *OPEN BOUNDARY CONDITIONS SPECIFICATION FILES* is not fully implemented. The GUI will always write the first file group, *REQUIRED INPUT FILES FOR ALL SETUPS*, and will write other files according to options chosen by the user. The GUI pre-processing stage can be exited after the necessary input files needed have been written. Multiple model setups are possible without having to exit the GUI, which is convenient for the preparation of a set of model runs with varied parameters or forcings.

The post-processing module of the GUI is designed to visualise and analyse the information contained in *FVCOM* solution files. The program flow is summarised in Figure 4.6. The first stage involves selection and opening for read access of an *FVCOM* -generated *NetCDF* file (see `**NetCDF file (Mod.)` in Figure 4.6). Several additional options are available here. These include options to read a *netCDF* file containing relevant observational data in a compact format; a *NetCDF* file containing information from a particle tracking simulation; and/or the meteorological forcing data file `casename_mc.dat` which is used as one of the input files for an *FVCOM* model run. These optional files facilitate comparison between model predictions and observations, and also allow convenient visualisation of the relationship between modelled outcomes and the main (in this case meteorological) forcings used in the model run.

Once the *NetCDF* data files are read, the GUI invites the user to select from various visualisation options:

- `1D analysis (One variable):` This option allows the user to plot either the time evolution or the variation with depth of a variable, at one or more locations within the model domain (selection of up to five locations is currently supported). The time evolution and the depth variation plots differ from each other in that, in the case of the former the user must specify the start and end time, whereas for the latter only a single time is required. The x, y and z (σ level) coordinates of the points chosen can be set interactively by selecting points in the mesh. At this

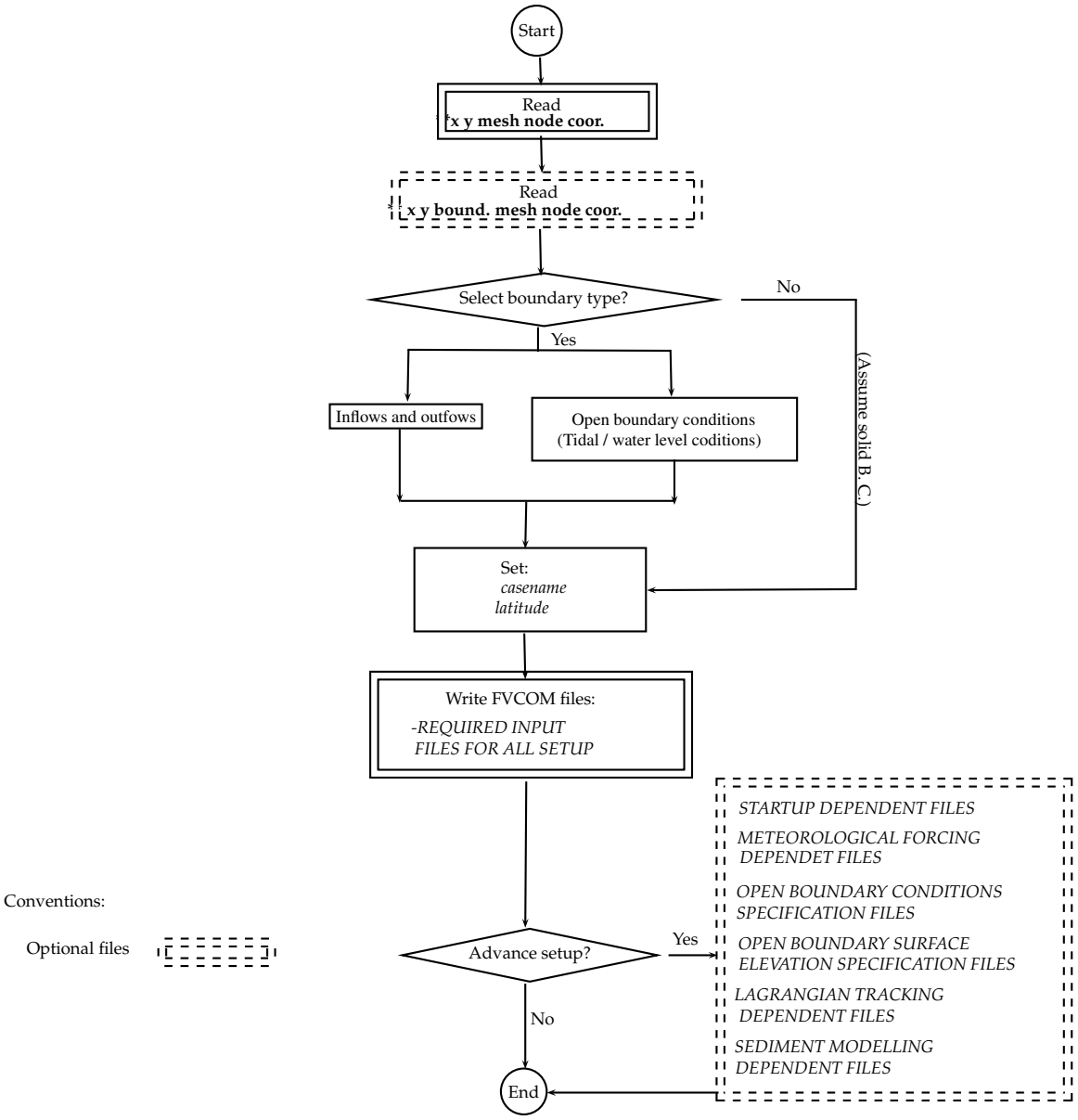

Figure 4.5: Pre-processing *FVCOM-GUI* flow diagram.

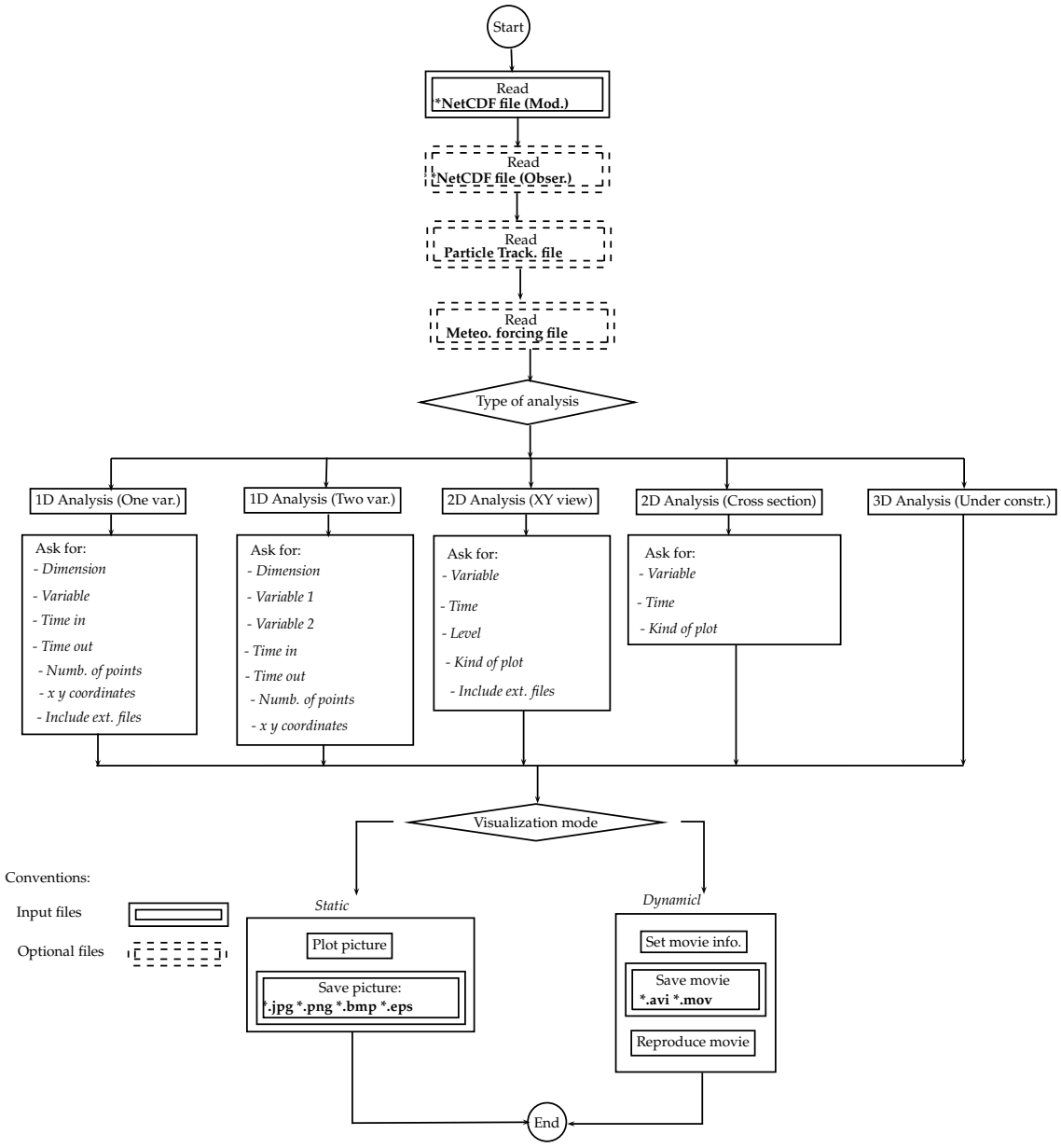

Figure 4.6: Post-processing *FVCOM-GUI* flow diagram.

stage there is also an option to plot meteorological forcing data and/or observed variables along with the modelled information.

- `1D analysis (Two variables):` This option allows the user to plot two different variables through time or the water depth in the same axes for an specific point, with the aim of comparing both series.

- `2D analysis (XY view):` This option is used to plot an XY view of a variable for a specific time and level within the water column (σ level). This option offers the possibility of plotting the information in any of the three following ways: contours, filled contours and as a vector field. These plot types are enabled for all the variables listed in a pop-up `Variable` menu, with the exception of the vector field plot type, which is only available for the velocity variable. As with the two 1D options described above, this option includes the possibility of including a meteorological forcing variable for a specific time. There is a further option to plot the positions of particles simulated using particle tracking features in *FVCOM*.

- `2D analysis (Cross section):` This option is used to plot the values of a variable along a cross section (or transect) for an specific time. The cross section is defined by entering the x, y and z coordinates for two points to define the start and end points of a transect. An algorithm within the GUI firstly searches the triangular elements that are intersected by the line, then projects perpendicularly the vertices of the elements found onto the transect and calculates the new x and y coordinates along the line; the σ coordinates are kept untouched. To visualise information contained in the projected nodes, the algorithm transforms the σ coordinates to real coordinates and interpolates the attribute (value of the variable choosen) of each node onto a orthogonal rectangular grid adapted to transect.

- `3D analysis:` This option is still under construction but, when completed, will allow plotting of results in three dimensions.

After the analysis type has been specified using one of the options described above, the user is ready to visualise the information using either a `Static` or `Dynamic` mode. The `Static` mode plots the information already defined for the chosen `Type of Analysis` option. On the other hand, the `Dynamic` mode is used to produce

Table 4.1: Geographical information for Llyn Cowlyd.

Location	Snowdonia National Park, North Wales
Coordinates:	$53^o08'N\ 3^o55'W$
Altitude:	355.00 m
Maximum length:	2.78 km
Surface area:	1.1 km^2

and save a movie animation, and this is available only for a sub-set of the `Type of Analysis` options: `2D analysis (XY view)`, `2D analysis (Cross section)` and `3D analysis`. The user must set under the `Dynamic` label, the number of frames to be recorded, the start time and the end time of the movie; the water level for the option `2D analysis (XY view)` must be set in its own menu. Movie animations are saved using the *AVI* format, and can replayed using any software that supports this format. To save the *AVI* file, an algorithm divides the time interval by the number of frames and sets a series of new times that are approximated to the nearest simulated times, with the aim of retrieving the information from the *NetCDF* file for each time. The files can also be played using the `implay` tool in *Matlab*, which offers multiple options to play, pause, and step through an animation.

4.3 Example Application of GUI to Pre- and Post-process *FVCOM* Simulation

In order to demonstrate further the functionality provided by the new *FVCOM-GUI*, a hypothetical model set up for Llyn Cowlyd (Lake Cowlyd) is presented. This is another small upland lake in North Wales, and provides a good illustration of the tasks involved in implementing an *FVCOM* model and visualising the modelled hydrodynamic behaviour. Table 4.1 summarises the principal geographical and physical characteristics of the lake. This demonstration *FVCOM* simulation is setup using null values for all the meteorological forcing data included in the `Cowlyd_mc.dat` file, with the exception of the wind forcing, which was set up with a constant northerly wind of 10 m/s. The properties of the computational mesh and the run control parameters are summarised in Table 4.2.

Table 4.2: Llyn Cowlyd *FVCOM* model setup information.

No. of Nodes	831
No. of Elements	1492
No. of layers	15
Mean length element edge:	$\approx 32\ m$
Duration	15 days
Δt:	$1\ s$

Installation of the GUI is straightforward. First, the user must obtain and uncompress the archive `FVCOM-UCL-GUIv1.0.tar.gz`. Next, *Matlab* must be started and its path set to the `FVCOM-UCL-GUIv1.0` directory path. The GUI has been tested under linux (*RedHat Enterprise Linux*), *MacOS-X* (10.6.8 Snow Leopard), and *Windows XP/Vista/7* operating systems with *Matlab2008b* or later pre-installed. To start the GUI, the user must type `fvcom_gui` at the *Matlab* command line. The *FVCOM-GUI* start-up screen is then displayed (Figure 4.7).

At this stage, the user can choose between pre- and post-processing functionalities. The GUI can also be exited at this stage. Pressing the pre-processing button, results in the window shown in the Figure 4.8 being displayed. The Select new mesh file button is used to open the *SMS* `Llyn_Cowlyd.2dm` file that contains information about the mesh configuration, and the `Select new BC files` button is used to open the `Llyn_Cowlyd.bc` file that identifies which nodes are located on the mesh boundary. Both files are then read into memory using the `Read files` button.

Display of the computational mesh is toggled by the `Show/Hide mesh` button. Boundary types are then selected interactively by stepping through the set of boundary node segments specified in the BC input file. An undo option has been implemented here so that any mistakes can be immediately rectified. For the purpose of this illustrative example, the lake is considered to be enclosed by a closed solid boundary (the default option in *FVCOM*).

Once the `Casename` and `Latitude` fields have been populated, the `Write FVCOM files` button is used to write the minimal set of *REQUIRED INPUT FILES FOR ALL SETUP*. This set of files is sufficient for this GUI test case. The *FVCOM* model can now be executed.

Once *FVCOM* model execution has been finished successfully, the user can visualise the results using the post-processing mode. On selecting the post-processing option

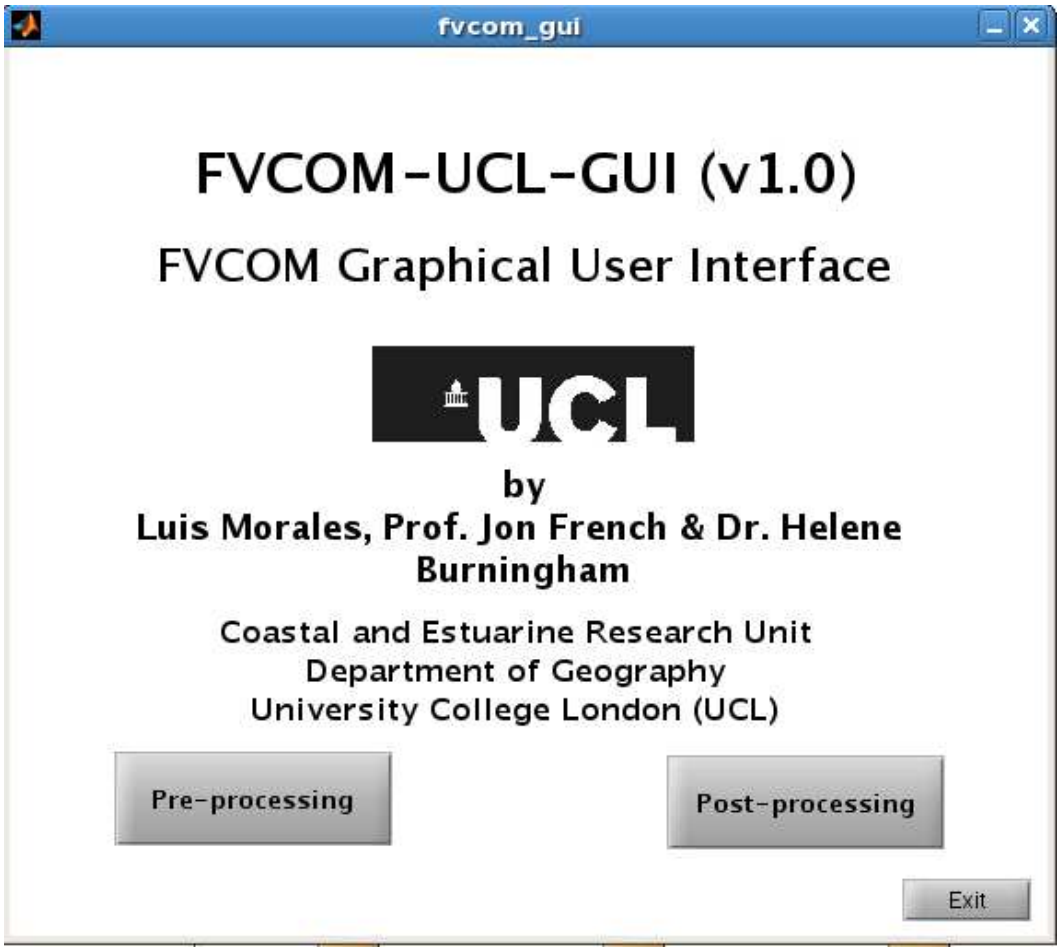

Figure 4.7: *FVCOM-GUI* startup 'splash screen' and menu to choose between pre- and post processing modes.

(see Figure 4.7), the window shown in Figure 4.9 prompts the user to open a *NetCDF* solution file. A filesystem browser dialogue filters files with a `*.nc` filename extension.

Once the *NetCDF* file is opened and read, the interface is transformed and new functions become available, as is shown in the Figure 4.10. In this case, a file `Cowlyd_0001.nc` generated by a previous *FVCOM* run has been selected. This window allows the user to open and read additional files at any time during the post-processing usage. For example, if the user wants to include the meteorological data use to force the model run, they can check the square box under the `Meteorological Forcing File` frame and a dialogue will be displayed to open the relevant file. A list of meteorological forcing variables will then be displayed under the `Meteo. Forcing Var.` popup menu,

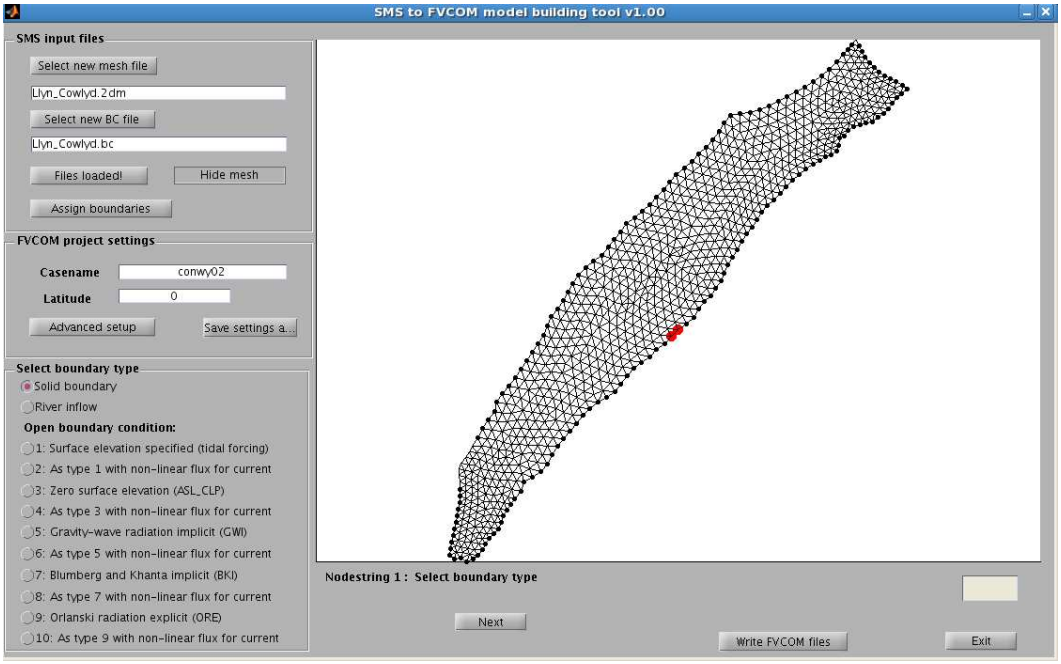

Figure 4.8: Pre-processing window where the SMS files are read, and the required files are created.

ready to be selected.

The `Type of Analysis` pop-up allows the user to select from the five different modes of analysis outlined in Section 4.2. Each type of analysis has its own `Input Values` frame, so each time the user changes the type of analysis a new frame will appear underneath. In the current example, the `1D Analysis (One variable)` option has been chosen. A `temporal` analysis has been selected here (the default) with `Velocity` as the variable chosen using the `Variable` pop-up menu. Additionally, the values of `Time in` and `Time out` must be set using either the manual entry field or the slider. The user will notice that any value introduced in the manual entry field will cause a movement in the slider. Likewise, the time indicated by the slider position will automatically appear in the entry field. The user will also see that the time set under `Time in` frame can not be greater than the one under `Time out` frame, so if the first one is set greater than the second one both sliders are pulled back to the minimum time.

For the `1D Analysis (One variable)` option, it is also necessary to choose the number of points at which to plot the variable chosen. Using the `Number of points`

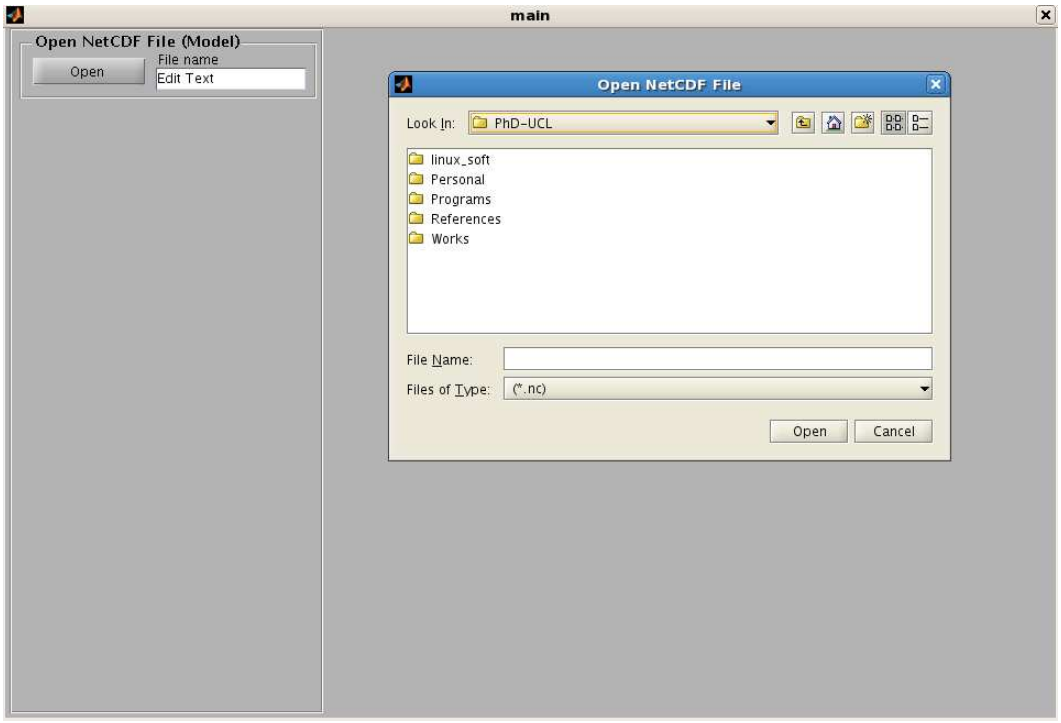

Figure 4.9: Post-processing window where the *NetCDF* file is read.

pop-up menu 5 points have been chosen (the maximum number of points available) and the window shown in Figure 4.11 then appears. This allows the user to set the x and y coordinates and the water level of the points interactively using the mouse or by entering coordinates manually in the relevant fields. To select a point, the user has to press its associated radio button (the small circular buttons) and then click on any node on the mesh. Each time the user clicks on a node on the mesh, the x and y coordinates fields are updated along with the lower (water surface level) and upper (bottom level) limits of the `Sigma-level` slider. If the coordinates are already known, these can be entered manually, and the interface will automatically find the nearest mesh node. Once the points have been chosen, it is possible to save, then using the `Plot` button to plot the points using numbered red spots (see Figure 4.11). Additionally, the `Clear plot` remove the points plotted.

Once the information required for the `1D Analysis (One variable)` option has been set, the user is ready to plot the `Variable` from `Time in` to `Time out` at the points already selected by pressing the `Plot` button. The time series are plotted within the graphic pane on the right hand side of the window (see Figure 4.10). In the event

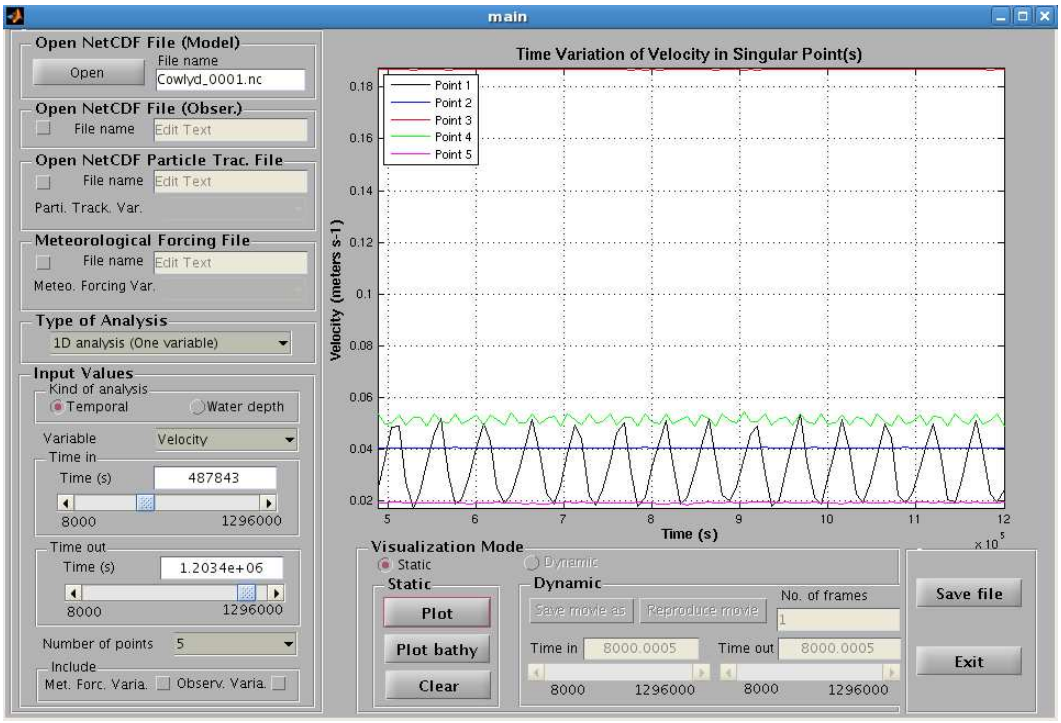

Figure 4.10: Post-processing window showing the multiples files available to read, so that the input information for the `1D Analysis (One variable)` type of analysis.

that multiple points are specified, the plot lines are colour coded.

Vertical variation in a variable over the water depth can be plotted by selecting the `Water depth` radio button under `Kind of analysis` and by setting the parameters available under this option. Figure 4.12 shows plots of the x, y and z components of the vector velocity and its magnitude, where each colour represent a different point. Note that shorter velocity profiles correspond to shallower locations in the lake.

Further analysis can be chosen from the `Type of Analysis` pop-up menu. In Figure 4.13 the type `2D Analysis (XY view)` has been chosen to represent the velocity field, most of the options for which are set up in the way described above for the `1D Analysis (One variable)`. The user will notice that the lower limit (water surface level) of the `Level` slider will change according to the the time. Additionally, the user can choose between three different `kind of plots`: `contours`, `filled contours` and `vector field`. The user can either pick one or all three of these options using the square check boxes placed in the `Kind of plot` frame.

Figure 4.13 shows a `2D Analysis (XY view)` analysis in which the user has also

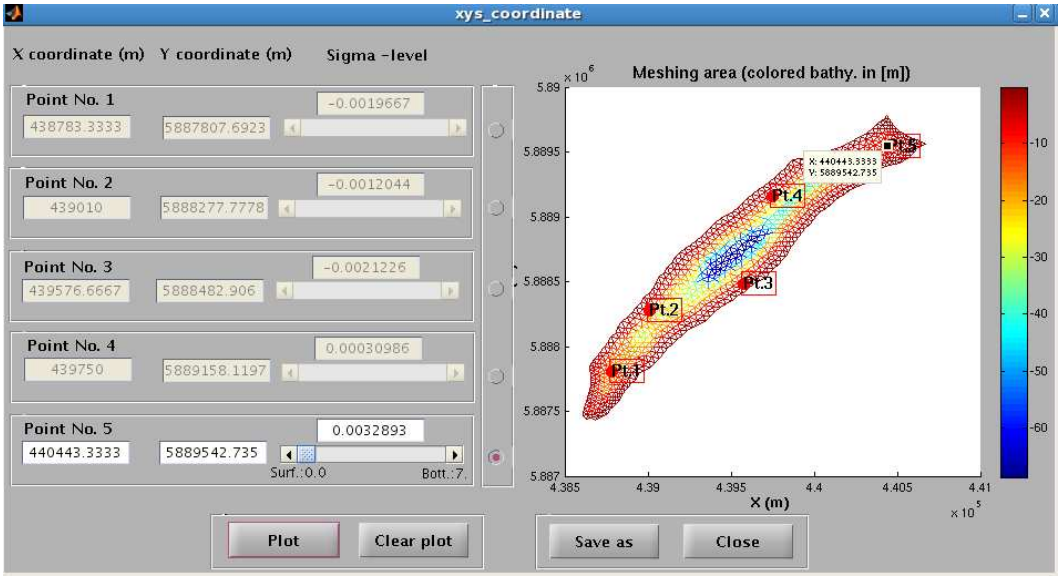

Figure 4.11: Post-processing window to select points on the computational mesh.

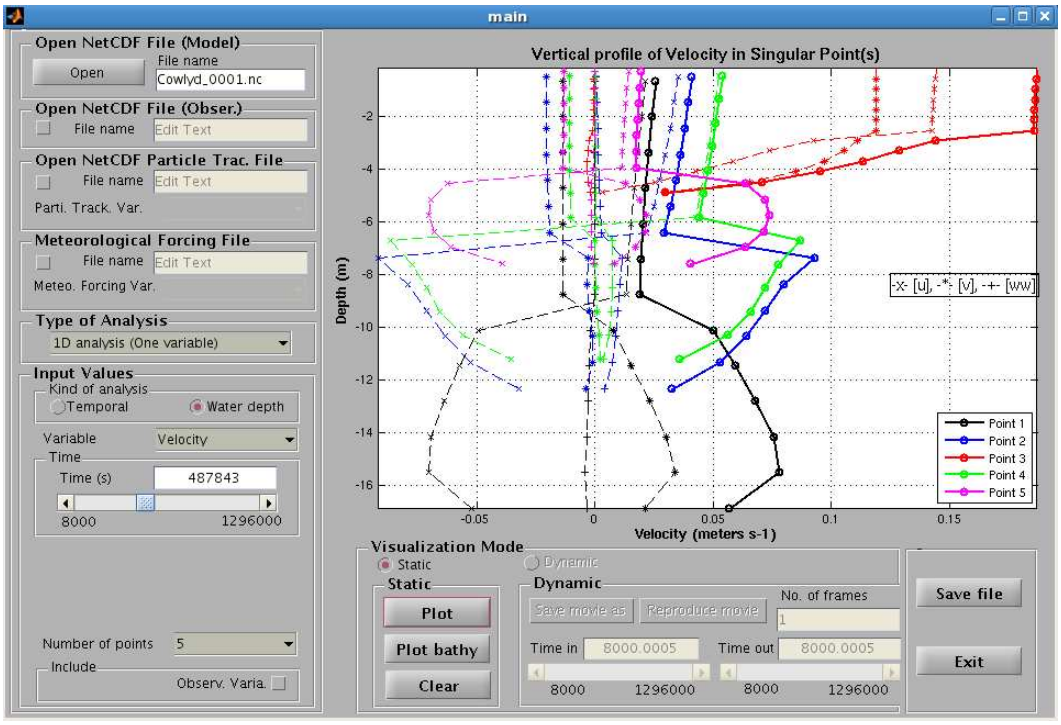

Figure 4.12: Post-processing window with velocity components and magnitude plotted.

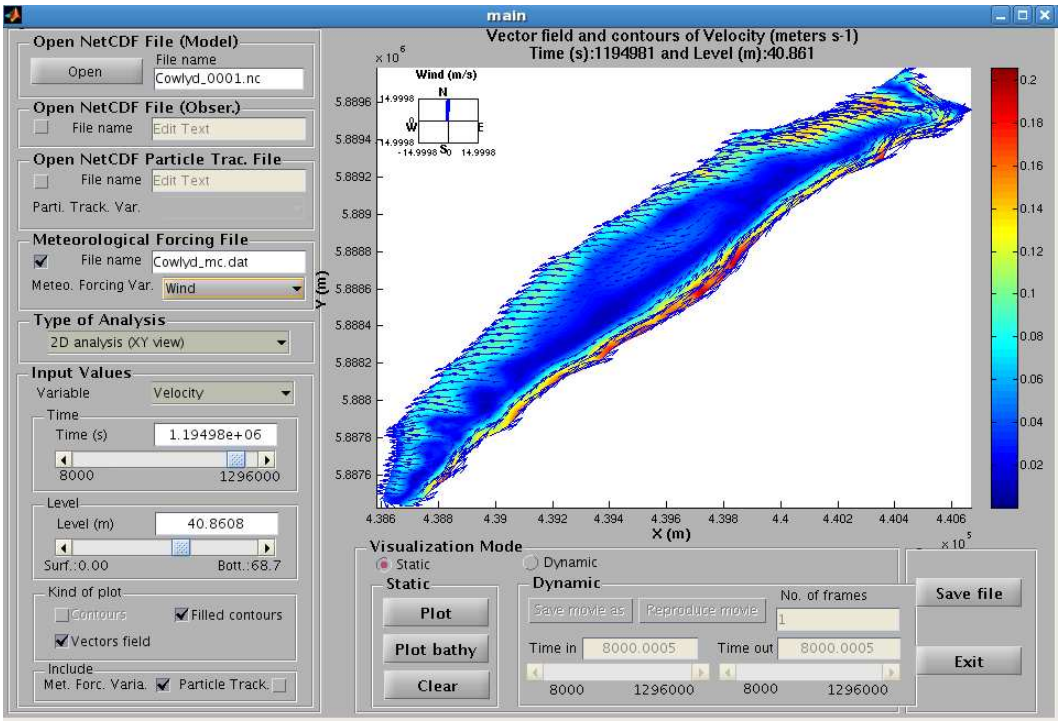

Figure 4.13: Post-processing window with velocity field and wind forcing information plotted.

selected and read in the `Meteorological Forcing File`. The graphic pane thus displays both the velocity vector field, including filled contours for a particular moment in time and a specified level. In addition, the wind forcing information (wind velocity and direction) is plotted in a small set of axes placed in the left upper corner.

The `2D Analysis (Cross section)` option is illustrated in Figures 4.14 and 4.15. In contrast to the `2D Analysis (XY view)`, this option does not require the user to specify a given water level, nor does this option support inclusion of external information (such as meteorological forcing or particle tracks). Instead, the `2D Analysis (Cross section)` option requires a cross section of the basin to be defined by interactively setting the x and y coordinates for its start and end points. Figure 4.14 shows this process after the user has just entered the transect co-ordinates. Both points are highlighted on the mesh and the transect line has been plotted. The velocity field for the section shown in Figure 4.14 is plotted in Figure 4.15.

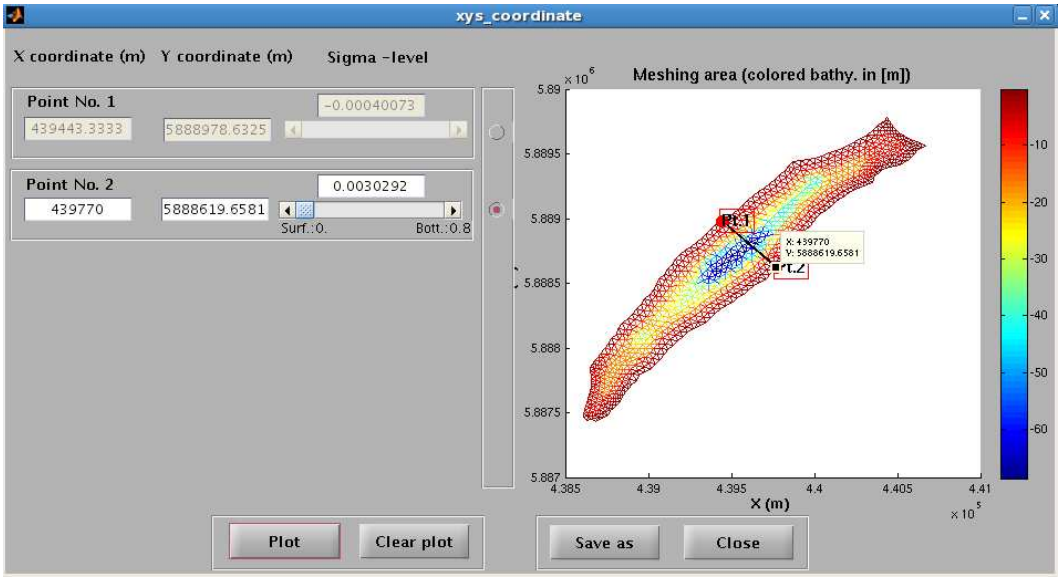

Figure 4.14: Post-processing window to define a cross section.

In conclusion, it should be noted that any plot displayed within the GUI can be saved using the `Save` file button. In the case of a movie animation, the Dynamic frame must be activated and the information required under it must be provided. As in the pre-processing module, the GUI can be shutdown using the Close button.

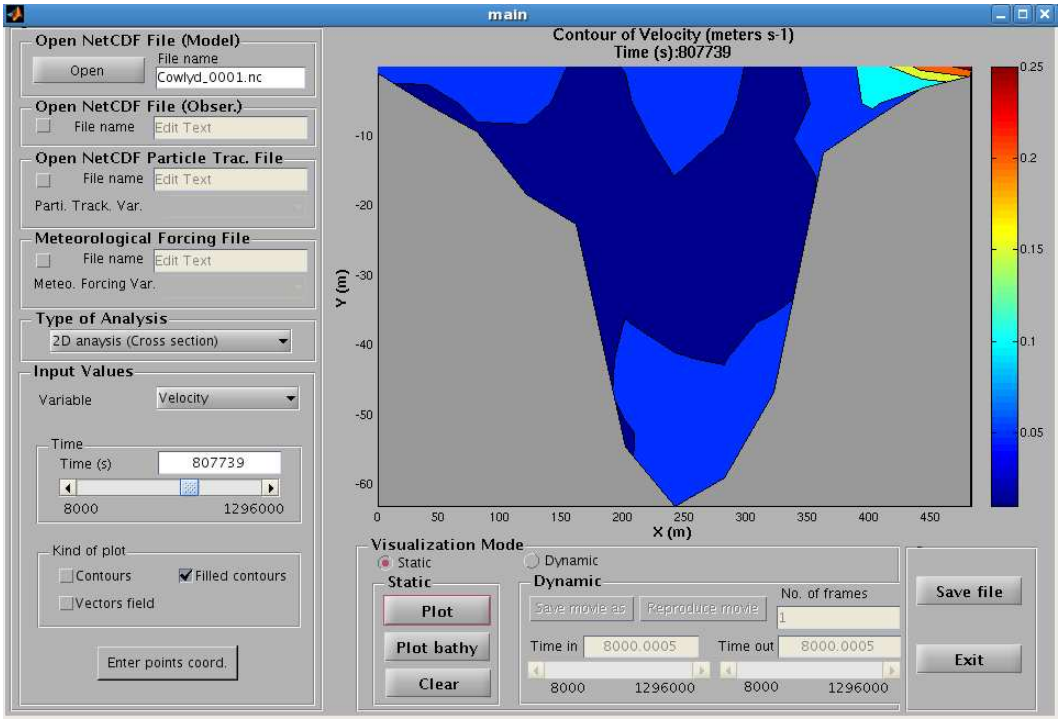

Figure 4.15: Post-processing window representing the field velocity in a cross section.

Chapter 5

3D Modelling of Wind-Driven Circulation and Bottom Stress

Resume

This chapter applies the 3D FVCOM *model to investigate various aspects of the hydrodynamics of Llyn Conwy.* FVCOM *is evaluated with respect to vertical velocity profiles measured by ADCP deployments in the second field campaign. This is complemented by an analysis of surface seiche and internal wave motions, aided by observations of pressure and temperature fluctuation. The simplified wind wave model,* UCL-SWM*, is calibrated and validated against time-series of surface wave variables obtained at selected locations around the lake shore. A comprehensive analysis of wind records from 1993 to 2011 is undertaken to determine the characteristics of extreme wind forcing events and the most prevalent wind directions. Multiple wind speed and wind direction scenarios along with water surface level scenarios are specified and the space and time variation in bottom stress due to the effects of wind-driven currents and waves is investigated in detail. The chapter concludes with the analysis of bottom shear stresses during December 1997, which includes the highest magnitude wind forcing event between 1993 and 2011.*

5.1 Introduction

As shown in Chapter 4, one-dimensional hydrodynamic models can provide valuable insights into the thermal evolution of lakes that are especially useful in characterising

lake behaviour over seasonal and multi-annual timescales. However, such models neglect aspects of the circulation that can be very important, even in small lakes, when the externally-imposed wind stress is strong, or when inflows and outflows are significant (e.g. Imberger & Hamblin, 1982, Hodges *et al.*, 2000). In lakes subject to strong wind forcing, horizontal gradients are no longer negligible and complex patterns of circulation arise due to the interaction with bathymetry. These water movements may exert a significant influence on the transport and deposition of sediments (Csanady, 1975) and knowledge of this aspect of lake hydrodynamic behaviour is thus very important to inform any subsequent analyses of lake depositional sequences (e.g. for palaeoenvironmental reconstruction).

This chapter demonstrates the application of the 3D *FVCOM* model to investigate various aspects of the hydrodynamics of Llyn Conwy. First, the ability of *FVCOM* to resolve the vertical velocity profiles generated by wind-generated surface stress is investigated with reference to the ADCP datasets obtained during the second field campaign. This is complemented by an analysis of oscillatory motions, both surface seiche effects and internal waves, aided by observations of high-frequency pressure fluctuations from the first field campaign and the vertical thermistor chain data from the CEH data buoy. Second, the space and time variation in bottom stress due to the effects of wind-driven currents and waves, in isolation and in combination, is investigated. This involves calibration and validation of the simplified wind wave model, *UCL-SWM*, against time-series of surface waves obtained at selected locations around the lake shore during the second field campaign. In addition a comprehensive analysis of wind records from 1993 to 2011 is undertaken to determine the characteristics of the most extreme wind forcing events, and also the most prevalent wind directions. From the wind forcing frequency analysis, multiple wind speed and wind direction scenarios along with water surface level scenarios, are established with the aim of analysing the effects of the wind forcing and water surface level changes on the bottom shear stress distribution. The chapter concludes with the analysis of bottom shear stresses during the month of December 1997, which is a period of strong winds and includes the highest magnitude wind forcing event between 1993 and 2011. This analysis informs the subsequent analysis of the nature and controls on bottom sediment accumulation in Chapter 6.

Table 5.1: Set-up of *FVCOM* for calibration.

Parameter	value
Starting date	03/04/2011 14:00:00
Finishing date	08/04/2011 07:00:00
# of elements	2028
# of nodes	1097
# of σ levels	12
Δt(s)	1.0
Mean element edge length (m)	13.2

5.2 Calibration and Validation of *FVCOM*

5.2.1 Calibration

Full calibration of 3D hydrodynamic models is not always undertaken because of the high computational requirements. Many 3D models thus use parameter values obtained from previous sensitivity analysis with simpler 1D and 2D models. Parameters such as bottom roughness (z_0) are established based on physical characteristics such as sediment grain size and density. For example in Clear Lake California, USA, where sediments are predominantly muddy, Rueda *et al.*, 2003 set $z_0 = 0.02$ *cm* to implement a 2D model. In Lake Okeechobee Florida, USA, a relative high value of $z_0 = 0.5$ *cm* was set to take account of abundant vegetation in littoral areas (Jin *et al.*, 2000). Other studies (e.g. Gross *et al.*, 1999) suggest a spatial distribution of z_0 based on the local depth, to account for the effects of wave motions in the hydrodynamic model. Despite an extensive literature on the roughness coefficient, its specification is often rather arbitrary.

Here, a calibration with respect to z_0 was carried out against the velocity profiles recorded using an ADCP at location 1 (ADCP1) shown in Figure 2.14. z_0 was assumed to follow a uniform distribution between 0.001 m to 0.06 m (Ji, 2008), with values sampled at random using a Monte-Carlo approach. Model performance was evaluated following the performance functions described in Chapter 2, with particular emphasis on the maximisation of the Nash-Sucliffe coefficient (NSE). The characteristics of the model setup used for each simulation are summarised in Table 5.1.

FVCOM was forced by the meteorological data recorded during the second field campaign (Figure 5.1). The meteorological wind forcing series shows that, a south-westerly wind is the dominant pattern (Figure 5.1b) with velocities fluctuating mainly between 12 and 16 $m\ s^{-1}$.

The initial conditions were established by spinning up the model over two days using a constant wind speed (11.2 ms^{-1}) and direction (241.92^o) which correspond to the wind forcing conditions at the start of the calibration period. To illustrate the model performance during the spin-up time, the temporal evolution of the vertical velocity structure is shown at two different points (Figure 5.2) chosen randomly in the lake basin (see Figure 5.3 for the point locations). At both points, the velocity structure behaves chaotically over the first two days because the water body is accelerated from a static condition by the wind forcing. After the first day the flow becomes more stable, and a more organised velocity structure is observed, but still with no steady structure at P2 (Figure 5.2b). Only after the end of the two-day spin-up period, does the velocity structure tends to be more stable.

The resulting flow velocity fields at the water surface (Figure 5.3a) and at the mid water depth (Figure 5.3b) after the spin-up period, give preliminary clues about the characteristic circulation patterns in the lake. A comparison between both shows similar patterns of circulations especially at the northern and the eastern sides of the lake. In these areas, the formation of an anticyclone gyre is visible after the confluence of two strong current flows at the east of the lake. The first originates from the north, and the second from the south centre of the lake.

Not only are initial conditions for the flow field required, but also scalar magnitudes such as water temperature need to be defined at the initial time step. A uniform distribution of the water temperature was set, equal to 4.71 ^oC based on the thermal structure analysis described in Chapter 3. This showed that in the month of April, the lake stays mixed more than 40% of the time and during intermittent stratified periods, the thermocline is not significantly sharp.

Simulations were performed for 90 different values of z_0, from which the best parameter was found by the maximisation of the NSE (Figure 5.4a). The results of the calibration show a generally acceptable model performance (NSE > 0.5) for all the z_0 values. Figure 5.4b shows that as the values of z_0 grow between 0.001 and 0.02 m, NSE increases rapidly, reaching its maximum value of 0.84 when $z_0 = 0.0227\ m$. Then, NSE

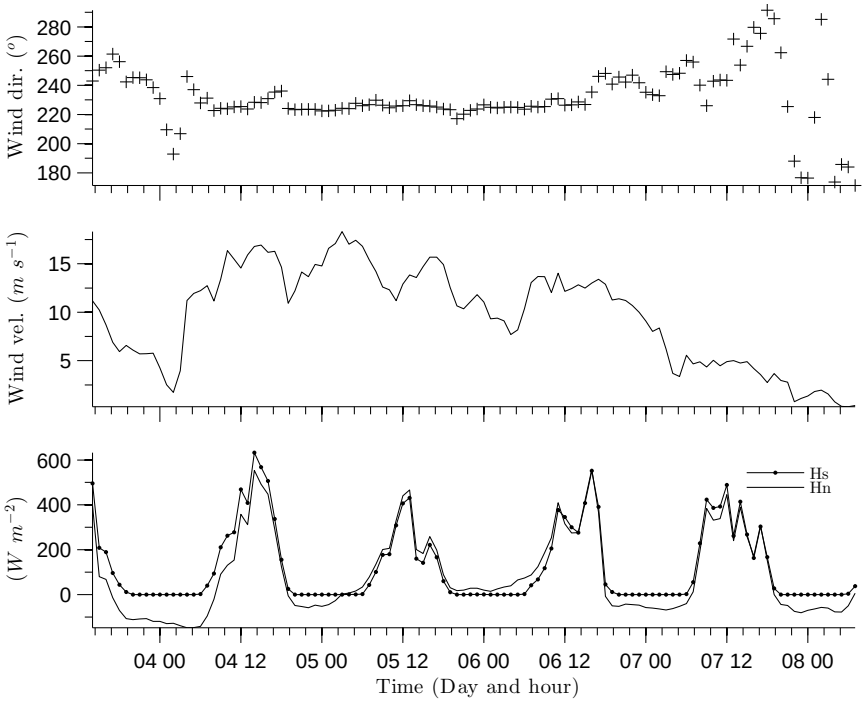

(a)

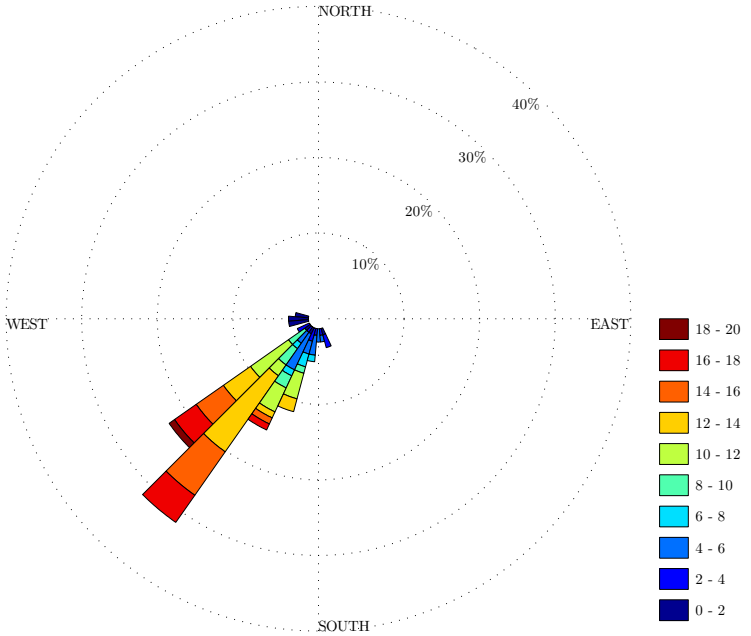

(b)

Figure 5.1: Hourly meteorological forcing from 03/04/2011 to 08/04/2011. a) Wind direction, wind speed measured 10 m above the ground and, incoming solar radiation (Hs) and net heat flux (Hn). b) Wind rose where the colour scale and the concentric circles indicate the wind speed ($m\ s^{-1}$) frequency.

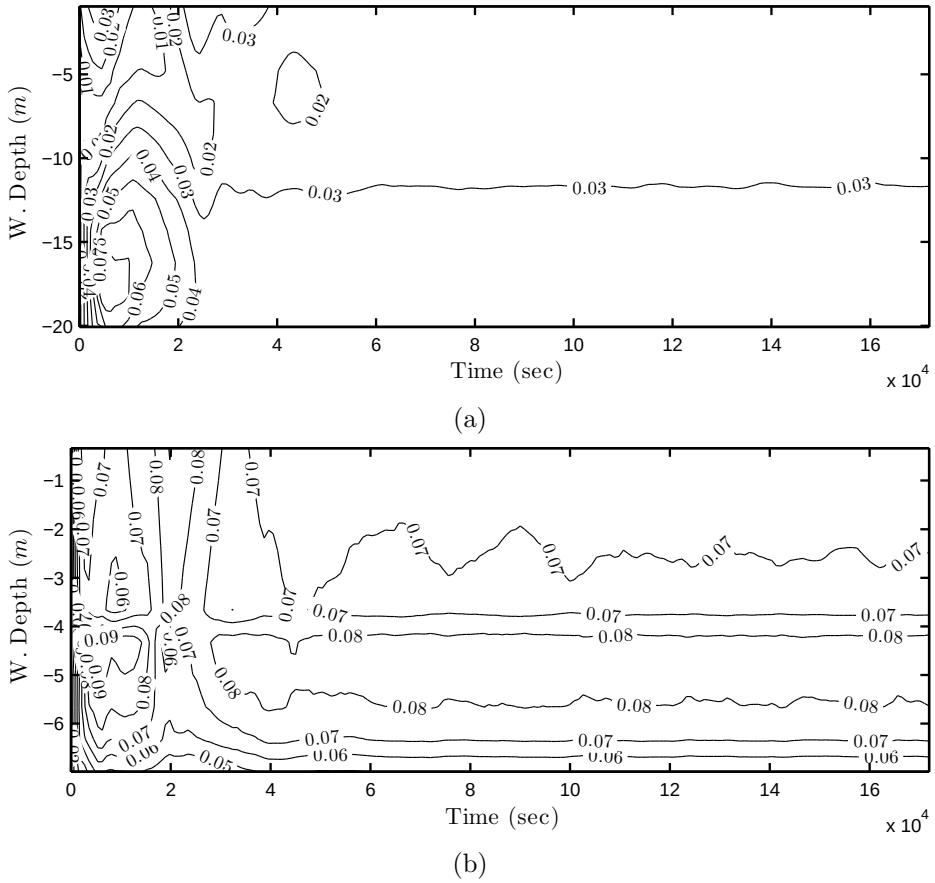

Figure 5.2: *FVCOM* model spin-up of the flow velocity structure at two different points during 2 days of simulation time. a) Magnitude of flow velocity at P1; and b) at P2. The locations of the points are shown in Figure 5.3.

function decreases slightly to ∼0.80 for $z_0 > 0.0227\ m$, indicating model insensitivity for that set of z_0 values.

Additional model performance analysis yields a correlation coefficient of ∼0.9 between the wind speed and the depth-averaged observed and best simulated flow velocity series. This shows that both the lake and the model are thus very sensitive to changes of wind speed and respond quickly to wind forcing changes despite the relative shortness of the meteorological data time step (1 hour).

Although the model performs well for the best z_0 values, it underestimates the flow speed by almost 25% at the velocity peak that occurred around 6 am on 5 of April. In contrast, model overestimation occurs around 6 am on 04 of April and is even more

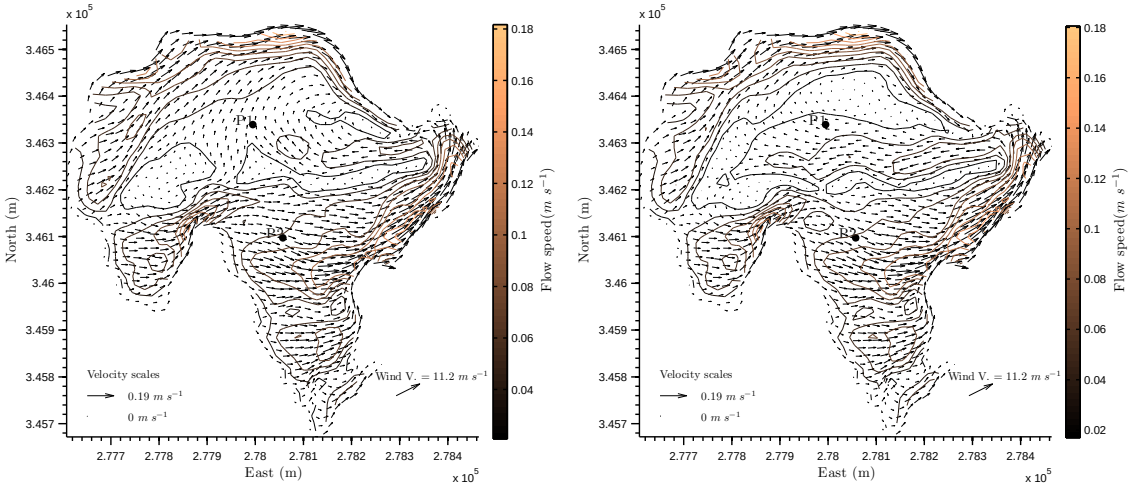

(a) (b)

Figure 5.3: Initial conditions of the water velocity field at a) surface layer and b) mid layer for *FVCOM* model on 03/04/2011 at 2 pm.

significant at the end of the period when overestimation is nearly 30% when the flow is relatively low. Such discrepancies are also visible in the sensitivity analysis of z_0 (Figure 5.5). Observing Figure 5.5 (b), it is evident that the sensitivity index varies through time, so it may be eventually possible to obtain not only a unique value for z_0 but different ones for different periods. The sensitivity index shows also that the model is relatively sensitive ($> 30\%$) to changes of z_0 when flow velocities are greater than 0.05 $m\ s^{-1}$, and less sensitive ($< 20\%$) when flow velocities are lower. The behaviour of the sensitivity index suggest that the model performance would be improved if z_0 were $\leq 0.005\ m$ for relatively high flow velocities and $\geq 0.01\ m$ for lower velocities.

5.2.2 Validation

Validation was carried out against the velocity profiles from the second ADCP deployment (ADCP2; see Figure 2.14 for location). Comparisons between observed and simulated flow magnitudes and components during the deployed time (Figure 5.6) at three different levels, show that observed and simulated flow series have similar behaviour at the three levels. The velocity series for the top (Figure 5.6 (b)) and mid layers (Figure 5.6 (c)) show a high correlation with wind forcing. In contrast, the velocity series in the bottom layer (Figure 5.6 (d)) shows certain insensitivity for wind speeds

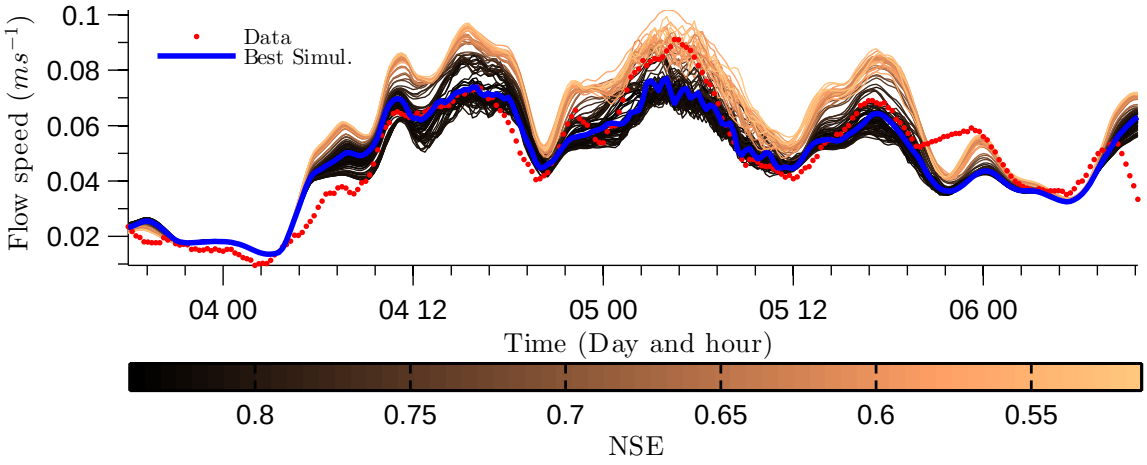

(a)

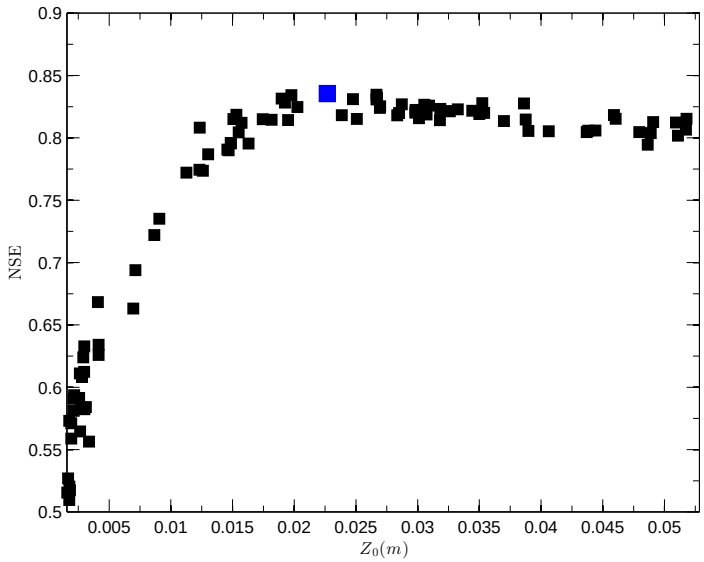

(b)

Figure 5.4: Calibration of z_0 based on the comparison between the simulated and observed depth-averaged velocities. a) Comparison between hourly observed depth-averaged velocity time series at ADCP1 (see Figure 2.14) and the simulated series for different values of z_0 (degraded lines). Best model simulation is also plotted in blue. b) z_0 vs NSE. The blue square highlight the best z_0 that correspondent to the maximum value of NSE.

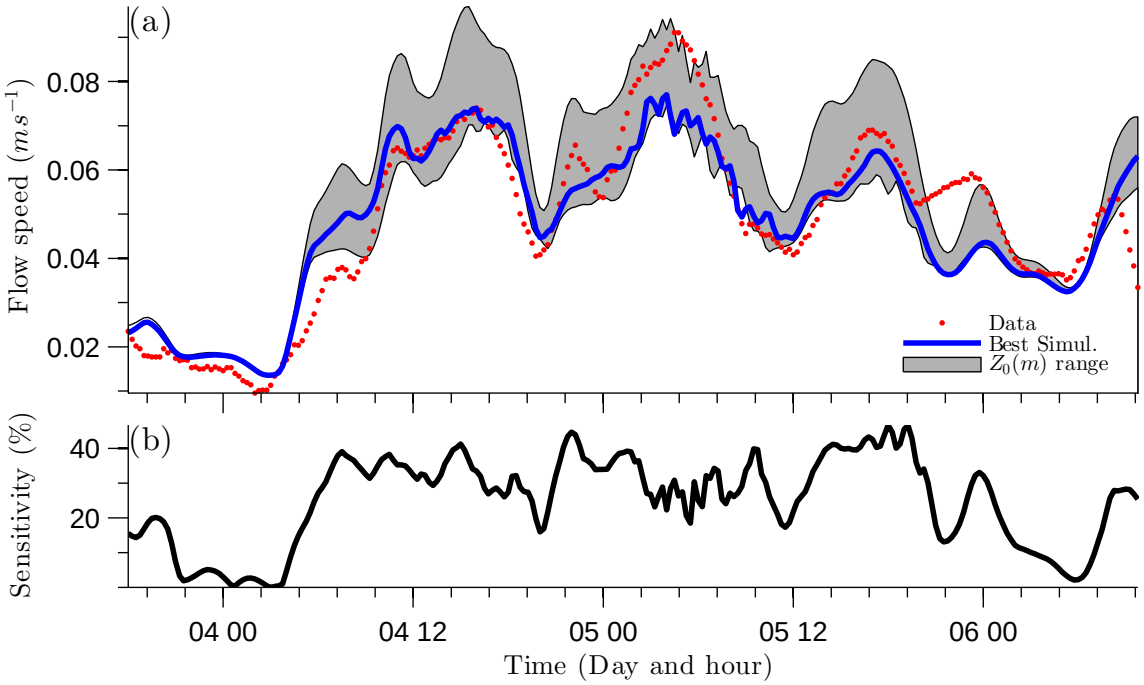

Figure 5.5: (a) Depth-averaged observed (red dots) and simulated (blue line) velocity series, and the range of depth-averaged velocities (shaded area) limited by the velocity series for $z_0 = 0.001$ (upper line) and for $z_0 = 0.06$ (lower line). (b) Sensitivity index estimated using Equation 3.2.

below 3 $m\ s^{-1}$, since the velocity tends to remain constant as wind speed decreases.

A comparison between the x and y component of simulated and observed flow velocity reveals certain similarities. In both observed and simulated series, marked return flows are observed. These occur during the whole period and are more intensive during the first four hours when the wind speed is above 3 $m\ s^{-1}$. As wind speed decreases, the magnitude of the return flows decreases too and the flow velocity tends toward 0 $m\ s^{-1}$ (Figure 5.6 (d)).

Comparing the flow vector directions of observed and simulated velocities (Figure 5.7), both demonstrate the presence of oscillatory motions in the lake. In the first half of the period, the observed and simulated flow vectors follow similar directions, specially in the mid and bottom layers where return flows take place. In the top layer a small shift between the wind direction and flow direction (Figure 5.7 (a)) occurs because of the bi-directional interaction of currents. In the second half, a return flow in

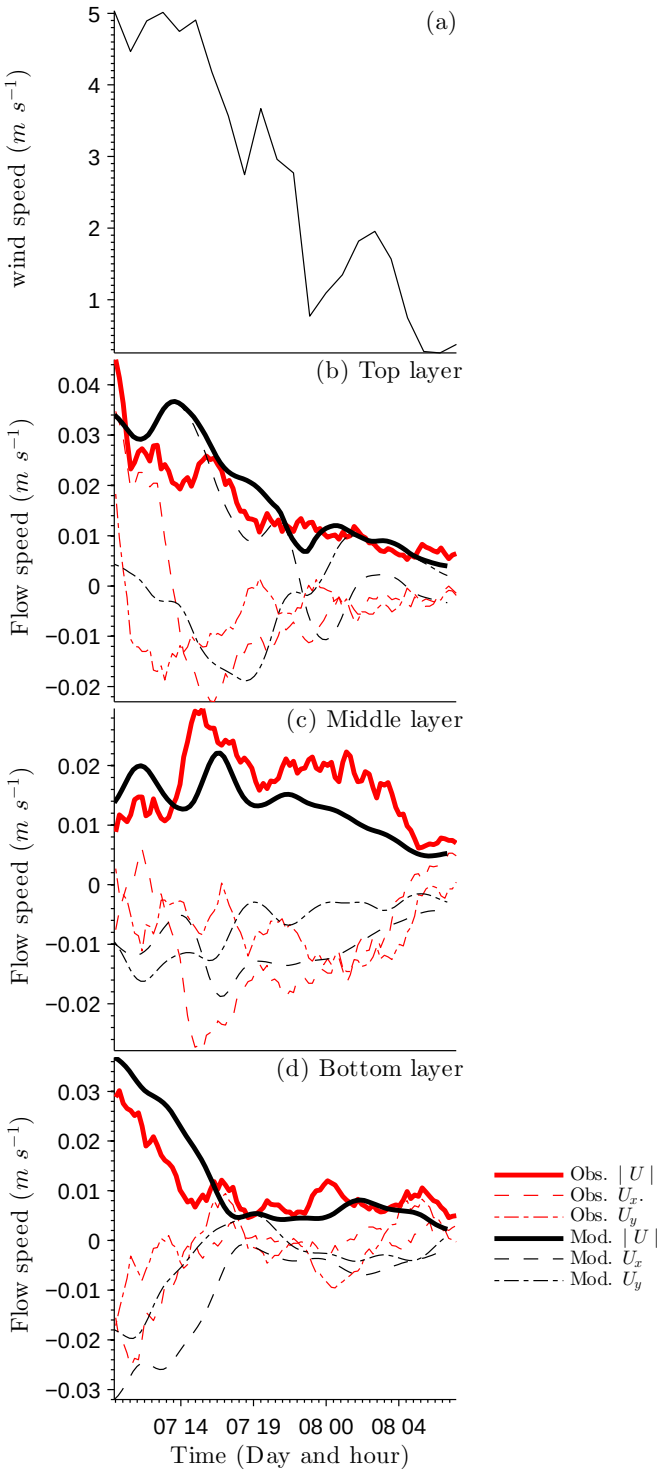

Figure 5.6: Comparison between observed and simulated velocity magnitude, and x and y components at top (b), middle (b) and bottom (c) levels. The plot (a) represent the wind speed. Time period presented is 10 am 07/04/2011/ to 8 am 08/04/2011 8:00.

the top and mid layer is noted in the observed and simulated vectors, triggered by lake seiching. This oscillatory behaviour occurs as soon as wind speed decreases to $< 3\ m\ s^{-1}$, which leads to relaxation of the water body, after the water surface tilting driven by wind forcing. At the end of the second half, the simulated and observed current vectors differ substantially in the bottom layer since the velocities at the bottom are relatively small ($< 0.5\ cm\ s^{-1}$) and therefore difficult to simulate.

A striking feature evident at the water surface (Figure 5.7(b)) is that neither the simulated nor observed current vectors match the wind direction. Such behaviour is presumably caused because the wind forcing is relatively weak during the whole period and unable to drive the top layer flows in this direction. This means that lake circulation and velocity field in general, are temporarily controlled by the topological and bottom stress moment respectively in the vorticity equation (Laval *et al.*, 2003). Studies of the mechanisms affecting circulation in Lake Michigan showed that, when the lake was forced with uniform wind field, the topological moment was the dominating factor during unstratified periods (Schwab & Beletsky, 2003). On the other hand, a combination of internal waves and topological moments was found to be as the dominating factor in the set-up of meso-scale vorticity in lake Stechlin, Germany (Kirillin *et al.*, 2008). Such combinations may apply to the discrepancies between wind and flow directions, in the second half of the Llyn Conwy data.

Return flows are more clearly visible in the comparison of observed and simulated flow velocity profiles at ADCP2 (see Figure 5.8). During the first three hours of the measurement period some discrepancies are noticeable between observed and simulated flow profiles, especially in the middle layers where the model tends to over estimate the velocity magnitude. Remarkable coincidences between observed and simulated flow profiles is observed in the last 6 hours, where magnitudes and components match each other well. In general, the validation procedure shows that the model is able to reproduce the field velocity in Llyn Conwy with a good approximation. The analysis indicates that the model is not only sensitive to wind forcing, but to also bathymetry and bottom roughness effects. These are reflected in more complex motions such as seiches and in the dissipation of return flows within the bottom layers.

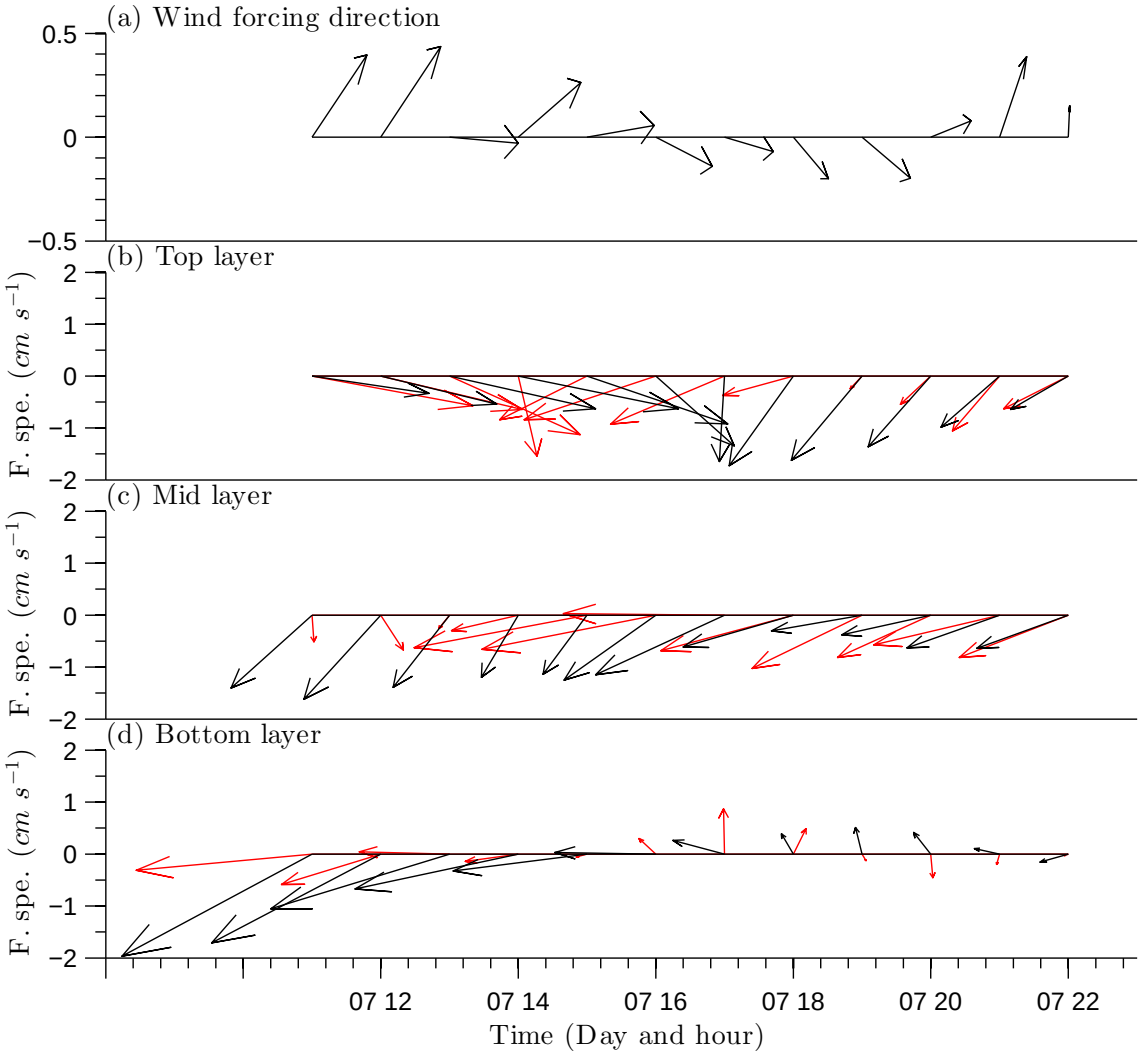

Figure 5.7: Comparison between observed (red) and simulated (black) flow current vectors at ADCP2 at top (b), middle (c) and bottom (d) layers. Plot (a) represents the wind forcing direction for the same period.

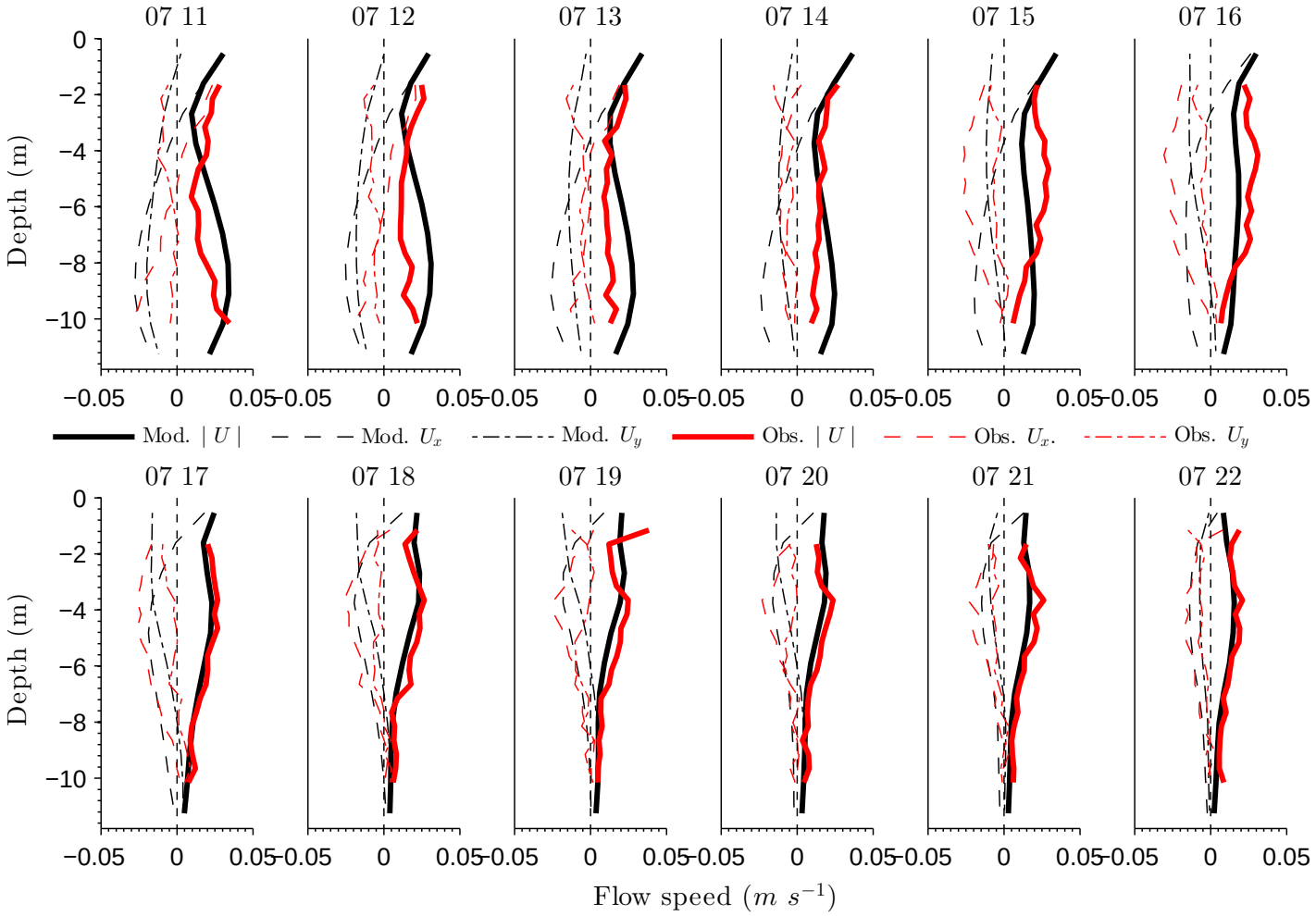

Figure 5.8: Comparison of observed and simulated flow velocity profiles at 12 different hours between 11:00 and 22:00 07/04/2011/ at ADCP location 2. The red curves represents the observed series and black the simulated ones. The comparison includes the x (x comp.) and y (y comp.) components of the flow. Time is indicated at the top of each profile in the format: *day hour*.

5.3 Analysis of Flow Circulation

In order to investigate the nature of the water circulation, *FVCOM* was set up according to the information given in Table 5.1, and was forced using meteorological data acquired during the first field campaign (Figure 5.9). The initial conditions were established by spinning up *FVCOM* using the meteorological information corresponding to the first hour of the simulation period (4 days).

Hourly averaged simulated velocity fields at three different water layers: surface, middle and bottom, are shown in Figure 5.10. At the water surface (Figure 5.10a) the circulation is essentially free of any gyres. Instead, the flow within the surface layer increases along the predominant southwesterly wind direction, with regions of more rapid flow along the north shore (between B and C). At mid-depth, the hourly average velocity field (Figure 5.10b) shows the existence of two different gyres: an anti-cyclone gyre (clockwise rotating) on the north of the lake whose maximum velocity is reached below B, and a cyclone gyre (counterclockwise rotating) formed on the east of the lake extending from the southeast of A to C. Both gyres converge northwest of C and return toward the centre of the lake. The central return flow is completely developed at the bottom of the lake (Figure 5.10c) where, also most of the bottom area is affected by return currents that follow the opposite direction of the predominant wind direction.

The hourly averaged velocity field provides a useful preliminary insight into the predominant circulation patterns. However, the persistence of the circulation patterns may not be reliably inferred from the averaged field, so analysis of the variance in flow pattern is required. Accordingly, Empirical Orthogonal Function (EOF) analysis (Emery & Thomson, 2001, Ji & Jin, 2006) was used to remove the mean velocity field from the velocity fields at each time and then decompose it into principal circulation modes. EOF analysis (summarized in Table 5.2) shows that approximately 100% of the total variance (energy) is represented by the first five EOF modes, with EOF mode 1 containing > 85 % of the variance. The concentration of the variance in a simple mode implies that the circulation pattern does not vary significantly through time, which is not entirely unexpected given the persistent southwesterly wind forcing conditions.

The EOF mode 1 at the water surface layer (Figure 5.11a) accounts for 89.7% of the total spatial variance. This mode shows the existence of two gyres: a small one toward the northeast and another toward the east. Such gyres strengthen the mean circulation patterns (see Figure 5.10a) on the north and on the east of the lake. In contrast, weakening of the mean field velocities on the south and on the west of the

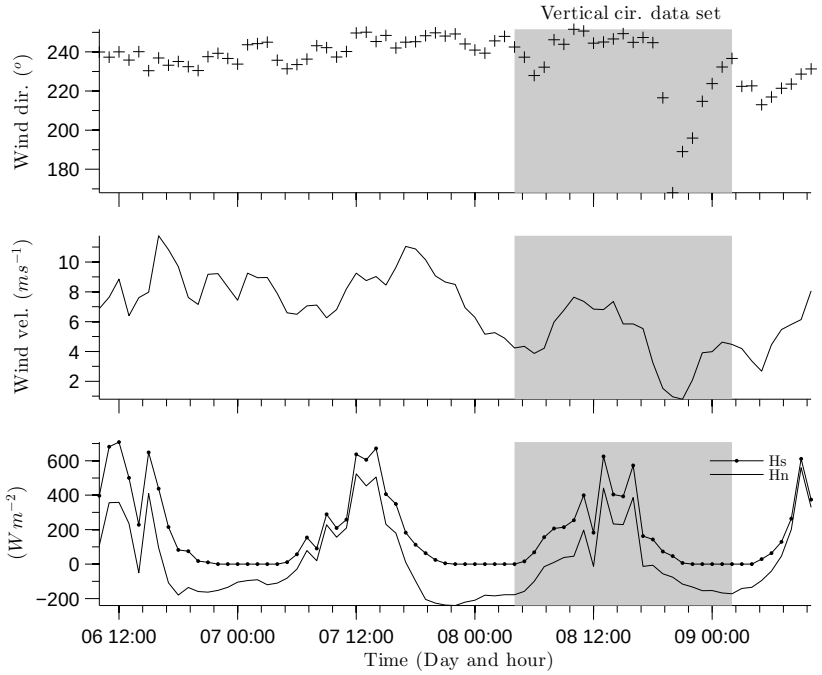

(a)

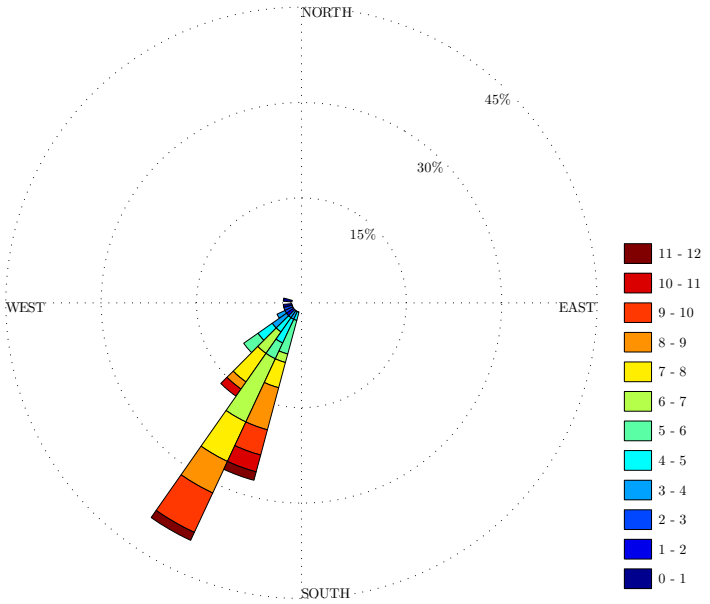

(b)

Figure 5.9: Meteorological forcing information recorded during the first field campaign from 06/07/2010 to 09/07/2010. a) Wind direction, wind speed measured 10 m above the ground and, incoming solar radiation (Hs) and net heat flux (Hn). Shaded area indicates the dataset used to analyse vertical circulation (see Figure 5.14). b) Wind rose. The colour scale indicate ranges of W_s ($m\ s^{-1}$) and the concentric circles indicate the wind speed frequency.

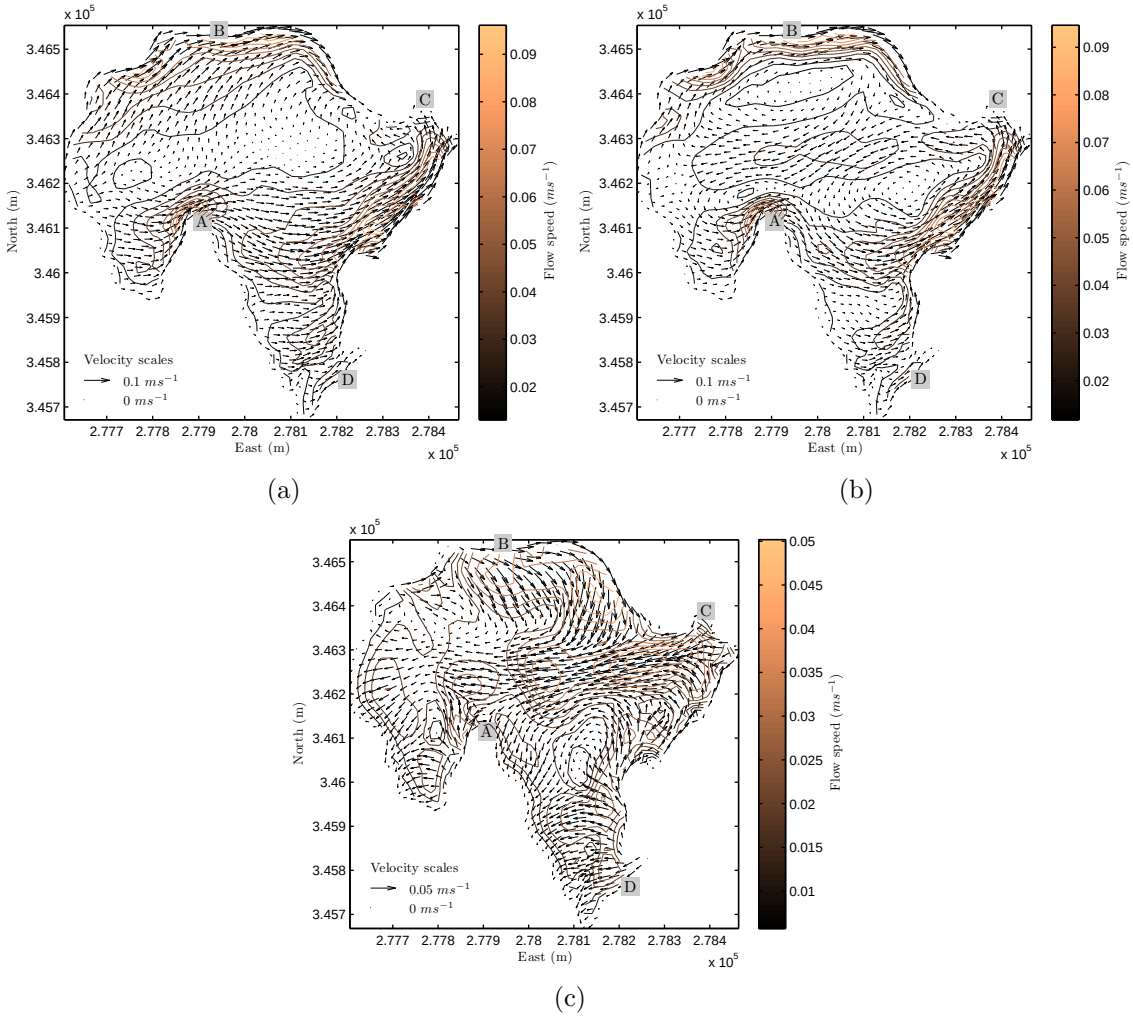

Figure 5.10: Hourly averaged velocity fields simulated between 06-Jul-2010 and 09-Jul-2010 at a) surface layer, b) mid layer and c) bottom layer.

lake is due to the currents flowing in an opposite direction to the mean ones in the EOF mode 1. The EOF mode 1 at the mid layer, which accounts for 94.40% of the total spatial variance (Figure 5.11b), shows the existence of two large gyres: one in the north and the other on the east of the lake. Both gyres strengthen the mean circulation at the mid layer especially near the centre of the lake. The current patterns show by the EOF mode 1 at the bottom layer (Figure 5.11c) strengthen the mean circulation in the north and the flow from the east towards the centre of the lake.

The two-gyre pattern shown by EOF mode 1 at the surface and mid layers is

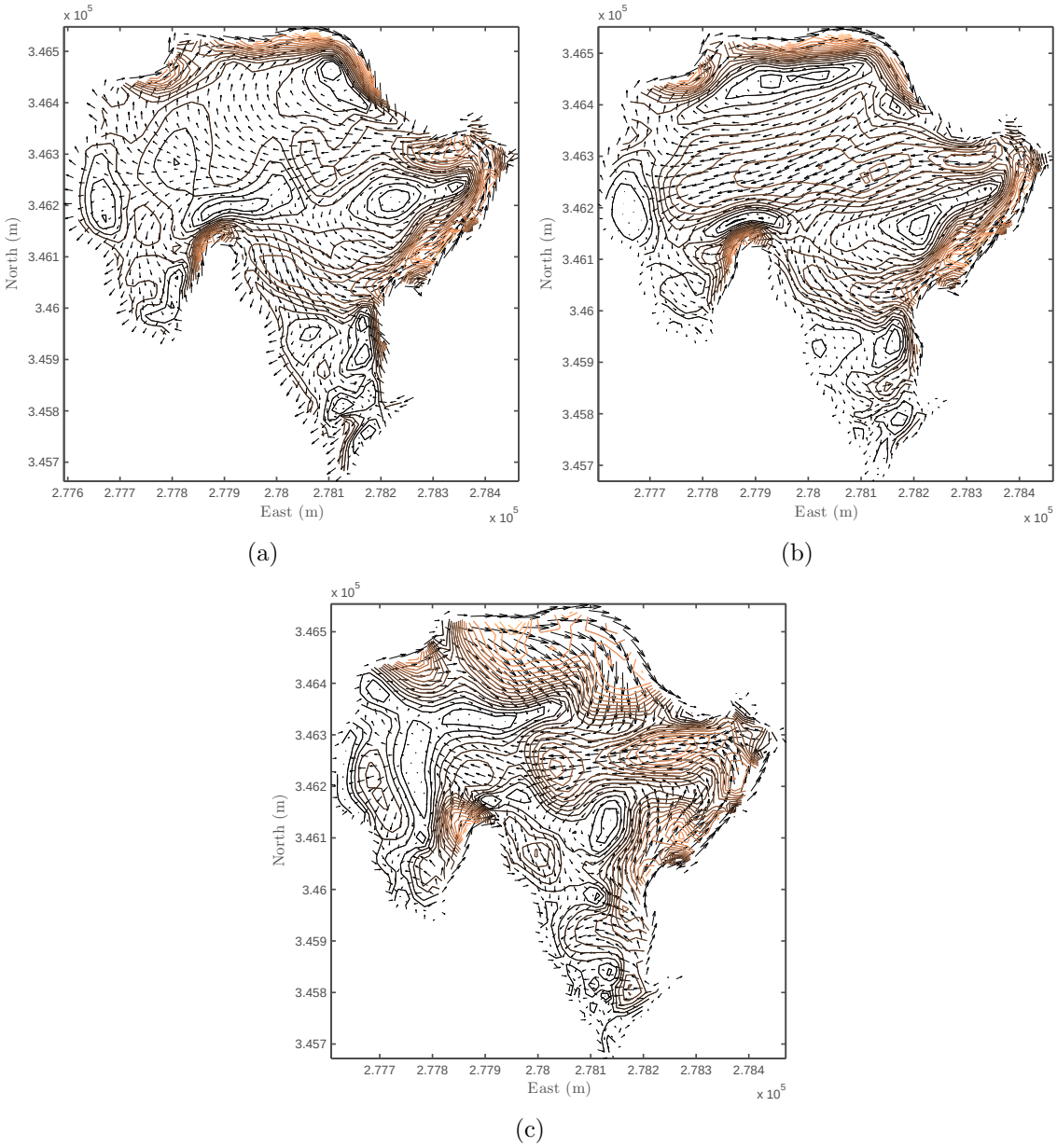

Figure 5.11: EOF mode 1 at a) surface layer, b) mid layer and c) bottom layer.

	Surface layer		Mid layer		Bottom layer	
EOF Mode	Var. (%)	$\sum$ Var. (%)	Var. (%)	$\sum$ Var. (%)	Var. (%)	$\sum$ Var. (%)
1	89.70	89.70	94.40	94.40	85.10	85.10
2	4.50	94.20	2.10	96.50	7.00	92.10
3	2.45	96.65	1.45	97.95	4.35	96.45
4	1.70	98.35	1.00	98.95	1.95	98.40
5	1.45	99.80	0.85	99.80	1.35	99.75

Table 5.2: Variance (σ^2) and accumulated variance ($\sum \sigma^2$) of the first five EOF modes of velocity field at three different layers.

mainly driven by the action of the predominantly southwesterly winds. Analysing the principal components (PCs) of EOF mode 1 and 2 (see Figure 5.12), which give the amplitudes through the time of a EOF mode, a correlation of about 95% is found between the scaled wind speed series and the PC Mode 1 series. This confirms the strong dependecy of lake circulation on wind forcing. On the other hand, since PC Mode 1 is positive during the whole period, the two gyre patterns exposed by the EOF mode 1 at the surface (Figure 5.11a) and mid (Figure 5.11b) layers can be considered to represent the characteristic patterns in the lake.

The PCs for EOF Mode 2 (PC Mode 2) (see Figure 5.12) represent a correction to the PC Mode 1. PC Mode 2 to some extent compensates for aspects of the circulation represented by EOF mode 1. At high wind speed events (e.g. around 18:00 on 06/07/2010), for example, PC Mode 1 shows high positive values whereas the PC Mode 2 shows negative values that balance the effects of large changes in wind forcing. PC Mode 1 and PC Mode 2 are often out of phase during strong wind forcing changes, such that the combination of both modes constitutes a complex circulation pattern.

The modelled flow circulation was compared against the surface track of five GPS drifters deployed at different places on the water surface (see Figure 5.13) during the July 2010 field campaign. A summary of these drifter deployments is shown in Table 5.3. In general, the drifters travelled very short distances ($150 < D_{tra}(m) < 620$) over very short times ($16 < T_{tra}(min) < 40$) at moderately high velocities ($0.15 < \bar{V}(ms^{-1}) < 0.25$). No drifters took more than 1 hour to traverse the lake, except drifter 3, which moved 618.45 m in 66.62 min (from the south to the small bay located at the east side of the lake; See D3 and R3 in Figure 5.13). Despite the differences between the distances travelled by each drifter, their mean velocities are quite consistent,

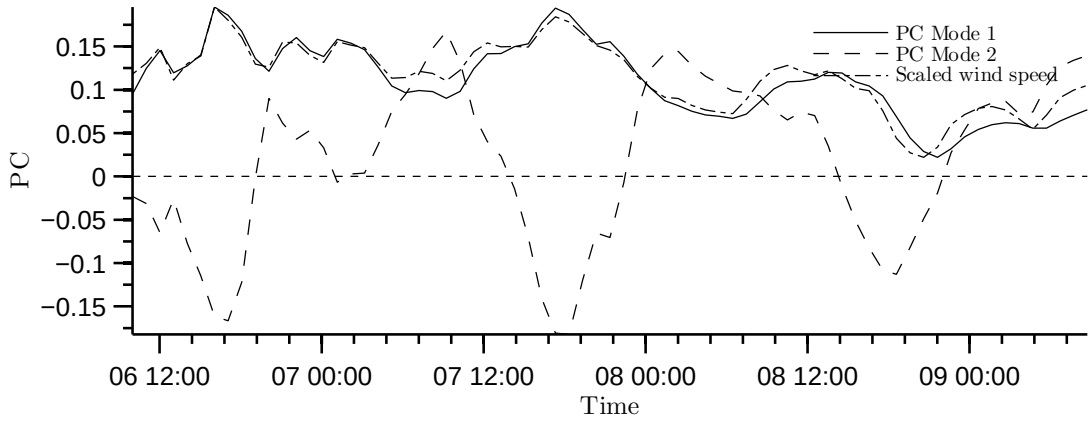

(a)

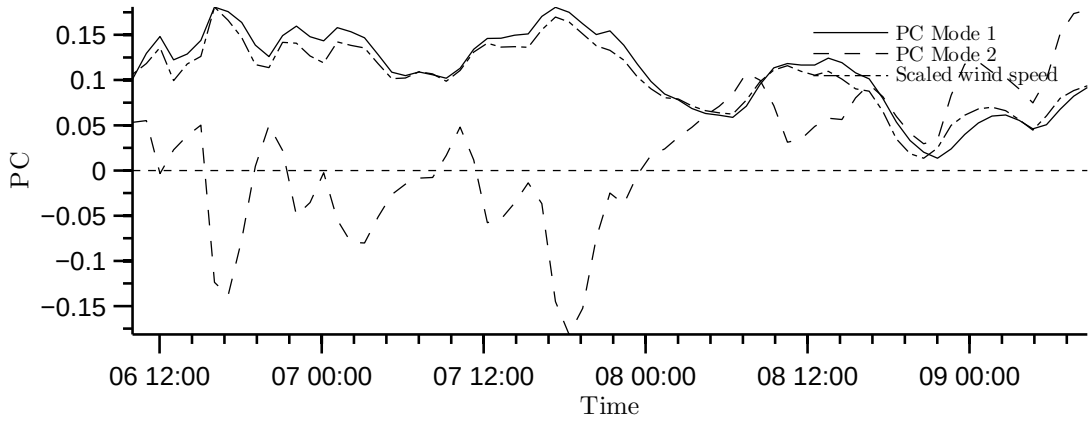

(b)

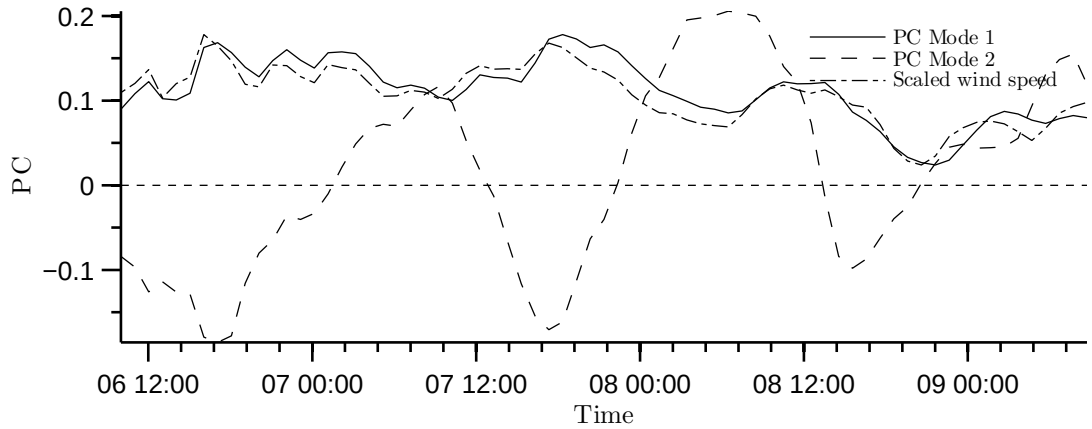

(c)

Figure 5.12: Principal components (PCs) of flow circulation patterns for EOF modes 1 and 2 at a) surface layer, b) mid layer and c) bottom layer.

Drifter	Deployment	Retrieval	T_{tra} (min)	D_{tra} (m)	$\bar{V}$ (ms^{-1})
1	06-Jul-2010 14:25	06-Jul-2010 14:42	17	157	0.16
3	06-Jul-2010 12:13	06-Jul-2010 13:20	67	618	0.15
4	06-Jul-2010 12:03	06-Jul-2010 12:42	40	490	0.20
6	06-Jul-2010 11:58	06-Jul-2010 12:37	39	567	0.24
7	08-Jul-2010 10:39	08-Jul-2010 11:08	29	255	0.15

Table 5.3: Summary of the deployment of five GPS surface drifter during the July 2010 field campaign. T_{tra} and D_{tra} represents the drifter travel time and distance respectively. $\bar{V}$ represents the mean drifter velocity.

indicating homogenity in the wind-driven currents across the lake surface.

Based on the drifter trajectories an attempt to validate the modelled circulation at the surface layer was made by tracking five massless particles released at the same drifter initial deployments using the *FVCOM* Lagrangian module. The comparison between particle and drifter trajectories (see Figure 5.13) reveals significant coincidences in almost all the deployments. However particles 1 and 6 diverge significantly from the corresponding drifters trajectories, since particles tend to match the circulation trajectories that are affected by sudden shifts in the predominant wind forcing direction. In contrast, drifters are dragged by wind-waves and tend to follow the wave propagation direction, which commonly follows a straighter path. However, when the circulation is quite strong such as along the northern shore, the flow circulation is more closely matched by the final path (drifters 1 and 4).

The analysis of horizontal circulation is complemented by further analysis of the vertical circulation. For this purpose, a one day period characterized by drastic changes in wind speed and direction (see grey shaded area in Figure 5.9) was selected. A sample transect along the predominant southwesterly wind track was chosen to analyse the variation in vertical velocity structure at different times. The analysis shows (Figure 5.14) that the flow is generally accelerated by wind forcing from point 1 toward point 2, at which point a strong return flow commences along the downwind bed slope. Observing the circulation between 08:00 and 12:00 hour, during which time the wind speed rises from nearly 4 to 8 $m\ s^{-1}$ (see Figure 5.9a), a large vertical circulation spanning the whole water column is initiated at $x = 200\ m$. The maximum water velocities ($\sim 0.08\ m\ s^{-1}$) occur at this time at the deepest part of the section. A noteworthy characteristic of the vertical circulation is that, in the shallowest regions

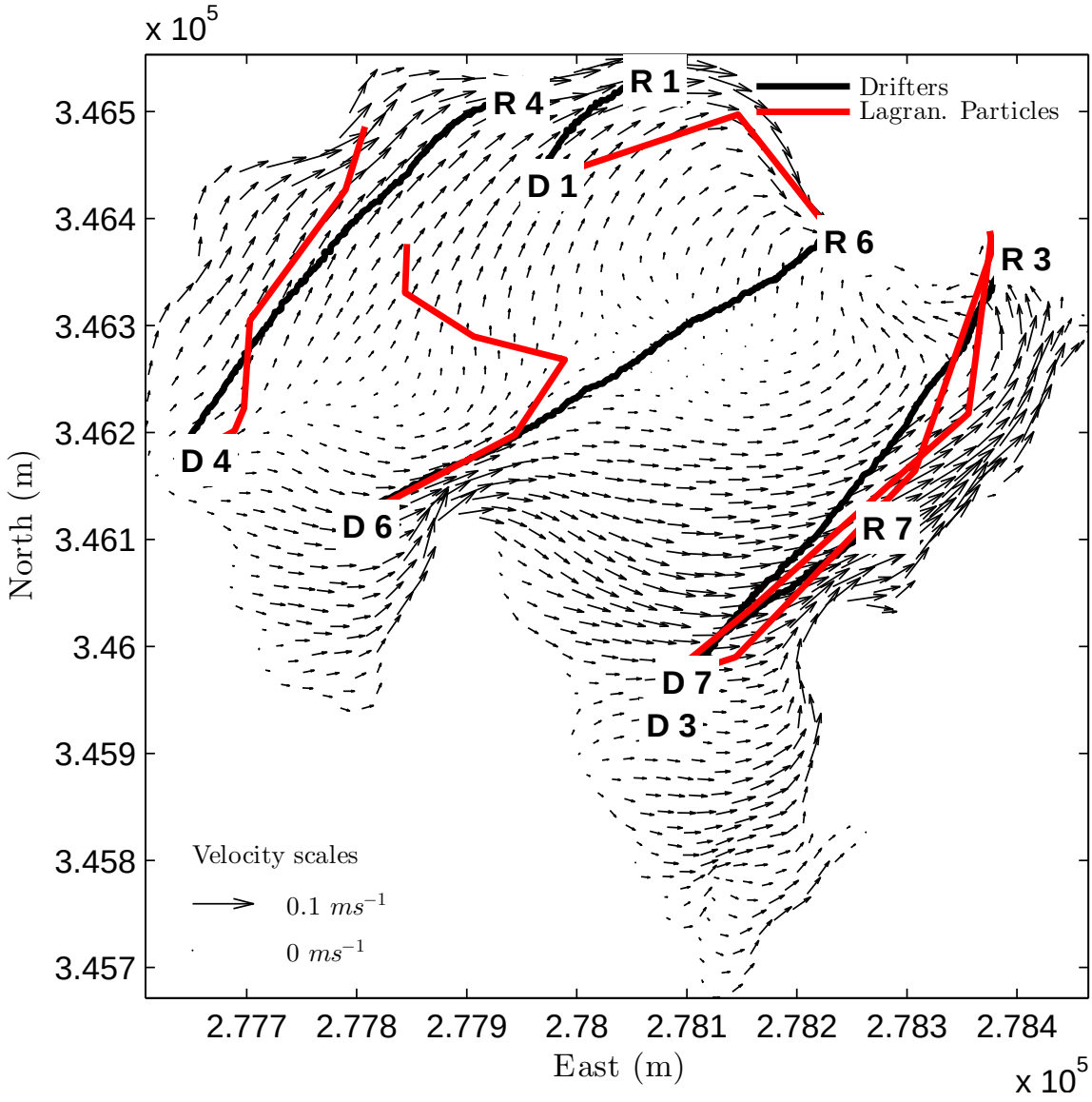

Figure 5.13: Drifter and Lagrangian particle trajectories during 6 July 2010 experiment. Background vectors represent averaged velocity field at the water surface. Letter D represents the deployment point and R the retrieval point of each drifter.

(corresponding to the proximal end of the transect where $x < 200\ m$), the velocities are always $< 0.01\ m\ s^{-1}$ because the return flow circulation does not extend this far and remains bounded by the deeper basin.

A significant feature of the vertical circulation occurs when the wind speed drops below $4\ m\ s^{-1}$. Because the water column is not completely stirred, a more intense circulation develops in the upper layers and a weaker one in the lower ones (see section at 08-Jul-2010 16:00 and 18:00 in Figure 5.14). The upper circulation, which extends from 0 to -8 m below the water surface, leads to the formation of a mixed layer that is limited by the depeest sectors of the section. The weaker circulation, which extends from -8 to -21 m depth and rotates counter-clockwise, may partly reflect the remnants of past circulation events across the whole water column that were driven by strong wind forcing events. This weaker circulation tends to dissipate as it loses its energy by friction against the bottom and the circulation enclosed within the upper mixed layer.

The double vertical circulation is disrupted by significant changes in wind direction. Looking at the wind forcing series between 18:00 and 20:00 on 08-Jul-2010, the wind direction shifts by $70\ ^o$ from the predominant southwesterly direction to a southeasterly direction. Around this time (see Figure 5.14), the double circulation pattern is substantially disrupted leading to the formation of a unique anti-clockwise circulation and a chaotic flow field at the interface between the shallow and deep regions between $200 < x < 300\ m$ (see transect section at 08-Jul-2010 20:00 in Figure 5.14). This chaotic flow field is formed when the quiescent current flowing from point 1 meets the energetic new vertical circulation, yielding a turbulent regime at the interface. At subsequent times, this chaotic interface is smoothed and the currents tend to recover their characteristic vertical circulation as wind shifts back to a more typical southwesterly direction.

5.4 Analysis of Oscillatory Motions

As noted in the introductory review of this thesis, oscillatory motions are a common feature of lakes, especially those subject to strong and/or variable wind stress. Barotropic seiches are initiated when the water surface is tilted downwind by the action of wind shear stress, such that when the wind slackens, the water body oscillates back and forth. Internal seiche motions can also arise in stratified lakes, where the two-layer

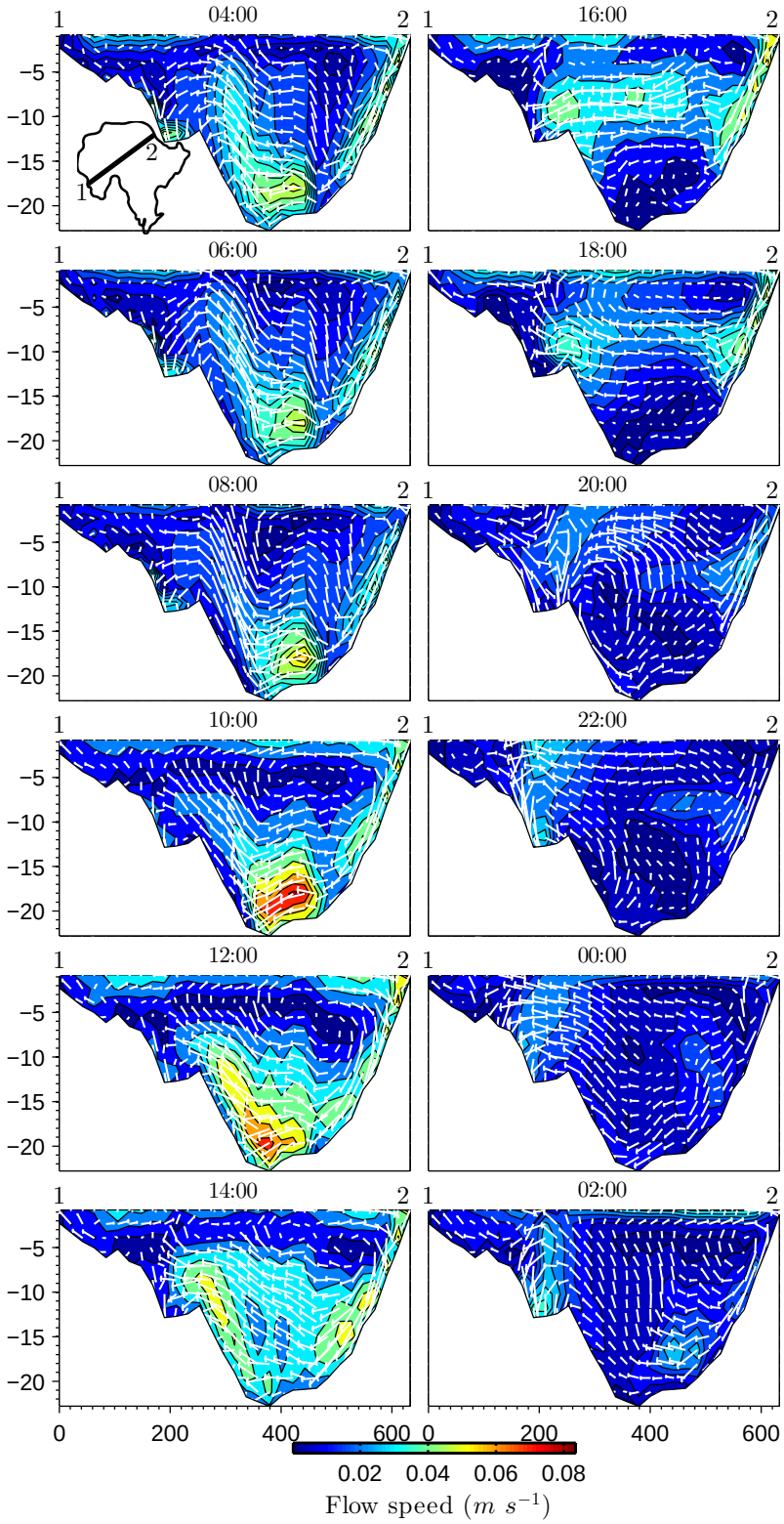

Figure 5.14: Transects of flow velocity from point 1 (upwind) to point 2 (downwind) (see inset at the top left) every two hours starting from 06:00 07-Jul-2010 to 04:00 08-Jul-2010.

vertical structure of the water column facilitates the formation of internal waves at the interface (metalimnion) (Spigel & Imberger, 1980, Imberger & Hamblin, 1982)).

The theoretical free-surface seiche amplitude for Llyn Conwy can be calculated with Equation 2.47 using values for L and H of 800 m and 7 m respectively. Given a value of 1.2×10^{-3} for C_D, seiche amplitude is just 0.2 cm for a windspeed of 10 $m\ s^{-1}$, which is barely resolvable. Seiche amplitude increases to 0.5 cm at 17 $m\ s^{-1}$ and 1.6 cm at 30 $m\ s^{-1}$. The period for the first seiche mode, given by Equation 2.48, is approximately 3.25 min. The existence of such motions was investigated with reference to time-series of bottom pressure recorded by the CERA-Diver sensors placed at five locations around the lake shore (Figure 5.15). The raw pressure series were converted to water level and de-meaned to remove datum offsets. Low frequency variation due to changes in water balance (rainfall, evaporation) was removed using Singular Spectrum Analysis (SSA), which was also used to investigate higher frequency oscillations.

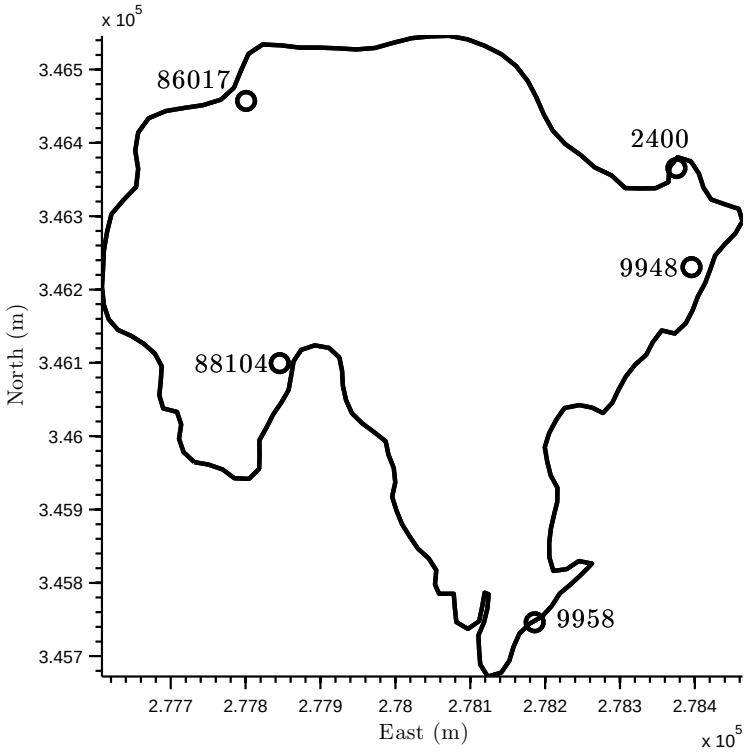

Figure 5.15: Locations of CERA-Diver pressure sensors used to investigate high frequency oscillations in lake level.

SSA is essentially a principal component analysis performed in the time domain.

An autocorrelation matrix is formed by lagging a normalised time series over zero to M-1 time steps, where M is a lag window size. Eigenvalues, λ_k ($k = 1 \cdots M$), and eigenvectors (empirical orthogonal functions) of the lagged autocorrelation matrix are then computed. These contain successive fractions of the variance of the time series. A plot in order of their decreasing magnitude typically exhibits a steep initial slope containing the signal components, which is terminated by a flatter floor that represents noise. Principal components are calculated for each eigenvector, and a set of reconstructed components (RCs) are then obtained by multiplying these by their corresponding eigenvectors. SSA thus decomposes a time series into a set of independent components that represent low frequency trend, periodic and quasi-periodic variation, and noise. Typically, one or two RCs contain variations at periodicities greater than the lag window size, M. Periodic components are represented by paired RCs with similar λ_k, and periods in the range $0.2M$ to M can generally be identified (Schoellhamer, 2002).

Application of SSA to the Llyn Conwy series with a window size, M, of 60 (equivalent to 15 minutes), allowed separation of low frequency variation and two dominant RCs representing oscillatory motion. Across the five stations, RCs 1,2 and 3 accounted for between 90% and 98% of the variance in the raw level series, with the remaining terms being considered to represent noise. Figure 5.16 summarises the analysis for a site on the northwest shore of the lake (sensor 86017). The oscillatory variation for all five stations (see Figure 5.15 for locations) is plotted in Figure 5.17. For much of the roughly 40 hour measurement duration, oscillation in lake level as represented by RC2 and RC3 is close to the sensor resolution. Mid-way through the deployment, however, windspeeds increased from around 7 to over 12 $m\ s^{-1}$, leading to marked oscillation at sites 86017 (northwest), 88104 (western shore of southern headland) and 9948 (eastern shore). The peak amplitudes of about 0.5 cm are broadly in accordance with theoretical amplitudes as calculated above. Data for two sensors, 9958 (southern basin adjacent to outflow sluice) and 2400 (sheltered bay in northeast corner of the lake) show less marked excitation of the free surface at these times. Within the southern bay, sensor 9958 shows weaker oscillation at a higher frequency, possibly due to a separate seiching motion across the shorter west to east fetch and within an area of generally shallower water.

The Power spectral density functions of each of the RC2+RC3 series (Figure 5.18) show a very consistent behaviour of the oscillatory motions at the water surface. The

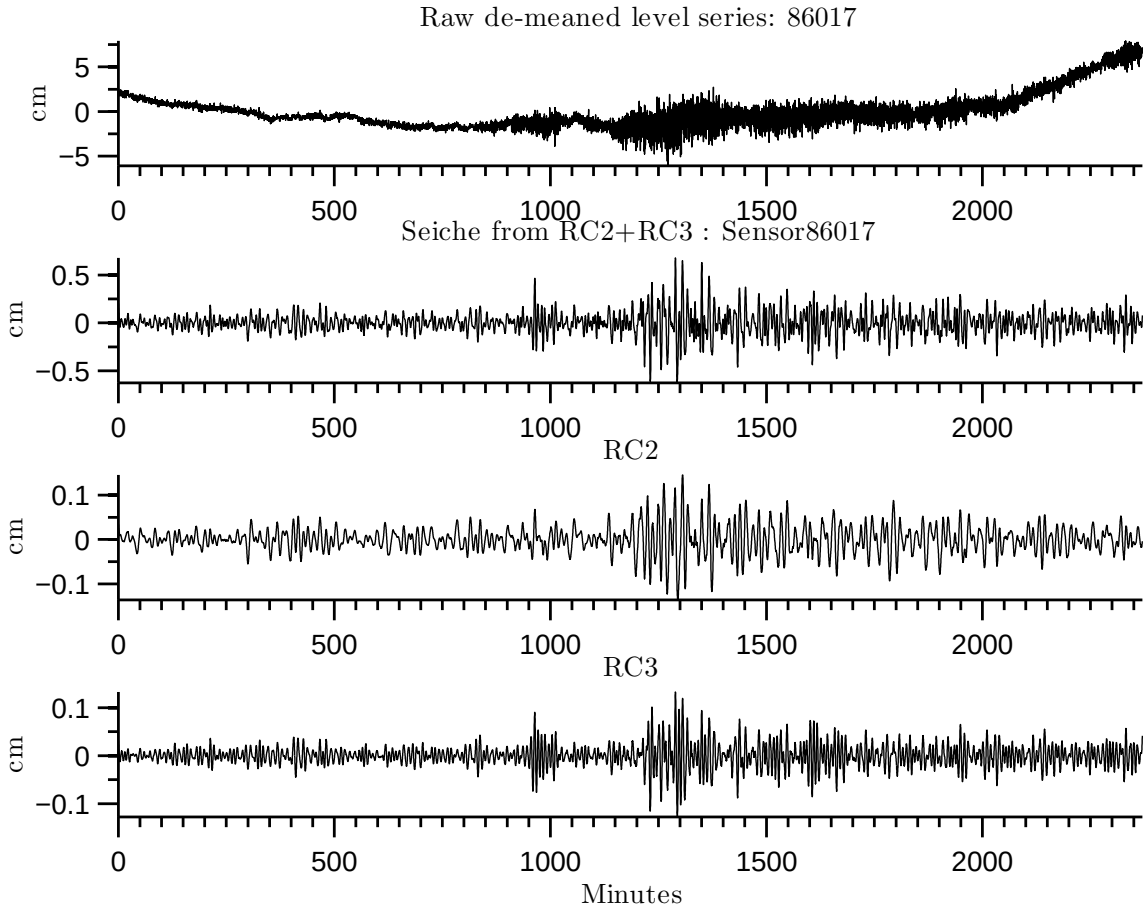

Figure 5.16: Singular Spectrum Analysis (SSA) applied to water-level series from sensor 86017 obtained for 5 to 7 July 2010 at a site on the northwest shore of the lake (see Figure 5.15 for locations). RC1 through RC3 account for 92% of the series variance. RC2 and RC3 in combination represent higher frequency oscillations, which show excitation due to higher wind speeds in the second half of the record.

spectral analysis reveals the existence of a seiche-type oscillation with a predominant period of ~ 12 *min* (see Figures 5.18) at the stations 86017, 88104 and 9948 stations, but slightly lesser at the station 2400 since the oscillations are affected by the sheltering provided by the northeastern bay. At station 9958, the lake basin appears to oscillate at the more rapid ~ 5 *min* period, which may be due to the much shorter west to east fetch in this part of the lake basin.

A more detailed analysis of the seiche motions was made by comparing the water level variation at the two most widely separated sensors (88104 and 9948) along the

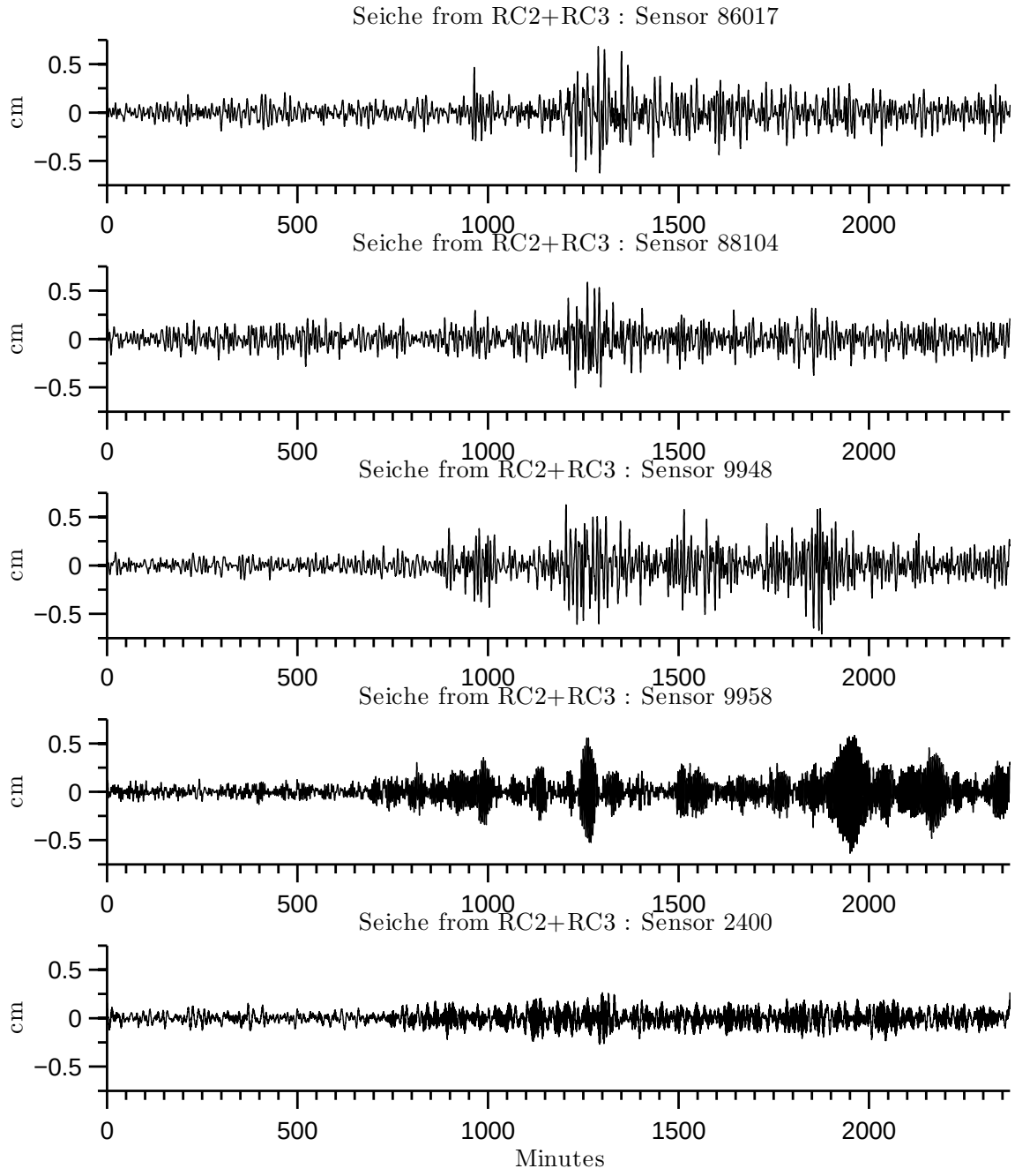

Figure 5.17: Comparison of lake-level oscillation series obtained through application of SSA, and based on RC2 and RC3 in combination, for 5 sites around lake shore (locations given in Figure 5.15).

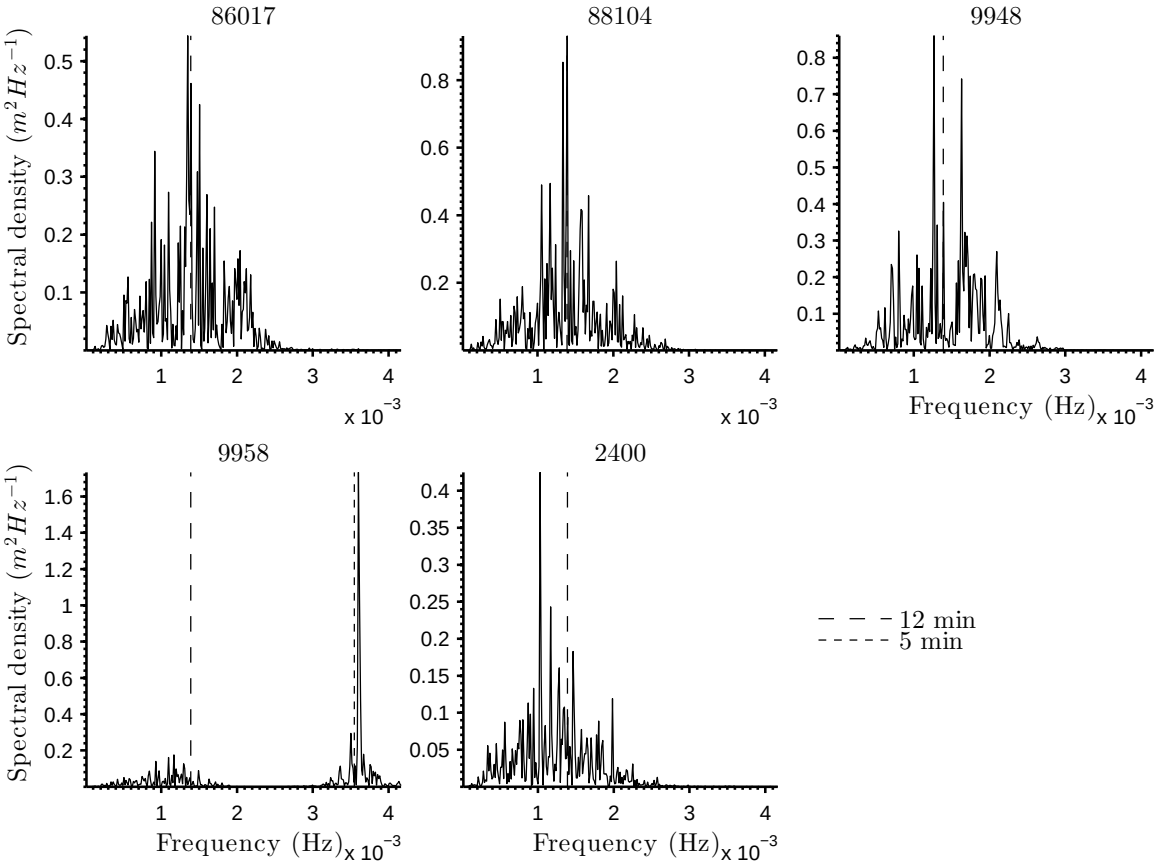

Figure 5.18: Power-spectral functions for RC2 and RC3 in combination extracted from the lake margin pressure series for 05 to 07 of July 2010. Vertical lines indicate the most prominent frequencies, corresponding to periods of 12 and 5 *min*.

predominant southwesterly wind track (see Figure 5.15 for locations). The analysis concentrated on a particularly windy period between 16:00 and 18:00 on 06/07/2010. Wind speed increased from around 8 to 14 $m\ s^{-1}$ in this period, which was also marked by significant shift in wind direction. A comparison of the records for upwind (88104) and downwind (9948) sensors (Figure 5.19) shows that the water level oscillates regularly out of phase with an amplitude up to 0.5 *cm*. Thus, when an upwelling occurs at 9948 downwelling is noted at 88104. The oscillation out of phase is quite regular, however, around the middle of the period when the wind direction shifts (Figure 5.19 (a)) toward the south and the wind speed temporarily decreases to 8.2 $m\ s^{-1}$, the water level oscillates more-or-less in-phase. These changes in the oscillatory mode given by shifts of wind directions, suggest the existence of multiple horizontal modes of seiches

in Llyn Conwy. The energy and persistence of these will depend on the duration of the wind forcing shifts.

Interestingly, it is also evident from Figure 5.19 (b), that the period at which both out-of-phase water level series fluctuate is $\sim$ 12 *min*. This coincides with the most energetic period in the spectral function analysis summarised in Figure 5.18. Spectral analysis of wind speed series shows a peak corresponding to a period of around 13 *min* and it seems reasonable to suppose that this may account for the superimposition of 12 *min* variation in level on the theoretical seiche period of around 3 *min* predicted by Equation 2.48.

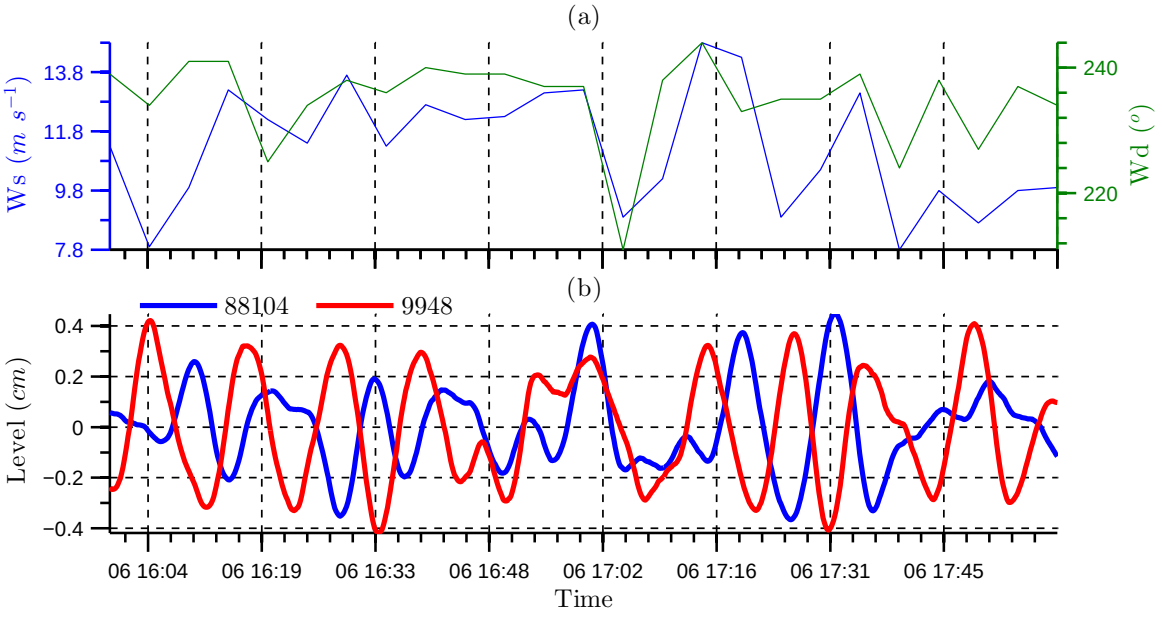

Figure 5.19: (a) Wind speed and wind direction recorded at 5 minute intervals. (b) RC2+RC3 reconstructed seiche series for sensors 88104 (upwind) and 9948 (downwind) between 16:00 and 18:00 06/07/2010.

Llyn Conwy is characterised by a strong vertical circulation activity modulated by wind forcing changes that lead to short periods of stratification during summer. This makes the existence of intermittent internal seiches quite likely. Accordingly, the occurrence of internal seiches in Llyn Conwy was investigated through an analysis of the hourly temperature profiles recorded by the thermistor chain on the CEH data Buoy (Figure 2.13). This focused on a portion of the data series corresponding to the period 06-Jun-2007 to 18-Jun-2007. In this period, wind speed varies diurnally, with

calm periods in the morning (wind speeds below 4 $m\ s^{-1}$) and peak wind speeds in the afternoons (speeds up to 8 $m\ s^{-1}$, see Figure 5.20 (a)).

The analysis of the isotherms shows a gradual intensification of the stratification in the first half of the period and, in the second, significant thickening of the mixed layer (see Figure 5.20). Prior to 11 June, the thermal structure is characterized by a broad thermocline ($\sim$8 m in thickness) and a thin mixed layer ($\sim$2 m in thickness) on account of regular high solar irradiation input and relatively weak wind forcing. It is noticeble that during this period, the nights are characterized by slight deepenings of the mixed layer as thermals plunge downward and cool the mixed layer. During the 11th and 13th of June a rapid increase in the mixed layer temperature is triggered by high solar irradiation input. This leads to temperature differences of 9^oC between the epilimnion and the hypolymnion. This intense stratification period is momentarily interrupted by intermittent but sustained increases in the wind speed from 5 to 12.5 $m\ s^{-1}$ that rapidily deepen the mixed layer from 2 m to 4 m. However, the mixed layer recovers its previous level when the wind decreases. On morning of 12th June, when the low solar irradiation accompanied by a sudden increase in wind velocity of nearly 10 $m\ s^{-1}$, the mixed layer deepens from 2 to 3.5 m. It is sustained at this level until midnight, when wind speeds $>$ 15 $m\ s^{-1}$ deepen the mixed layer again to 6 m. In the subsequent days, the mixed layer is maintained approximately at this level by high wind speed events and a relatively low solar irradiation, and the thermocline is compresed to a thickness of 5 m.

The behaviour of isotherms are characterized by different features. The 12.5^oC isotherm located at the low part of the metalimnion (see Figure 5.20 (c)) oscillates approximately every 24 h with an amplitude of 0.8 m. Comparing the power-spectral density functions of wind speed and the 12.5 ^oC isotherm (see Figure 5.21) shows that the excursion of the isotherm is dictated by the diel periodicity in wind forcing. This 24 h oscillatory motion of the thermocline means that, at certain hours in the day when the wind speed is low, the lake becomes characterised by a stable water column, shallow mixed layer and thick metalimnion. However, as soon as wind speed rise to its diurnal maximum value, a slight upwelling of the isotherms at the metalimnion takes place.

Additionally, observing the isotherms at the middle section of the metalimnion (from 3 to 7.5 m depth) between the 11th and 13th of June (see isotherms in white in Figures 5.20 (c)) these oscillate rapidily and regularly every $\sim$7 h with a well defined

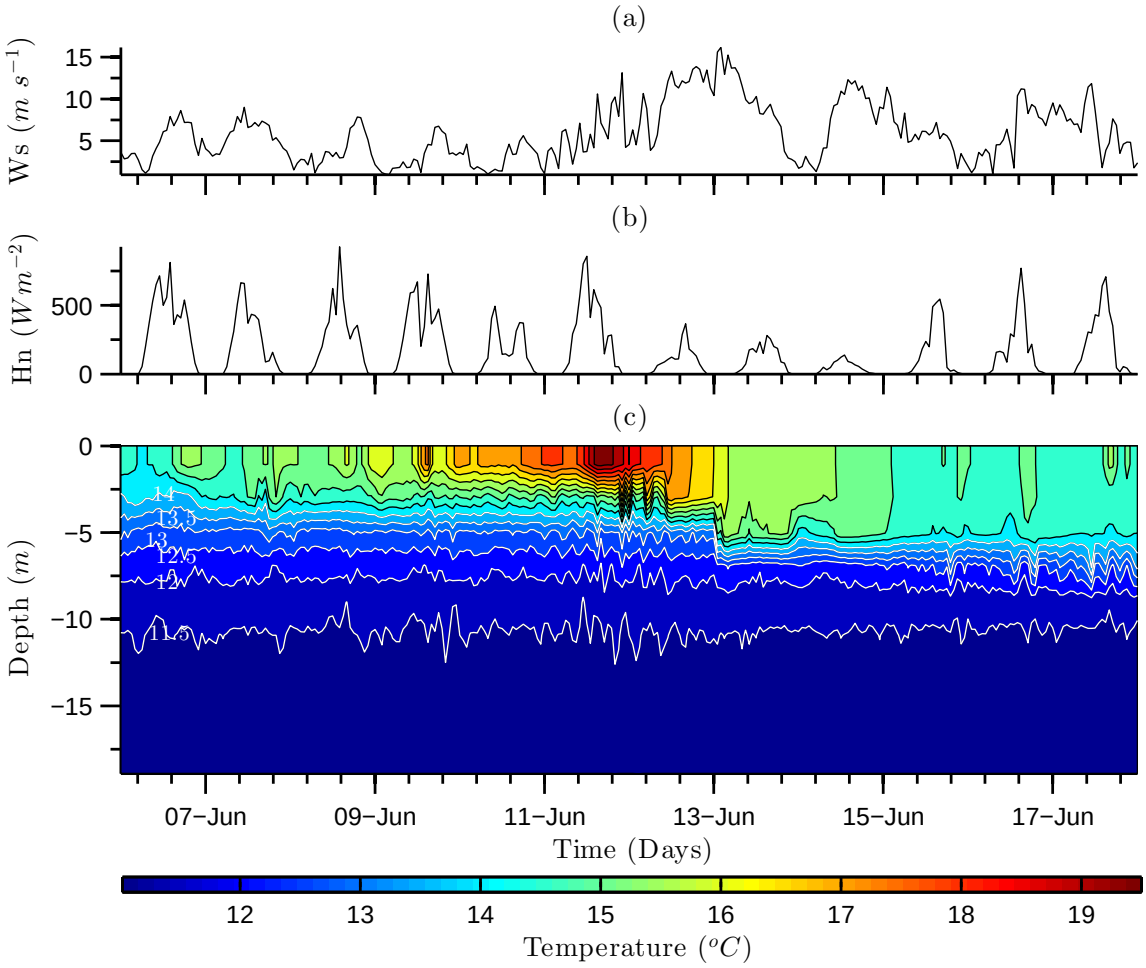

Figure 5.20: (a) Wind speed, (b) Net heat flux and (c) isotherms between 6 and 18 June 2007 from data acquired by CEH Bangor. Isotherms in white indicate those chosen for spectral analysis (see Figure 5.21).

amplitude of ∼1.0 m. The spectral density functions indicate that this frequency is more energetic at the bottom and in the middle of the metalimnion (see Figures 5.21 (c) and (d), respectively). Although such oscillatory behaviour is not easily noted in those isotherms just below the mixed layer, it is consistent with vertical mode 1 seiching (Lemmin, 1987) characterised by short duration and high amplitudes. This then dissipated into higher harmonics, resulting in slow wave decay and little vertical mixing.

On the other hand, comparing the excursion of the 12^oC and 11.5^oC isotherms

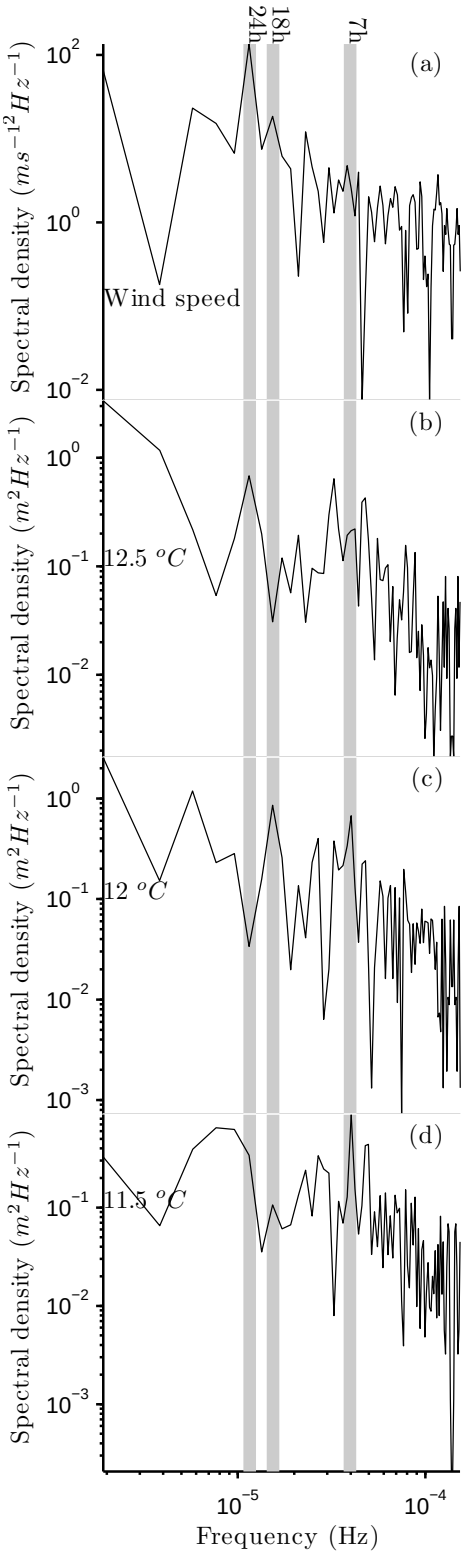

Figure 5.21: Power spectral density analysis for: (a) wind speed, and for three different isotherms (b) 12.5 ^oC (c) 12 ^oC and (d) 11.5 ^oC. Analysis based on data from the CEH data buoy between 6 and 18 June 2007.

(Figure 5.22) an out-of-phase oscillatory behaviour is observed. Such behaviour is consistent when the wind speed has a daily periodicity, especially between the 6th and 9th of June and after the 14th of June. These out-of-phase oscillations are interrupted between 11th and 13th of June, when the wind speed begins to vary rapidly. They give way to the vertical mode 1, where the isotherms oscillate in-phase rapidly with a period of $\sim 7\ h$. The amplitude of the out-of-phase seiching varies between $\pm\ 0.5$ and $\pm\ 1.0\ m$ and occurs about every 18 h as is indicated by the spectral density functions (Figure 5.21). Such internal waves are classified as a vertical mode 2, which is usually predominant between periods of first vertical mode dominance (Pannard *et al.*, 2011).

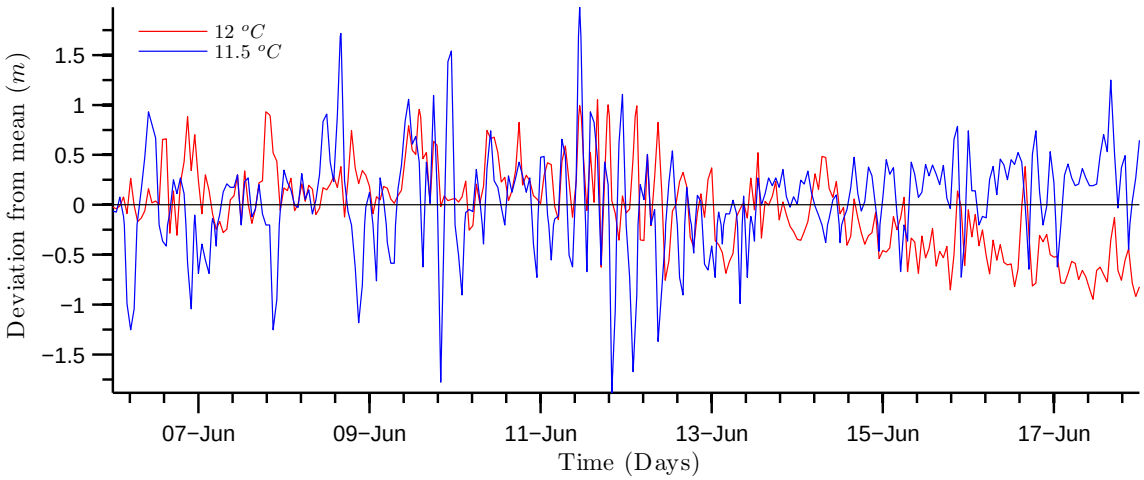

Figure 5.22: Deviations, from the mean depth, of the 12 and 11.5 ^oC isotherms. Analysis based on records taken at the Buoy Station by CEH Bangor between 06/06/2007 to 18/06/2007.

The internal seiches identified between 06 and 18 June 2007 are characterised by alternating oscillatory modes. The 24 h period internal wave identified in the 12^oC isotherm is driven by daily periodic wind forcing, but its persistence is countered by sudden large increments of wind speed in excess of 15 $m\ s^{-1}$ that deepen the mixed layer and eventually can overturn the thermal structure when the lake is only weakly stratified. The vertical mode 1, with a period of about 7 h and which is excited by wind speeds oscillating at high frequencies, is amplified with depth, achieving maximum amplitude at the interface between the metalimnion and hypolimnion. Vertical mode 2, characterized by an out-of-phase oscillatory motion between the metalimnion and

hypolimnion isotherms, is caused by a more complex interaction between the thermal structure and the diurnal scale wind forcing events. This analysis should be considered preliminary and is necessarily constrained by the extent and quality of the available data. In particular, higher frequency and also longer duration temperature profiles at multiple locations are needed to corroborate the internal waves identified here. Such data would also facilitate the investigation of higher horizontal oscillatory modes.

5.5 Calibration and Validation of *UCL-SWM*

The calibration and validation of the semi-empirical linear wave model, *UCL-SWM*, was carried out against high frequency water level measurements at four locations around the shore of Llyn Conwy (see Figure 2.14). These data were acquired during the April 2011 field campaign. The water level measurements were first subjected to quality controls to remove outliers and to de-trend the series. Then, using spectral analysis and following the methodology described by Lee & Wang, 1984, the significant wave height (H_{sig}) and the spectral peak period (Tp) series in each sensor location were obtained from the cleaned-up time series.

A preliminary sensitivity analysis indicated that the most sensitive parameters in *UCL-SWM* are α_1 and α_2, included in the non-dimensional energy Equation 2.39 and in the non-dimensional peak frequency Equation 2.40 respectively. This preliminary analysis also served to establish the most probable ranges for these parameters (see Table 5.4), and also demonstrated that the parameters γ_1 and γ_2, also included in the aforementioned equations and used for calibration in earlier work by Young & Verhagen, 1996a, were insensitive under the conditions in Llyn Conwy.

Table 5.4: Calibration parameter ranges for *UCL-SWM*.

Parameter	Young & Verhagen, 1996a	Present study
α_1	3.64e-4	$0.1\alpha_1$ - $10\alpha_1$
α_2	0.133	$0.6\alpha_2$ - $2\alpha_2$

UCL-SWM was run for fifty different combinations of α_1 and α_2 (see Figures 5.23a and 5.23b), with values chosen randomly from a uniform probability distribution bounded by the ranges listed in Table 5.4. *UCL-SWM* was run over an irregular triangular mesh and was set up using the new bathymetry that resulted from the April

2011 field surveys. The model was forced by the wind data recorded during the same field campaign.

The results of the calibration processes indicate that it is possible to get different best values of α_1 and α_2 for each pressure sensor location (see Table 5.5). However, having different optimal parameter values for different lake areas is not very practical, because a lake zonification would be required for α_1 and α_2, affecting the parsimony of the model. Therefore, a unique best value was chosen for each parameter, based on the average NSE value for each pressure sensor. The resulting optimal values were $\alpha_1 = 8.3{\times}10^{-3}$ and $\alpha_2 = 0.154$ (see Figures 5.24a and 5.24b), which are quite close to those determined by Young & Verhagen, 1996a. These are used hereafter for all modelling of waves in Llyn Conwy.

Comparing the best H_{sig} simulated series against the observed ones (Figure 5.25a) the model performs well estimating H_{sig} for sensors 3, 5 and 6, with NSE values greater than 0.65 (see Table 5.5a). The correlation between the observed and the simulated H_{sig} series for these sensors is > 0.85 (see Table 5.6a and Figure 5.26a), which further demonstrates the ability of the model to estimate H_{sig} correctly. However, some discrepancies are visible at site 3, where the model tends to underestimate H_{sig} during the windiest event between 6 pm on 04/04/11 and 6 am on 05/04/11. Additionally, model overestimation of H_{sig} is observed at sites 5 and 6 between 10 pm on 05/04/11 and 10 am on 06/04/11 (see Figure 5.25a), when the wind forcing decreases considerably. On the other hand, comparing the observed and the best simulated series of Tp (Figure 5.25b) an acceptable correlation coefficient $r > 0.73$ (see Table 5.6b and Figure 5.26b) is obtained for the four sensors. However, acceptable results of NSE are obtained only for sensors 3 and 5. At site 6, a persistent offset of ≈ 0.4 s is evident throughout the evaluation period, which leads to a very low NSE of -1.28.

In contrast with the more acceptable results for sites 3, 5 and 6, comparison between simulated and observed H_{sig} and Tp at site 4 reveals a constant bias. This can be attributed to the existence of a small island not initially included in the computational domain (see Figure 2.11 for island location), which blocks incident waves and shortens the effective fetch at this part of the shore. After incorporation of the island into the *UCL-SWM* computational domain, the fetch is shortened at site 4, and predicted H_{sig} and Tp are correspondingly lower. This improves estimation of H_{sig} and Tp, increasing the NSE values to 0.37 and 0.54 respectively.

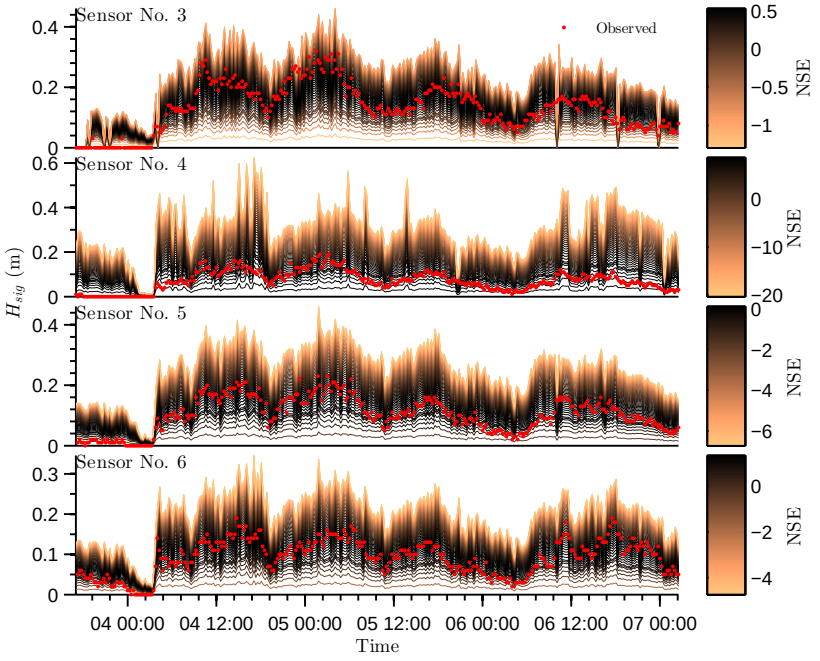

(a)

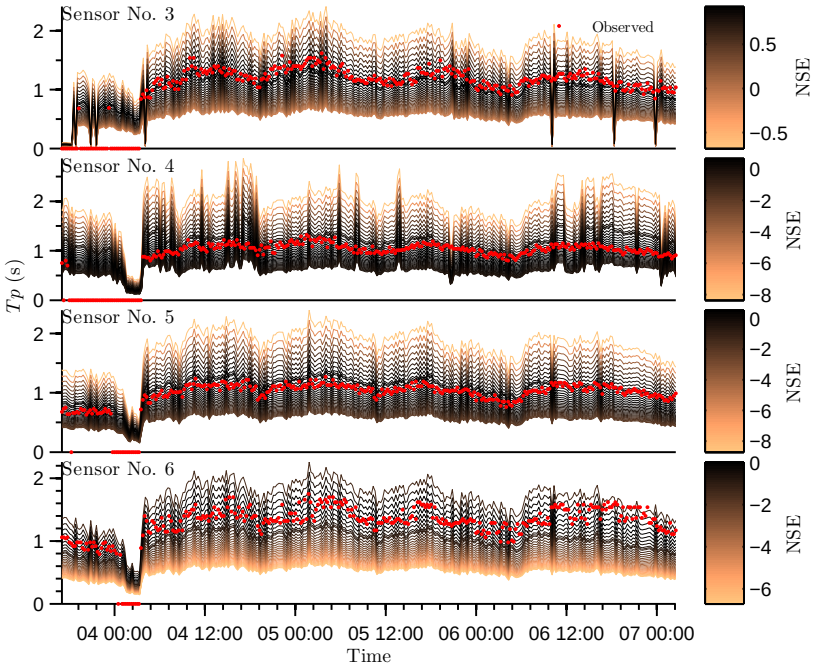

(b)

Figure 5.23: Simulated and observed (red dots) a) significant wave height (H_{sig}); and b) spectral peak period (Tp) between 3 and 8 of April 2011 for four different pressure sensors (see Figure 2.14 for location). The colour of simulated series corresponds to NSE in the colourbar.

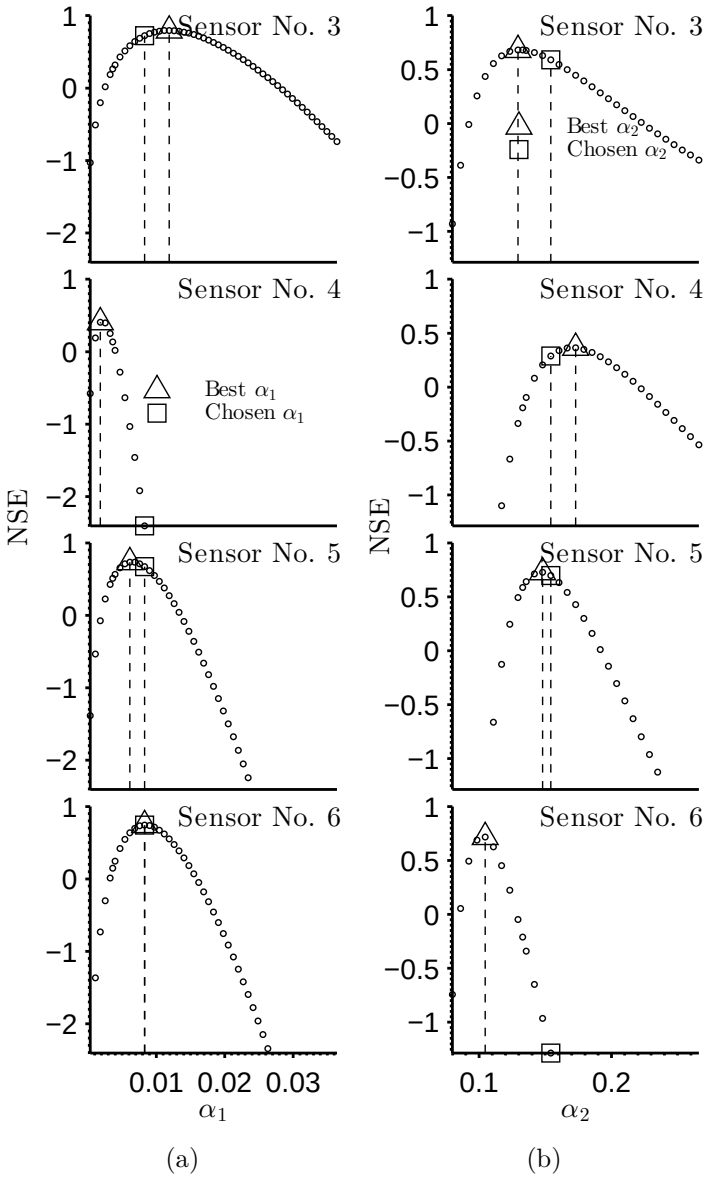

Figure 5.24: a) NSE against α_1; and b) against α_2 for each pressure sensor. The chosen parameters (squares) ($\alpha_1 = 8.3\times10^{-3}$, $\alpha_2 = 0.154$) and the best parameters (triangles) are indicated in the figure.

Sensor No.	Run	NSE	$\alpha_1(\times 10^{-3})$
3	17	0.7954	11.9
	16	0.7934	11.2
	18	0.7924	12.6
	15	0.7859	10.4
	19	0.7848	13.3
	12	**0.7247**	**8.3**
4	3	0.4052	1.8
	4	0.3952	2.5
	5	0.2515	3.2
	2	0.1883	1.1
	52	0.1331	3.6
	12	**-2.4041**	**8.3**
5	9	0.7341	6.1
	10	0.7334	6.9
	11	0.7119	7.6
	8	0.7100	5.4
	12	**0.6724**	**8.3**
6	**12**	**0.7441**	**8.3**
	13	0.7366	9.0
	11	0.7320	7.6
	14	0.7121	9.7
	10	0.6977	6.9

(a) For α_1.

Sensor No.	Run	NSE	α_2
3	9	0.6827	0.129
	32	0.6819	0.133
	10	0.6778	0.136
	8	0.6682	0.123
	11	0.6587	0.142
	13	**0.5910**	**0.154**
4	16	0.3653	0.173
	15	0.3628	0.167
	17	0.3506	0.179
	14	0.3391	0.161
	18	0.3223	0.185
	13	**0.2890**	**0.154**
5	12	0.7274	0.148
	11	0.7126	0.142
	13	**0.6974**	**0.154**
	10	0.6401	0.136
	14	0.6326	0.161
6	5	0.7159	0.105
	4	0.6893	0.098
	6	0.6249	0.111
	3	0.4935	0.092
	7	0.4522	0.117
	13	**-1.2847**	**0.154**

(b) For α_2

Table 5.5: The best five values of α_1 and α_2 for each sensor corresponding to the five highest values of NSE. Bold values indicate the chosen parameter.

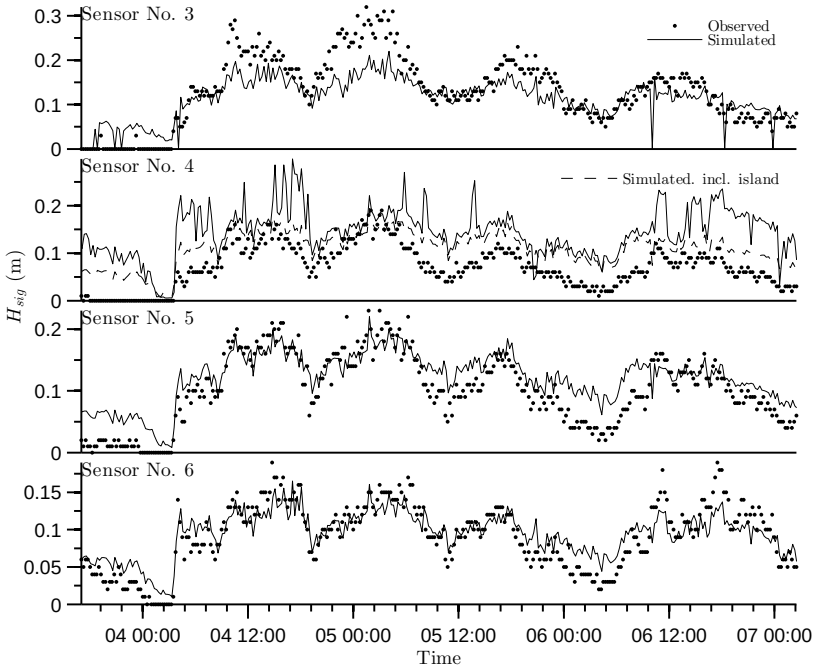

(a)

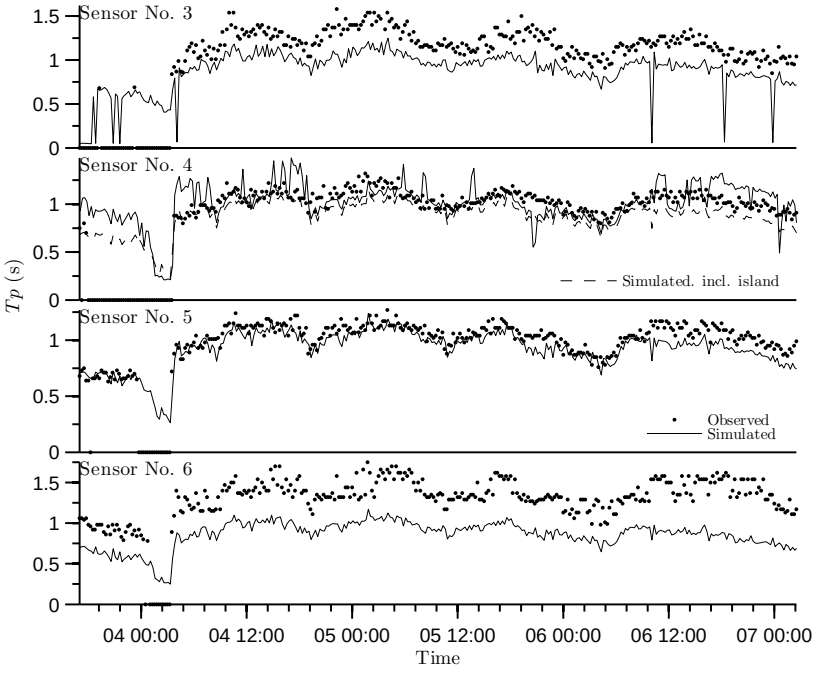

(b)

Figure 5.25: Comparison of observed versus best simulation series of a) H_{sig}; and b) T_p for each sensor location for 3 to 8 of April 2011.

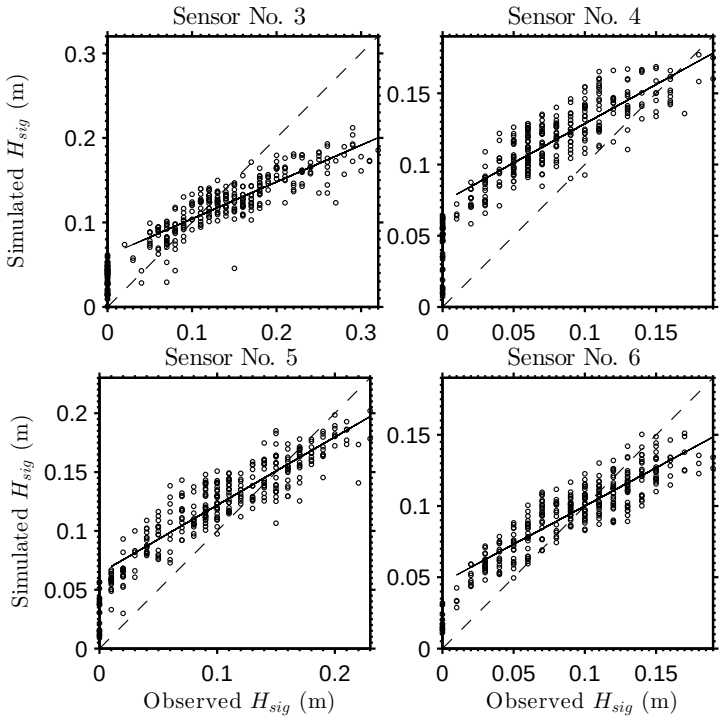

(a)

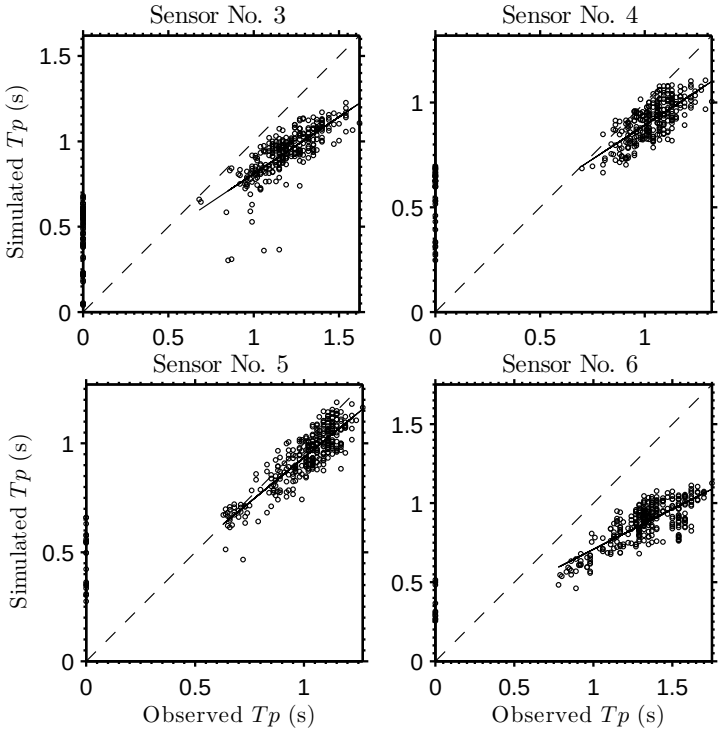

(b)

Figure 5.26: a) Simulated against observed H_{sig}; and b) T_p for the period 3 to 8 of April 2011. Simulated series for sensor 4 includes the effects of the lake island.

Table 5.6: Summary statistical information for simulated and observed wave parameters between 3 and 8 April 2011. Information for the simulated data at site 4 includes the effects of the lake island referred to in the text.

	Site 3		Site 4		Site 5		Site 6	
	Obs.	Sim.	Obs.	Sim.	Obs.	Sim.	Obs.	Sim.
Maximum (m)	0.32	0.22	0.19	0.19	0.23	0.22	0.19	0.17
Mean (m)	0.15	0.13	0.08	0.12	0.11	0.13	0.09	0.10
Std. Dev. (m)	0.07	0.04	0.04	0.03	0.05	0.03	0.04	0.02
Corr. Coef.	0.86		0.85		0.91		0.89	
RMSE (m)	0.05		0.04		0.03		0.02	
Linear fit.:								
-Slope	0.44		0.55		0.58		0.54	
-Intercept (m)	0.06		0.07		0.06		0.05	
NSE	0.72		0.37		0.67		0.74	

(a) Wave Height, H_{sig}

	Site 3		Site 4		Site 5		Site 6	
	Obs.	Sim.	Obs.	Sim.	Obs.	Sim.	Obs.	Sim.
Maximum (s)	1.62	1.25	1.32	1.16	1.27	1.24	1.75	1.17
Mean(s)	1.19	0.94	1.04	0.92	1.01	0.94	1.33	0.87
Std. Dev. (s)	0.16	0.14	0.10	0.09	0.14	0.13	0.20	0.13
Corr. Coef.	0.76		0.73		0.88		0.78	
RMSE (s)	0.28		0.14		0.09		0.47	
Linear fit.:								
-Slope	0.67		0.65		0.83		0.51	
-Intercept (s)	0.14		0.24		0.11		0.20	
NSE	0.59		0.54		0.70		-1.28	

(b) Wave period, Tp

Intermittent spikes appear in both the modelled H_{sig} (Figure 5.25a) and Tp (Figure 5.25b) series. These are associated with sudden and significant changes in the fetch given by deviations of the wind from the predominant direction. Comparing the fetch computed using *UCL-SWM* and the wind direction at the four locations (Figure 5.27) it is evident that the fetch is very sensitive to wind direction changes. This means that small changes in the wind direction will trigger significant changes in the fetch, which may greatly affect calculations of H_{sig} and Tp. The occurrence of these spikes caused by sudden increase in the fetch will become more frequent for more complex and irregular basin shapes.

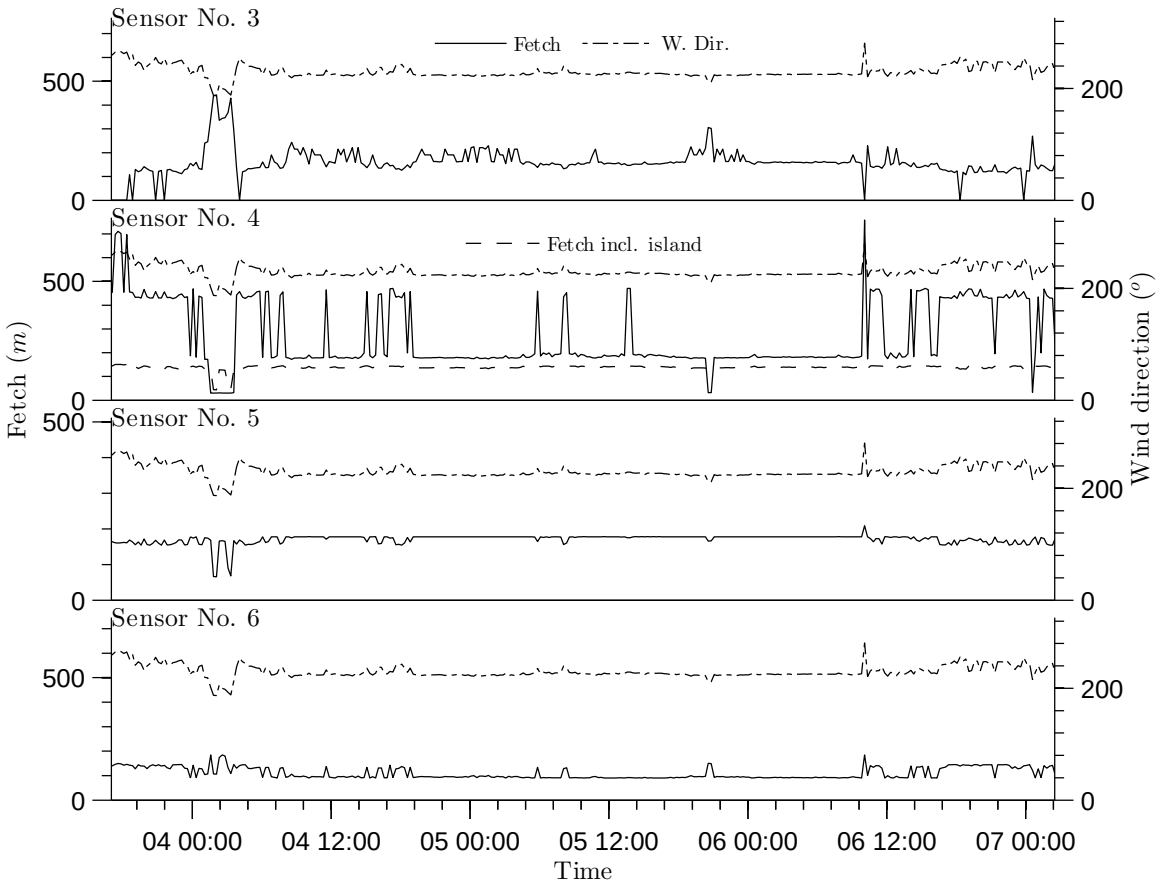

Figure 5.27: Comparison between fetch and wind direction at the different sensor locations for period 3 to 8 of April 2011.

More generally, discrepancies between simulated and observed H_{sig} and Tp might originate in various ways. One of the common mistakes in the set-up of wind-wave

propagation models is that the time at which the waves are triggered is computed wrongly, so the arrival time and the frequency of waves are affected (Hawley *et al.*, 2004). Also, since *UCL-SWM* is based on linear wave theory, the estimation of the wave information is made at every point of the computational grid without considering the effects induced by its neighbours. The bi-directional propagation of waves and processes such as diffraction and refraction of waves are not considered. This bi-directional behaviour is particularly important near the shoreline because when waves break, secondary currents and oscillations are initiated, which feedback into the incident waves. Errors in the estimation of H_{sig} and Tp are also induced by the way that the wind field is introduced (Schwab *et al.*, 1984, Hawley *et al.*, 2004). Although the wind forcing in Llyn Conwy was set up to be spatially uniform over the whole lake, a more precise spatial distribution of the wind field might improve the simulation of wave propagation, by considering the effects of wind gradients locally on the displacement of waves.

The advantages of modelling wind-wave bi-dimentional propagation is easily visualized by comparing H_{sig} and Tp maps (Figure 5.28) computed using *UCL-SWM* and the spectral wave model, *SWAN* (Booij *et al.*, 1999), for $W_s = 12\ m\ s^{-1}$ and $W_d = 210^o$ (the most frequent wind forcing conditions in Llyn Conwy). Whereas *UCL-SWM* does not consider a 2D bidimensional propagation, *SWAN* is a bidimensional model which includes quadruplet wave-wave interactions, bottom friction, and depth-induced wave breaking. Such *SWAN* features significantly influence the discrepancies between both calculations that occur especially along the sectors of longer fetches, where relative spatial discontinuities toward the central and eastern sectors coincide with significant contiguos fetch changes. Despite the spatial differences, the magnitude of H_{sig} and Tp are quite similar for both models and discrepancies are below 10%.

Significant differences exist between the computational performance of *UCL-SWM* and *SWAN*. Clocking the run time of both models on a Sun Ultra 24 workstation with 3 GHz Intel quad-core processor, shows that whereas *UCL-SWM* takes 1 s, *SWAN* requires 10 s. The much longer time required by *SWAN* is because it uses an implicit numerical scheme where performance is linked to numerical convergence, which is quite sensitive to bathymetric resolution, boundary conditions and wind forcing data. Computational performance can be more critical when *SWAN* is coupled with 3D hydrodynamic models (e.g. Zhang & Li, 1997, Warner *et al.*, 2008), because the data exchange between models usually increases run time and required expertise to determine the optimum synchronization interval. *UCL-SWM* thus offers a robust and computationally

efficient alternative suitable to couple with 2D/3D hydrodynamic models to estimate the wind-wave parameters in complex lake basins.

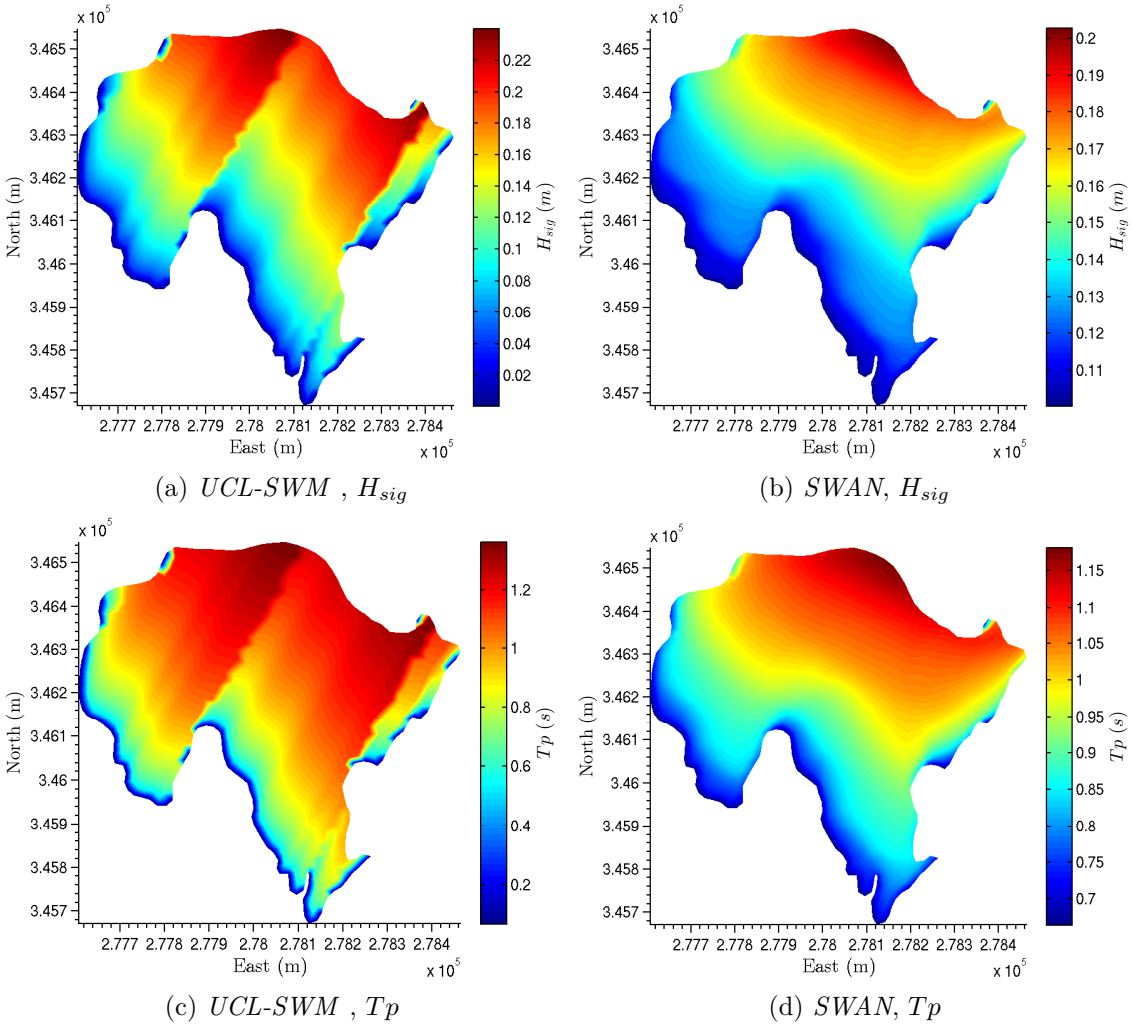

(a) *UCL-SWM* , H_{sig}

(b) *SWAN*, H_{sig}

(c) *UCL-SWM* , Tp

(d) *SWAN*, Tp

Figure 5.28: Comparison of H_{sig} and Tp computed with *UCL-SWM* and *SWAN* for $W_s = 12\ m\ s^{-1}$ and $W_d = 210^o$.

5.6 Bottom Stresses for Wind Forcing and Water Level Scenarios

5.6.1 Introduction

Analysis of bottom shear stresses resulting from both currents and wind-waves was undertaken for hypothetical scenarios based on long time series of observed wind speed and wind direction for the Llyn Conwy catchment, and the observed variation in water surface level. The selection of wind speed and wind direction scenarios was based on a frequency analysis of the records from the CEH data buoy and the catchment AWS (see Figure 2.13) between November 2006 and December 2008, and a longer series for nearby Capel Curig from August 1993 and August 2011. Since the difference of altitude between Llyn Conwy and Capel Curig No.3 station is $\approx 238\ m$, the data recorded at the station were corrected empirically following the wind profile power law (Justus & Mikhail, 1976):

$$Ws_z = Ws_0 \left(\frac{z}{z_0}\right)^{\alpha} \tag{5.1}$$

where Ws_z is the resultant wind speed at height z, Ws_0 is the known wind speed at height z_0, and α is an empirical exponent. A linear regression analysis between hourly wind speed recorded at the weather stations and at Llyn Conwy for the period 2006-2008 (see Figure 5.29) was used to obtain the optimum value of α. This yielded a regression equation of the form $Ws_{Buoy} = 1.29 Ws_{CapelCur.}$. It should be noted that, since the values z, z_0 and the fitted exponent α are known, the fraction in the Equation 5.1 reduces to 1.29. No corrections were made to the hourly wind direction series measured at the weather station, since comparison against the records at Llyn Conwy coincided with the predominance of southwesterly wind.

The frequency analysis of the fitted wind speed series at Capel Curig No.3 began with a preliminary analysis of the series at different levels of aggregation (see Figure 5.30). The hourly series contains peak wind speeds over 40 $m\ s^{-1}$ during winter months. The monthly aggregation also shows that the windiest months are at the beginning and at the end of every year. On the other hand, the yearly wind speed aggregation shows more subdued interannual variation between 6 and 8 $m\ s^{-1}$, with no evidence for any progressive trend.

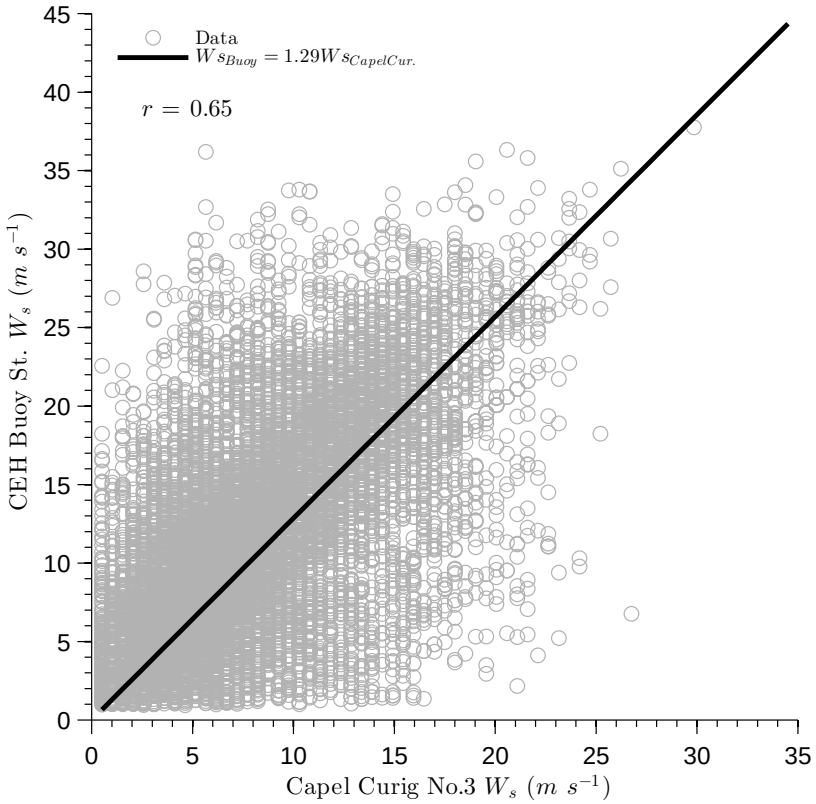

Figure 5.29: Regression analysis between the hourly wind speed measured at the CEH data buoy and at Capel Curig No. 3, from November 2006 to December 2008.

An analysis of the seasonal variation in hourly wind speed based on the whole 18 year dataset (Figure 5.31) shows that the wind speed varies sustantially year by year since standard deviations (σ) of the mean wind speed varies between 3 and 10 $m\ s^{-1}$ over the year (see Figure 5.31 (b)). The variability is less in summer ($\sigma \approx 4\ m\ s^{-1}$) when the averaged wind speeds are relatively low ($\approx 6\ m\ s^{-1}$) and much higher in winter ($\sigma \approx 8\ m\ s^{-1}$) when averaged wind speeds are around 10 $m\ s^{-1}$.

Aggregating by months (see Figure 5.32) shows that the windiest months are January and February, with a monthly mean wind speed close to 10 $m\ s^{-1}$, which varies between 1 $m\ s^{-1}$ and 25 $m\ s^{-1}$. In contrast, the lowest monthly mean wind speeds occur in August and September when the mean wind speed decreases to around 7 $m\ s^{-1}$ (range 2 $m\ s^{-1}$ to 16 $m\ s^{-1}$).

Further analysis by grouping the hourly wind speed data to hour of the day (from 00 h to the 23 h) (Figure 5.33) shows that the wind speed can vary from 0 to over 30

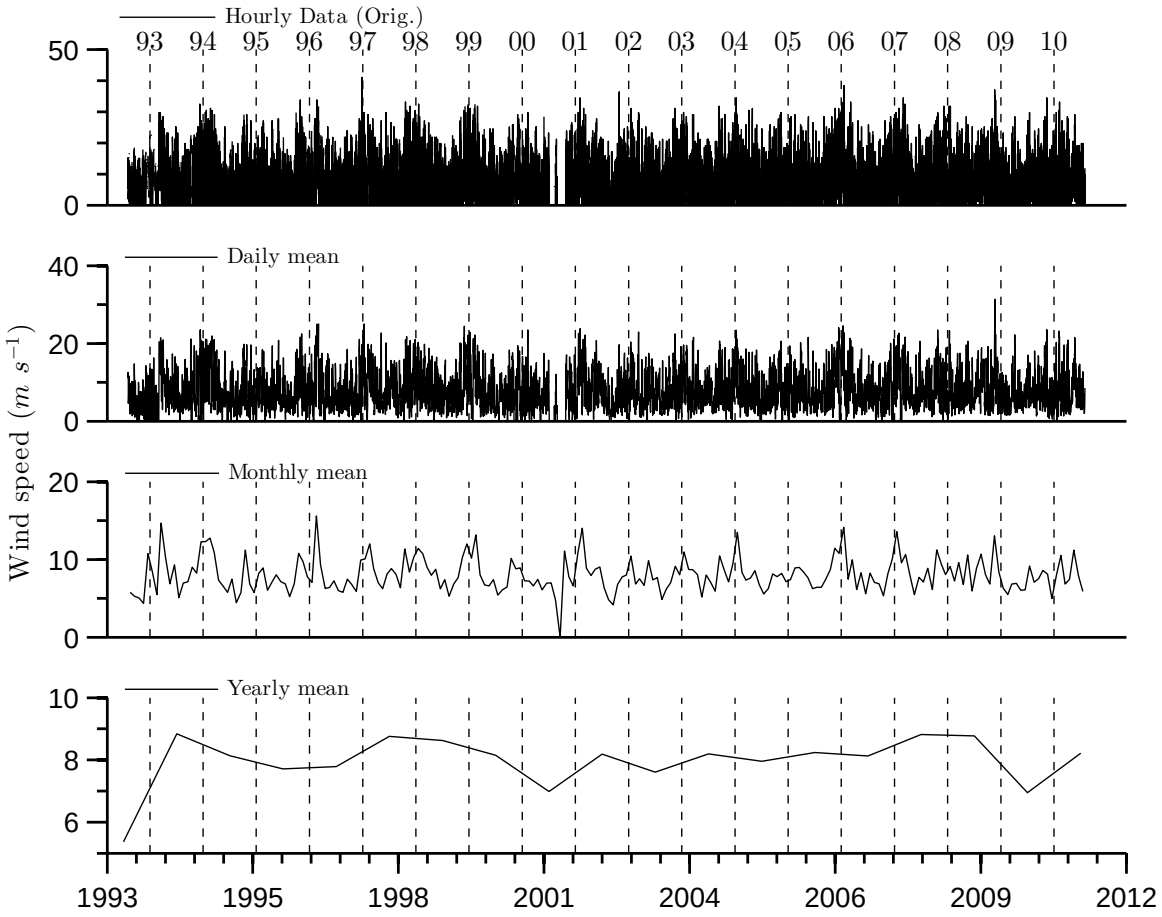

Figure 5.30: Daily, monthly and yearly aggregations of the hourly wind speed series based on Capel Curig No. 3 Station data for August 1993 to August 2011 corrected for the location of Llyn Conwy.

$m\ s^{-1}$ at any hour during the day. However, a weakly periodic mean daily behaviour of wind speed can be discerned. The mean wind speed remains relatively constant at about 7.5 $m\ s^{-1}$ for the first hours of the day. It gradually increases after 07:00, reaching a maximum value of 9.8 $m\ s^{-1}$ at 15:00. Mean wind speed decreases gradually reaching the initial value of 7.5 $m\ s^{-1}$ around 21:00 remaining at this level until the end of the day. Diurnal wind speed variation is quite commonly encountered in lake catchments (e.g. Lake Geneva and Lake Kinneret) and has been used to force daily average hydrodynamic processes in lakes (e.g Lemmin & D'Adamo, 1997; Pan *et al.*, 2002). The preceding analysis of the wind speed regime for Llyn Conwy allows the

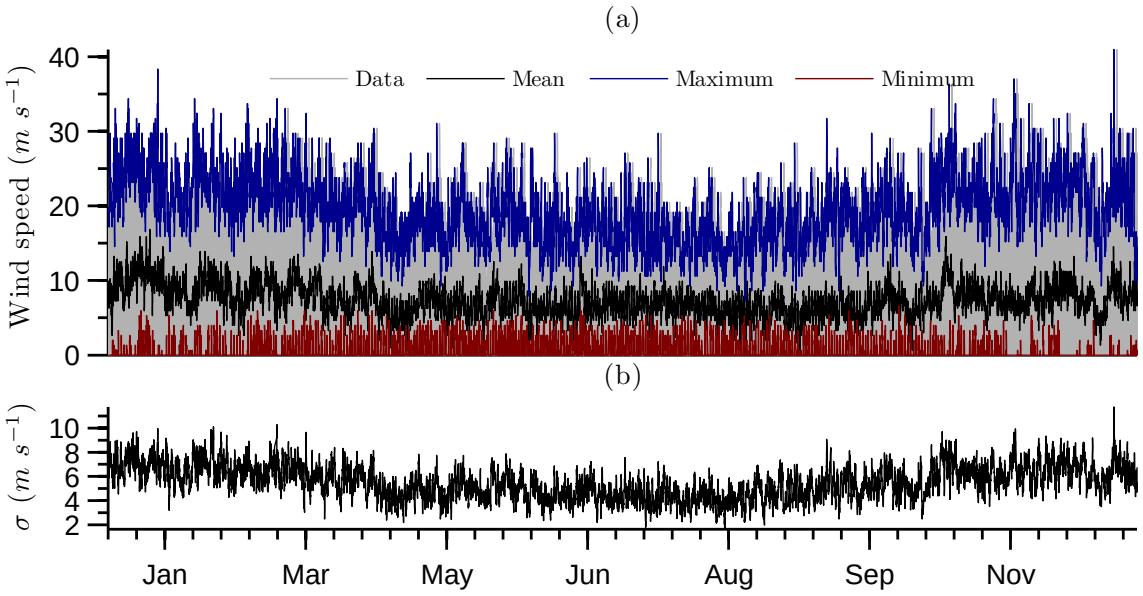

Figure 5.31: Seasonal analysis of hourly wind speed data. (a) Hourly, mean, maximum and minimum wind speed. (b) standard deviation (σ) of the mean wind speed. Capel Curig No. 3 Station data for August 1993 to August 2011 corrected for Llyn Conwy location.

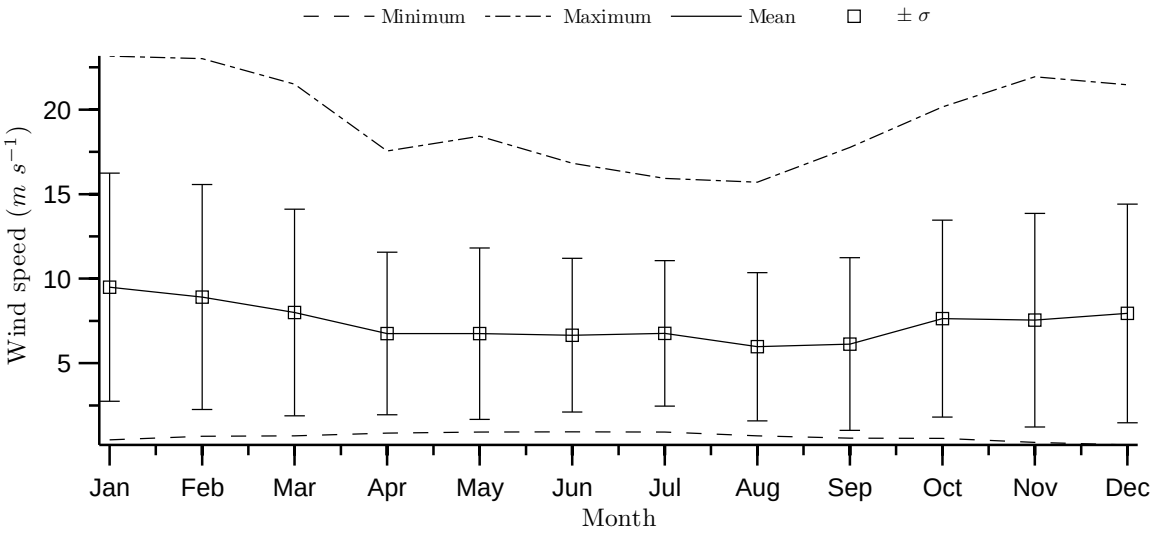

Figure 5.32: Aggregation by months of the inter-annual wind speed series (See Figure 5.31 (a)). Records taken at Capel Curig No. 3 Station between August 1993 and August 2011 fitted to Llyn Conwy location.

quantification of three key aspects of the wind forcing scenarios: the range within which wind speed fluctuates; the calmest and windiest months during an average year; and the diurnal wind speed variation.

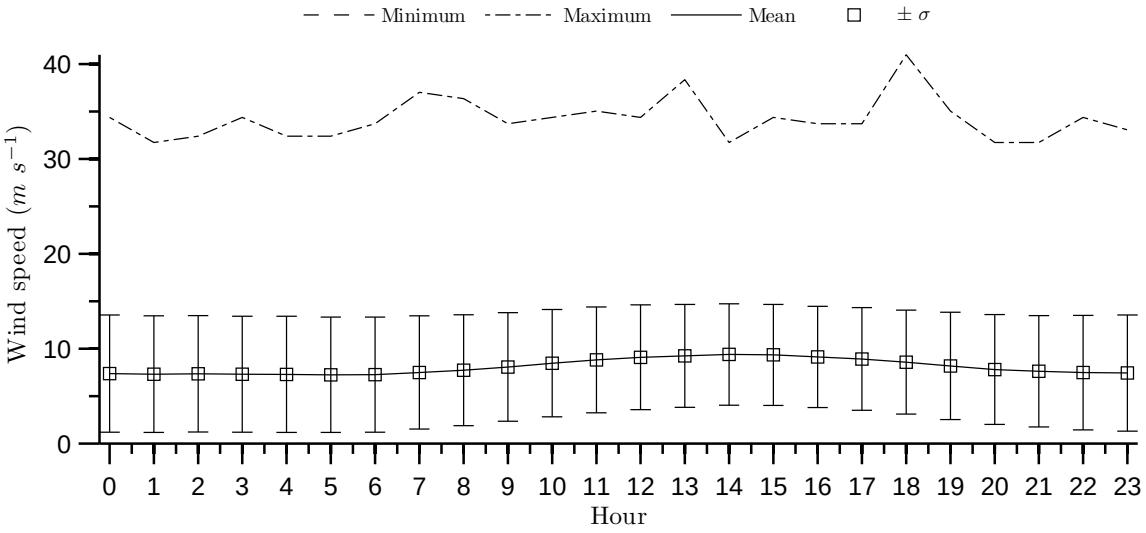

Figure 5.33: Grouping of the hourly wind speed series by hour of the day. Data for Capel Curig No. 3 Station between August 1993 and August 2011 corrected for Llyn Conwy location.

Analysis of the wind-wave parameters obtained from the high resolution water level measurements versus the meteorological data reveals that wind speeds under 12 $m\ s^{-1}$ do not generate significant waves capable of sediment resuspension (see Figure 5.34). Accordingly, a threshold wind speed of 12 $m\ s^{-1}$ was applied in setting up the scenarios. A lower threshold has been reported in other studies of sediment resuspension in estuaries and lakes. For example, Luettich Jr *et al.*, 1990 used wind speeds within a range of 5 to 6 $m\ s^{-1}$ to study the resuspension of sediments in a large shallow lake. French *et al.*, 2000 studied muddy sediment dynamics in the Blyth estuary, Suffolk UK, and established a wind speed threshold of 4.5 $m\ s^{-1}$ for sediment resuspension. Other studies by Bengtsson & Hellström, 1992 and Chao *et al.*, 2008 considered a wider wind speed range of between 1 and 12 $m\ s^{-1}$.

Frequency analysis of the wind speed time series shows that wind speed follows an exponential probability distribution function (Figure 5.35a). The most frequent wind speeds are around 4 $m\ s^{-1}$ and wind speeds $> 35\ m\ s^{-1}$ are very rare. On the other hand, the frequency analysis of the wind direction time series (Figure 5.35b) shows

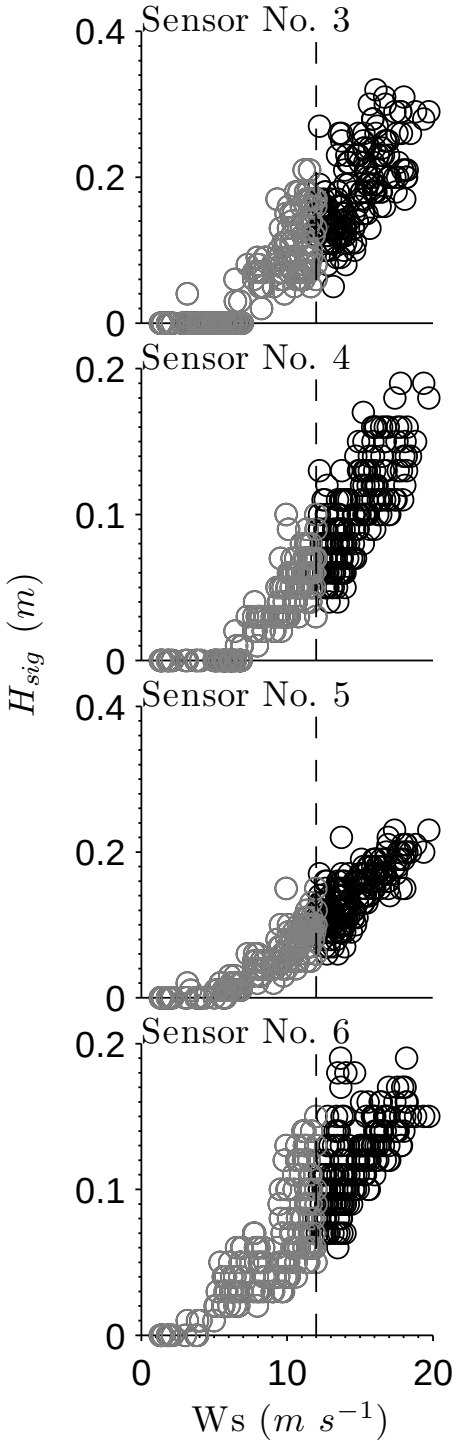

Figure 5.34: Wind speed (W_s) versus significant wave height (H_{sig}) at different sensor locations for 3 to 8 of April 2011. Dashed line indicates the $W_s = 12\ m\ s^{-1}$ threshold.

clearly a dominant southwesterly wind direction between 200^o and 250^o. Although the probability mass functions in Figures 5.35 show individually the most frequent wind speed and wind direction events, it is useful to know their joint probability of occurrence. To do this, a joint probability mass function (JPMF) for wind speed and wind direction (Figure 5.36) was obtained. The JPMF analysis shows that the most frequent event is represented by a wind speed of 12 $m\ s^{-1}$ and a wind direction of 210^o. It is also evident that 210^o is the predominant direction for wind speeds between 6 and 14 $m\ s^{-1}$ (see Figure 5.36). Table 5.7 summarises the five most probable wind forcing events.

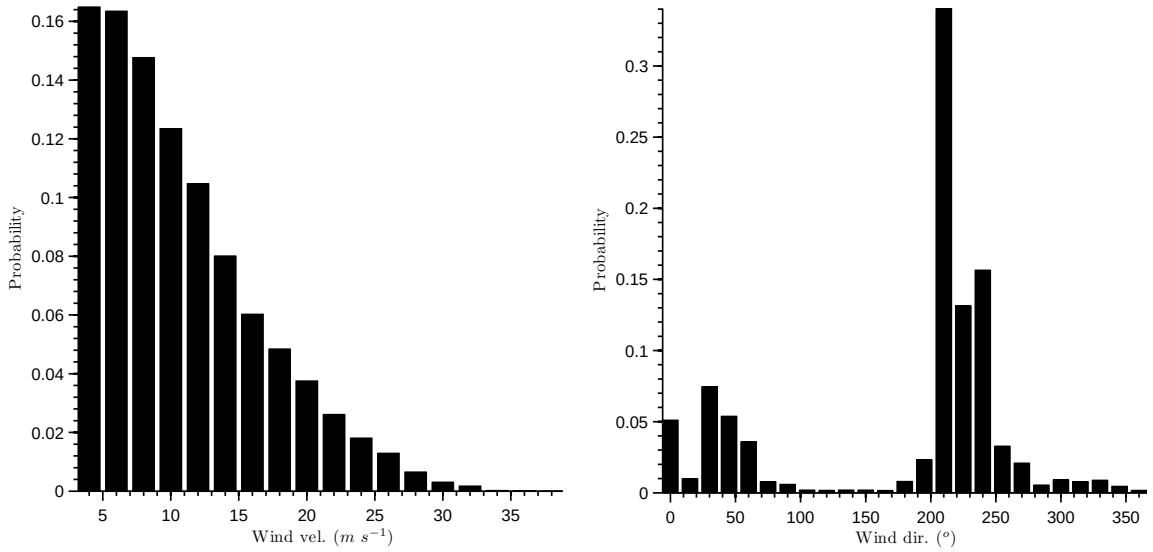

Figure 5.35: Probability mass functions for a) wind speed and b) direction, computed for hourly wind forcing series recorded at Capel Curig No. 3 station between August 1993 and August 2011 and corrected for Llyn Conwy location.

Based on the frequency analysis of wind forcing data two different groups of scenarios were established: wind direction scenarios and wind speed scenarios. The wind direction scenarios consider a constant 12 $m\ s^{-1}$ wind speed and different wind directions binned every 45^o from 0^o (North) to 315^o (Northwest). The wind speed scenarios consider a constant wind direction of 210 ^{o} and different wind speeds binned every 4 $m\ s^{-1}$ from 12 to 40 $m\ s^{-1}$. A summary of the wind forcing scenarios is shown in Table 5.8.

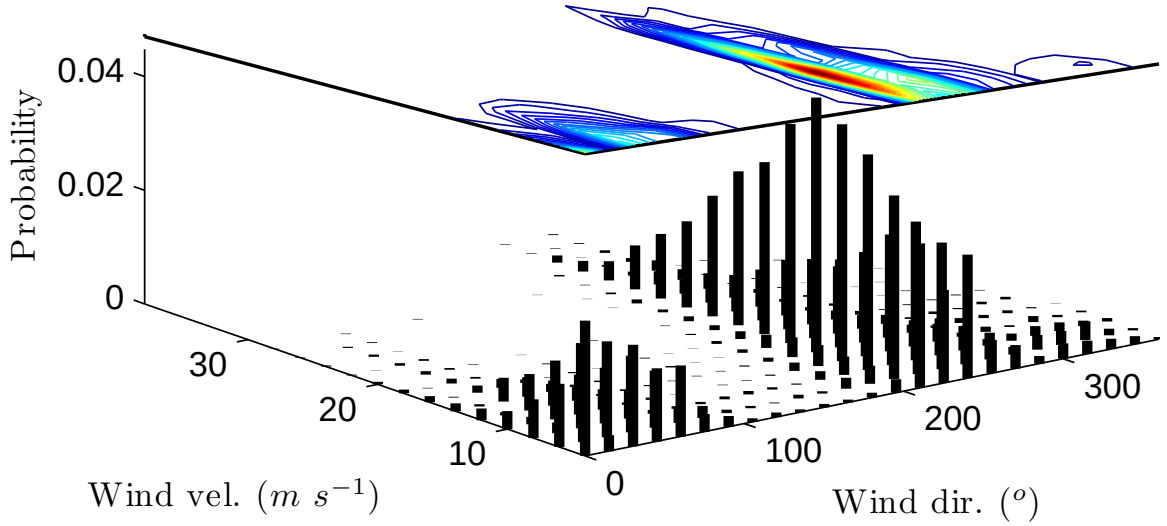

Figure 5.36: Joint probability mass function of the hourly wind speed and wind direction for Llyn Conwy.

Table 5.7: The five most frequent wind forcing events at Llyn Conwy. Values taken from the JPMF shown in Figure 5.36.

Id	Wind Dir. Bin (^{o}) ± 15	Wind Vel. Bin ($m\ s^{-1}$) ± 1	Frequency $\times 10^{-2}$
1	210	12.0	4.5
2	210	10.0	4.2
3	210	14.0	3.9
4	210	8.0	3.8
5	210	6.0	3.2

Table 5.8: Wind forcing scenarios to investigate the bottom stresses due to the combined action of currents and wind-waves. The letter V and D represent the wind speed and wind direction scenarios respectively. The letters in bold highlight the most frequent event.

		Wind direction bins (^{o})								
		0	45	90	135	180	**210**	225	270	315
Wind velocity bins ($m\ s^{-1}$)	**12**	D	D	D	D	D	V	D	D	D
	16						V			
	20						V			
	24						V			
	28						V			
	32						V			
	36						V			
	40						V			

Despite the very low probability of occurrence of wind speeds $> 32\ m\ s^{-1}$ (Figures 5.35a and 5.36), such extremes are included in the scenarios evaluated. The reason is twofold. First, due to the non-linear relation between bottom stress and sediment entrainment and transport, infrequent high magnitude stress events can be very significant contributors to overall sediment redistribution. Second, rare stress peaks can extend sediment resuspension to parts of a lake that are ordinarily dominated by deposition. Understanding the location and timing of such events is critically important for the understanding of the completeness of lake sediment sequences and their palaeoenvironmental archives.

Along with the wind forcing scenarios, surface water level variations are also considered. Observations and measurements of water marks on the sluice at the southern outlet (see Figure 2.12c) indicate that the average water level may drop about -1 m in summer, when lower rainfall and higher evaporation are compounded by water abstraction. In contrast, when rainfall events are persistent, excess lake water is discharged via the outflow at the south leading to a regulated maximum water surface increment of about +0.5 m. Based on this, four different water surface level scenarios were established: -1, -0.5, 0 ('typical') and 0.5 m. The wind forcing scenarios sumarised in Table 5.8 were evaluated for each water surface level scenario.

5.6.2 Wind-wave bottom stress

The computation of the wind-wave shear stress (τ_w) on the lake bottom was made using *UCL-SWM* in isolation from the wind forcing (wind speed and wind direction) and the water surface level ($\Delta level$) scenarios.

Wind direction and water surface level scenarios

The results for the wind direction (W_d) scenarios show that the highest maximum $\tau_w = 1.2\ N\ m^{-2}$ occurs when $W_d = 90^o$ (easterly wind) and $\Delta level = 0\ m$ (see Figure 5.37). High values of maximum τ_w also occur for the same level when $W_d = 0^o$ and $W_d = 270^o$. The maximum stresses computed for $\Delta level = -0.5\ m$ are slightly lower than to those computed for $\Delta level = 0\ m$. In contrast, the lowest maximum $\tau_w = 0.7\ N\ m^{-2}$ occur when $W_d = 45^o$ (Northeasterly wind) and $\Delta level = 0.5\ m$.

Integration of the maximum τ_w in Figure 5.37 for each $\Delta level$ shows that the greatest fraction of maximum τ_w occurs for $\Delta level = 0\ m$, and not for $\Delta level = -1\ m$ when water depths are the lowest and shallow sectors become more exposed to wave action. As is expected, the lower fraction of maximum τ_w occurs for $\Delta level = 0.5\ m$ when a large proportion of the lake bed is protected from the action of waves by the greatest water depths. Similarly, integrating the maximum τ_w for each W_d, reveals that the greatest fraction of maximum τ_w occurs when $W_d = 270^o$ (westerly wind) and $W_d = 0^o$ (northerly wind). This is consistent with the maximum value of fetch and therefore the development of the largest wind-waves. In contrast, the lowest fraction of maximum τ_w occurs for $W_d = 135^o$ (southeasterly wind) and $W_d = 45^o$ (northeasterly wind) because the relatively short fetch and the less extensive shallow water zones along these directions impedes the formation of bigger waves.

In general, the homogeneous behaviour of the maximum τ_w shown in Figure 5.37, which varies between 0.8 and 1.2 $N\ m^{-2}$, demonstrates the low spatial variability of the bottom shear stresses due to wind-waves in Llyn Conwy for typical and reduced water levels. In contrast, a notably reduction of τ_w, which does not exceed 0.8 $N\ m^{-2}$, is observed when the water level rises ($\Delta level = 0.5$). On the other hand, the variation of the maximum τ_w in terms of wind direction scenarios demonstrate the complex shape of Llyn Conwy, where the fetch is sustantially different between wind directions. Also, the distribution of the shallow areas is not concentric to the deepest areas of the main lake basin. Rather, these are distributed largely toward the south and in places along

the western and eastern shores. Such diversity of fetch and heterogenous distribution of shallow sectors affects the growth of wind-waves and therefore the magnitude of τ_w.

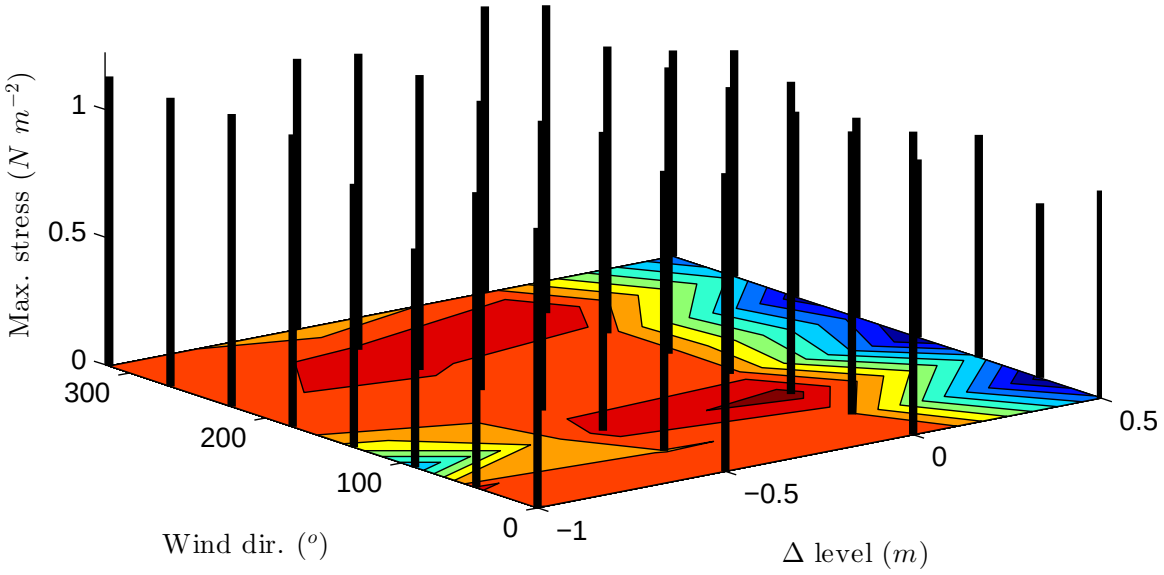

Figure 5.37: Maximum wind-wave bottom stresses for wind direction and water surface level scenarios. Wind speed of 12 $m\ s^{-1}$.

The potential bottom area resuspended (BAR) was quantified by comparing the computed bottom stresses against a critical bottom stress (τ_{cri}). The selection of $\tau_{cri} = 0.1\ N\ m^{-2}$ was made based on a review of diverse studies of sediment resuspension in lakes (Sheng & Lick, 1979; Kang *et al.*, 1982; Bengtsson & Hellström, 1992; Lou *et al.*, 2000), which indicate the choosen value as the most appropriate. The results, shown in Figure 5.38, indicate that the % of BAR is very similar among $-0.5 < \Delta level < 0.5\ m$ ($> 2.8\%$), but less for $\Delta level = -1\ m$ (BAR $< 2\%$), because as water level falls, this removes more of the extensive low gradient shallow marginal areas from the computation. In terms of the wind direction scenarios, the maximum % of BAR ($> 2.8\%$) occurs for $W_d = 0^o$ (northerly wind) and $W_d = 225^o$ (southwesterly wind). In contrast, the minimun % of BAR ($< 2.5\%$) will occur for W_d between 45 ^{o} (northeasterly wind) and 180^o (southerly wind).

The spatial distribution analysis of τ_w for different wind directions (e.g. Figure 5.39) shows that the BAR is, for most of the wind direction scenarios, distributed in a band

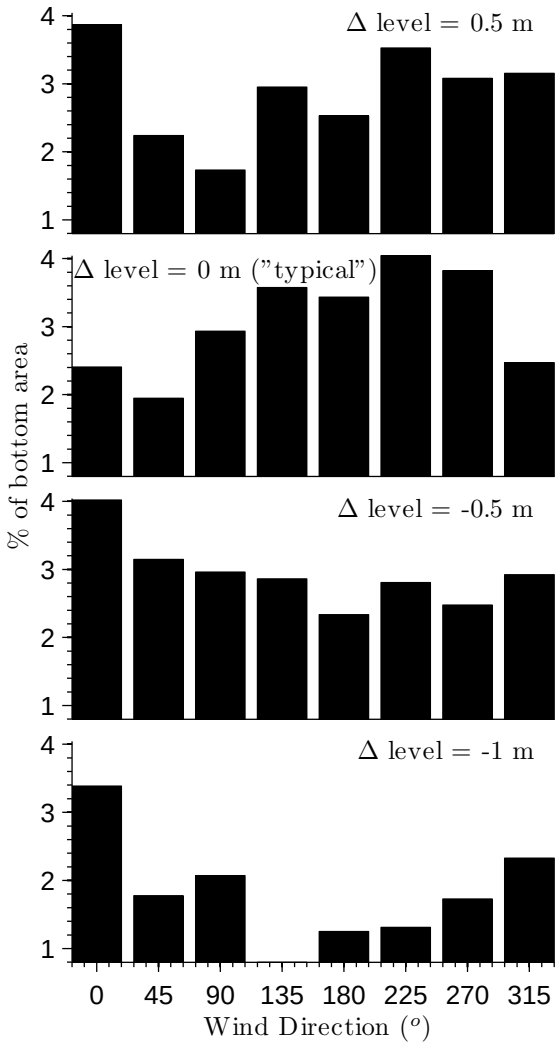

Figure 5.38: % of bottom area resuspended (BAR) by wave-induced bottom stress versus wind direction and for different water surface levels. Wind speed is constant at 12 $m\ s^{-1}$.

along the shores, exept for $W_d = 0^o$ and $W_d = 270^o$ where the BAR covers small shallow inshore areas. τ_w usually reaches its maximum values close to the shore where the maximun fetch is reached. On the other hand, analysing the spatial distribution of τ_w under different water surface levels (see Figure 5.40), it is observed that the proportion of BAR remain nearly constant for $-0.5 < \Delta level < 0.5\ m$, and decrease when $\Delta level = -1\ m$ since some sectors along the shore become dry areas. Observing the distribution of τ_w at different levels for $W_d = 0^o$ (Figure 5.40a), the BAR around

the western headland and some sectors along the eastern shore disappears as $\Delta level$ decreases, whereas BAR grows in the south of the lake. On the other hand, analysing the distribution of τ_w at different levels for $W_d = 225^o$ (see Figure 5.40b) it is observed that the proportion of BAR in the north-eastern bay stays approximately constant between for $-0.5 < \Delta level < 0.5\ m$, and this almost disappears for $\Delta level = -1\ m$. At the northern sectors, larger bottom areas might experience resuspension for $\Delta level \geq 0\ m$.

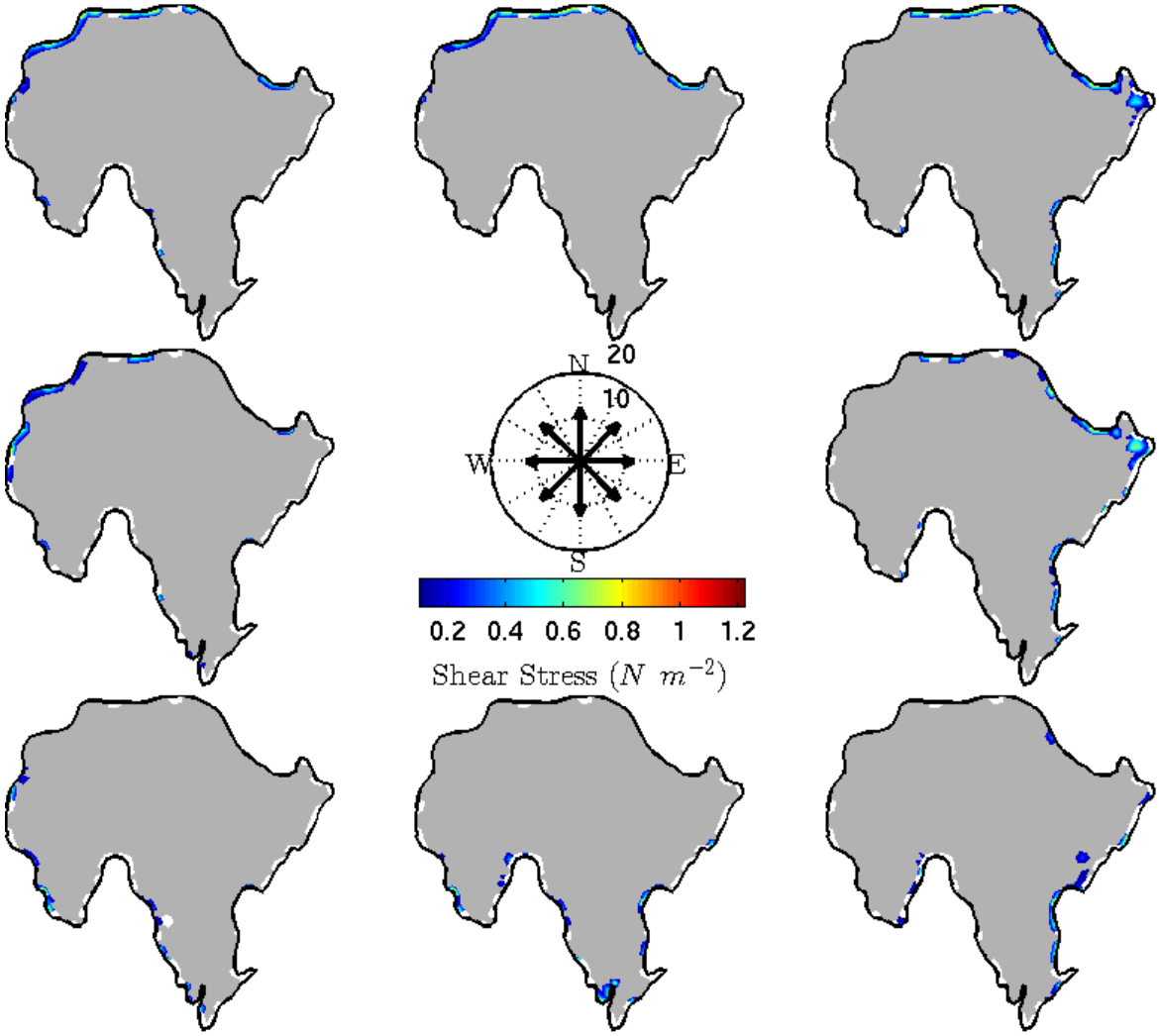

Figure 5.39: Wind-wave shear stresses for different wind directions at $\Delta level = 0\ m$ using a constant wind speed of 12 $m\ s^{-1}$. The arrows in the wind rose indicate wind direction. Grey shaded areas correspond to bottom stresses $< \tau_{cri}$.

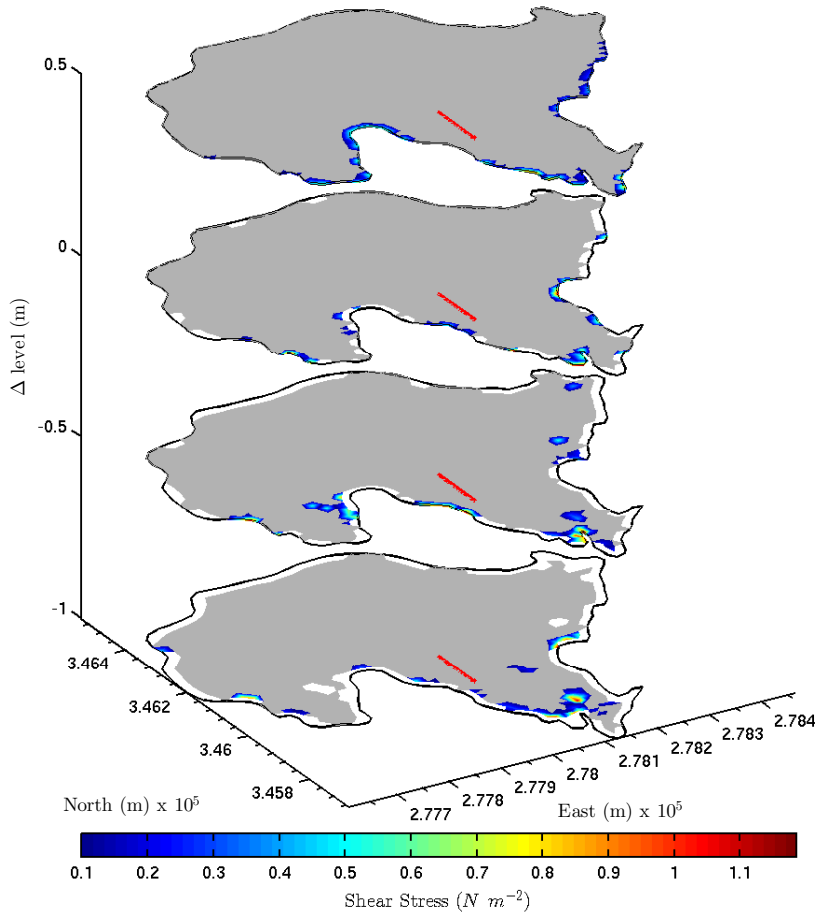

(a) Wind direction 0^o (Northerly wind).

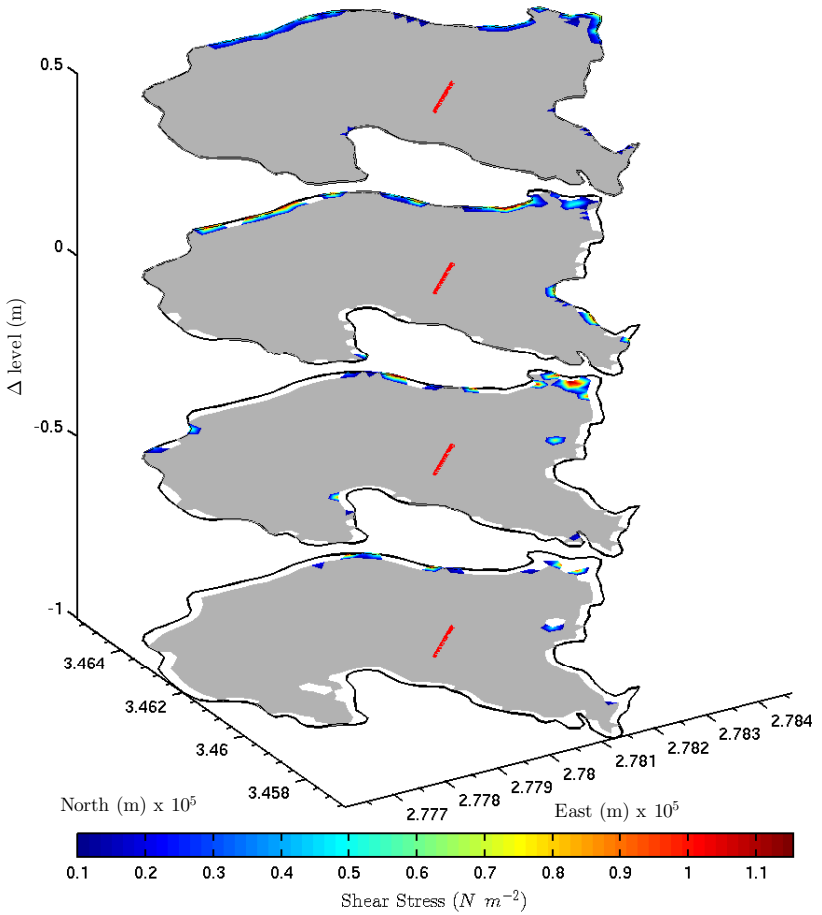

(b) Wind direction 225^o (Southwesterly wind).

Figure 5.40: Wind-wave bottom stresses for wind direction and water surface level scenarios. Constant wind speed of 12 $m\ s^{-1}$. Grey shaded areas correspond to bottom stresses $< \tau_{cri}$.

Wind speed and water surface level scenarios

The computation of τ_w for wind speed and water surface level scenarios shows an approximate linear growth of the maximum τ_w for each $\Delta level$ (see Figure 5.41). The linear growth of the maximum τ_w is more accentuated for $\Delta level = 0\ m$, where the highest value of the maximun τ_w is reached for $W_s = 40\ m\ s^{-1}$. In contrast, a less accentuated growth in maximum τ_w is observed for $\Delta level = 0.5\ m$, which reflects the fact that less of the bed is exposed to wind-waves when the water surface rises.

Integrating the maximum τ_w in Figure 5.41 for each $\Delta level$ shows that the greatest proportion of maximum τ_w occurs for $\Delta level = 0\ m$. Since similar results were found in the analysis of wind direction and water level scenarios, this means that $\Delta level = 0\ m$ (i.e. the approximate 'typical' lake level) might be considered to represent the optimum for the occurrence of the maximun τ_w and therefore for the most widespread sediment resuspension irrespective of the weather conditions.

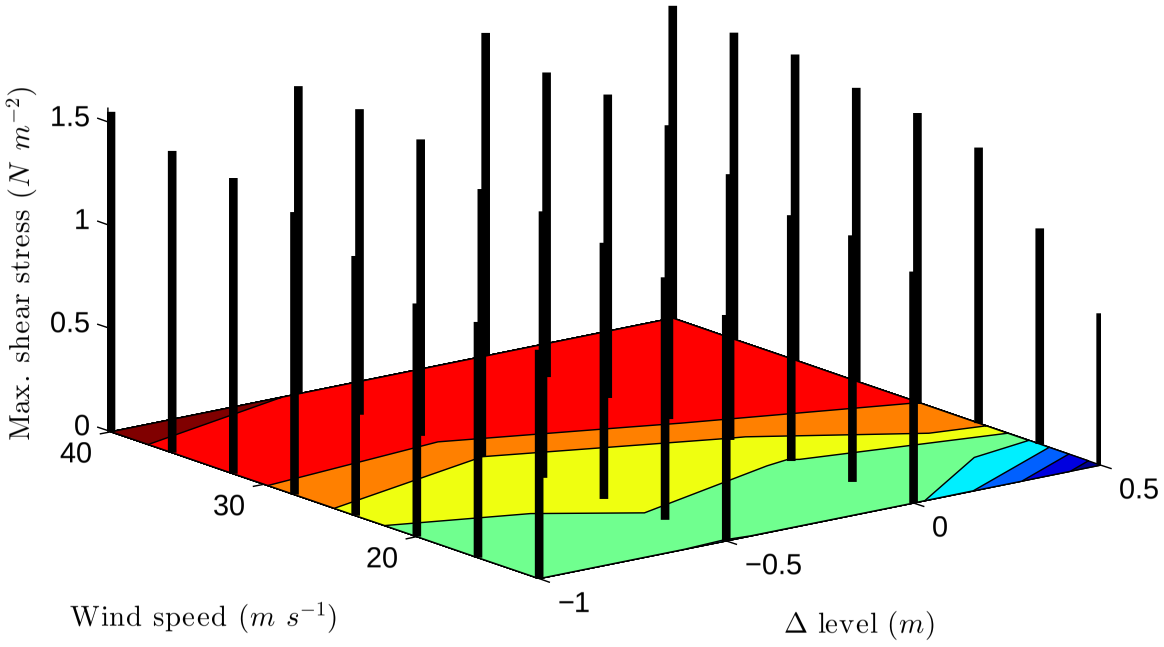

Figure 5.41: Maximum wind-wave bottom stresses for wind velocity and water surface level scenarios. Wind direction of 210 ^{o} (southwesterly wind).

Observing Figure 5.42, it is clear that the BAR grows linearly for W_s between to 12 and 40 $m\ s^{-1}$ under each water surface level scenario, except for $\Delta level = -1\ m$ where the growth start from 16 $m\ s^{-1}$. The linear behaviour means that the rate at which

BAR increases is proportional to the incremental change in W_s. This relationship might serve to obtain approximate values of BAR by interpolating for W_s within the range studied.

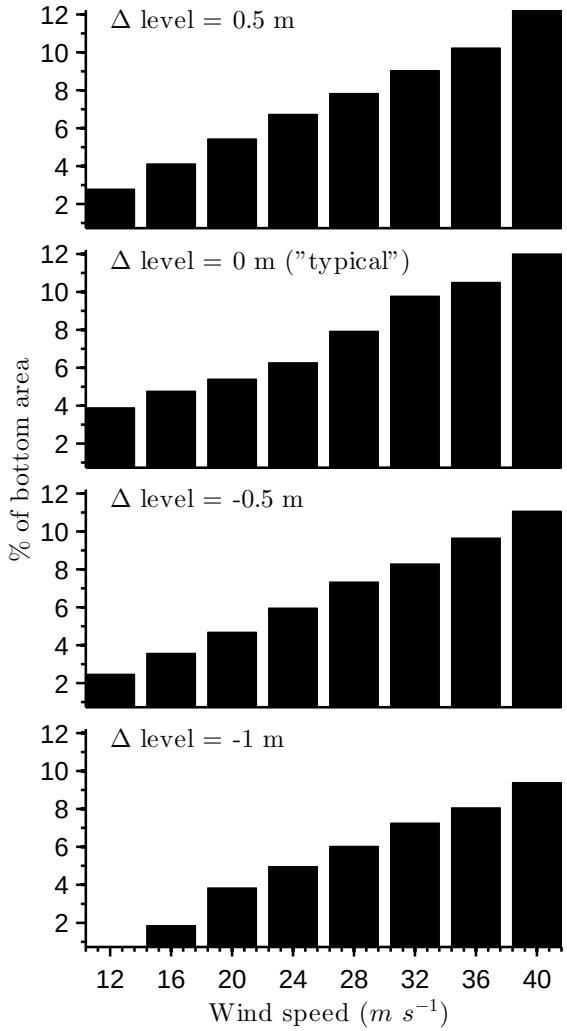

Figure 5.42: % of bottom area resuspended (BAR) by wind-wave bottom stresses versus wind speed for different water surface levels. Wind direction of 210 ^{o}.

A spatial analysis of the change in BAR with increasing wind speed (see Figure 5.43) shows that small areas along the north, northeast and east shores of the lake are always resuspended for any wind speed $> 12\ m\ s^{-1}$. As wind speed increases, BAR extends slowly from the northeast toward the southwest, ending as a broader band along the shore. Towards the southwest of the easterly bay and at the windward side of the

westerly headland, BAR starts to grow at $W_s = 24\ m\ s^{-1}$. Small central bottom sectors in the south can be also resuspended when $W_s \geq 36\ m\ s^{-1}$.

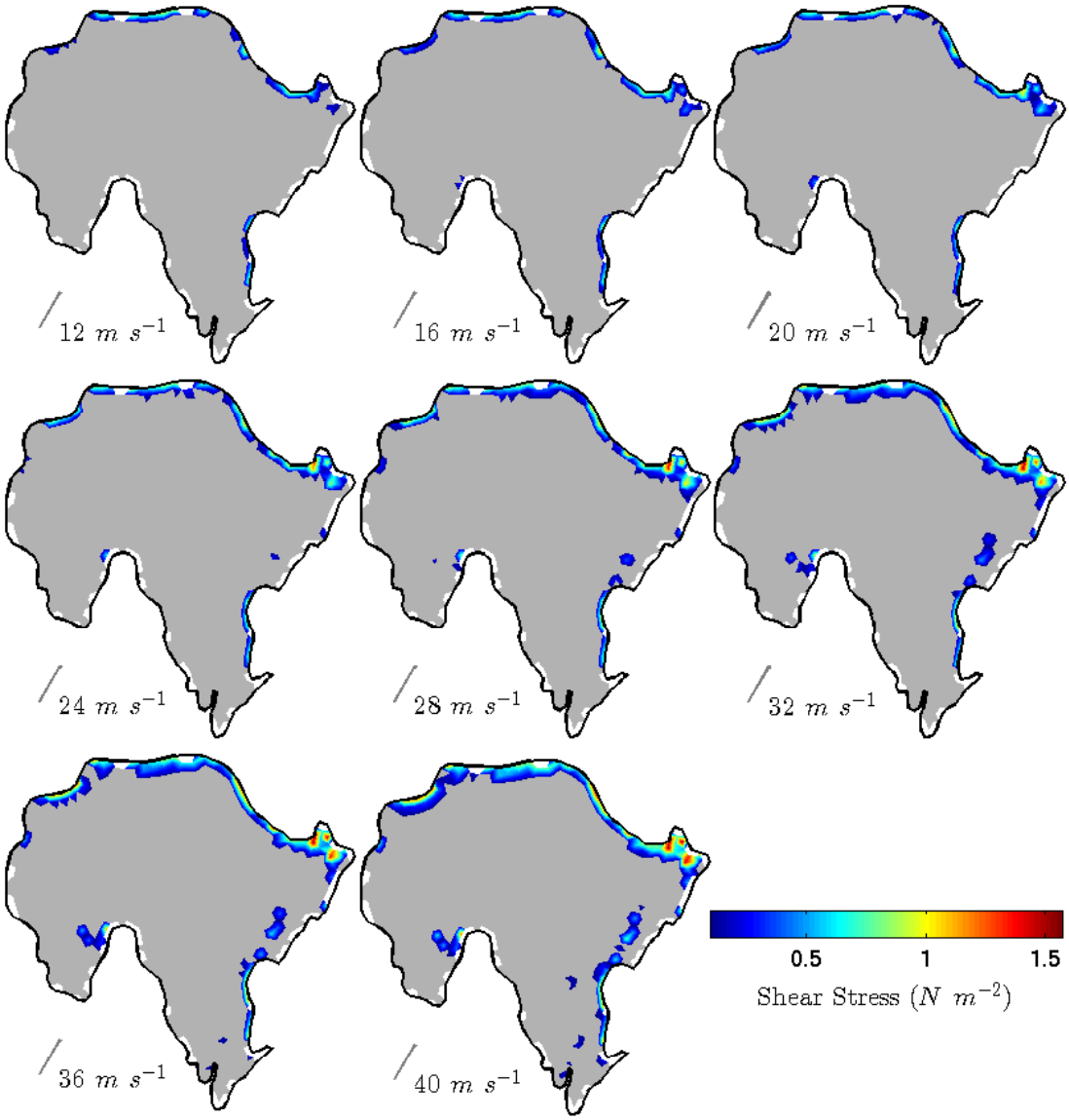

Figure 5.43: Wind-wave bottom stresses for wind speed scenarios, $\Delta level = 0\ m$ and constant wind direction of 210 ^{o} (Southwesterly wind). Grey shaded areas correspond to bottom stresses $< \tau_{cri}$.

5.6.3 Current-induced bottom stress

The bottom shear stresses produced by currents (τ_c) were computed using *FVCOM* in steady-state mode, for each of the wind direction and wind velocity scenarios, and the water surface level scenarios. *FVCOM* was run at variable time steps to guarantee numerical stability under higher wind speeds.

Wind direction and water surface level scenarios

The analysis of maximum τ_c (see Figure 5.44) for different wind direction scenarios at different water surface levels shows that the highest maximum τ_c is equal to 0.05 $N\ m^{-2}$ and occurs when $W_d = 90^o$ and $\Delta level = 0.5\ m$. Integrating the maximum τ_c for each wind direction in Figure 5.44 yields that the highest proportion of maximum τ_c occurs when $W_d = 90^o$. On the other hand, integrating Figure 5.44 for each water level shows that the proportion of maximum τ_c is slightly higher for $\Delta level = 0.5\ m$.

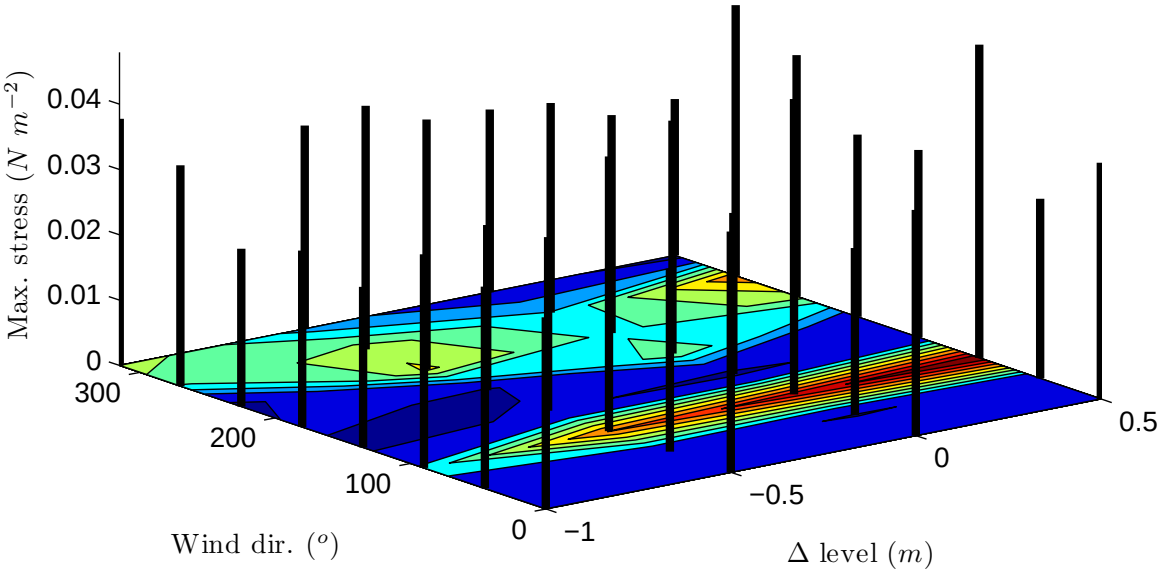

Figure 5.44: Maximum current-induced bottom stresses for wind direction and water surface level scenarios. Constant wind speed of 12 $m\ s^{-1}$.

Interestingly, the τ_c computed for the wind direction and water level scenarios does not exceed the τ_{cri}. Thus, no resuspension of bottom sediment by currents is predicted for any combination of wind direction and water surface level when wind speed is $\leq$

12 $m\ s^{-1}$. That said, the spatial distribution of the τ_c for the wind direction scenarios (see Figure 5.45) shows that τ_c is usually higher at the downwind end of the fetch, where the return flow over the lake bottom reaches its maximum magnitude. However, for some wind direction scenarios such as $W_d = 0^o$ (see Figure 5.46), some mid-fetch locations are affected by high τ_c, because the bottom currents are strongly influenced by the bathymetry. In the particular case of $W_d = 0^o$, those intermediate sectors are located at the transition between the deeper central basin and the shallower water of the southeastern shelf. This bathymetric transition zone dissipates part of the energy of the bottom currents. On the other hand, variation of the water surface level has little effect on the spatial distribution of τ_c, but does affect its magnitude and the extent of the bottom area affected.

Wind speed and water surface level scenarios

The computations of τ_c for wind speed scenarios show that the maximum τ_c increases linearly for each $\Delta level$ as the wind speed increases (see Figure 5.47). For $\Delta level = 0\ m$ the growth of the maximum τ_c is much more accentuated. By integrating the maximun τ_c along each $\Delta level$ in Figure 5.47, it is observed that the greatest proportion of maximum τ_c will occur for $\Delta level = 0\ m$. This result is similar to that already obtained in the previous section.

The % BAR normally grows linearly from $W_s = 24\ m\ s^{-1}$ (BAR $< 10\%$) to $W_s = 40\ m\ s^{-1}$ (where the BAR is $> 60\%$; see Figure 5.48) for all $\Delta levels$. Although the tendency is similar for all $\Delta levels$, the magnitude of % of BAR for each wind speed is different and grows in proportion to the increment in water surface level as more extensive shallow areas are flooded. In all cases, no resuspension of sediments due to currents is predicted below $W_s = 24\ m\ s^{-1}$, except for $\Delta level = 0\ m$ where a small portion of the area (2%) is resuspended when $W_s = 20\ m\ s^{-1}$.

The spatial distribution of BAR (see Figure 5.49) shows that bottom areas on the north and in the northeast of the lake are always affected by $W_s \geq 20\ m\ s^{-1}$. These areas are characterised by strong surface currents that lead to the formation of strong near-bed return flows that generate high τ_c values. On the other hand, as wind speed grows, the BAR begins to expand from the northern and northeastern sectors toward the soutwestern part of the lake. The expansion is not restricted to this direction, since BAR simultaneously increases in shallower places along the western and southern margins where τ_c is relatively low. It is clear that a large area immediately southeast

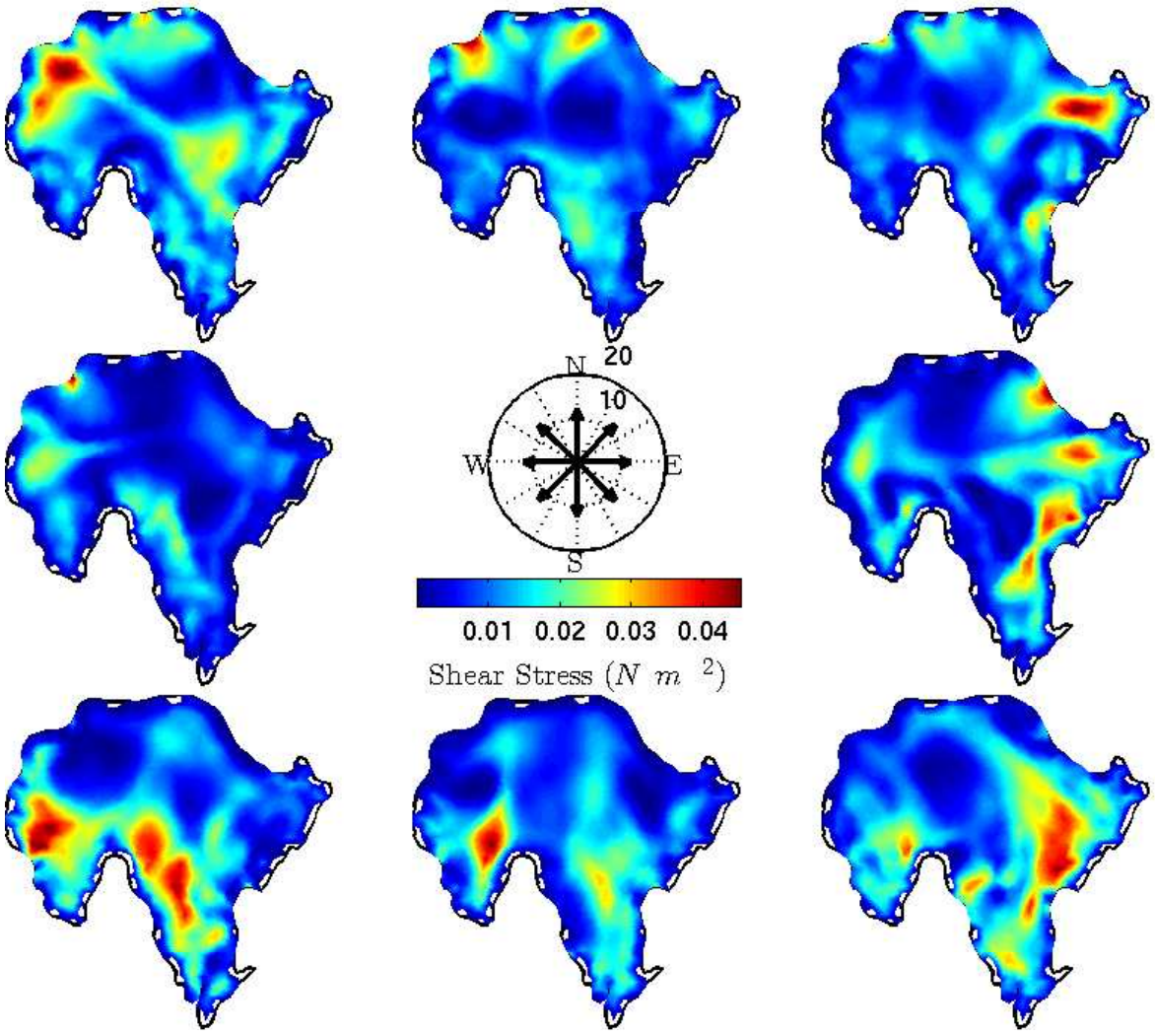

Figure 5.45: Current-induced bottom stresses for different wind directions at $\Delta level = 0\ m$ using a constant wind speed of 12 $m\ s^{-1}$. Arrows in the wind rose indicate wind direction.

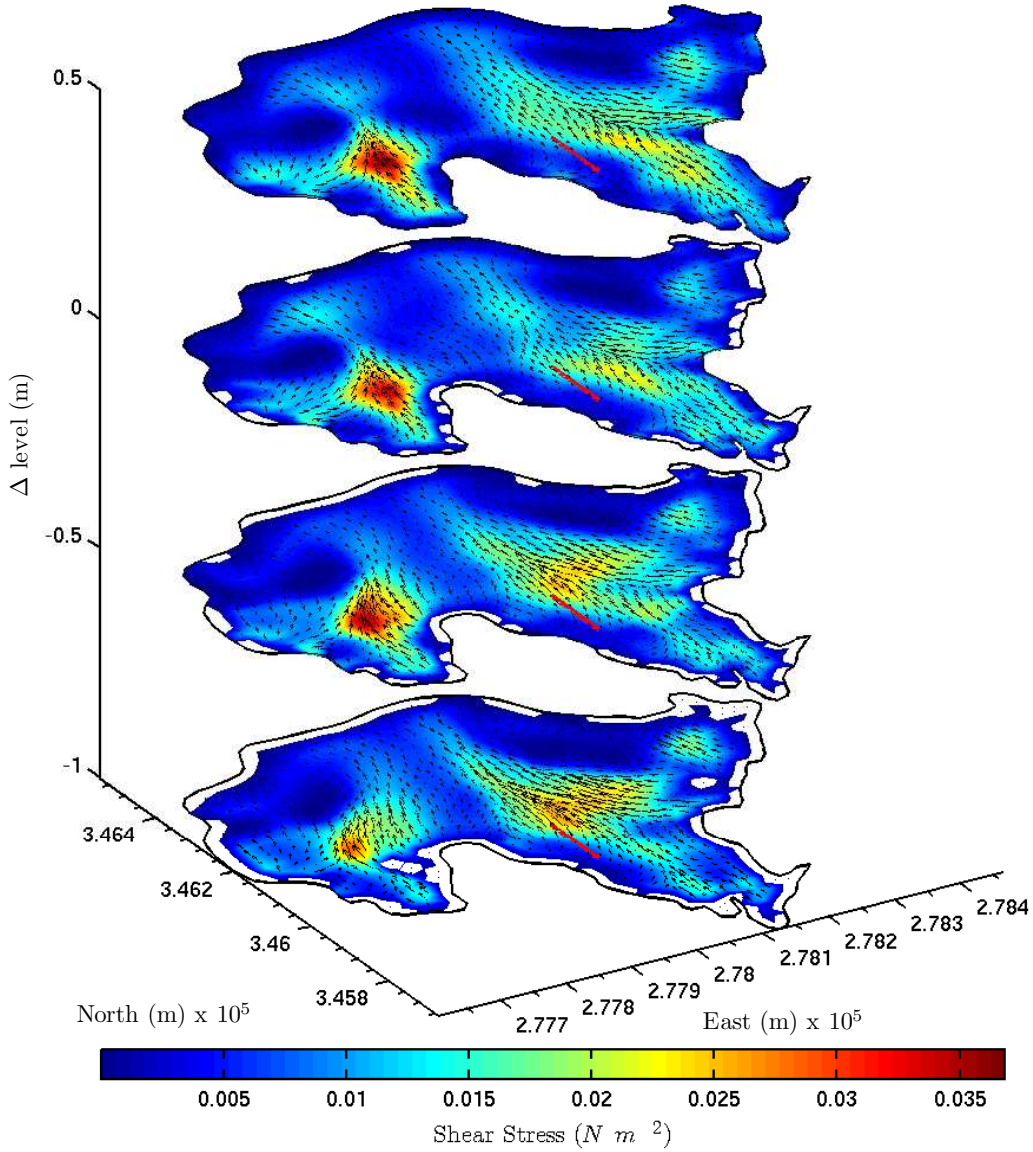

Figure 5.46: Flow current bottom stresses for $w_d = 0^o$ at different water surface level scenarios. Constant wind speed of 12 $m\ s^{-1}$.

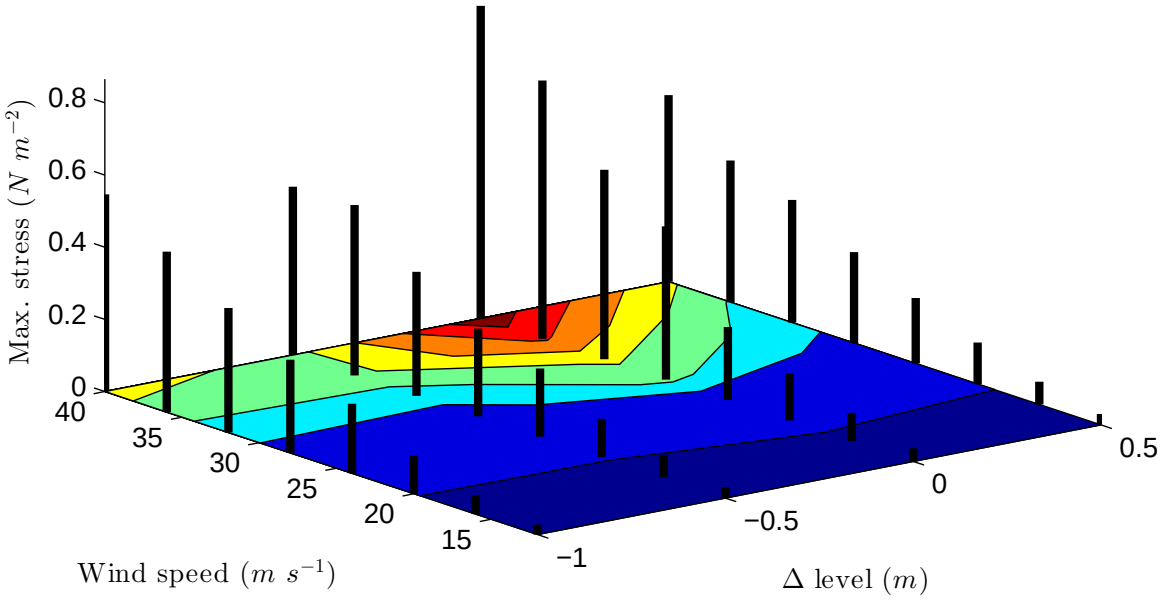

Figure 5.47: Maximum current-induced bottom stresses for wind speed and water surface level scenarios. Wind direction of 210^o.

of the lake centre is always unaffected by flow currents even, when wind speed reaches 40 $m\ s^{-1}$.

As mentioned above, the % of BAR grows as the water level rises. Figure 5.50 shows that as the water surface level increases new areas, especially along the shores, are flooded. These are zones where resuspension of sediment is likely. But the increments of the water surface level are not the only factor that influence the variation of the BAR. In particular, the lake hydrodynamics are also affected and thus the configuration of bottom currents, which changes the magnitude and distribution of τ_c. Comparing how BAR changes as water surface level increases for two different wind speeds (Figures 5.50a and 5.50b) it is evident that BAR grows more rapidly for $W_s = 40\ m\ s^{-1}$ than for $W_s = 24\ m\ s^{-1}$ where also, the growth is always around the same bottom sectors. For both wind speed scenarios it is also observed that northern and northeastern parts of the lake always experience current-induced bed stresses that are high enough to resuspend sediments, irrespective of the water level.

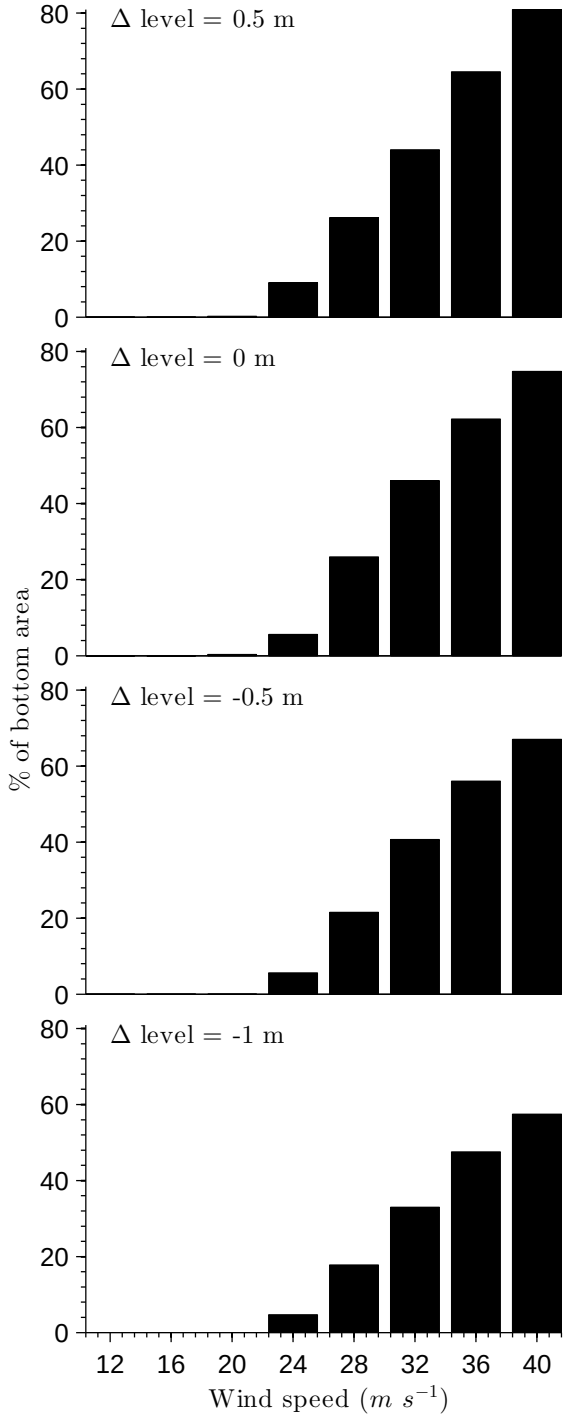

Figure 5.48: % of bottom area resuspended (BAR) by current-induced bottom stress versus wind speed and for different water surface levels. Constant wind direction of 210 ^{o}.

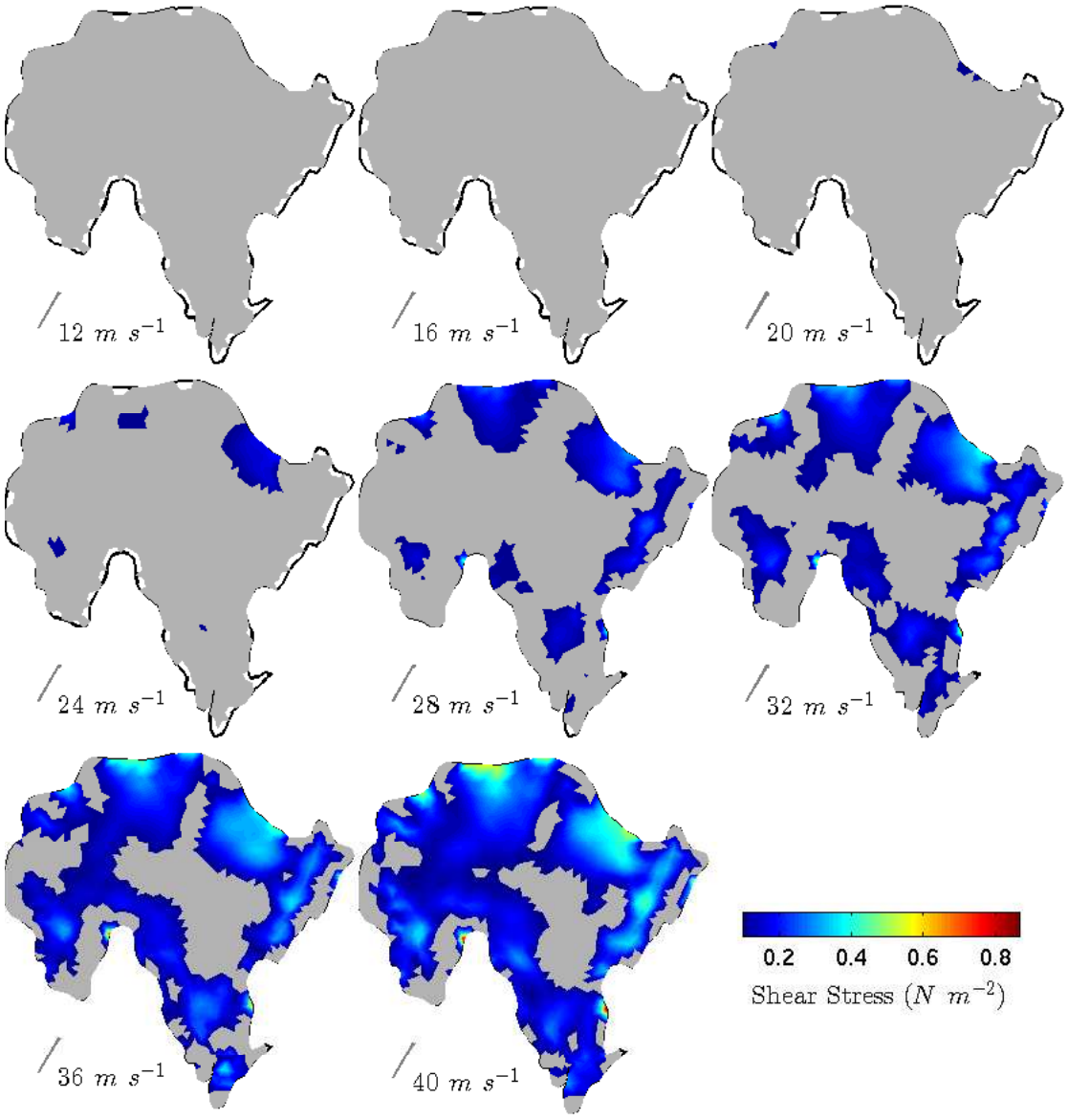

Figure 5.49: Current-induced bottom stresses for different wind speeds at $\Delta level = 0$ m using a constant wind direction of 210 ^{o} (southwesterly wind). Grey shaded areas correspond to bottom stresses $< \tau_{cri}$.

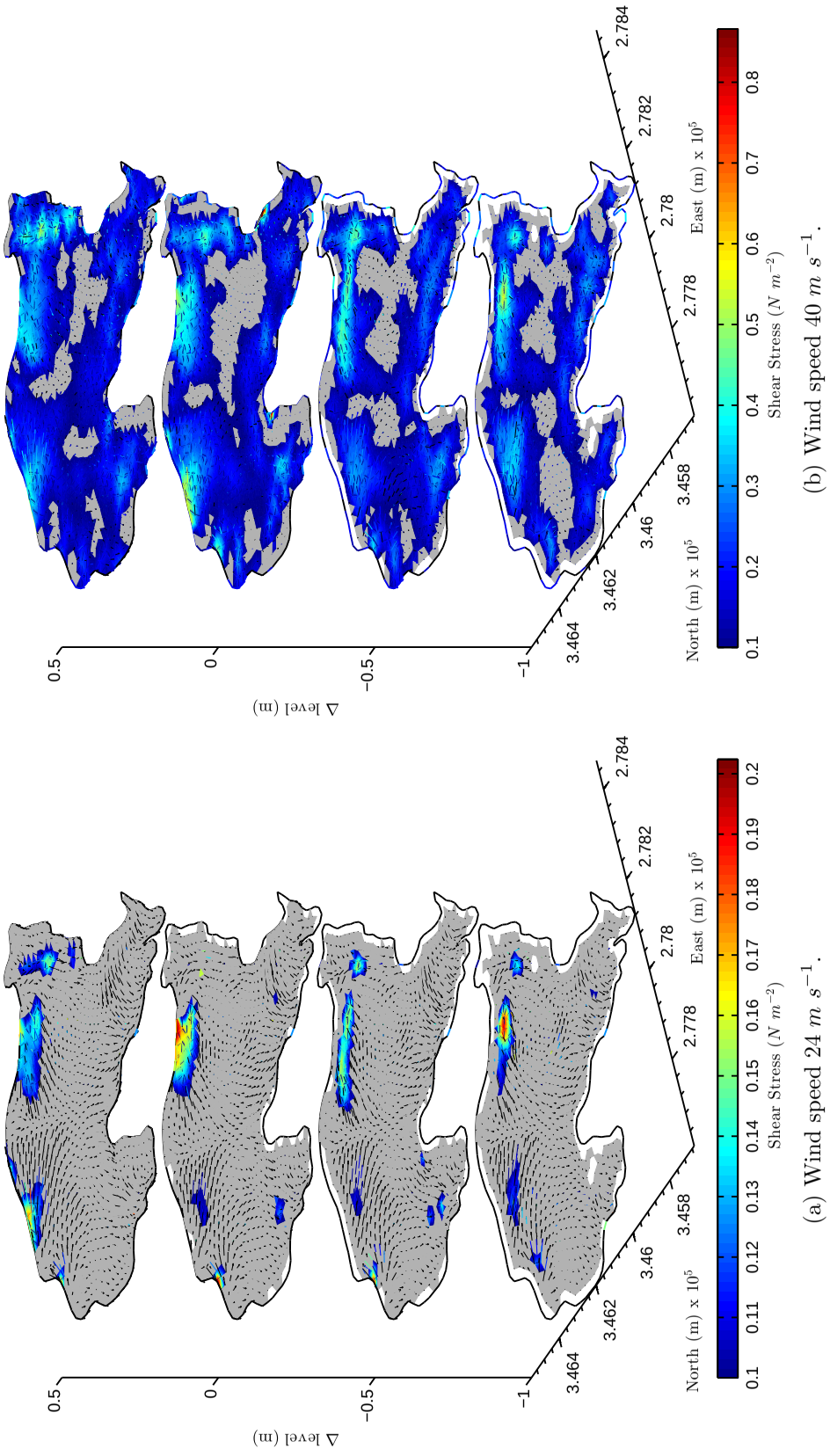

(a) Wind speed 24 $m\ s^{-1}$.

(b) Wind speed 40 $m\ s^{-1}$.

Figure 5.50: Current-induced bottom stresses for wind speed and water surface level scenarios. Wind direction of 210 ^{o} (southwesterly wind). Grey shaded areas correspond to bottom stresses $< \tau_{cri}$.

The analysis of τ_w and τ_c for the wind speed, wind direction and water level scenarios provide some potentially important insights into how wind forcing drives complex hydrodynamic processes that, in turn, control the dynamics of sediment accumulation. The results clearly have implications for the validity of the sediment focusing theory as a basis for predicting the location of the deepest and most complete sediment sequences. In Llyn Conwy, the comparison of τ_w and τ_c clearly indicates the dominance of τ_w over τ_c for much of the lake area. Comparing the maximum τ_w (Figure 5.41) and the maximum τ_c (See Figure 5.47) for the wind direction and water level scenarios, it is seen that τ_w is on average 15 times greater than τ_c. This is consistent with comparisons carried out by Chao *et al.*, 2008, who found that τ_w is about ten times greater than τ_c for a wind speed of 10 $m\ s^{-1}$ in a oxbow lake. Similarly, studies of sediment resuspension made by Luettich Jr *et al.*, 1990 in a shallow lake found that τ_w is more than ten times greater than τ_c.

In general, the relative importance of these two bottom stress components will vary depending of the magnitude of the wind speed. Low wind speeds will likely cause slow growth of τ_c and therefore a ratio of τ_w/τ_c greater than 15. But when the wind speed is high, τ_c grows more rapidly than τ_w and the ratio decreases closer to 1. This ratio is also affected by how the shallower areas are distributed around the lake. Thus, a large expanse of shallow water downwind will increase the probability of the occurrence of higher τ_w over such areas.

The analyses of maximum τ_w and τ_c computed for wind speed and water surface level scenarios, indicate that for both the most extensive areas of high bottom stress occur for $\Delta level = 0\ m$. This contradicts the intuitive thinking that, as water level decreases the bottom becomes exposed to wind-waves and currents, so stronger stresses will be exerted. However, the scenario-based analysis demonstrates that for water levels under $\Delta level = 0\ m$ much of the potentially resuspended bottom areas become dry, and the reduction of water depth dampens the wind-wave and current-induced stresses.

The analyses of τ_w and τ_c versus wind speed scenarios lead to the identification of certain bottom areas in the north, northeast and east of the lake (see Figures 5.43 and 5.49), within which bottom sediments are likely to be regularly resuspended under a wide range of wind speeds. The distributions of those areas affected by τ_w are strongly determined by the fetch growth and are preferentially located downwind along parts of the shore where the wind-wave energy is greater. In contrast, those bottom areas

affected by high values of τ_c are more complex to predict since they depend on the three dimensional behaviour of flow.

5.7 Combined Current and Wave Bottom Stresses for a Winter Month

The analysis of bottom stress distributions arising under a range of hypothetical wind forcing and water surface level scenarios provides an idea of which areas of the lake are susceptible to sediment resuspension by waves and currents. All these scenarios were computed for steady-state forcing conditions, however, it is important to also investigate the evolution of the bed stress field under unsteady wind forcing conditions. Accordingly, this section presents an unsteady analysis of the bottom stresses in Llyn Conwy for the month of December 1997. As shown in Figure 5.51, this month was characterized by a high mean wind speed (13.4 $m\ s^{-1}$) and, in fact, the highest wind speed between August 1993 and August 2011 occurred in this month (see also Figure 5.31). December 1997 was also characterised by high wind direction variability (Figure 5.51 (a)), such that a wide range of bottom stress distributions can be expected. As before, computation of wind-wave bottom stresses (τ_w) and current bottom stresses (τ_c) was made using *UCL-SWM* and *FVCOM* respectively.

Bottom stress time series computed at different points distributed around the lake all show a strong correlation with the wind speed (see Figure 5.52). Wind speed is better correlated with τ_w ($r \approx 0.75$) for the inshore points (Points 1, 2, 4, and 6) than with τ_c ($r \approx 0.67$), since the former depends almost linearly on the wind forcing data, which are explicitely given in the equations resolved in *UCL-SWM*. The latter are affected by the non-linear behaviour of the lake circulation. Analysing the bottom stresses in the inshore points 1, 2 and 4, it is found that τ_c are low relative to τ_w since bottom currents are sustantially dampened in shallow places, in contrast with wind-waves, which increase in energy on approaching the shore. In the inshore point 6 τ_w is low relative to τ_c, since the short fetch at this point impedes the formation of bigger waves. At offshore points (Points 3 and 5) bottom stresses are only due to currents since τ_w are rarely induced at these sectors. Data for point 3, in particular, demonstrate that the deepest sector of the lake is stronger affected by currents for $W_s > 30\ m\ s^{-1}$. At all the near shore locations (i.e. wave sensor sites), bottom stresses are dominated by τ_w since flow currents are relatively weak.

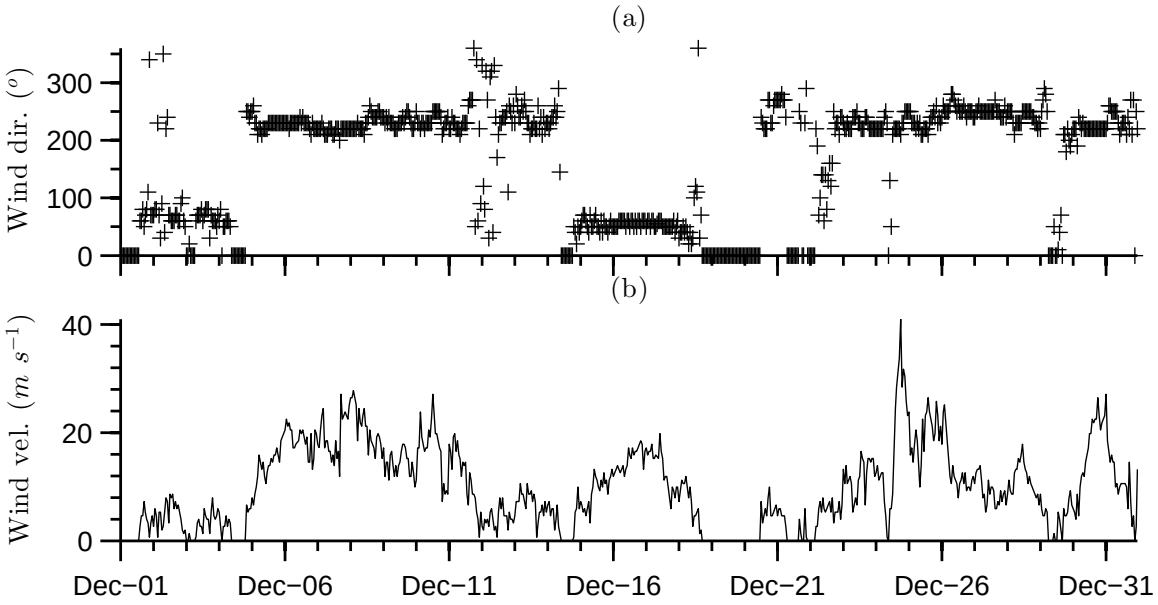

Figure 5.51: Hourly wind direction (a) and wind speed (c) from 01 to 31 of December 1997.

The weighted-area spatial average of τ_w and τ_c (see Figure 5.53) provides a more general idea of how bottom stresses vary through time in response to sequential forcing events. The spatial average stress series also exhibit a high correlation ($r = 0.88$) between wind speed and τ_t. The biggest contribution to that correlation is made by τ_w, which has a $r = 0.96$ with wind speed, whereas $r = 0.81$ for the relationship between wind speed and τ_c. It is observed that 2.3% of the time τ_t exceeds τ_{cri}, which means that sediment resuspension would likely have occurred during these extremely high wind forcing conditions. During such sediment resuspension events, τ_c would contribute 18% of the time whereas the combinations of both type of stresses would contribute 82% of the time, showing that sediment resuspension is mainly due to currents. The contribution of wind-waves to sediment resuspension may thus be restricted to very shallow areas, in contrast with bottom currents where resuspension would come also from medium and deeper sectors too.

An indication of the proportion of the lake bed affected by sediment resuspension during December 1997 is given by Figure 5.54. This analysis shows that, on average during the whole month, 4.4% of the bottom area is resuspended by τ_t, 2.8% by τ_w and 1.6% by τ_c. It is notable that about 10% of the lake bottom is eroded continuously by

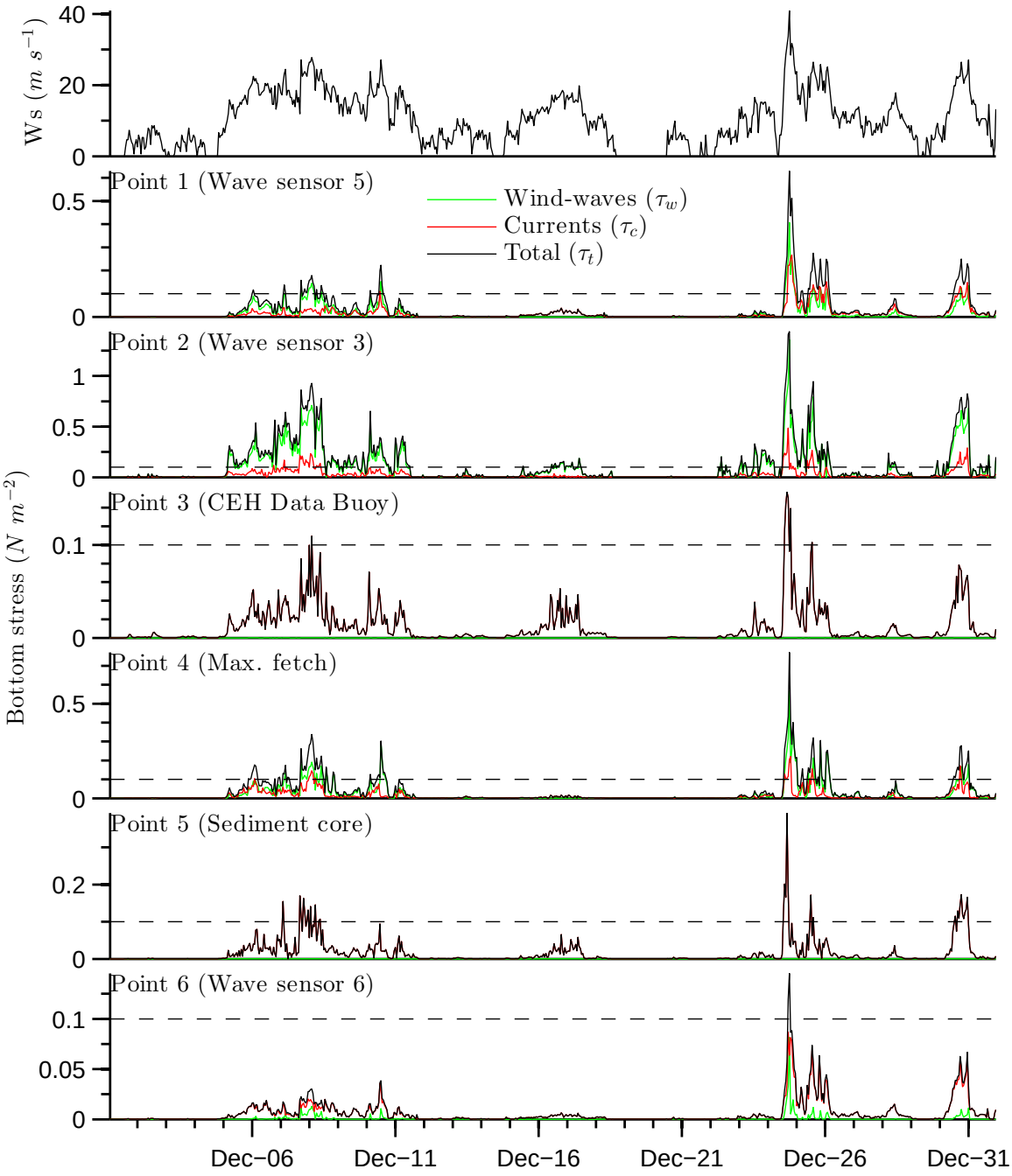

Figure 5.52: Wind-wave, current-induced and total bottom stresses between 01 and 31 of December 1997 at different points in Llyn Conwy. See Figure 5.55 for the location of points. Horizontal broken line represents estimated τ_{cri}. Note different scales on vertical axes.

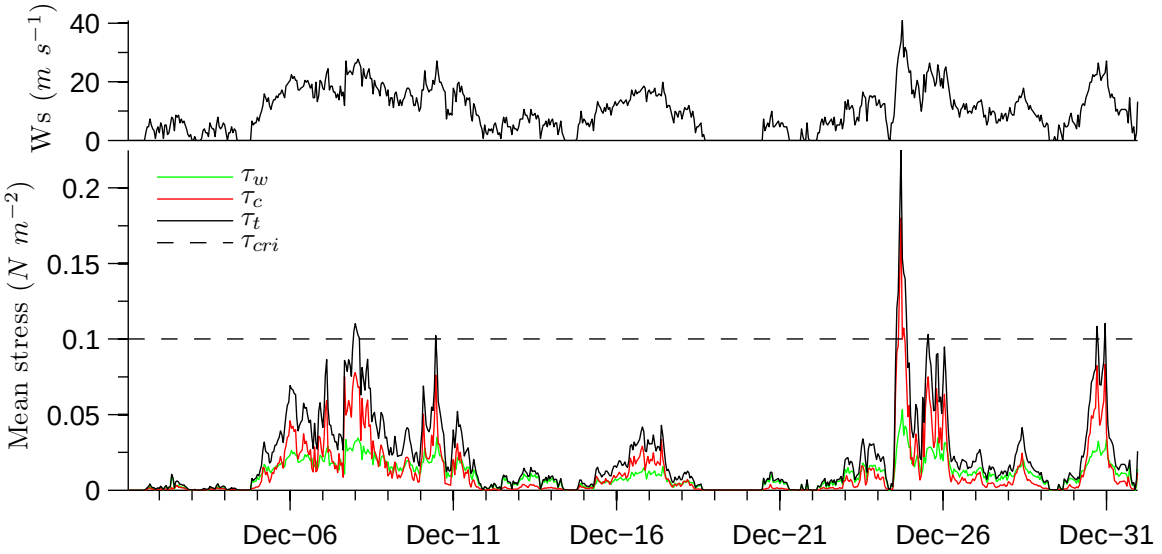

Figure 5.53: Weighted-area spatial average of wind-wave, current-induced and total bottom stresses between 01 and 31 of December 1997.

τ_w between the 5 and 13 of December, whereas the % of bottom area resuspended by τ_c in the same period is affected only intermittently for short periods (but with more intensity). During the maximum wind speed event (around 25 of December) about 83% of the lake bottom is resuspended, where τ_c contributes with 95% and τ_w with 5% of this area.

A spatial analysis of bottom areas resuspended (BAR) (see Figure 5.55) shows that, of the 4.4% of BAR by τ_t, nearly 95% is located along the northerly, northeasterly and easterly shores, and the 5% remaining corresponds to isolated areas on the southern margin of the lake. This distribution coincides broadly with the steady state south-westerly wind direction and multiple wind speed scenarios analysed in the previous section. Here and in the scenario results, the resuspension zones were mainly determined by the action of wind-waves whose maximum energy was expected along the northeasterly shore. However, for higher wind speeds ($> 20\ m\ s^{-1}$) current bottom stresses contribute significantly to sediment resuspension in most diverse areas. Currents might also play a role in the transport of resuspended sediments away from these areas towards the southerly and westerly areas, where deposition might be favoured.

An analysis of the temporal variation of % of BAR at different water depth ranges (Figure 5.56) shows that only at the shallower depth range at least a sector of the

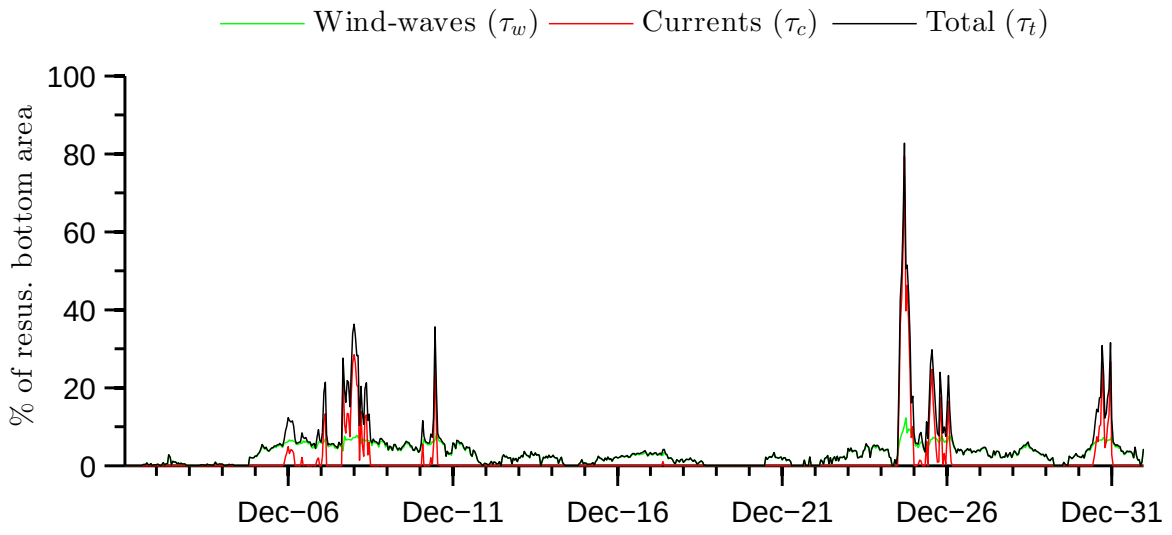

Figure 5.54: % of bottom area resuspended by wind-wave, current-induced and total bottom stresses between 01 and 31 of December 1997.

lake is resuspended at every hour during the whole month due mainly to the action of τ_w. As the depth increase resuspension events are limited to extreme wind forcing conditions and only due to the action of τ_c. Averaging the % of BAR along the time at different water depth ranges (Figure 5.57), only those % BAR due to τ_w have a fairly consistent tendency to decrease with depth, but only from 0 to 6.6 m. The behaviour of the % of BAR due to τ_c does not decrease with depth but instead has a gaussian distribution where the maximun is in the intermediate depth-range of 6.61-8.81 m. This behaviour mean that the flow circulation is stronger at the depth-range of 6.6-8.8 m, so the transportation of sediments eroded at shallower areas mainly by wind-waves is likely to be more intensive at these depths. Such a strong circulation is observed in Figure 5.14 along the depth-range of 6.6-8.8 m, where a vertical circulation in the upper half of the section yields a maximun velocity at this range. The % of BAR due to τ_t decrease consistently from the shallower areas where the contribution is mostly made by τ_w to the deepest sectors where the contributions is only made by τ_c. The behaviour of % of BAR at deepest areas indicates that despite the depth, sediment deposits could be eroded by currents.

The Håkanson, 1984 approach to classifying the lake bottom, which divides it into erosion, transport and accumulation zones based on water depth and fetch, shows that

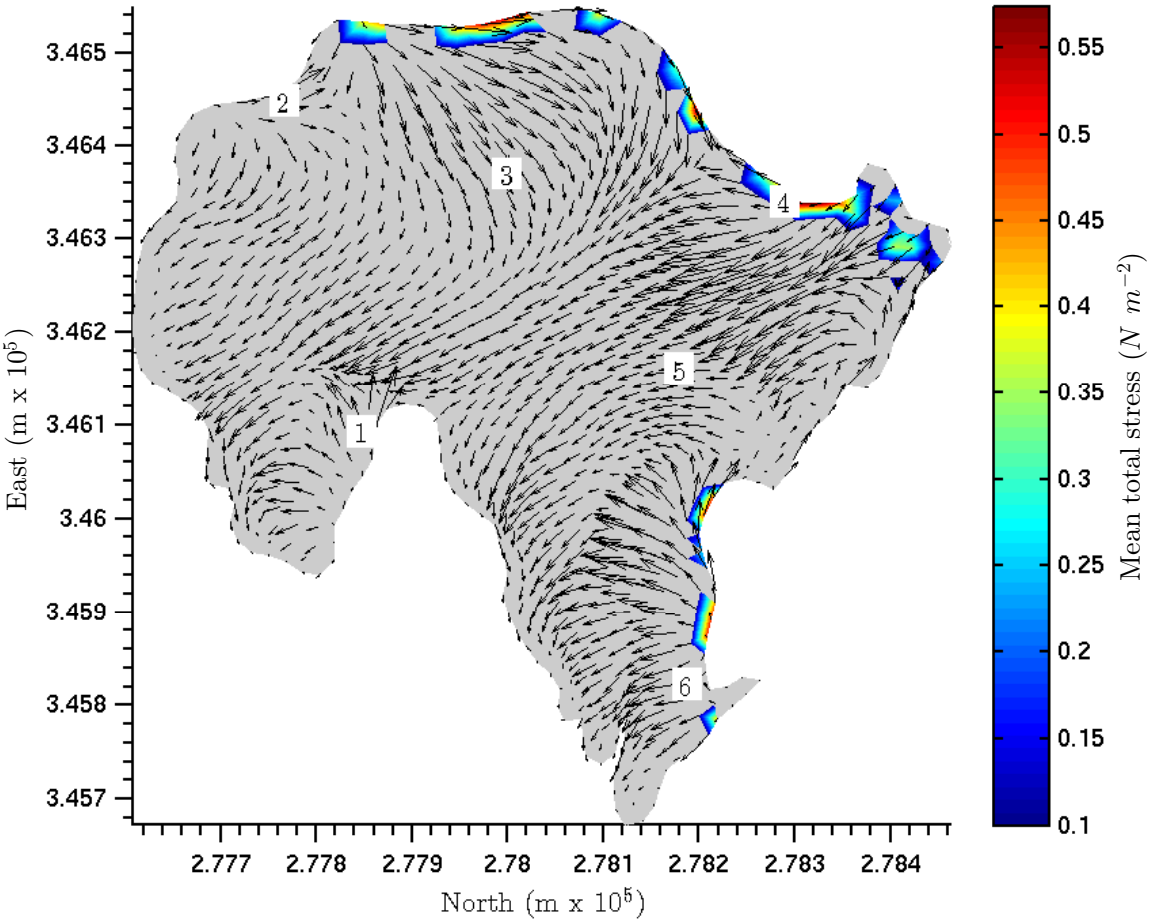

Figure 5.55: Average of the total bottom stresses during December 1997. Grey shaded areas correspond to bottom stresses $< \tau_{cri}$. Numbered squares correspond to location of the time-series plotted in Figure 5.52. The vectors indicate the mean velocity field at the bottom.

the erosion zone will generally grow as function of fetch and will cover the bottom areas above 20 m depth. In contrast, the transportation zones will be those areas below the erosion zone but not deeper than about 40 m depth and the accumulation areas will correspond to areas below 40 m. This classification serves as a starting point for identifying the spatial extent of the sediment remobilization. An approximate sub-division of these zones in Llyn Conwy based on Figure 5.57 indicates that the erosion zones would be constituted by those shallow areas between 0 and 5 m affected mostly by wind-waves, transportation sectors would correspond to those located between 5 to 15

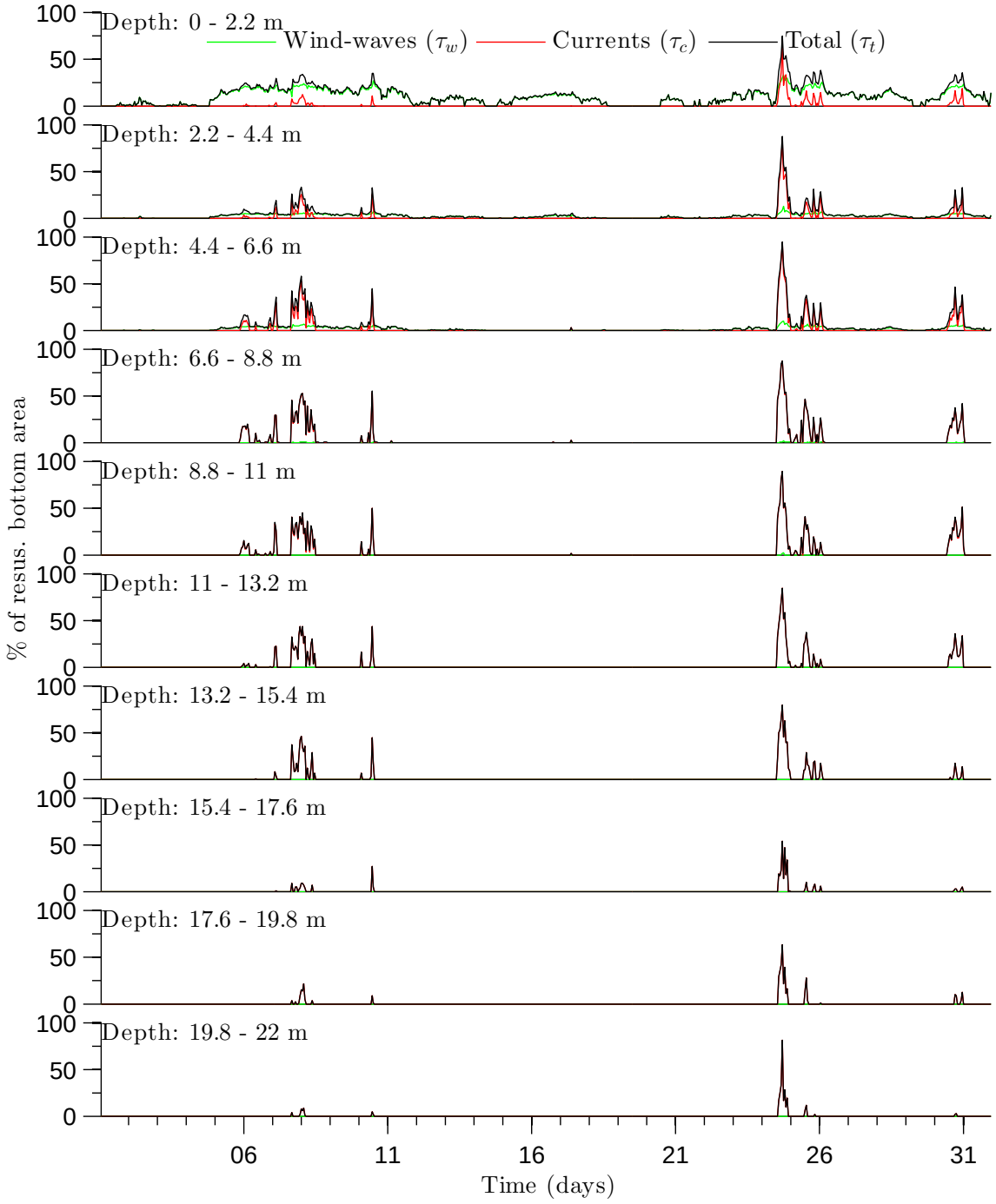

Figure 5.56: Temporal variation of resuspended bottom areas (%) at different water depth ranges due to different bottom stress contributions.

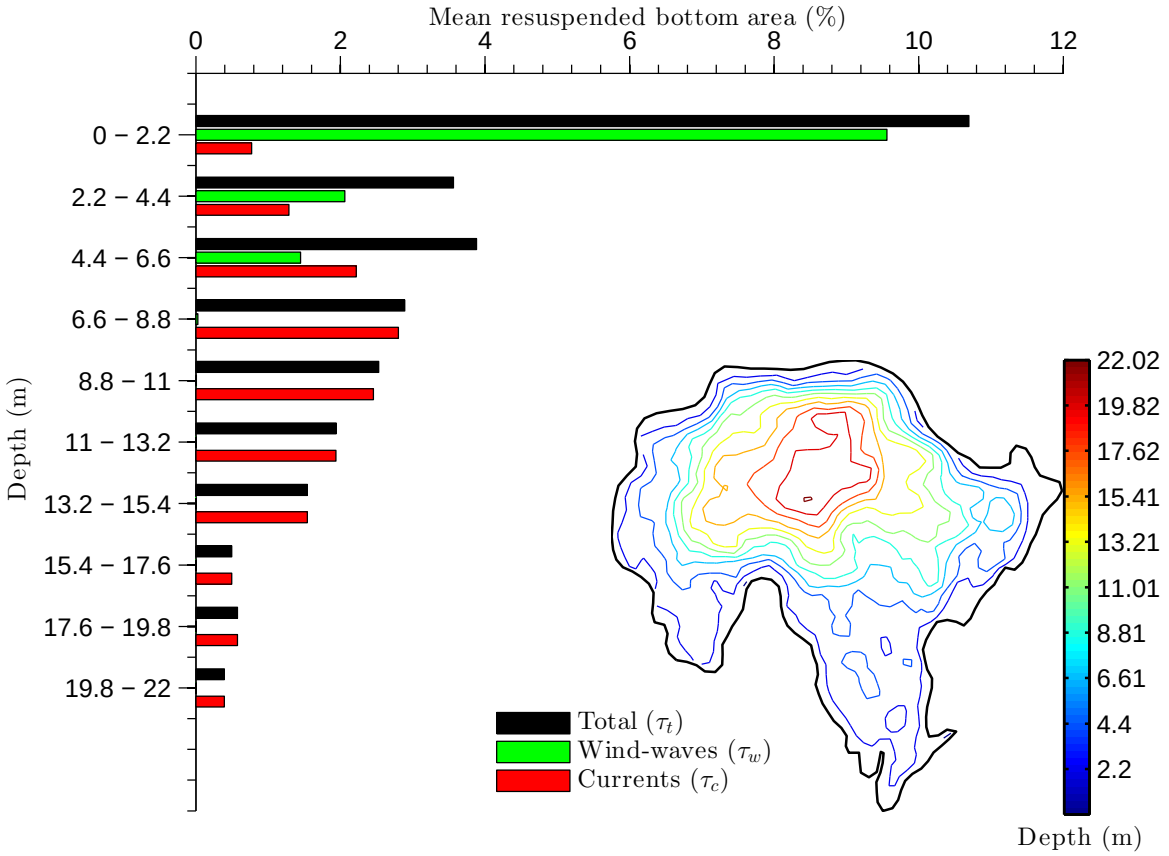

Figure 5.57: Temporal and spatial average of resuspended bottom areas (%) at different water depth ranges due to different bottom stress contributions. Llyn Conwy bathymetry map shows extent of water depth ranges.

and deposition would occur over the sectors below 15 m depth. However, the nonlinearity of the hydrodynamic processes demonstrated in this chapter and the complex time-variation in meteorological forcing make such prediction more difficult in practice. Analysing, for example the % of BAR below 15.4 m where, according to hypothetical zone division deposition of sediments is supposed to occur, intermittent resuspension due to currents is also predicted. The next chapter investigates the spatial and temporal variation in the extent of these three sediment transport zones, and the implications for the applicability of the sediment focusing theory in more detail.

Chapter 6

Analysis and Modelling of Lake Sedimentation

Resume

This chapter examines the dynamics of sedimentation in Llyn Conwy, with reference to sedimentological analysis of its bottom sediments and modelling of sedimentary processes using FVCOM *coupled with the* UCL-SWM *wind wave model. Ekman grab samples of bed material are analysed to determine the spatial extent of sediment accumulation and the physical properties of the deposits. Suspended sediment settling characteristics are inferred from determinations of particle size and density. Results from dated sediment cores provide insight in historical sediment accumulation rates at two locations within the lake. The dynamics of sediment movement are modelled using hydrodynamics forced by meteorological data for a one-month period dominated by very strong southwesterly winds in an effort to understand the potential for current- and wave-generated bed stresses to influence the spatial extent of erosion and deposition. Modelling results are compared with both the spatial variation in bed composition and historical variation in sedimentation, and then used to inform an evaluation of the relative importance of sediment focusing processes in Llyn Conwy.*

6.1 Introduction

The resuspension, transport and deposition of sediments in lakes is complex and requires significant physical and human resources to investigate empirically over timescales

long enough to capture the full range of environmental conditions. This is especially true of upland lakes, where sedimentation may be controlled by wind forcing that is inherently intermittent, and where extreme conditions with long recurrence intervals may be important in mediating the location, thickness and completeness of bottom sediment sequences. Various early empirical studies attempted to infer the dynamics of sediment resuspension based on data obtained from arrays of sediment traps combined with simultaneous wind data (e.g. Kristensen *et al.*, 1992, Bengtsson & Hellström, 1992, Luettich Jr *et al.*, 1990). More recently, studies of large lakes have combined field measurements with computational hydrodynamic models to investigate the sensitivity of sediment dynamics to both current- and wave-generated shear stresses and the fate of resuspended material (e.g. Blom *et al.*, 1992,Jin & Ji, 2004, Lee *et al.*, 2005), and the implications of resuspension for sediment and water quality (e.g. Blom & Toet, 1993, Lee *et al.*, 2007, Jin & Ji, 2004, Chao *et al.*, 2008). To date, however, few studies have attempted to model spatial variation in sediment accumulation from the perspective of longer-term lake infilling or have attempted to test the extent to which infilling can be explained with reference to the various sediment focusing mechanisms. Accordingly, this chapter considers further the extent to which conventional sediment focusing processes can account for the occurrence of significant accumulations of lake sediment and, also, the extent to which sedimentation in the main accumulation zones of the Llyn Conwy basin can be expected to proceed continuously or else be subjected to intermittent resuspension.

The Ekman grab samples of bottom sediment obtained in the April 2011 field campaign are first used to map the extent of the sediment accumulation zones. Sediment samples are analysed for key physical properties, grainsize distribution and particle settling characteristics. These data are then used to constrain numerical sediment transport simulations carried out using the suspended sediment module of *FVCOM*. *FVCOM* is run in conjunction with the *UCL-SWM* wind wave model, driven by meteorological data for a one-month period of extreme southwesterly winds, to provide indicative insights into fine sediment dynamics under conditions of strong wind forcing. Model runs are used to identify zones of erosion and deposition and the time variation in sedimentation in relation to variation in wind speed. The preservation potential of the sediment sequence is also considered in the context at longer term accumulation rates from ^{210}Pb dated cores and with reference to the likely interval between resuspension events. Finally, the modelling results are used to evaluate the extent to which

the operation of sediment focusing processes can explain the pattern of sedimentation in Llyn Conwy.

6.2 Analysis of Lake Bottom Sediments

6.2.1 Spatial extent of lake sediment accumulation

Over the two field campaigns in 2010 and 2011, 28 deployments of an Ekman grab resulted in sample recovery from 25 locations, with 3 locations returning no sediment. In addition, five attempts were made to obtain sediment cores, of which four resulted in the recovery of at least some lake sediment, with one complete core (CONLM1). The material recovered can be divided into a number of distinct types. Lake muds comprised either poorly consolidated organic peat or a mixture of peat with clay. In a few locations, notably in the northeastern part of the basin, a sparse cover of fine pebbles of compacted peat class (mean diameter $\approx 5\ mm$) were observed overlying pre-Holocene deposits of buff clay and silt with a variable fine gravel component. Along the north shore of the lake and in part of the deepest central basin, no sediment was recovered, again implying the absence of any Holocene lake sedimentation. Figure 6.1 summarises the distribution of these sediment types. It is notable that much of the eastern half of the basin is essentially devoid of continuous lake sediment sequences, in contrast to the western basin and sheltered southern tip of the longer eastern basin. This is broadly consistent with the wave-stress acting as a mediator of bed sediment stability. However, it is also clear that deeper parts of the basin that lie well below the wave base also lack deposits of lake mud.

6.2.2 Physical properties of lake muds

The lake muds (organic peat with small fractions of silt and clay samples) and the silt and clay fraction of the pre-Holocene samples (i.e. excluding any gravel or fine peat pebble components) were subjected to further analysis to determine water content, loss on ignition (LOI) and grainsize distribution. After drying of sub-samples at 105 ^oC for 6 hours the water fraction (W_w) was computed from

$$W_w = \frac{W_t - W_s}{W_t} 100 \tag{6.1}$$

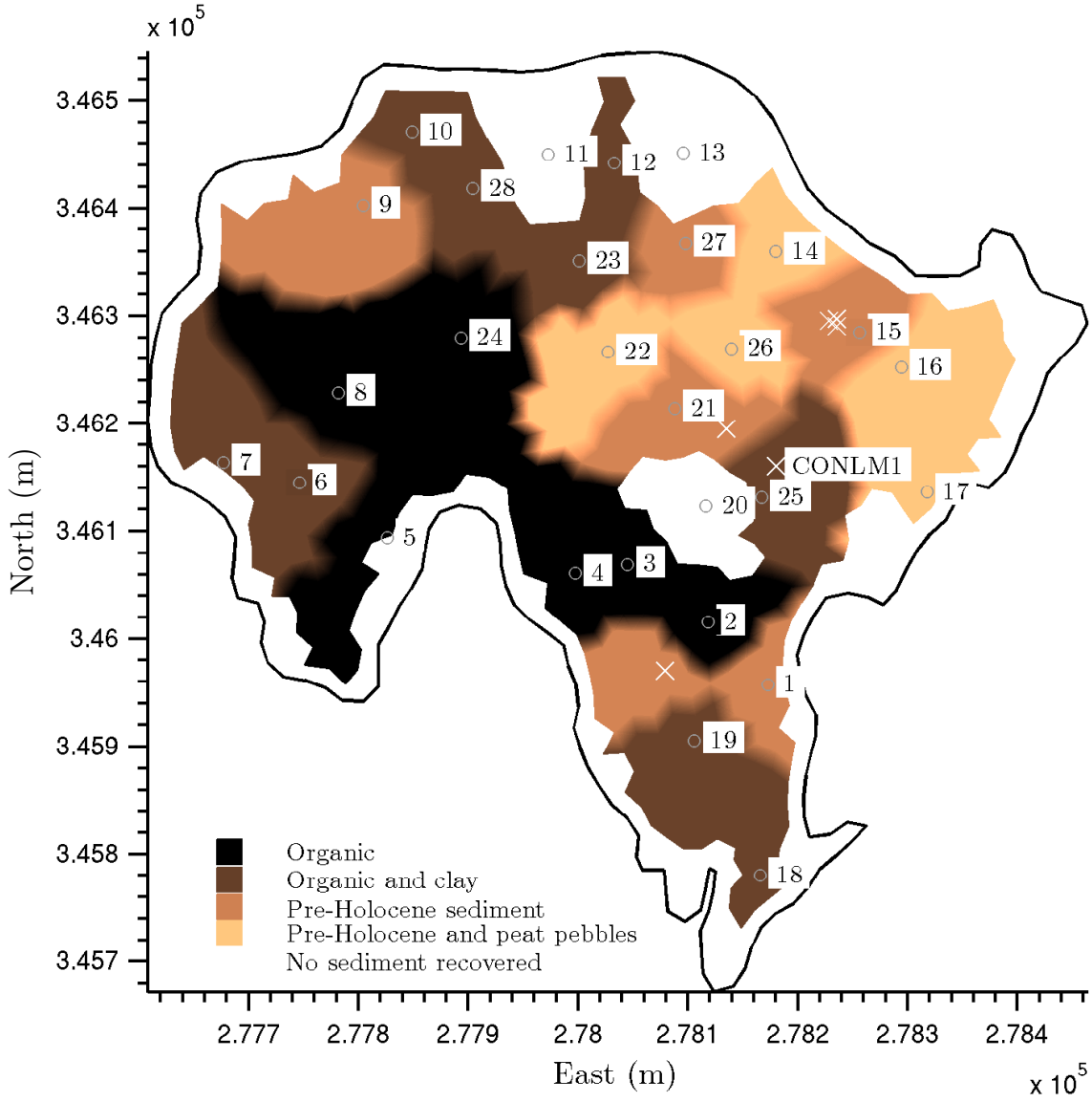

Figure 6.1: Classification of bottom sediment types based on Ekman grab and coring attempts during the two field campaigns. Numbers refer to grab samples, CONLM1 is the core location, and 'x' denotes coring attempts that yielded sediment information but no complete core.

where W_t is the total weight and W_s is the dry weight of sediments. The spatial distribution of water content in the bottom sediments (Figure 6.2) reveals two distinct zones. The first extends over western and southern areas and comprises sediments with the highest water content (> 75 %). These are generally highly organic and poorly consolidated peats, including those samples with some clay and silt component. In contrast, the second zone is distributed across parts of the northwest and eastern basin, and comprises the pre-Holocene deposits dominated by clays and silts with a lower water content (< 45 %).

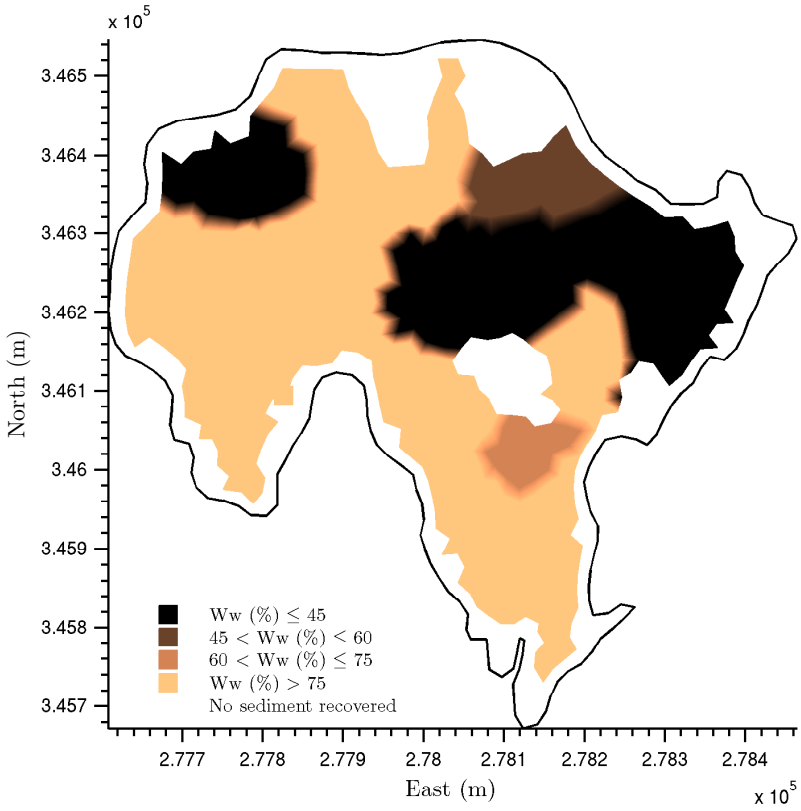

Figure 6.2: Distribution of % of water content in Llyn Conwy bottom sediments.

LOI was used as a proxy for the % of organic matter (W_{org}). Dried sub-samples were heated at 550 ^oC in a furnace for 2 hours and W_{org} computed from

$$W_{org} = \frac{W_s - W_{Norg}}{W_s} 100 \tag{6.2}$$

where W_{Norg} is the inorganic fraction (e.g. mineral content) in the sample.

The spatial distribution of W_{org} (Figure 6.3) shows an slightly heterogeneous pattern. The highest W_{org} ($> 60\%$) is found in an small area located at the most southern part of the lake. Here, one of the few streams within the catchment flows into a sheltered area of shallow water. A more extensive area is covered by sediments with $25 < W_{org} < 60\%$. In contrast, the lowest W_{org} values ($< 20\%$) are observed in the east, northeast and centre of the lake where lake muds are absent and pre-Holocene clays persist on the bed.

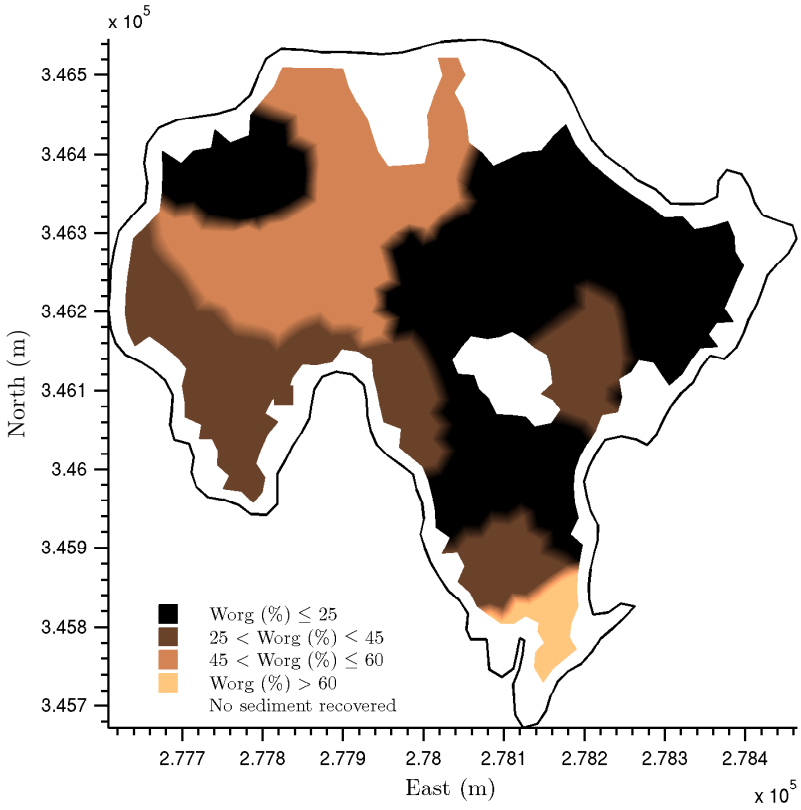

Figure 6.3: Distribution of % of organic matter (W_{org}) in Llyn Conwy bottom sediments.

There is a strong correspondence between the spatial distributions of W_{org} and W_w distributions. This is unsurprising since sediments with high organic content are generally characterised by high porosity (see, for example, Håkanson & Jansson, 1983). A linear correlation analysis between W_{org} and W_w yielded $R^2 = 0.72$ (n = 25, p = 0.02).

6.2.3 Sediment size distributions

All samples were additionally subjected to grain size analysis using a Malvern Master-Sizer 2000 laser granulometer. Grainsize was computed and selected summary statistics (median (d_{50}) diameter, sorting and sediment classification) determined using the Folk & Ward, 1957 arithmetical measures. Two sets of analyses were run. The first was conducted using gently agitated samples; the second included 10 minutes of ultrasonic pre-treatment to disaggregate any composite particles. The resulting grainsize distributions are summarised in Figures 6.4, 6.5 and 6.6. Each distribution represents the average of three successive laser granulometer analyses. Distributions are grouped into the three main bottom sediment types: organic peat; clay-rich peat; and pre-Holocene clay. Curves for samples with and without ultrasonic pre-treatment are shown. Ultrasonic pre-treatment invariably results in a significant shift in the both the mode and median particle size, although these shifts are smaller for some of the pre-Holocene samples. With the exception of sample 27, areas lacking in Holocene lake sediments are characterised by much finer clay-rich silts (d_{50} approximately 11 to 13 μ). Summary statistics for samples, grouped by sediment type, are provided in Table 6.2. Based on conventional classificatory schemes (e.g. Blott & Pye, 2001), the ultrasonically-treated lake muds all lie in the coarse silt range, and most are poorly sorted, with some very poorly sorted (see Figures 6.7, 6.8 and 6.9).

6.2.4 Density and settling velocity

The bulk density (ρ_{bs}) for each sediment sample was estimated using the density bottle technique, which offers good accuracy for the analysis of soft lake bed sediments (Hilton *et al.*, 1986b). As seen in Table 6.2, the sediment density is very low owing to the high organic fraction. Computed densities were then used in conjunction with the Stokes settling law to to estimate the settling velocity (w_s). This assumes spherical particles settling in a quiescent and homogeneous water column. The latter is a reasonable representation of the lake environment. The assumption of spherical particles is clearly hard to justify, however, given the fibrous nature of the organic component of the lake deposits. Various modifications to take account of shape effects on settling have been proposed (e.g. Baba & Komar, 1981; Hallermeier, 1981) but in the absence of any shape information, the original Stokes formulation has been used here. It is not entirely clear to what extent the larger reduction in particle size for the peat-dominated samples

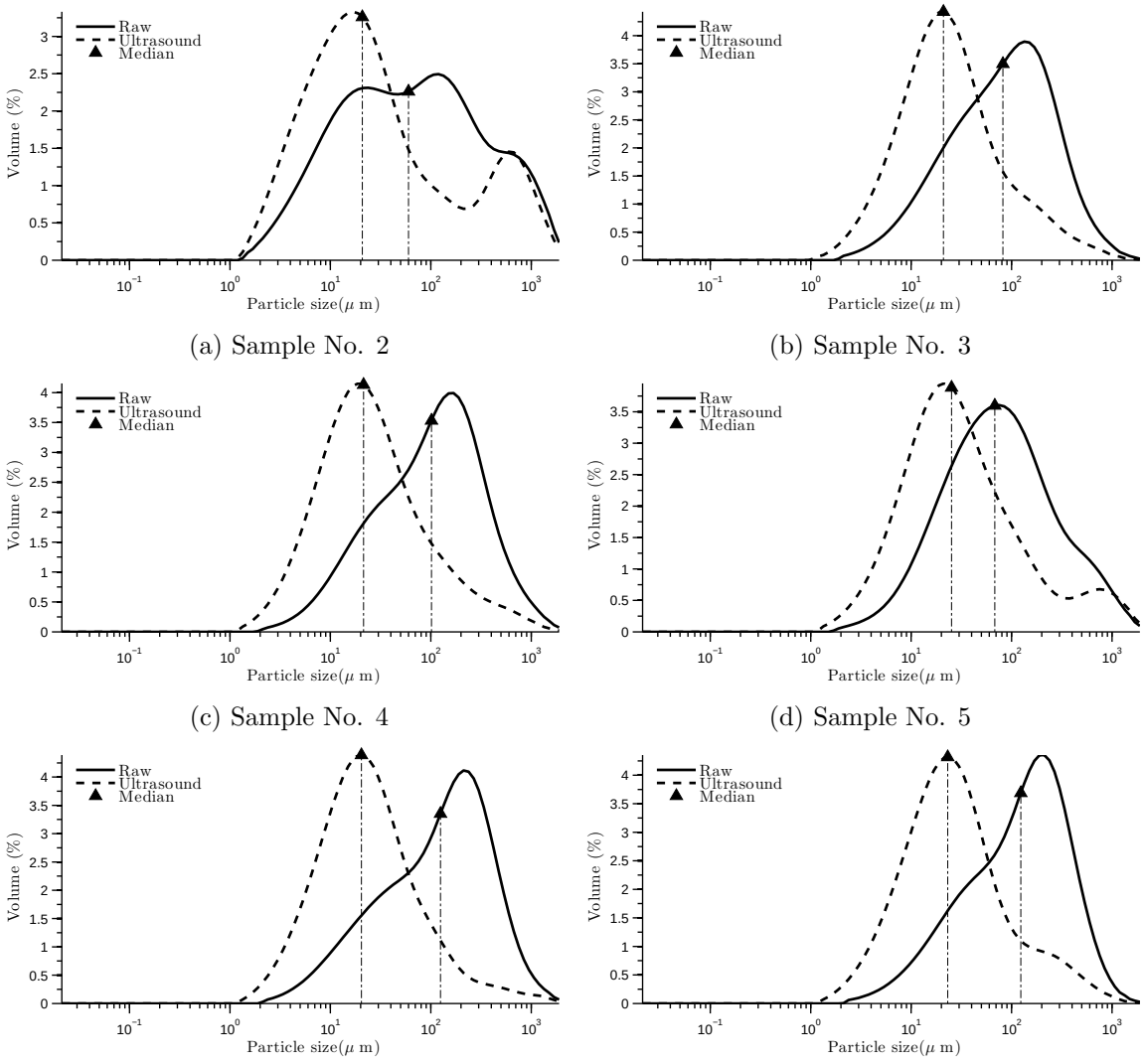

(a) Sample No. 2

(b) Sample No. 3

(c) Sample No. 4

(d) Sample No. 5

(e) Sample No. 8

(f) Sample No. 24

Figure 6.4: GSD for organic peat.

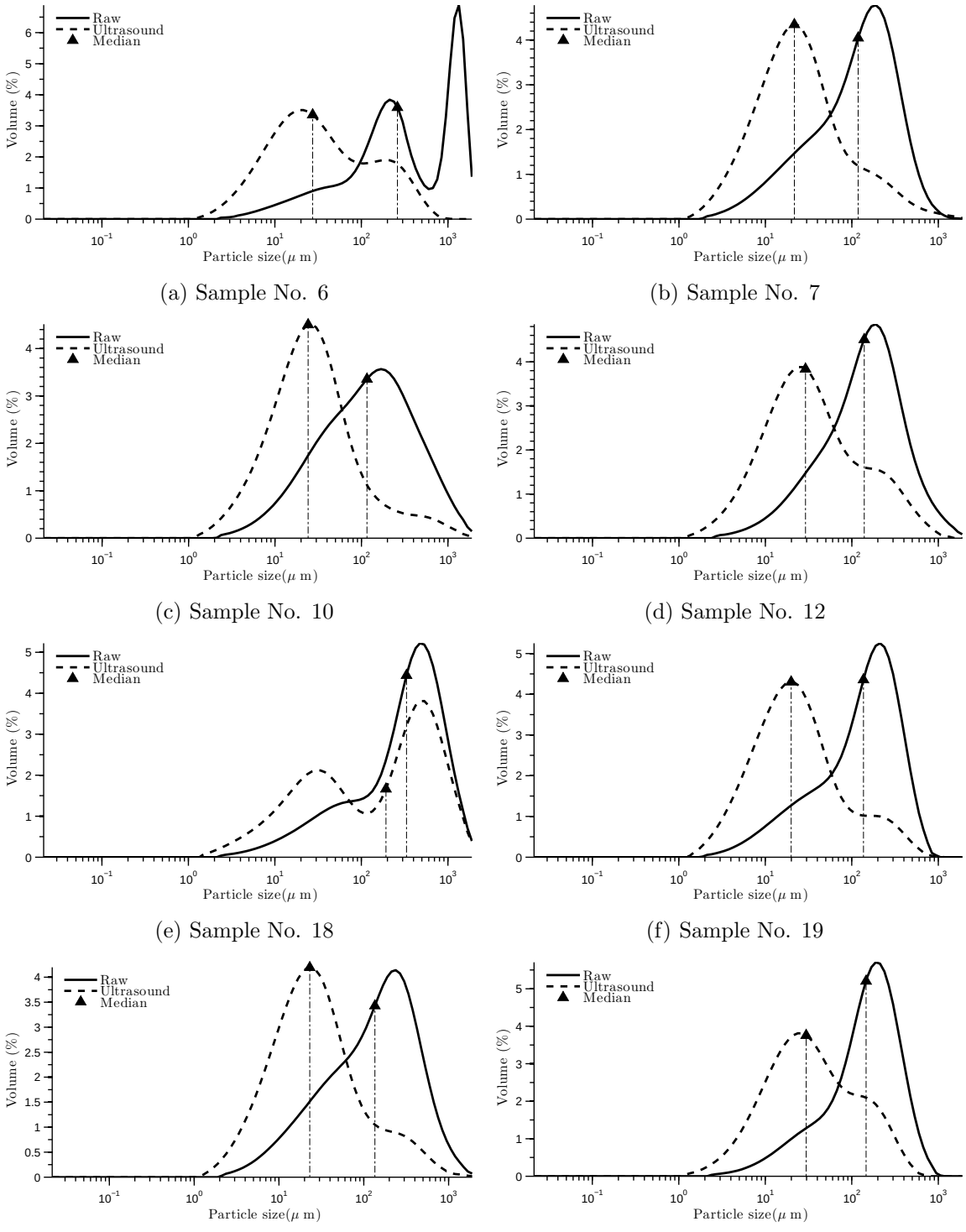

(a) Sample No. 6

(b) Sample No. 7

(c) Sample No. 10

(d) Sample No. 12

(e) Sample No. 18

(f) Sample No. 19

(g) Sample No. 23

(h) Sample No. 25

Figure 6.5: GSD for clay-rich peat.

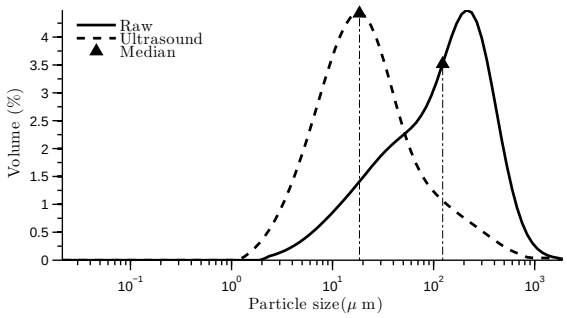

(i) Sample No. 28

Figure 6.5: Continued.

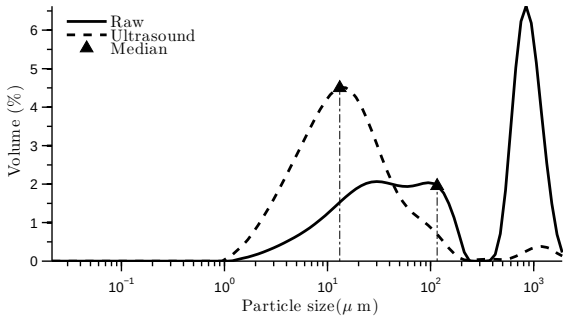

(a) Sample No. 1

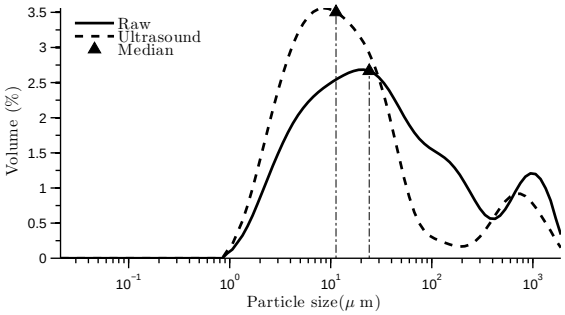

(b) Sample No. 9

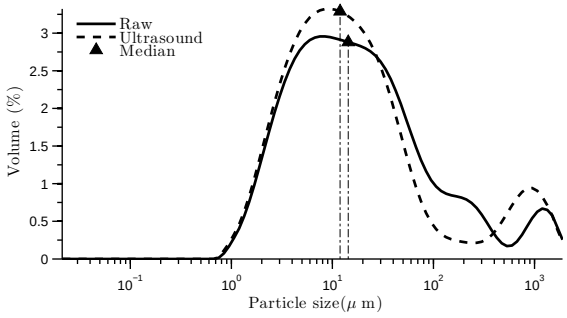

(c) Sample No. 21

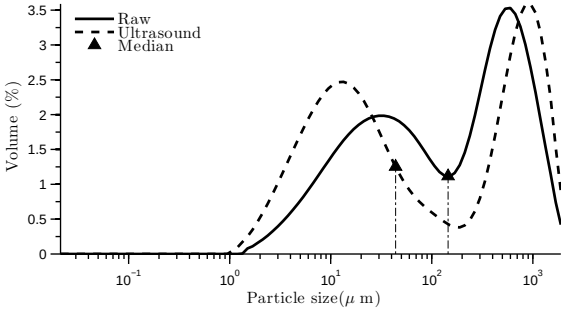

(d) Sample No. 27

Figure 6.6: GSD for pre-Holocene clay.

Table 6.1: Mean, sorting and sediment classification for each sediment sample based on the GSDs.

Sample	Test	Median (μ m)	Sorting (μ m)	Description
2	Raw	59.98	5.03	Very poorly sorted very coarse silt.
	Ultrasound	20.79	5.54	Very poorly sorted coarse silt.
3	Raw	82.02	3.32	Poorly sorted very fine sand.
	Ultrasound	20.97	3.29	Poorly sorted coarse silt.
4	Raw	101.54	3.44	Poorly sorted very fine sand.
	Ultrasound	21.39	3.50	Poorly sorted coarse silt.
5	Raw	68.04	3.55	Poorly sorted very fine sand.
	Ultrasound	25.27	4.04	Very poorly sorted coarse silt.
8	Raw	125.02	3.57	Poorly sorted fine sand.
	Ultrasound	20.38	3.25	Poorly sorted coarse silt.
24	Raw	123.70	3.28	Poorly sorted very fine sand.
	Ultrasound	23.12	3.39	Poorly sorted coarse silt.
Average	*Raw*	*91.28*	*3.74*	*Poorly sorted very fine sand.*
	Ultrasound	*21.930*	*3.83*	*Poorly sorted coarse silt.*

(a) Organic peat.

Sample	Test	Median (μ m)	Sorting (μ m)	Description
6	Raw	260.84	4.28	Very poorly sorted medium sand.
	Ultrasound	27.33	3.85	Poorly sorted coarse silt.
7	Raw	118.39	3.24	Poorly sorted very fine sand.
	Ultrasound	21.63	3.38	Poorly sorted coarse silt.
10	Raw	115.92	3.59	Poorly sorted very fine sand.
	Ultrasound	24.19	3.39	Poorly sorted coarse silt.
12	Raw	139.16	3.02	Poorly sorted fine sand.
	Ultrasound	29.09	3.65	Poorly sorted coarse silt.
18	Raw	332.40	3.60	Poorly sorted medium sand.
	Ultrasound	192.49	5.37	Very poorly sorted fine sand.
19	Raw	136.55	3.16	Poorly sorted fine sand.
	Ultrasound	19.89	3.32	Poorly sorted coarse silt.
23	Raw	135.34	3.54	Poorly sorted fine sand.
	Ultrasound	23.09	3.47	Poorly sorted coarse silt.
25	Raw	146.23	2.80	Poorly sorted fine sand.
	Ultrasound	29.69	3.34	Poorly sorted coarse silt.
28	Raw	122.86	3.39	Poorly sorted very fine sand.
	Ultrasound	18.46	3.19	Poorly sorted coarse silt.
Average	*Raw*	*152.06*	*3.58*	*Poorly sorted fine sand.*
	Ultrasound	*26.02*	*4.00*	*Poorly sorted very coarse silt.*

(b) Clay-rich peat.

Table 6.2: Continued.

Sample	Test	Median (μ m)	Sorting (μ m)	Description
1	Raw	115.70	6.35	Very poorly sorted very fine sand.
	Ultrasound	13.12	3.42	Poorly sorted medium silt.
9	Raw	24.04	5.88	Very poorly sorted coarse silt.
	Ultrasound	11.28	5.12	Very poorly sorted medium silt.
21	Raw	14.33	5.01	Very poorly sorted medium silt.
	Ultrasound	11.90	5.38	Very poorly sorted medium silt.
27	Raw	144.98	5.79	Very poorly sorted fine sand.
	Ultrasound	43.82	8.65	Very poorly sorted very coarse silt.
Average	*Raw*	*40.23*	*6.95*	*Very poorly sorted very coarse silt.*
	Ultrasound	*14.65*	*6.25*	*Very poorly sorted medium silt.*

(c) Pre-Holocene clay.

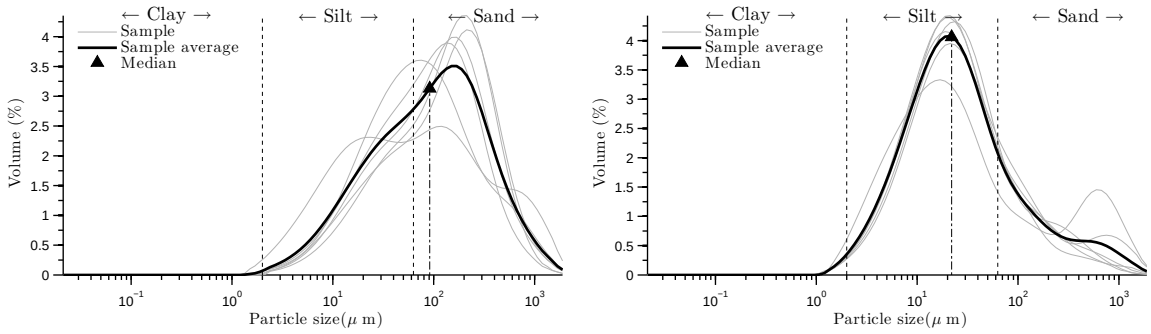

(a) Without ultrasound pre-treatment.

(b) With ultrasound pre-treatment.

Figure 6.7: Averaged GSD distribution of organic peat.

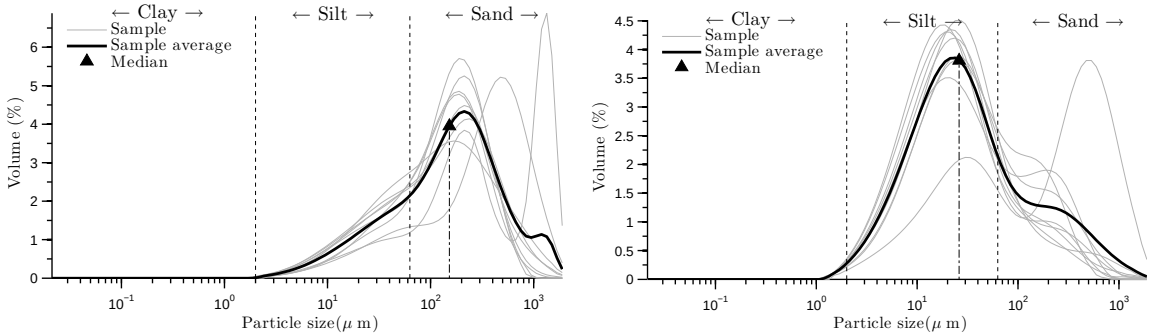

(a) Without ultrasound pre-treatment. (b) With ultrasound pre-treatment.

Figure 6.8: Averaged GSD distribution of clay-rich peat.

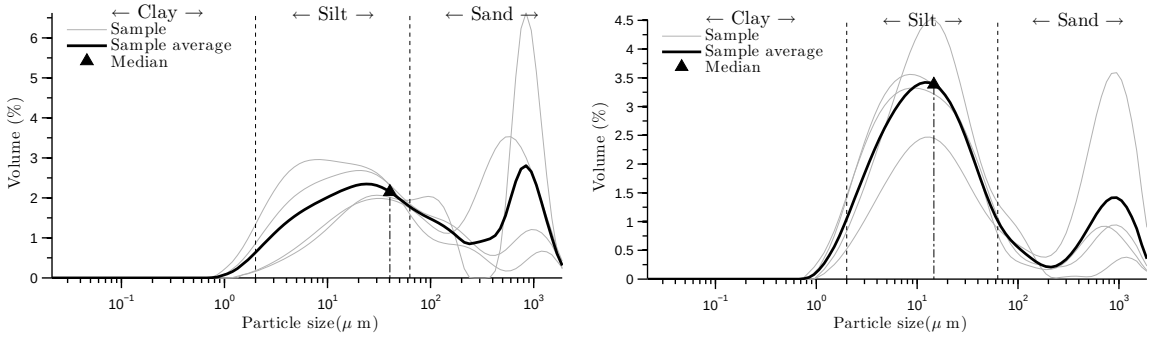

(a) Without ultrasound pre-treatment. (b) With ultrasound pre-treatment.

Figure 6.9: Averaged GSD distribution of pre-Holocene clay.

follow ultrasound treatment reflects the existence of more complex post-depositional aggregations of peat fibres, or whether the ultrasonic treatment is actually aiding the disintegration of individual peat fragments. Therefore, the raw untreated particle sizes are used in all the settling velocity calculations. An approximate spatial distribution of ρ_{bs} is shown in Figure 6.10. This reveals two distinctive zones. First, a region of higher density pre-Holocene clays and silts that are also characterised by higher w_s (see Table 6.2). Second, a region of low density organic lake sediments, with low w_s (≤ 0.3 $cm\ s^{-1}$).

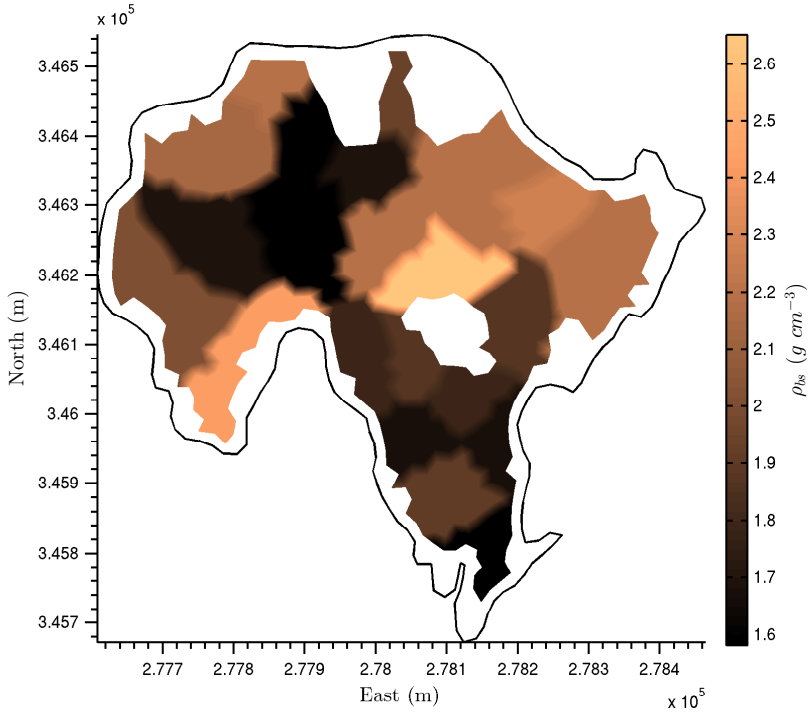

Figure 6.10: Spatial distribution of ρ_{bs} in Llyn Conwy.

6.2.5 Historical sedimentation rate

Radiometric dating analysis of the upper 0.40 m of the sediment core (CONLM1) for ^{210}Pb, ^{137}Cs and ^{241}Am was undertaken in the BEIF at UCL by Dr Handong Yang. The results of this analysis are summarised in Table 6.3. Total ^{210}Pb activity reaches equilibrium with the supported ^{210}Pb at a depth of around 0.27 m in this core. Unsupported ^{210}Pb activities, calculated by subtracting supported from total ^{210}Pb

Table 6.2: Diameter (d), bulk density (ρ_{bs}), settling velocity (w_s) and minimum time to reach the bed (T) for Llyn Conwy bottom samples.

Sample	d (μ m)	ρ_{bs} ($g\ cm^{-3}$)	w_s ($cm\ s^{-1}$)	Depth (m)	T (s)
2	60.0	1.8	0.1	3.0	2529
3	82.0	1.9	0.2	5.1	2075
4	101.5	1.8	0.3	2.7	795
5	68.0	2.4	0.3	2.6	945
8	125.0	1.7	0.4	16.2	3616
24	123.7	1.6	0.4	21.2	5711
Mean	*91.3*	*1.7*	*0.3*	*8.5*	*2612*

(a) Organic peat.

Sample	d (μ m)	ρ_{bs} ($g\ cm^{-3}$)	w_s ($cm\ s^{-1}$)	Depth (m)	T (s)
6	260.8	2.0	2.9	7.0	244
7	118.4	2.0	0.6	3.9	666
10	115.9	2.2	0.7	9.5	1418
12	139.2	1.9	0.8	20.0	2647
18	332.4	1.6	2.7	4.8	176
19	136.5	1.9	0.7	3.6	507
23	135.3	1.7	0.5	20.4	3824
25	146.2	1.9	0.8	18.1	2337
28	122.9	1.6	0.4	17.5	4742
Mean	*146.9*	*1.9*	*0.9*	*12.5*	*2048*

(b) Clay-rich peat.

Sample	d (μ m)	ρ_{bs} ($g\ cm^{-3}$)	w_s ($cm\ s^{-1}$)	Depth (m)	T (s)
1	115.7	1.7	0.4	2.9	774
9	24.4	2.1	0.0	9.0	31676
21	14.3	2.6	0.0	5.0	35355
27	145.0	2.2	1.0	14.5	1391
Mean	*40.2*	*2.2*	*0.5*	*7.9*	*17299*

(c) Pre-Holocene clay.

activity, decline irregularly with depth. This implies that the sediment accumulation has varied over time. However, as the decline is more-or-less exponential in nature, these variations in rate appear to have been fairly gentle. The inventory of unsupported ^{210}Pb in the core indicates a mean flux to the core location of c. 31 Bq $m^{-2}yr^{-1}$. This is lower than the atmospheric ^{210}Pb deposition flux for this region, which suggests that this location in the lake has experienced at least some degree of sediment focusing (i.e. preferential deposition).

Notably, the ^{137}Cs activity versus depth profile Table 6.4 shows that the peak is significant but at the sediment surface, with a tail of declining activity downwards within the core. There is also a significant ^{241}Am activity peak in the surface sediments; below the surface, ^{241}Am activity is below the limit of detection. ^{241}Am fallout was derived from the atmospheric testing of nuclear weapons and fallout peaked around 1963. Unlike ^{137}Cs, it is generally considered to be essentially immobile in vertical sediment sequences (Appleby *et al.*, 1991), and thus provides an unambiguous marker 1963 in lake sediment cores. The presence of a ^{137}Cs activity peak at the surface, together with ^{241}Am implies that the very top of the profile is missing. In some cases, this can happen through the coring and core handling process. However, this core was acquired and extruded with great care and with a seemingly intact sediment-water interface. The conclusion, therefore, is either that there has been a virtual cessation of sedimentation since the mid-1960s or, more likely, that several *cm* of surface mud have been lost through post-depositional reworking.

The core chronology Table 6.5 suggests an average post 1836 rate of sedimentation of 0.0063 $g\ cm^{-2}\ yr^{-1}$ or 0.22 $cm\ yr^{-1}$. In accordance with the account given by Patrick & Stevenson, 1986, the rate of sedimentation appears to increase significantly after the 1930s and this is likely due to enhanced sediment production within the catchment. A second core, CON4 (see Figure 2.13 for location), was acquired in 1987 by researchers from the ECRC and it is interesting to compare the sedimentation histories at the two sites. The CON4 core was obtained from a site in the western part of the central basin in 7.4 m of water. The mean sedimentation rate at this site is 0.28 $cm\ yr^{-1}$, which is very close to that seen in CONLM1. As Figure 6.11 shows, however, the age versus sedimentation rate curves are quite different. CON4 shows a single prolonged phase of increased sediment between about 1900 and the 1940s, which then declines through the 1960s, with minor insignificant peaks into the 1980s. The basal rate is averaged between 1900 and 1827 but, at 0.21 $cm\ yr^{-1}$, and is rather higher than the rates

Table 6.3: ^{210}Pb concentrations obtained for core CONLM1.

Depth	^{210}Pb						Cum. unsupported	
	Total		Supported		Unsupported		^{210}Pb	
cm	$Bq\ Kg^{-1}$	$\pm$	$Bq\ Kg^{-1}$	$\pm$	$Bq\ Kg^{-1}$	$\pm$	$Bq\ m^{-2}$	$\pm$
0.5	735.05	26.59	39.79	4.98	695.26	27.05	91.2	5.1
1.5	319.69	24.76	41.18	5.4	278.51	25.34	199.6	9.5
2.5	259.39	22.8	50.92	5.18	208.47	23.38	263.9	11.9
3.5	225.39	20.11	43.63	4.63	181.76	20.64	319.3	13.8
6.5	185.54	23.29	39.71	5.28	145.83	23.88	460.7	21.9
9.5	225.19	20.43	53.52	4.96	171.67	21.02	605.2	31.1
12.5	198.44	20.97	41.21	4.83	157.23	21.52	758.2	37.6
15.5	108.18	17.44	36.34	4.35	71.84	17.97	853.7	42.1
18.5	102.48	17.64	35.04	8.28	67.44	19.49	914.4	45.2
20.5	108.45	17.79	34.79	4.14	73.66	18.27	956.5	47
21.5	73.77	9.87	41.61	2.64	32.16	10.22	972.1	47.4
23.5	50.81	12.21	48.03	3.34	2.78	12.66	979.7	47.8
24.5	72.07	11.87	39.85	2.96	32.22	12.23	983.5	48.1
26.5	73.83	11.86	48.51	2.95	25.32	12.22	1000.6	48.5
27.5	42.58	8.36	42.21	2.17	0.37	8.64	1002.3	48.7
30.5	49.4	8.75	40.12	2.21	9.28	9.02	1005	49.2
35.5	41.86	10.33	35.64	2.76	6.22	10.69	1023.1	50.3
39.5	49.17	8.86	43.11	2.65	6.06	9.25	1031.1	51.8

for the same period in the CONLM1 core. The CONLM1 curve, in contrast, shows three distinct peaks in sedimentation around 1840, 1900 and 1960. One interpretation of this is that this site is generally conducive to sedimentation but also subject to infrequent erosion under extreme wind forcing events. This would have the effect of removing poorly consolidated material close to the water-sediment interface, thereby introducing a step-like discontinuity in the age versus sedimentation curve. Clearly, one of the main questions to be investigated through the subsequent sediment dynamics modelling is whether intermittent resuspension is plausible at the CONLM1 site in 9 m of water.

Table 6.4: ^{137}Cs, ^{134}Cs and ^{241}Am concentrations in CONLM1.

Depth	^{137}Cs		^{134}Cs		^{241}Am	
cm	$Bq\ Kg^{-1}$	$\pm$	$Bq\ Kg^{-1}$	$Bq\ Kg^{-1}$	$\pm$	
0.5	676.43	9.62	0	0	9.62	2.18
1.5	184.06	5.88	0	0	0	0
2.5	90.00	4.34	0	0	0	0
3.5	108.24	4.35	0	0	0	0
6.5	105.37	4.98	0	0	0	0
9.5	95.63	4.35	0	0	0	0
12.5	84.11	3.89	0	0	0	0
15.5	67.10	3.62	0	0	0	0
18.5	44.05	3.36	0	0	0	0
20.5	29.17	2.63	0	0	0	0
21.5	23.47	1.48	0	0	0	0
23.5	20.08	1.94	0	0	0	0
24.5	18.89	1.72	0	0	0	0
26.5	14.72	1.63	0	0	0	0
27.5	13.12	1.17	0	0	0	0
30.5	10.58	1.18	0	0	0	0
35.5	4.43	1.36	0	0	0	0
39.5	6.01	1.20	0	0	0	0

Table 6.5: ^{210}Pb chronology of core CONLM1.

Depth	Dry mass	Chronology			Sedimentation rate		
		Date	Age				
cm	$g\ cm^{-2}$	AD	yr	$\pm$	$g\ cm^{-2}\ yr^{-1}$	$cm\ yr^{-1}$	$\pm$ %
0	0	1963	47				
0.5	0.0119	1960	50	2	0.0041	0.171	6.9
1.5	0.0357	1956	54	2	0.009	0.356	11.1
2.5	0.0623	1953	57	2	0.011	0.401	13.1
3.5	0.0907	1951	59	2	0.0117	0.407	13.4
6.5	0.1774	1943	67	2	0.0116	0.390	18.2
9.5	0.2686	1933	77	3	0.0072	0.235	15.7
12.5	0.3617	1918	92	4	0.0048	0.161	19.3
15.5	0.4493	1902	108	6	0.0064	0.221	31.5
18.5	0.5366	1885	125	9	0.0041	0.138	40.0
20.5	0.5963	1864	146	16	0.0019	0.064	55.4
21.5	0.6274	1851	159	24	0.0029	0.094	80.0
23.5	0.6905	1839	171	30	0.0054	0.170	95.6
24.5	0.7224	1836	174	35	0.0018	0.060	107.6
				mean	*0.0057*	*0.1721*	

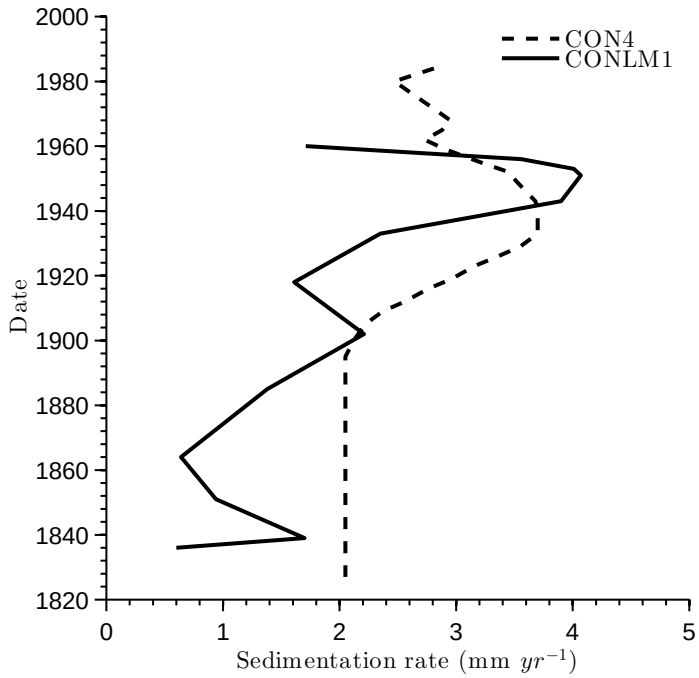

Figure 6.11: Sedimentation rate comparison between cores CON4 and CONLM1.

6.3 *FVCOM* Sediment Transport Model

In order to further understand the dynamics of sedimentation within Llyn Conwy the *FVCOM* hydrodynamic and sediment transport models were coupled with the *UCL-SWM* linear wind-wave model. To facilitate this, *UCL-SWM* was pre-compiled as a Fortran library that can then be called directly by *FVCOM*. This arrangement equips *FVCOM* with the ability to compute the bottom stress due to waves (τ_w) and combine this with the current-generated bottom stress (τ_c) prior to execution of the sediment transport module. The *FVCOM* sediment transport sub-model requires information including the initial concentration of suspended sediments, sediment particle properties used to compute their transport and settling behaviour (e.g. diameter, density, etc.) as well as a specification of the vertical variation in bed characteristics. Information on open boundary inflows and outflows is also required. All of this information is specified through an external file, as summarised previously in Figure 4.2 (see also Chen *et al.*, 2004a).

The sediment transport model accommodates multiple (non-interacting) sediment size fractions. Each class is described by a characteristic grain diameter (d_{50}), particle

density (ρ_s), critical stresses for resuspension (τ_{cri}), and deposition (τ_{cd}), and erosion rate constant (δ_E), a settling velocity (W_s) and a porosity (P_o). Not surprisingly given the diverse environmental contexts for lake sedimentation modelling, a wide range of values for these parameters can be found in previous studies. Table 6.6 reviews a selection of relevant modelling studies. For some parameters there is greater consensus over the most appropriate value. For τ_{cri}, a value around 0.1 $N\ m^{-2}$ in used in much of the literature. In contrast, the values and ranges of τ_{cd} and δ_E are more heterogeneous, suggesting that these parameters may be more lake-dependent.

Table 6.6: Literature review of key physical parameters used in lake sediment transport modelling studies.

Reference	Sediment class	d_{50} (mm)	τ_{cri} $(N\ m^{-2})$	τ_{cd} $(N\ m^{-2})$	δ_E $(Kg\ m^{-2}\ s^{-1})$	w_s $(cm\ s^{-1})$
Sheng & Lick, 1979	Clay and sil.	-	5×10^{-2}- 1.5×10^{-2}	-	3.6×10^{-5}	7×10^{-3} - 1×10^{-1}
Kang *et al.*, 1982	Clay and silt	1×10^{-3}-1	0.1	-	-	-
Luettich Jr *et al.*, 1990	Clay and fine silt	1.6×10^{-2}	5×10^{-2}	-	1.9×10^{-8} - 3.7×10^{-5}	2.2×10^{-2}
Bengtsson & Hellström, 1992	Sediment flocs	2×10^{-3}	0.15	-	5.56×10^{-6}	4×10^{-3}
Bailey & Hamilton, 1997	Cohesive, 50% organic matter.	-	-	-	2.3×10^{-7} - 3.5×10^{-7}	3×10^{-3}
Lou *et al.*, 2000	Silt and sand. Coarse sand along shores.	3×10^{-2}	5×10^{-2} - 0.2	-	-	5.8×10^{-3}
Jin & Ji, 2004	Cohesive	-	$1.2\tau_{cd}$	0.18	6×10^{-5}	1×10^{-3}
Lee *et al.*, 2005	Silt and clay	0.25	0.1	1.5	1.16×10^{-3}	$< 8\times10^{-2}$
Chao *et al.*, 2008	Clay	2.5×10^{-3} - 3.0×10^{-3}	2×10^{-2}	1×10^{-2}	1×10^{-5} - 4×10^{-4}	1×10^{-2}

No data exist with which to accurately quantify contemporary sediment inputs into the Llyn Conwy. Although two small streams enter the northeast and southeast corners of the basin, these have not been observed to generate visible plumes of suspended material under a range of rainfall conditions. However, during the period of low water level in the summer of 2010, peat deposits were exposed where the southeastern inflow enters the lake, implying that point sources may be significant at times. Such inputs may have been more numerous during much of the 20th century after the construction of drainage channels within the peat bog, especially in the eastern half of the catchment (Patrick & Stevenson, 1986). Most of these have since been blocked and total sediment input from the catchment accordingly reduced. It is likely that much of the contemporary input derives from erosion of the deposits exposed around the lake and basal seepage emerging from the peat cover. Given the uncertain nature of these boundary conditions, it was thus decided to only undertake indicative simulations of sediment exchanges between the bed and the water column in order to identify zones of erosion, deposition and resuspension under energetic metereorological forcing. External sediment inputs are thus neglected.

Simulations were run using a single particle class with size and settling characteristics given by $d_{50} = 91\mu$m and $w_s = 0.3\ mm\ s^{-1}$, corresponding to the average values determined empirically for the organic lake sediments. Other sediment model parameter values are given in Table 6.7. The fraction of sediment mobilised by bed load transport is generally not significant in lakes (Lee *et al.*, 2007) and the main interest here is the pattern of organic sediment accumulation. Bedload transport was therefore neglected and only the transport of sediments in suspension considered. The first model run was initialised with a cover of sediment with these characteristics in a layer of infinite thickness, effectively giving an unlimited sediment supply. This corresponds to a transport-limited situation and provides a useful first insight into the ability of the various lake hydrodynamic processes to redistribute material. A second set of runs were initialised with a 5 mm layer of mobile sediment with a view to investigating a more realistic supply-limited redistribution of sediment. This run was extended by using the end condition to initialise a second simulation with identical meteorological forcing to further mitigate the artificial nature of the initial state.

The model was forced by spatially uniform hourly interval wind data for the month of December 1997 (see Figure 5.51) employed in the earlier analysis in Chapter 5. These data were re-sampled to a much shorter model time-step of 1 s, which was

Table 6.7: Parameter values used in *FVCOM* sediment sub-model. The last column indicates the source of the information: [1]lLiterature review (see Table 6.6), [2] analysis of Llyn Conwy samples.

Parameter	Units	Values	Source
d_{50}	mm	0.091	[2]
ρ_s	$Kg\ m^{-3}$	1700	[2]
w_s	$mm\ s^{-1}$	0.3	[1], [2]
δ_E	$Kg\ m^{-2}\ s^{-1}$	4×10^{-5}	[1]
τ_{cri}	$N\ m^{-2}$	0.1	[1]
τ_{cd}	$N\ m^{-2}$	0.08	[1]
P_o	%	0.76	[2]

required to avoid numerical instabilities caused by wind speeds exceeding 30 $m\ s^{-1}$. As noted above, inflows and outflows were neglected and the water balance was assumed to be static over this short period. Model output included hourly values of suspended sediment concentration (SSC) at every (x, y, z) location within the computational mesh, and the net erosion or deposition at every (x, y) location at the bed.

6.4 Analysis of Sediment Dynamics

An initial insight into the temporal variation in SSC in response to wind forcing can be obtained by considering the spatially-averaged concentrations. Figure 6.12a) shows a strong correspondence between spatially-averaged SSC for the lake as a whole and the wind forcing (as represented by the wind speed series). So as wind speed increases above $\sim$ 12 $m\ s^{-1}$ bottom sediments are resuspended, while at lower W_s the concentration declines proportionally. Integrating the spatial-averaged SSC for each vertical layer over time (Figure 6.12b) shows a characteristic vertical profile that is consistent with the familiar Rouse, 1937 profile. The assumption of an unlimited thickness of mobile sediment across the entire lake bed clearly results in concentrations greater than would be expected to occur in reality, with an average of around 0.5 $mg\ l^{-1}$ in the upper half of the water column to around 2 $mg\ l^{-1}$ at the bottom layer. As Figure 6.12c) shows, peaks in wind speed result in average concentrations exceeding 10 $mg\ l^{-1}$, and over 30 $mg\ l^{-1}$ in response to extreme wind speeds of 40 $m\ s^{-1}$ (the highest wind speed within

the historical record for this site). SSC rapidly declines after such excursions, and is almost zero for wind speeds below 12 $m\ s^{-1}$.

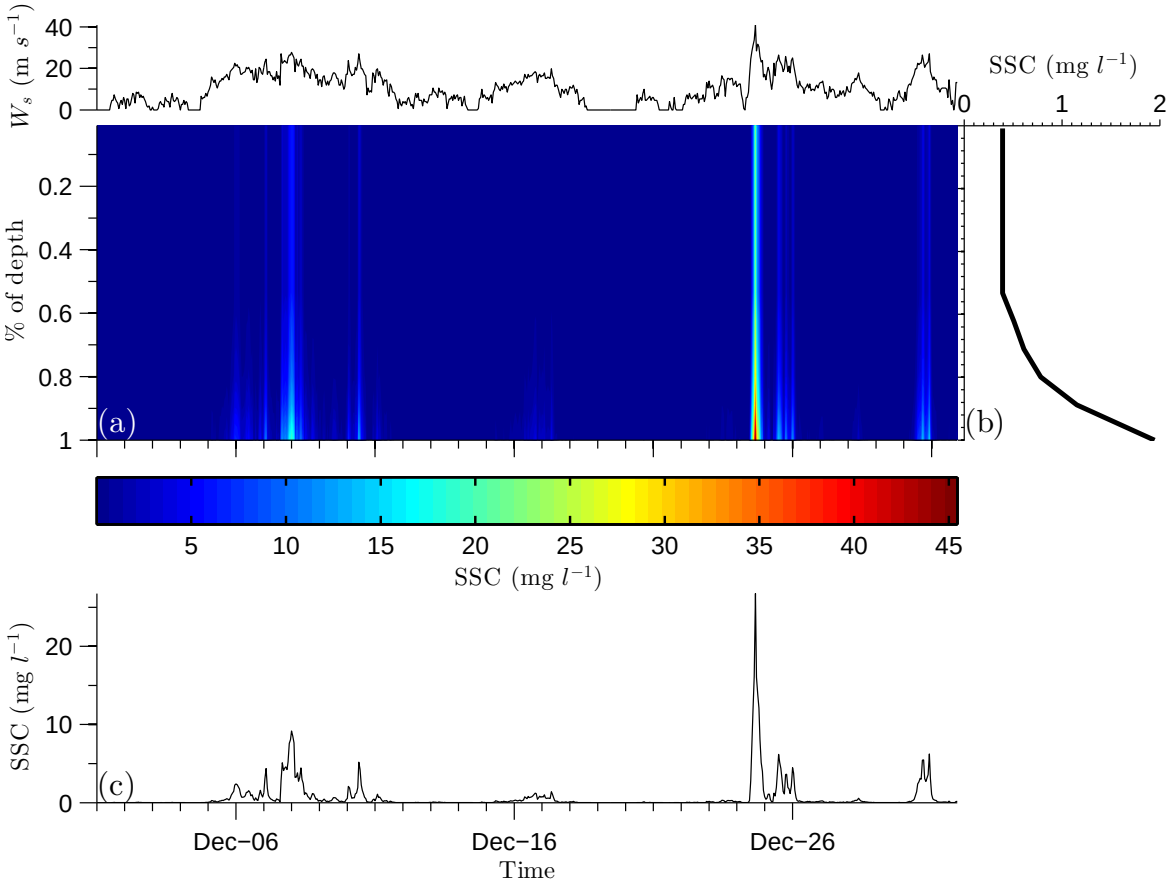

Figure 6.12: Spatially-averaged suspended sediment dynamics for December 1997 forcing period: a) vertical variation in spatially-averaged SSC; b) space- and time-average vertical SSC profile; and c) time series of spatially and vertically averaged SSC, with wind speed series also shown.

Figure 6.13 presents a more detailed analysis of SSC variability along a roughly north-south transect defining the longest axis of the lake basin for a five-hour period on 24 December. This period contains the strongest wind forcing and, not surprisingly, the highest SSC in the simulation performed here. High SSC values are restricted to the near-bed portion of the water column and are generally highest in shallow zones at the southern end of the transect, where the bottom gradient is lower, and along the north shore, where the strongest currents and highest wind-wave heights occur. The wind

speed peaks between 15:00 and 16:00 hours, at which time wind speed exceeds 40 m s^{-1}, generated waves that cause major resuspension of SSC through the water column ($\sim$ 5 m depth) in the south part of the lake. It is interesting to note that, whereas sediments in shallow areas are entrained almost instantaneously as soon as wind speed rises, entrainment in the deepest places is lagged by nearly an hour after the maximum intensity of the storm. This indicate that the wind forcing energy is rapidly transmitted to the bottom via wave-generated stresses in shallow water, whereas in the deepest parts of the basin the transmission of an incremental increase in wind forcing only takes place after a strong vertical circulation develops to entrain the bottom sediment.

Analysing the time-averaged spatial distribution of SSC at the bottom layer (see Figure 6.14a) a narrow band of very high SSC along the northern and eastern shores is evident where the unlimited supply provided by the bed in this idealised simulation is exploited by high bottom stresses due to waves. This contrasts with the low SSC elsewhere in the lake and a steep gradient is evident between the zone of entrainment and a zone more conducive to deposition. As demonstrated in Chapter 5, waves reach their maximum height along the northern and eastern shores under the predominant southwesterly winds, and the predicted significant wave heights under the extremely high winds driving this simulation reach 0.7 m. The return currents that flow upwind from the north and east reach values of 0.08 m s^{-1}, and are responsible for extending the zone of sediment entrainment into deeper water and also transporting suspended sediments away from the resuspension zone and distributing them into lower energy areas within the basin. This redistribution process can clearly be observed in the spatial distribution of SSC at the surface layer (Figure 6.14b)). The distribution of SSC at the surface layers contrasts with the more localised zones of SSC at the bottom (which is strongly related to the fetch), and reflects the complex current-driven driven circulation pathways.

The SSC distribution within the bottom layer is thus much more readily predicted since this is intimately linked to wind wave generation and propagation along the fetch. In contrast, the SSC distribution at the surface is more difficult to predict since it depends on the more complex 3D current circulation. An analysis of SSC at the water surface at successive hourly intervals during the period of strongest wind forcing (24 December) shows quite clearly how SSC reflects the evolution of the current velocity field (Figure 6.16). Concentrations are much lower than those at the bed, but the distinct zones of peak SSC occur in the western and southern margins, far removed

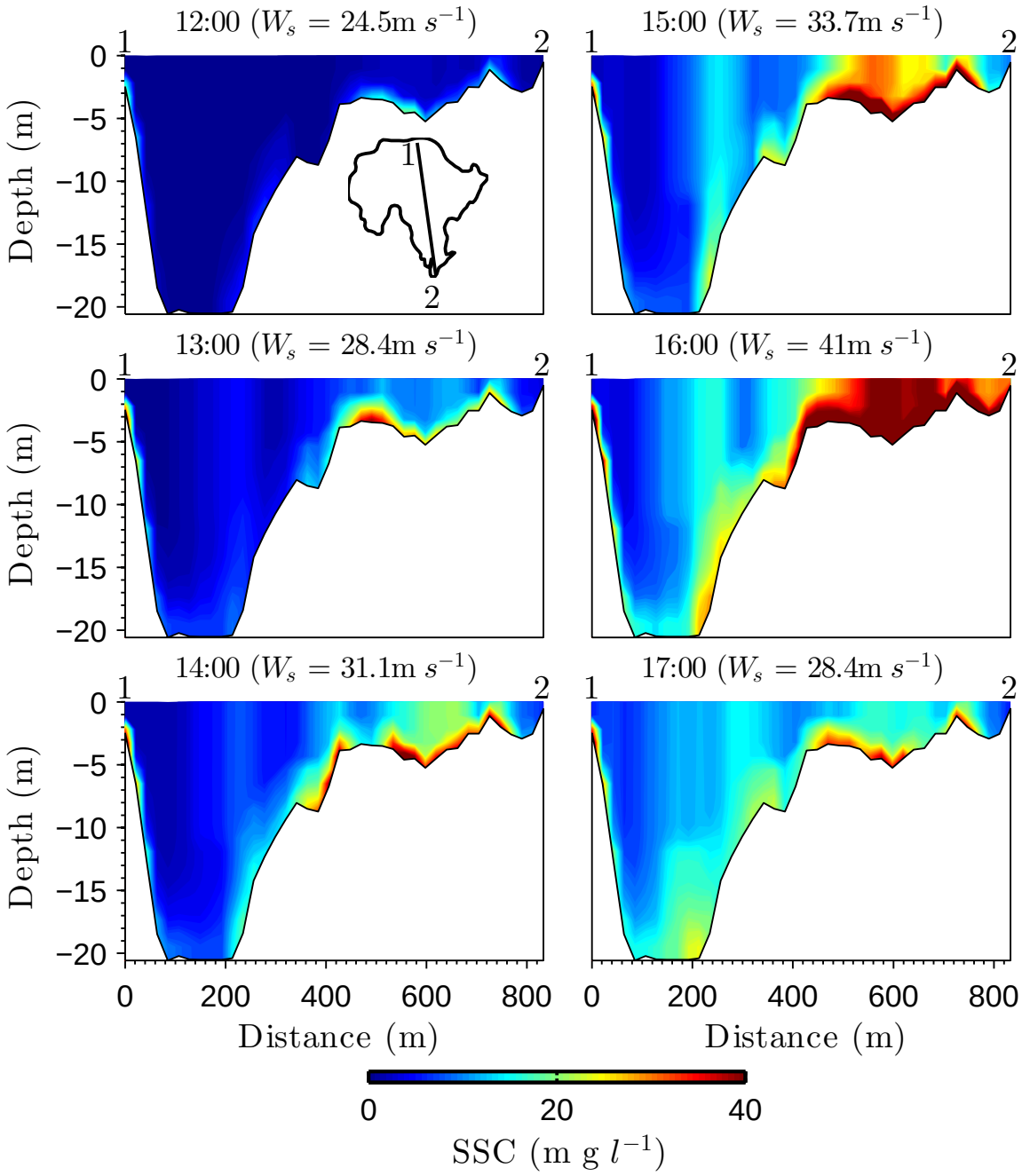

Figure 6.13: Vertical variation in SSC along a roughly north-south transect (see inset for location) at successive times during the period of strongest wind forcing between 12:00 and 17:00, day 24. Run initialised with unlimited mobile bed sediment.

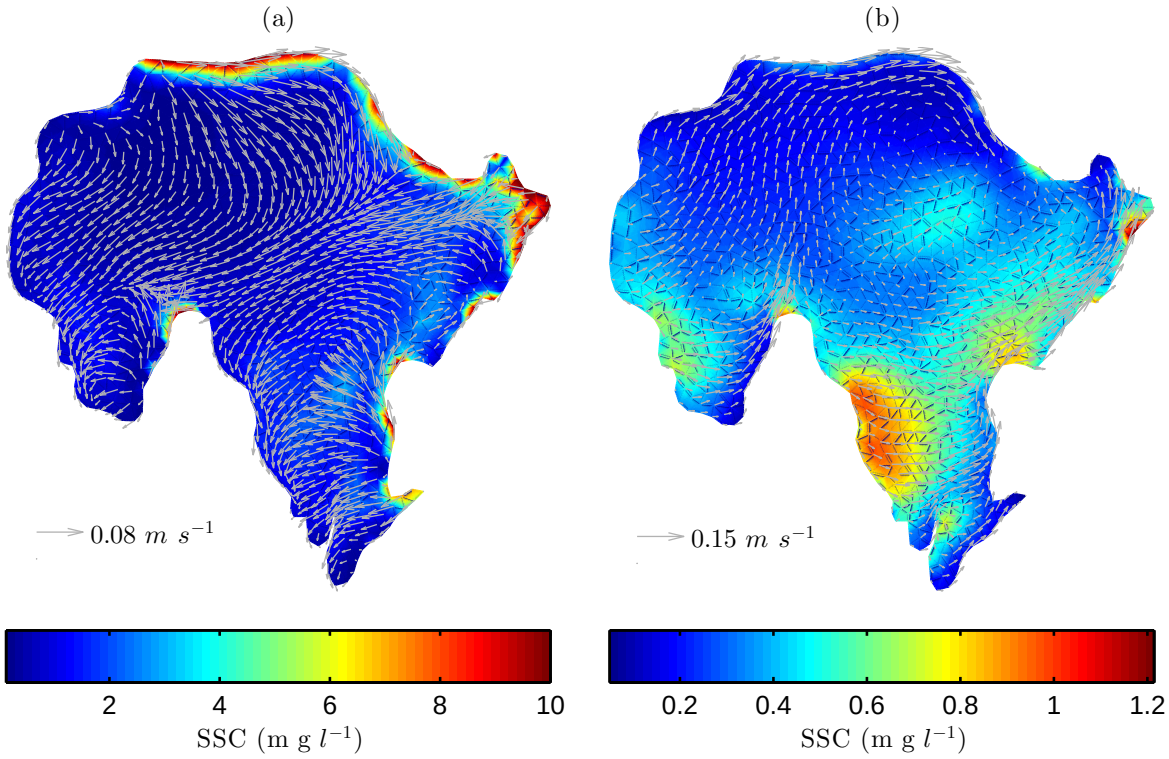

Figure 6.14: Time-averaged spatial SSC and velocity fields at the bottom (a) and (b) at the surface for December 1997. Run initialised with unlimited mobile bed sediment.

from the northern and eastern zones of entrainment from the bed. Wind-wave action in these areas is weak and it seems clear that the relative elevation of surface SSC in these parts is the result of redistribution by return flows and the circulation more generally.

A comparison between the SSC patterns for the three scenarios of boundary bottom sediment supply conditions show few differences. The spatial distribution of SSC for the unlimited bottom sediment supply scenario (Figure 6.14) and for the 5 mm layer of mobile bed scenario (Figure 6.15) show similar patterns but a slighly higher extension of SSC at the bottom layer for the first scenario because of the unlimited supply of sediment. Comparisons against the third scenario, where the final bottom configuration of the 5 mm layer of mobile bed scenario is used as the initial condition, indicate that SSC is reduced since no sediment sources remain.

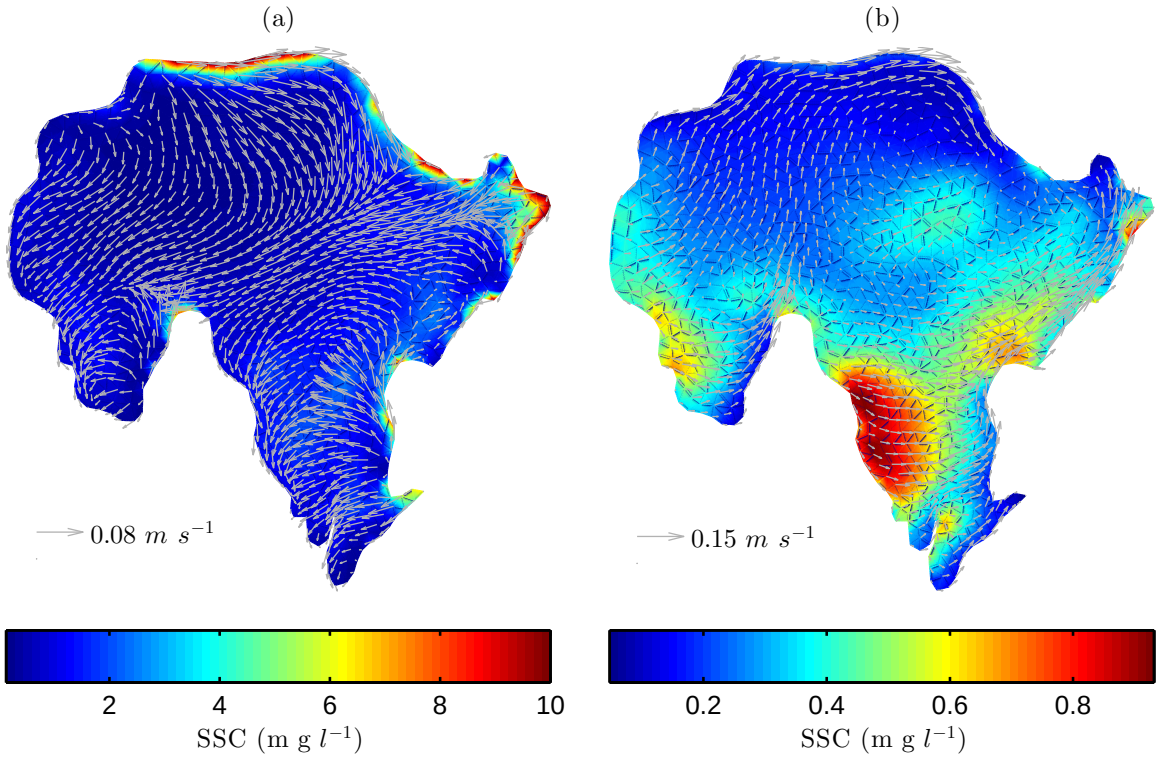

Figure 6.15: Time-averaged spatial SSC and velocity fields at the bottom (a) and (b) at the surface for December 1997. Run initialised with 5 mm mobile bed sediment.

6.4.1 Spatial pattern of erosion and deposition

Time series of spatially-averaged cumulative erosion and deposition are shown in Figure 6.17. These more-or-less mirror each other, with the mean rate of erosion exceeding the mean rate of deposition, since the area dominated by erosion is rather smaller than that dominated by deposition. Marked inflexions in both curves correspond to intervals of high wind speed. The net balance between erosion and deposition remains effectively constant, indicating that transfer of sediment from the bed is mainly restricted to the lower portion of the water column from which settlement occurs fairly rapidly when the bottom stress diminishes (over both space and time). This can also be visualised in a comparison of the average erosion and deposition rates over time (see Figure 6.18). At wind speeds below about 15 $m\ s^{-1}$ the erosion rate is almost zero and this is reflected in a similarly low deposition rate. In contrast, when wind speed rises above 15 $m\ s^{-1}$ marked erosional and depositional events are observed. Here again it should be noted

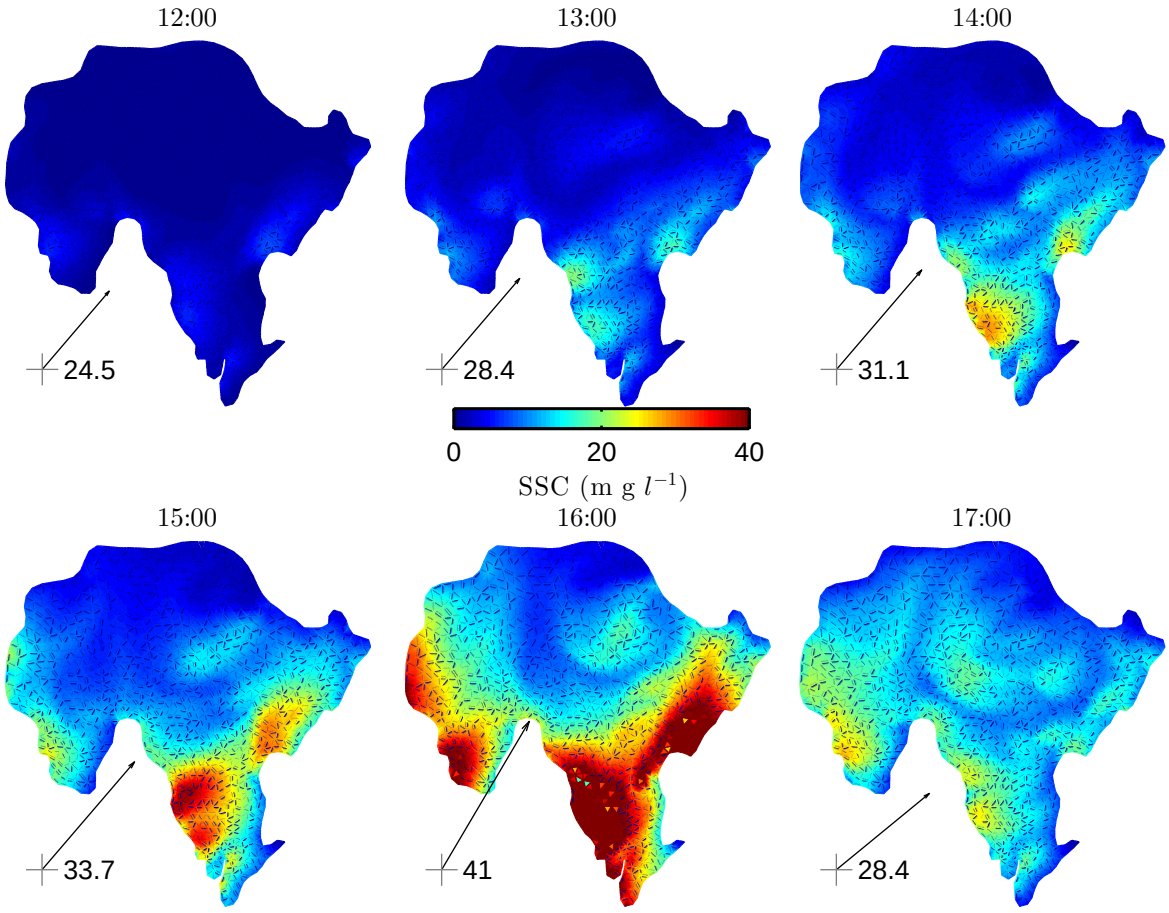

Figure 6.16: Water surface SSC at successive hourly intervals for period of maximum wind forcing for December 1997. Arrows indicates indicate wind direction, with wind speed also given ($m\ s^{-1}$). Run initialised with unlimited mobile bed sediment.

that the erosion rates tend to exceed the deposition rates because they are averaged over a smaller area that predominantly sources material, mainly under the action of the waves.

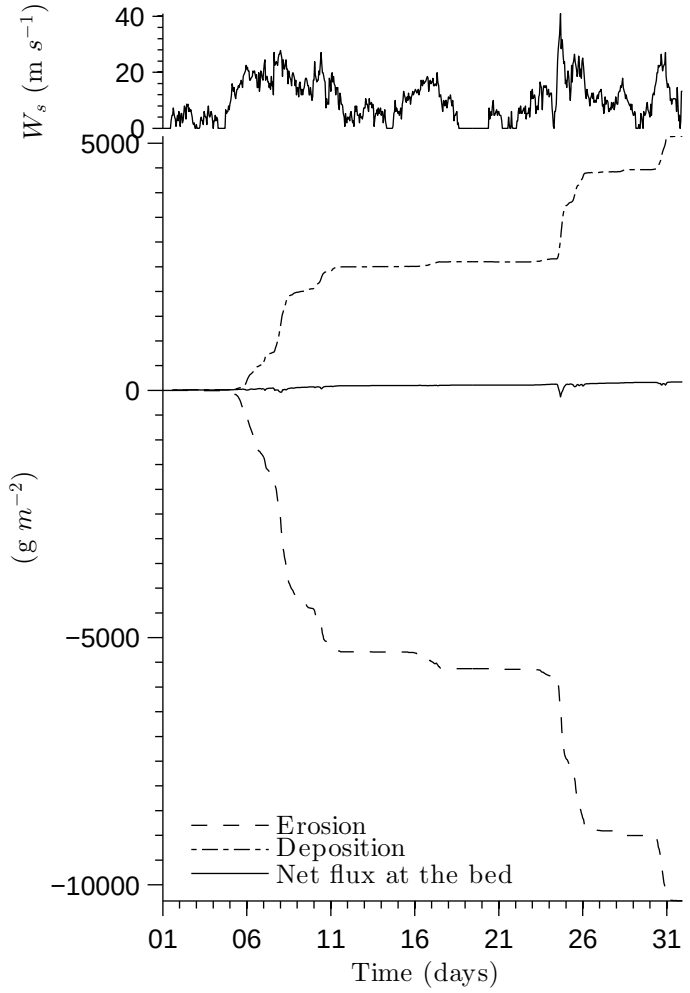

Figure 6.17: Spatial-average time series of erosion, deposition and net sediment accumulation. Wind speed (W_s) serie on the top.

Figure 6.19 summarises the spatial pattern of net bed evolution and also the separated patterns of net deposition and erosion. Absolute change in bed level is artificially high under this simulation on account of the unlimited sediment input from shallow marginal areas. Rates of the order of ± 2 *cm* over 1 month for much of the basin are two orders of magnitude higher than the recent historical rates inferred from the analysis of the sediment cores. Sediment deposition is more widely favoured over large parts of

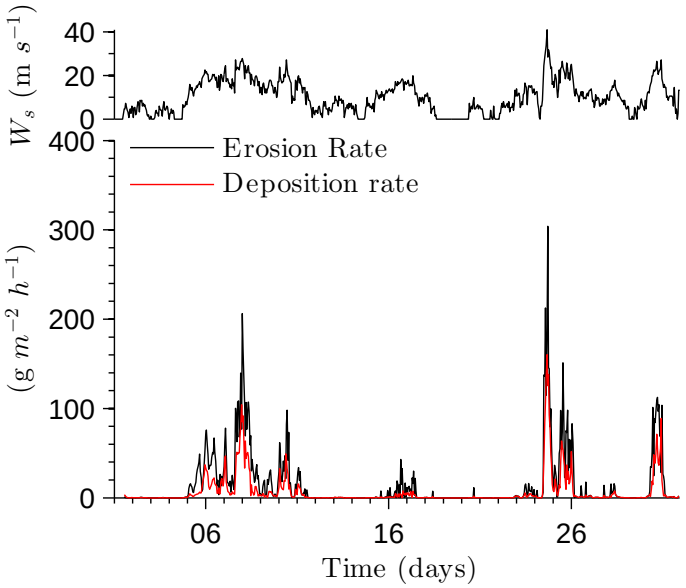

Figure 6.18: Spatially-averaged time series of erosion and deposition rates. Wind speed (W_s) serie on the top.

the basin, with erosion being more heterogeneous and highly concentrated in smaller areas. Depositional areas are preferentially located in the south, west and centre of the lake. Deposition is relatively high along western margins, including those within the lee of the main headland. Deepwater accumulation is relatively low and more uniform over a large extension of the central basin. Areas of rapid deposition broadly correspond to areas of elevated SSC in the surface layer (see Figure 6.14). Erosion 'hotspots' occur along the northern and eastern shores, where wave-generated bottom stresses are highest. Certain areas in the west and northwest experience erosion due to the return circulation currents that flow adjacent to the bed and dissipate on the upwind slope of the basin. Behind the headland that protrudes from the southern shore, erosion can also occur due to the strong circulation produced in this bay and, to some extent, wind-waves.

For the 5 mm mobile bed scenario (see Figure 6.20) the model clearly demarcates better the zones of erosion and deposition. Due to the limited sediment supply, lower absolute rates are obtained. Comparing against the extended 5 mm mobile bed scenario results (Figure 6.21), an incremental change from above is observed, with more subtle zones of erosion and deposition. Lower depositional rates for this last scenario

are broadly comparable with observed historical rates due to the limited supply. This is therefore a more realistic simulation that clearly differentiates depositional and erosional zones, which coincide broadly with the field observations.

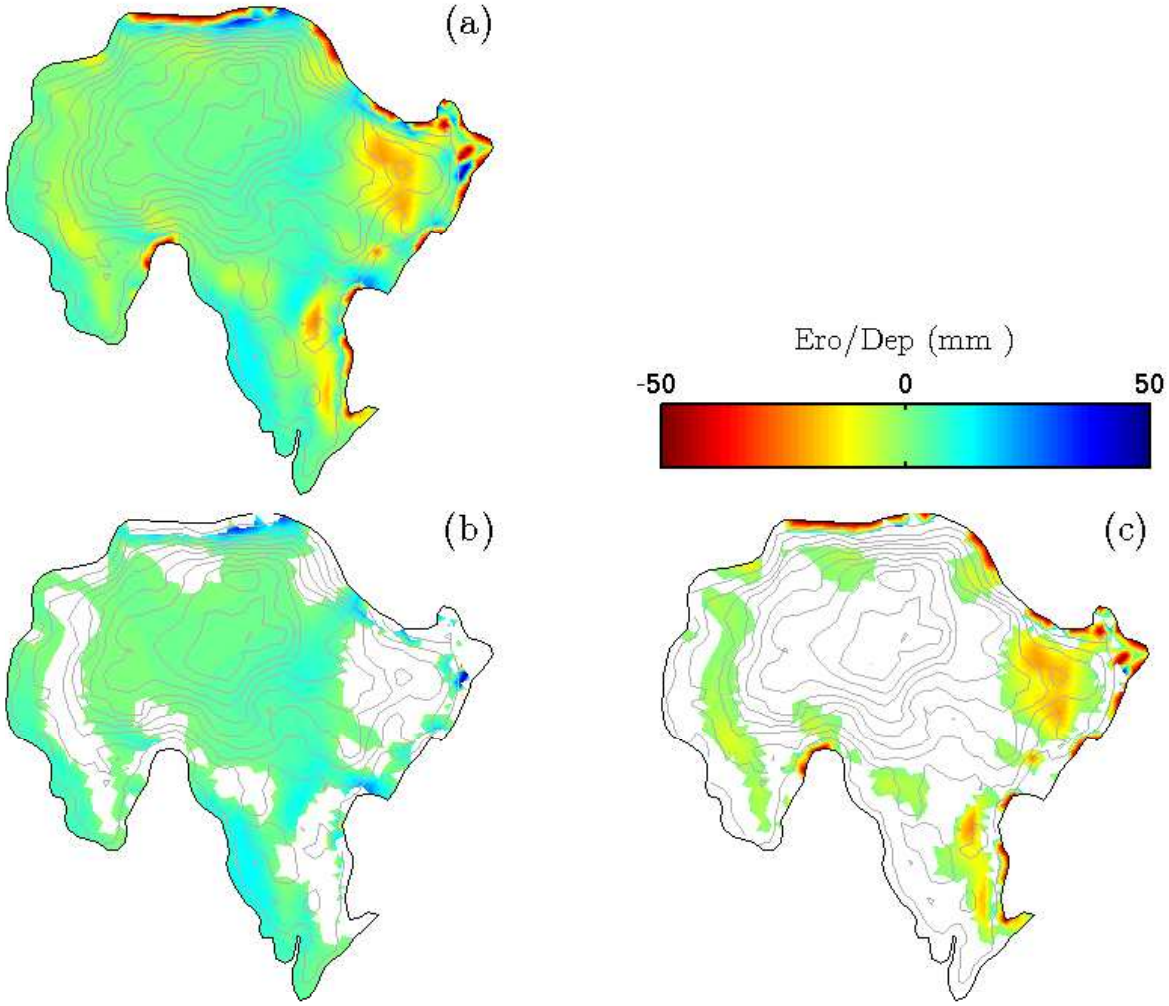

Figure 6.19: Spatial distribution of (a) net bed elevation change (mm); (b) area and magnitude of deposition (mm); and (c) erosion (mm) at end of model run. Run initialised with unlimited mobile bed sediment.

6.4.2 Sediment focusing analysis

Sediment focusing is a processes in which sediments are redistributed from shallower to deeper water by the action of multiple hydrodynamic processes (Likens & Davis,

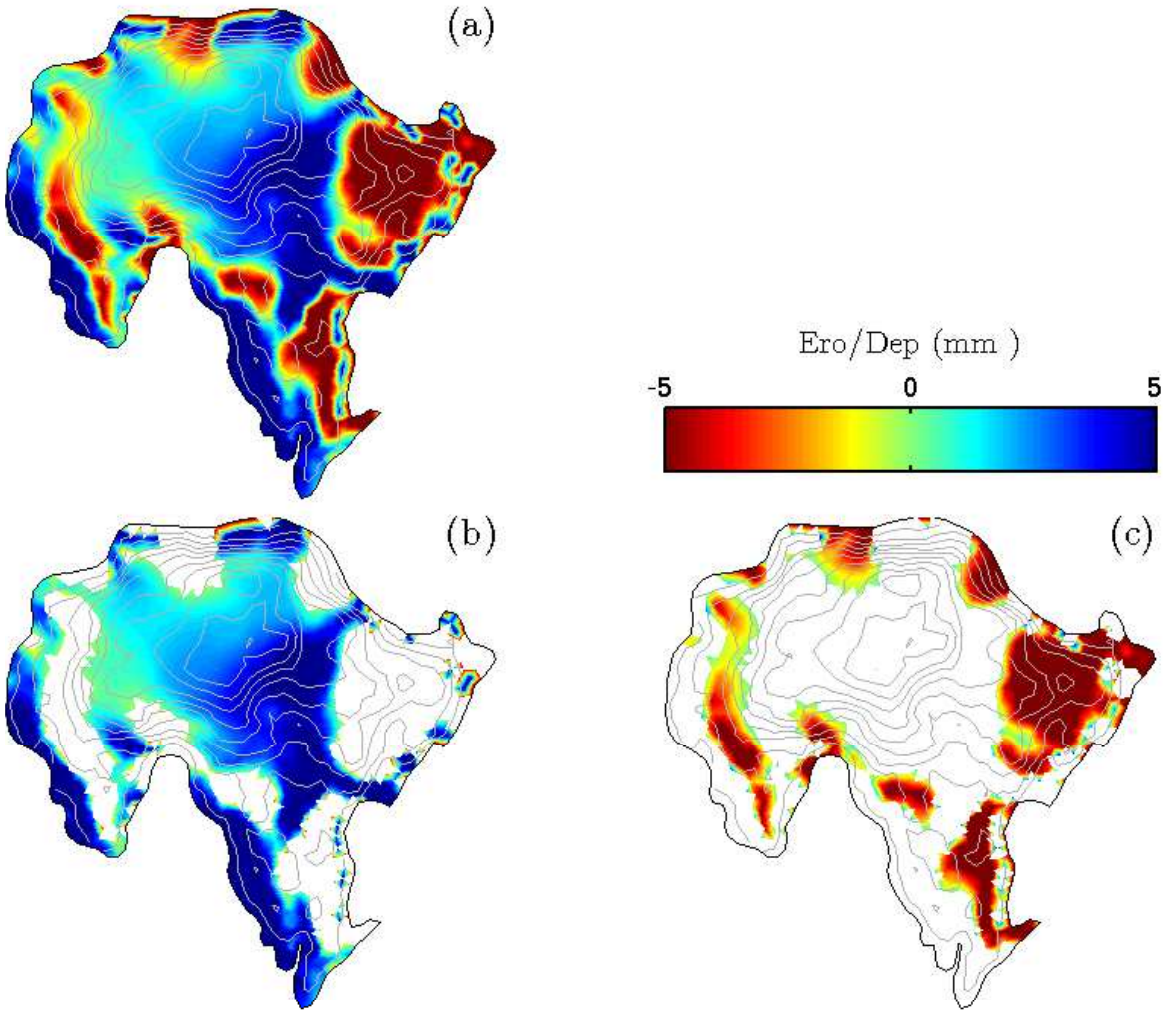

Figure 6.20: Spatial distribution of (a) net bed elevation change (mm); (b) area and magnitude of deposition (mm); and (c) erosion (mm) at end of model run. Run initialised with 5 mm mobile bed sediment.

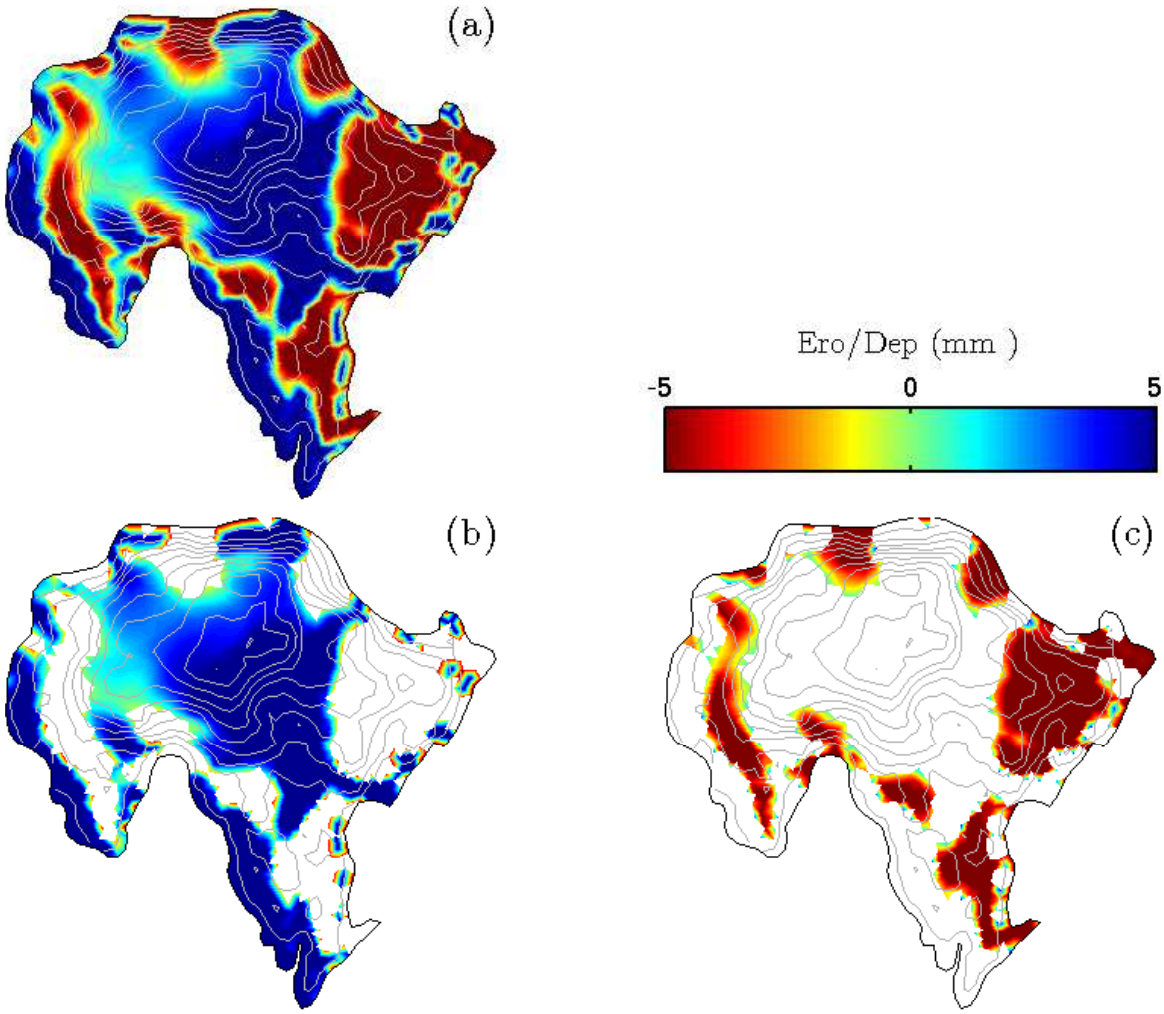

Figure 6.21: Spatial distribution of (a) net bed elevation change (mm); (b) area and magnitude of deposition (mm); and (c) erosion (mm) at end of model run. Run initialised using end sediment conditions of the initial 5 mm bed sediment run.

1975; Blais & Kalff, 1995; Weyhenmeyer *et al.*, 1997). As noted previously, the ^{210}Pb chronology for the CONLM1 core suggests that a degree of sediment focusing occurs in Llyn Conwy since the cumulative unsupported ^{210}Pb inventory exceeds the mean atmospheric flux for this region. However, both the distribution of lake sediment deposits within the basin and the modelled sediment dynamics suggest that the mechanisms determining sediment accumulation are more complex than envisaged in a simple focusing model. To further investigate the importance of sediment focusing processes in Llyn Cowy, the lake bed was divided into 10 different water-depth ranges (Figure 6.22) and the sediment dynamics in each zone evaluated in detail.

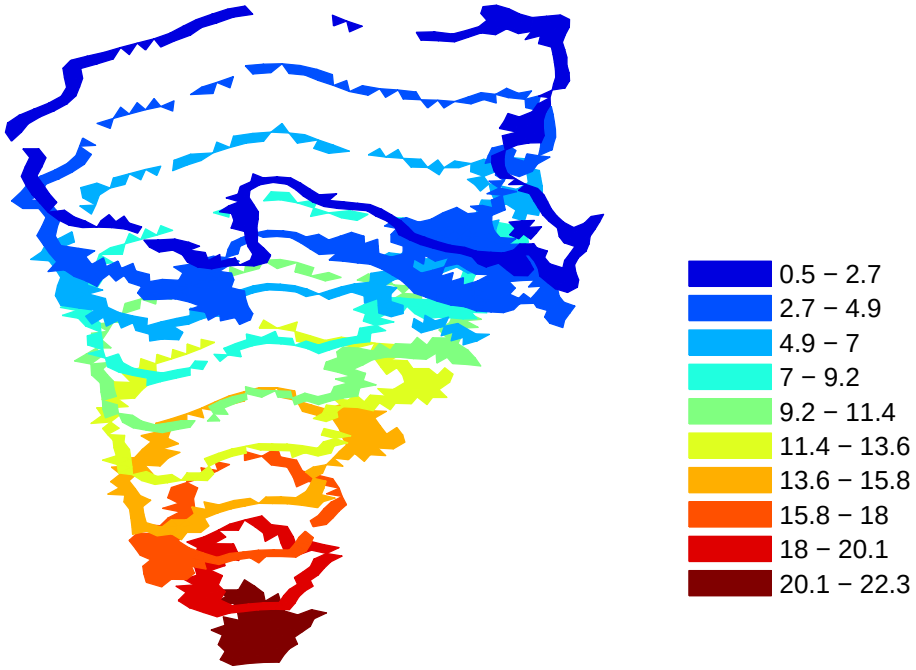

Figure 6.22: 3D perspective view of the spatial distribution of bottom areas for 10 successive water depth (m) intervals.

Curves for cumulative sediment flux at the bed, spatially averaged within each of these depth zones (see Figure 6.23) reveal several important aspects of the bed dynamics. First, it is evident that the shallowest region ($0.5 \leq h < 2.7$ m) effectively shows progressive erosion punctuated by stability (with imperceptible deposition) during calm days. Second, intermediate water depth zones ($2.7 \leq h < 13.6$ m), exept $4.9 \leq h < 9.2$ m depth zones where an overall erosion is presented, show overall net deposition but this

is punctuated by episodes of erosion under strong wind events. The interplay between these processes is also evident within times-series of the instantaneous bed flux (see Figure 6.26). Notably, the depth range from 2.7 to 11.4 m shows a more balanced alternation between deposition and accumulation with little cumulative change relative to the initial conditions (Figure 6.23). In contrast the zone between 11.4 and 13.6 m shows a much stronger depositional tendency interrupted only by the most extreme wind conditions. Third, it is interesting that in the 13.6 to 15.8 m depth zone, the rate of deposition exceeds that in deeper waters, especially between days 5 and 11 of the simulation. Finally, in areas deeper than 13.6 m, deposition is clearly the dominant processes (see Figure 6.23). Even here, however, the simulations shows that very slight erosion can occur on rare occasions when the wind speed exceeds 25 $m\ s^{-1}$ (see Figure 6.26).

Comparing the cumulative sediment flux at the bed within each of the depth zones given by the unlimited bed supply and the 5 mm mobile bed sediment conditions at the shallowest region ($0.5 \leq h < 2.7\ m$), the whole 5 mm sediment layer is eroded during the first strong wind forcing episode around day 6 followed by a strong accumulation of sediments during the rest of the period (Figure 6.24). This accumulation is preferentially in the western and southern sectors where the wind-wave action is weaker. More intermediate depths ($4.9 \leq h < 9.2\ m$) are still overall eroded since these are more affected by currents where erosion and deposition alternate depending on the wind forcing intensity (see Figure 6.27). Similarly to the first unlimited bed supply scenario, areas deeper than 13.6 m still show overall net deposition.

The extended 5 mm mobile bed sediment scenario, which is intiated with a concetration provided by the final concentration of the 5 mm mobile bed sediment scenario, imposes an initial displacement of the curves in Figure 6.25. This scenario shows overall net deposition in all the bottom depth zones (Figure 6.25). Erosion of sediments is limited to episodic wind speeds $> 25\ m\ s^{-1}$ at those intermediate depths ($4.9 \leq h < 13.6\ m$) affected mostly by currents. Erosion by wind-waves does not occur since sediments have already been redeposited below the wind-wave base. Deposition is preferently at the shallower and the deepest areas where the action of currents is weaker see (see Figure 6.28).

An analysis of the frequency of erosion and deposition in the various depth zones is presented in Figure 6.29. The frequency of erosion decreases exponentially from the shallowest waters ($h < 2.7\ m$) where erosion occurs $\sim 64\%$ of the time, to the

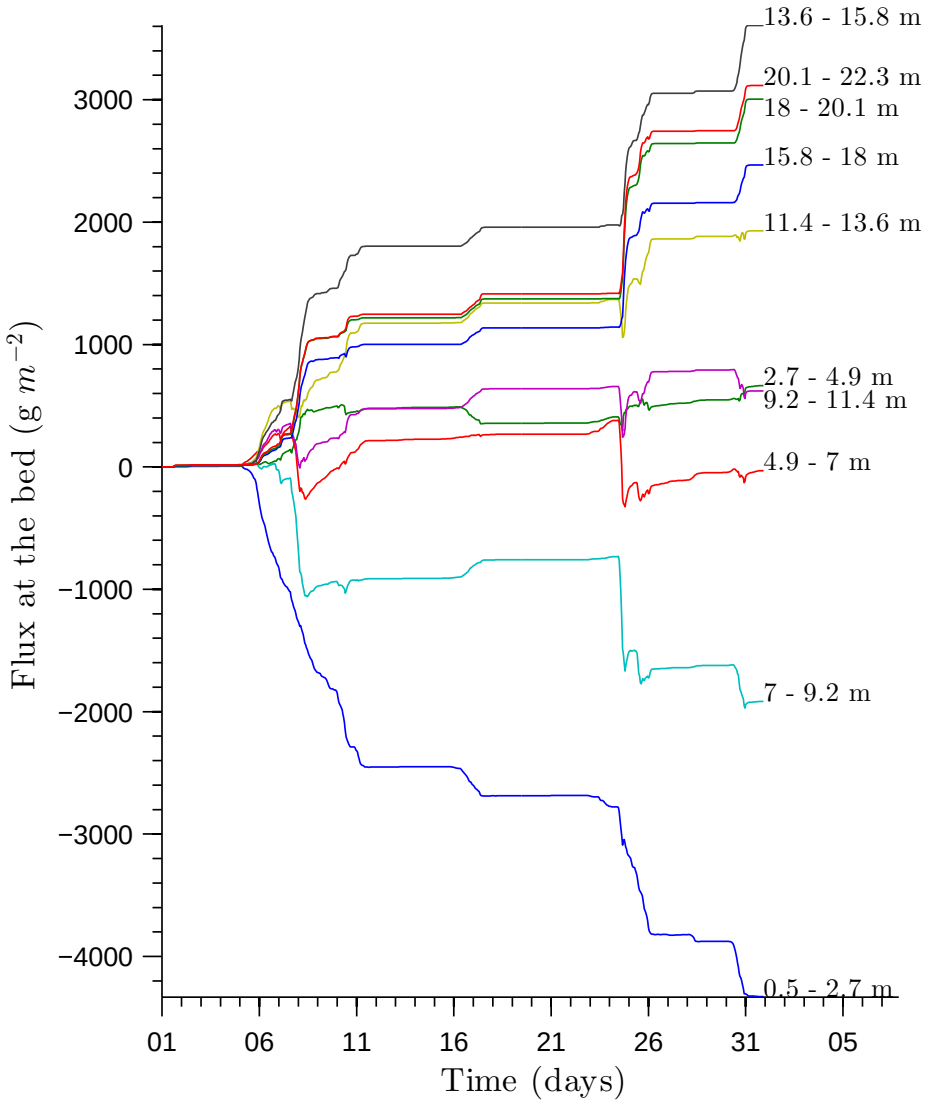

Figure 6.23: Spatially-averaged vertical flux at the bed (deposition positive, erosion negative) in 10 different water-depth ranges. Run initialised with unlimited mobile bed sediment.

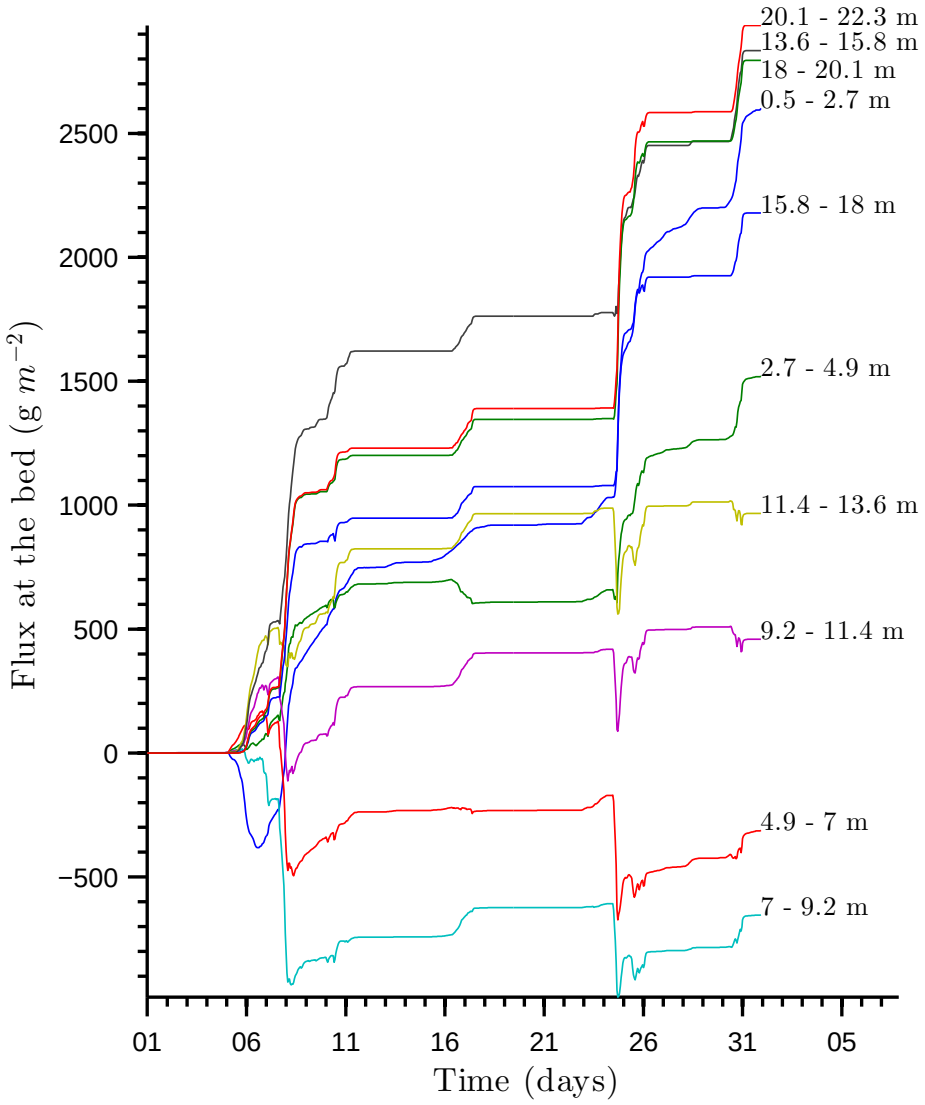

Figure 6.24: Spatially-averaged vertical flux at the bed (deposition positive, erosion negative) in 10 different water-depth ranges. Run initialised with 5 *mm* mobile bed sediment.

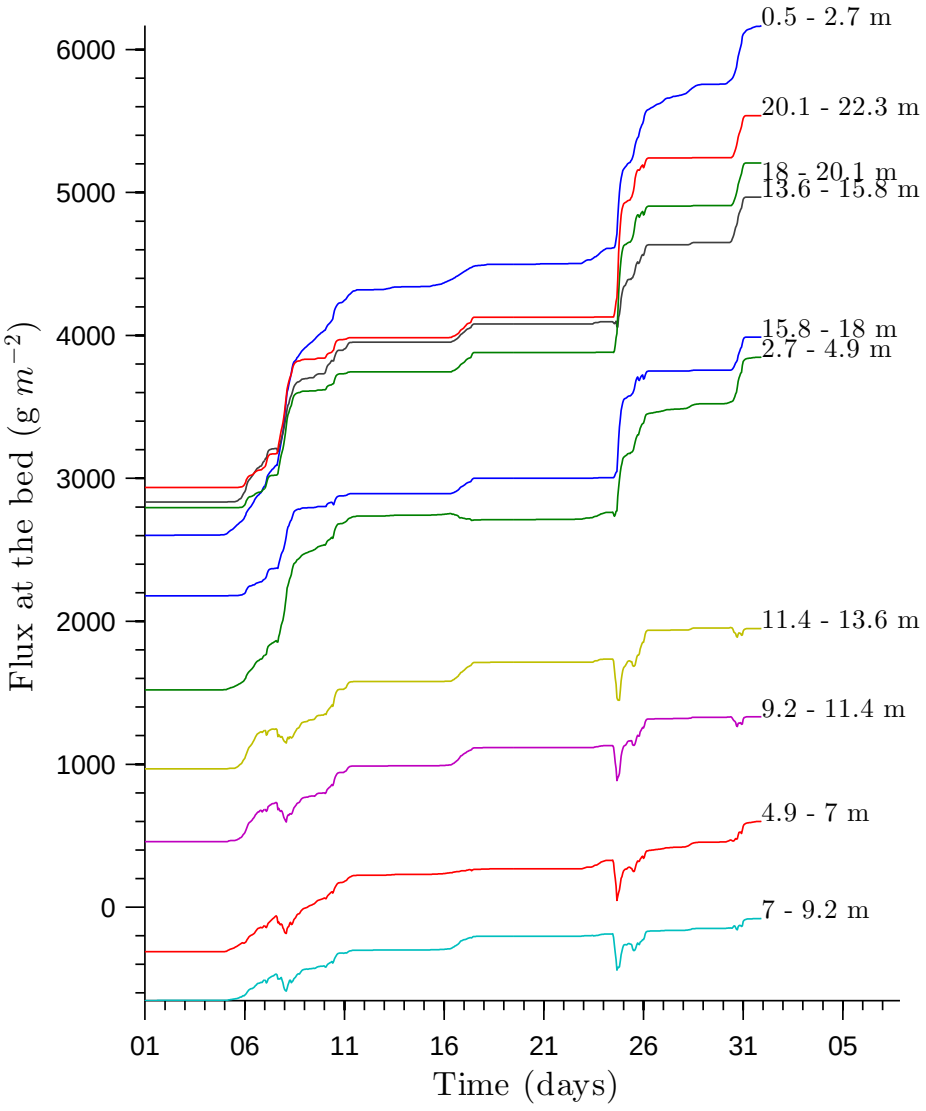

Figure 6.25: Spatially-averaged vertical flux at the bed (deposition positive, erosion negative) in 10 different water-depth ranges. Run initialised using end point of initial 5 *mm* bed sediment run.

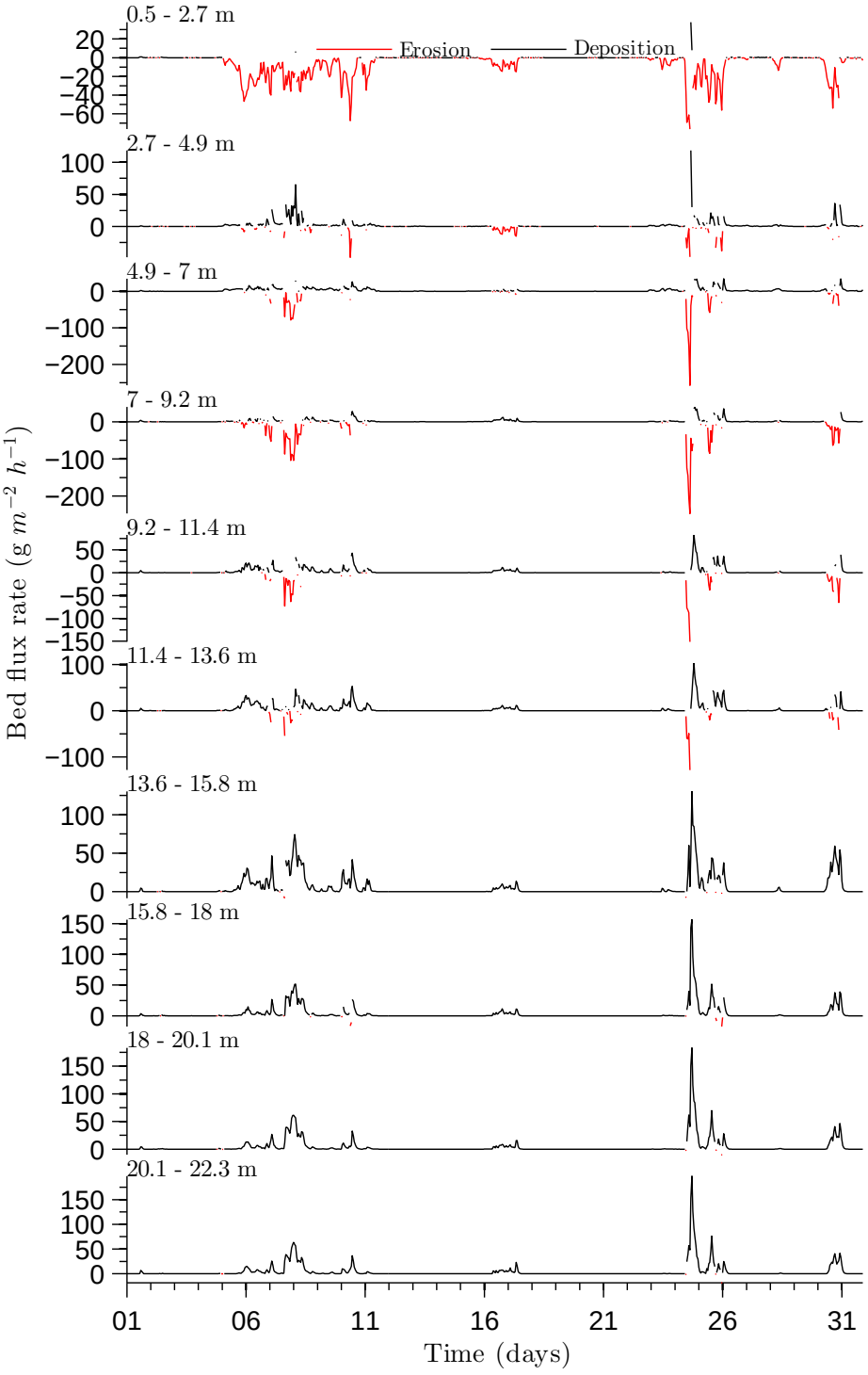

Figure 6.26: Time variation in spatially-averaged vertical flux at the bed (deposition positive, erosion negative) in 10 different water-depth ranges. Run initialised with unlimited mobile bed sediment.

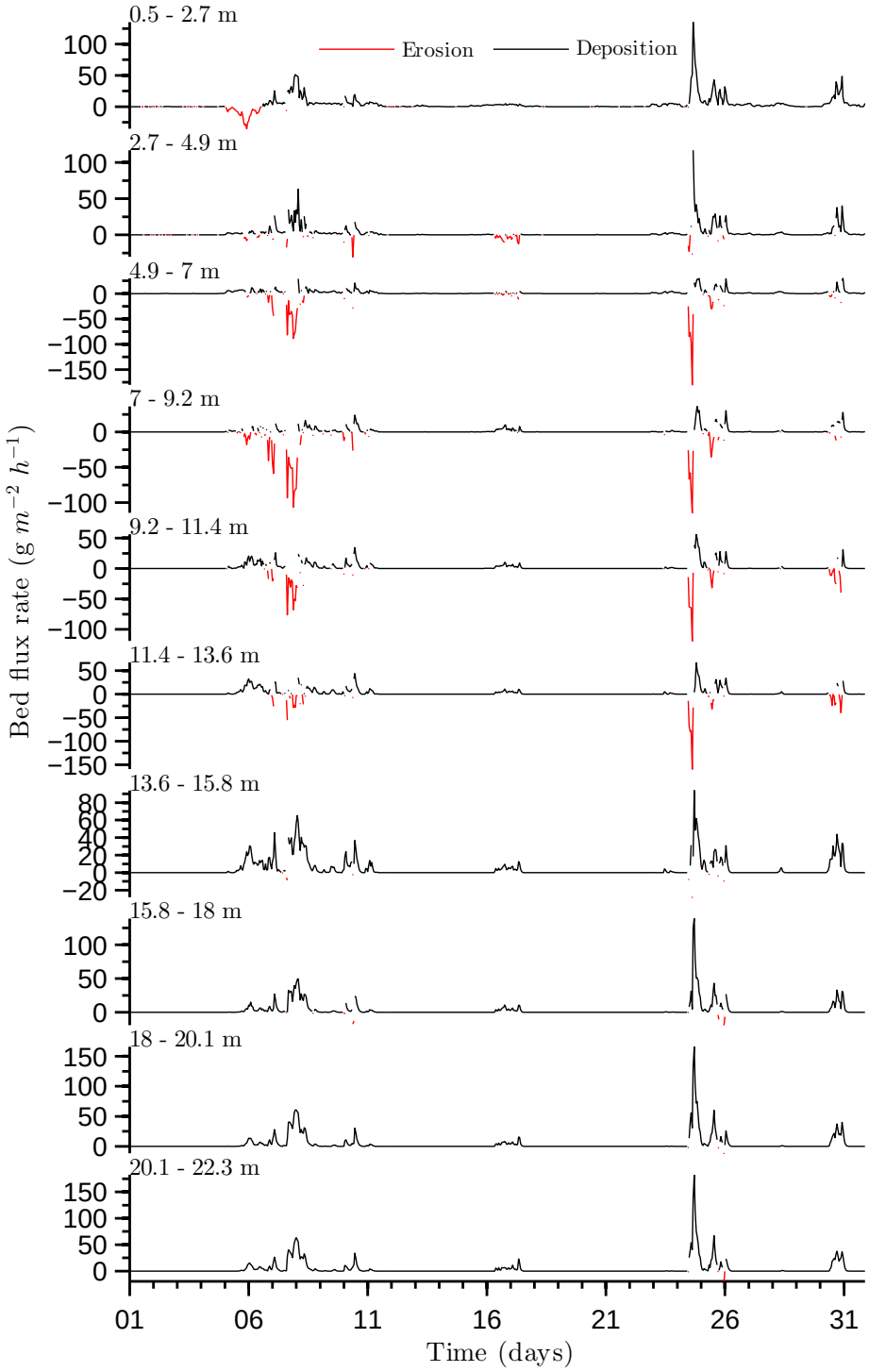

Figure 6.27: Time variation in spatially-averaged vertical flux at the bed (deposition positive, erosion negative) in 10 different water-depth ranges. Run initialised with 5 *mm* mobile bed sediment.

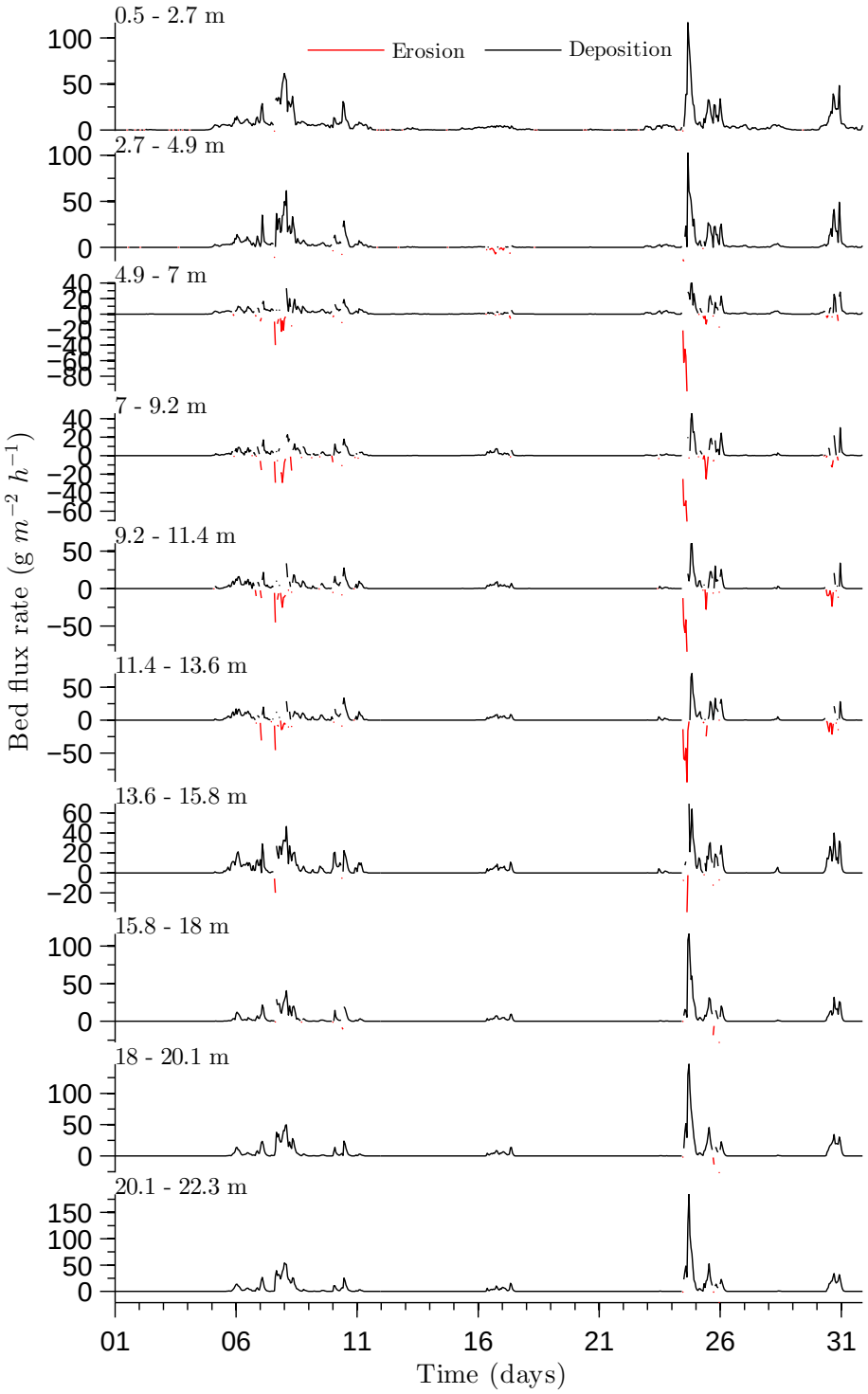

Figure 6.28: Time variation in spatially-averaged vertical flux at the bed (deposition positive, erosion negative) in 10 different water-depth ranges. Run initialised using end point of initial 5 *mm* bed sediment run.

the deepest areas where erosion occurs less than 2.5% of the time. This coincides with a negative sediment flux at the bed (erosion) in the shallow water zone and a positive (depositional) flux in deeper water (Figure 6.29 b). The most frequent deposition ($\sim$ 68%) occurs at intermediate water depths 4.9≤h<7.0 m, and not at the deepest sectors, where deposition occur less than 40% of the time. This interesting finding can be explained by the fact that the deepest areas are subject to current velocities associated with the overall hydrodynamic circulation that lead to long periods during which the bed stress exceeds the deposition threshold whilst remaining below the erosion threshold. Such periods of effective bed stability become much less frequent in shallower water, since they depend on an absence of wave action and therefore calm weather conditions, which are unusual at this site.

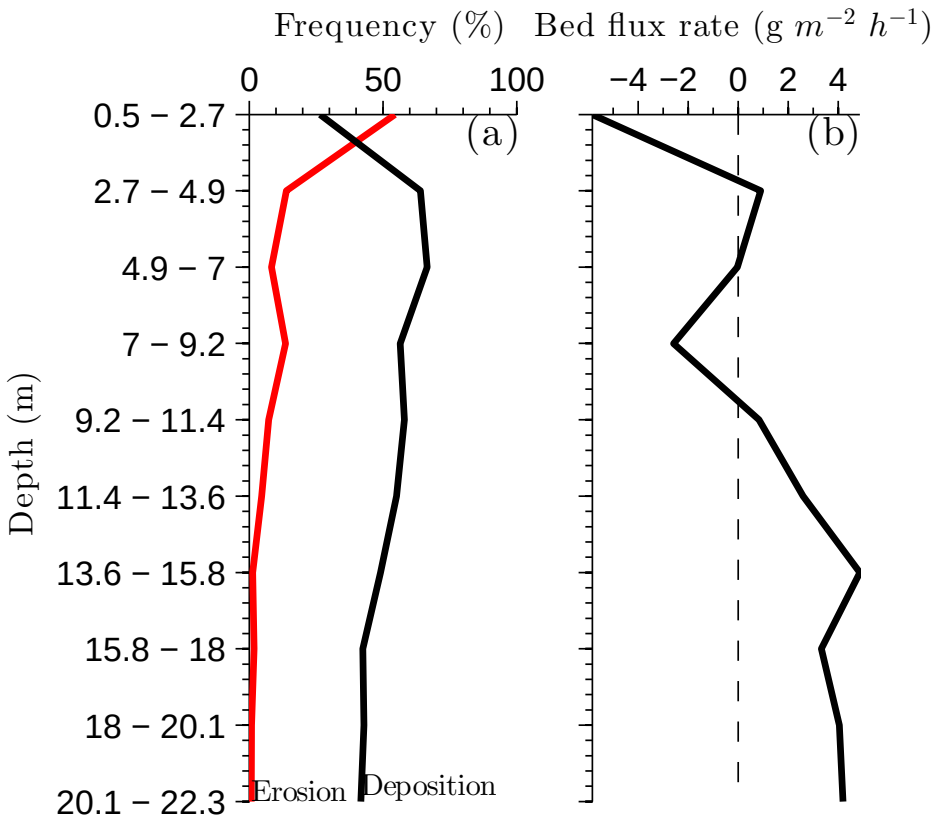

Figure 6.29: a) Frequency analysis of erosion and deposition within different water-depth ranges. b) time- and space-averaged bed flux (erosion negative) within different depth ranges.

These results indicate that sediment focusing in Llyn Conwy occurs partially and in

a complex manner. Sediments are not strictly deposited in the deepest part of the lake, although its conical shape may favour the deposition in the central basin. Instead, sediments are deposited irregularly in those areas below about 2.7 m reaching a maximum deposition rate at intermediate depths. The radiometric dating of the CONLM1 core (obtained in approximately 9 m of water) also suggests that this intermediate depth zone has been subjected to sediment focusing (see Figure 6.30).

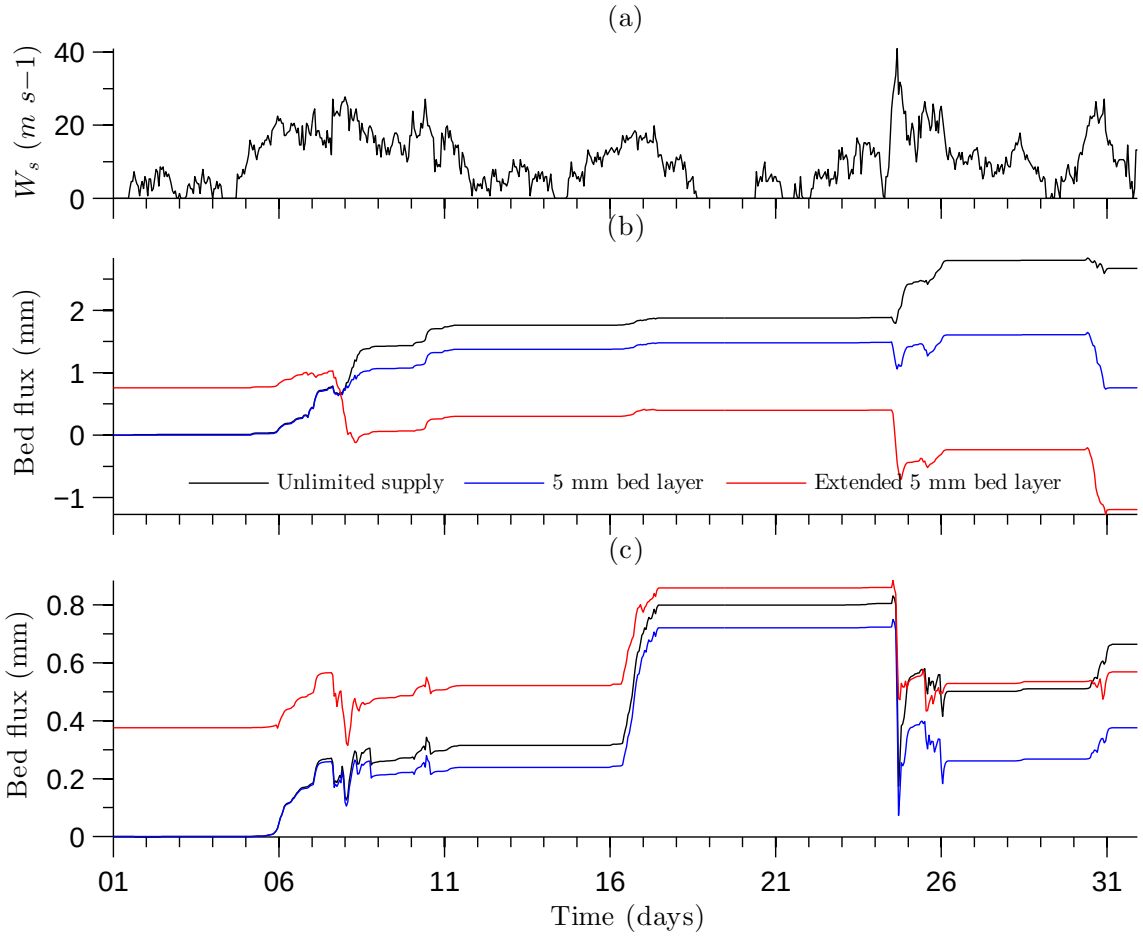

Figure 6.30: a) Wind speed; b) bed flux (mm) at the CONLM1 location; and c) at CON4 location.

A comparison of the sediment bed flux at the two core locations (Figure 6.30) indicates that for the unlimited sediment supply and the 5 mm bed layer supply scenarios accumulation is the dominant process at both sites. For both scenarios at both sites there is an overall increase in bed level over the month-long simulation period albeit

with some periods of erosion. The bed flux of sediments is larger at the CONLM1 site since eastern sectors of the lake are subjected to greater current and wind-wave activity compared to the more calmer zones in the west where CON4 was recovered. At both core sites, sediment accumulation increases substantially for those periods where $W_s > 10\ m\ s^{-1}$, but it is interrupted by erosion events when $W_s > 20\ m\ s^{-1}$. The behaviour of the bed flux for the more realistic extended 5 mm bed layer scenario (see Figure 6.30) supports the suggestion that the top of the CONLM1 core has been lost. Results for this scenario demonstrate that an overall negative (erosion) bed flux balance is obtained by the end of the simulation period. In contrast, for the same scenario sediment accumulation is the dominant process at CON4 site although short-lived periods of erosion still occur. This supports the hypothesis, based on core dating, that such western areas are more subject to sediment accumulation. The analysis of bed flux at both core sites therefore supports the spatial configuration of erosional and depositional sectors predicted by the model, and also the heterogenity of sedimentary processes including sediment focusing in Llyn Conwy.

6.4.3 Evaluation of alternative sediment focusing mechanisms

Hilton *et al.*, 1986a identified ten different mechanisms involved in sediment distribution within small lakes (see discussion in Chapter 1). Only four of those are strictly implicated in sediment focusing as such, and not all of these are relevant to upland oligotrophic lakes such as Llyn Conwy. Each is considered further below in the context of the empirical and modelling evidence presented thus far.

The first factor identified by Hilton *et al.*, 1986a is organic degradation. Llyn Conwy is very much an oligotrophic system in that it hosts virtually no aquatic macrophytes and has extremely low turbidity and nutrient loadings. Its catchment is isolated from urban influences and nutrient-rich discharges. Moreover, the lake is mixed through most of the year and is only weakly and intermittently stratified during summer. The low inflow of organic matter and the strong water mixing prevent the onset of anoxia and eutrophication processes that might otherwise cause the decomposition of organic matter and sediment focusing in the deepest areas. This mechanism can thus be completely discounted here.

The second factor involves sliding and slumping within the basin marginal areas. According to Håkanson, 1977b sediment will not accumulate on slopes > 14%, with accumulation becoming progressively more likely as the slope declines to 4%. Below

4%, the slope does not impart any significant spatial variation in accumulation. A map of bottom slope distribution in Llyn Conwy (Figure 6.31a) reveals a concentric zone of steep slope around the deepest basin in which slopes are relatively high > 10%, especially along the northern and northeastern shores where slopes attain values up to 23%. In contrast, more even areas with slopes < 5% are found in the centre of the basin and within the shallower areas near the western and eastern shores and within the southern embayment. Slopes around much of the shoreline are relatively consistent at around 7%, except in the north and northeast shores where the shoreline is steeper, reaching 13% in places. A summary of spatially-averaged bottom slopes within the depth zones defined in the preceding section (see Figure 6.31b) reveals that relatively low gradient areas are preferentially located in the deepest part of the lake, with a narrower range of shallow depths also characterised by low bed gradients.

The Hakanson classification of bottom slope is applied in Figure 6.31c, from which it is clear that most of the basin (more than 70% of the bottom area) is likely to accumulate sediments to at least some degree, whereas the other 30% would favour mobilisation, either by sliding or by rotational failure, of sediments covering shallower areas toward the deeper basin. Potential sediment pathways can be visualised by constructing a slope network of the kind presented in Figure 6.31d. This reveals long paths that extend from the peripheral areas outside the concentric zone of steepest slope, especially from the western and northern shores, into the deep central basin. These could conceivably facilitate sliding of material into the deepest parts of the lake.

A comparison of the slope zones with the observed distribution of bottom sediments (Figure 6.1) indicates that lake sediments are indeed absent from some areas of steep slope to the north. The western and southern margins of the deepest basin are, in contrast, mantled with sediment despite extensive areas of intermediate slope and localised slopes > 14%. The evidence for slope-control over sedimentation in Llyn Conwy is thus rather inconclusive. It is certainly a potential factor, and may be responsible for disturbance to the sediment sequence that the Ekman grab sampling cannot resolve. Some form of bed imaging (e.g. sidescan sonar) seismic survey would be required to investigate the prevalence of slope related slides and slumps. An early application of such techniques by Cronin *et al.*, 1993 to another small upland lake in Wales did find limited evidence for slumping of highly organic sediments on slopes of about 15 degrees (26%).

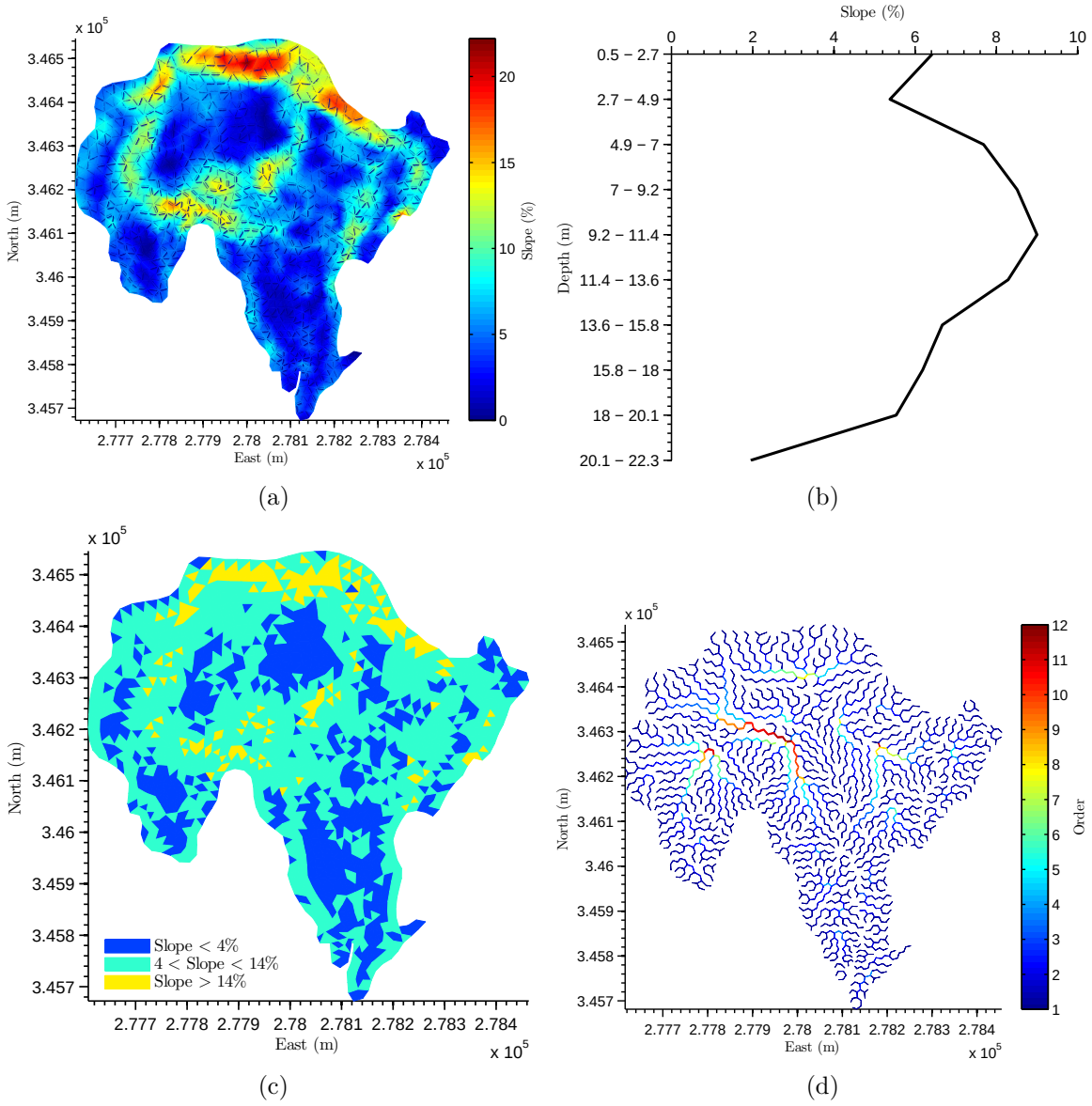

Figure 6.31: Summary analysis of Llyn Conwy bottom slopes. a) Spatial distribution of bed slope, b) spatial average bottom slope in different water-depth ranges, c) distribution of bottom areas according Håkanson, 1977b classification, d) downslope pathways, with colour map indicating network order.

Hilton *et al.*, 1986a also describe a process that they term intermittent complete mixing, driven by widespread resuspension, mixing, and settling. This leads to sediment focusing by virtue of the greater mass of material in the water column above deeper areas. The analysis of hourly wind forcing data presented in Chapter 5 revealed high variability in the wind speed record with annually averaged hourly $\sigma \approx 6$ $m\ s^{-1}$. The analysis also showed a weak daily periodicity, and wind forcing conditions dominated by southwesterly winds that can reach 40 $m\ s^{-1}$. A persistent overturn of the thermal structure during winter and autumn, and intermittent and high frequent mixing of water temperature during summer occur as the thermal structure responds to this meteorological forcing. Such behaviour is only possible in small lakes such as Llyn Conwy, where the thermocline is rapidly destroyed, thereby allowing the resuspension of sediment from deeper waters. Wind forcing conditions also lead to a complex spatial distribution of bottom stress and sediment dynamics around the lake. Over the duration of the sediment model runs, large incremental increases in wind forcing drive resuspension of sediments over virtually the entire lake bed via the action of strong vertical circulation that generates a spatially-averaged $\tau_t > 0.5$ $N\ m^2$. The initial transport-limited model runs predict erosion rates of up to 150 $g\ m^{-2}\ h^{-1}$ in the shallower northern and eastern areas, accompanied by deposition at a rate that increases progressively with water depth (see Figure 6.26). Intermittently eroded marginal sediments are thus efficiently redistributed to intermediate and deeper areas where the probability of deposition is higher (see Figure 6.29). As established by Bunge & Bryson, 1956, the occurrence of a stress-drop jet is a major factor in intermittent complete mixing that results in sediment focusing. This phenomenon emerges in the hydrodynamic simulations of Llyn Conwy and its existence is corroborated by the flow velocity profiles measured with the ADCP. Both data and model predictions show that a drastic drop in the wind forcing leads to a reduction of the flow intensity and also the reversal and attenuation of the vertical circulation in the deepest part of the basin, leaving the hypolimnion in a quiescent state. The dynamic of both thermal structure and hydrodynamics are thus consistent with the intermittent complete mixing processes, which can therefore be considered an important mechanism of sediment focusing in Llyn Conwy.

The fourth mechanism, peripheral wave action is clearly the most important driver of sediment resuspension in the near-shore regions of Llyn Conwy. This material is efficiently transported out to deeper water, where settling occurs. Despite the limited

fetch, significant wave heights of 0.3 m commonly occur along the northern and eastern shores, with heights exceeding 0.5 m under extreme conditions. Combined current and wind wave modelling shows that the wave-generated bed stresses are typically a order of magnitude greater than those resulting from currents in shallow water areas.

The frequency of strong winds makes peripheral wave action an important mechanism for sediment focusing in Llyn Conwy. Constant exposure to erosion in the northern and eastern sectors precludes the accumulation of lake sediments, and the bed is variously made up of coarse lag gravels and relatively resistant pre-Holocene deposits. Hilton *et al.*, 1986a found that 6% of the total variance of the accumulation rate estimated by the deployment of sediment traps in Esthwaite water, UK, was due to wave action. This is manifest as a negative correlation between sedimentation rate and wind fetch. Deposition rates estimated using sediment traps in lakes located in the Muskoba-Haliburton region of Canada (Hilton, 1985) similarly indicated that intermittent complete mixing and peripheral wave action were the main mechanisms of sediment focusing.

The above analysis suggests that three of the four mechanisms that Hilton *et al.*, 1986a associates with sediment focusing can be considered potentially important in Lly Conwy and possibly within oligotrophic upland lakes in general. Intermittent complete mixing and peripheral wave action appear to be the most important mechanisms to explain sediment focusing, since both are consistent with the observed and modelled hydrodynamics. There is presently no direct evidence to support a role for sliding and slumping along high gradient downslope pathways.

Chapter 7

Discussion

7.1 Introduction

The research presented here has shown that the hydrodynamics and sediment dynamics of upland lakes are driven by a complex interaction between the incident meteorological conditions, the lake bathymetry and the characteristics of the sediments. Processes such as water thermal stratification, vertical and horizontal circulation and sediment transport are driven by this interaction and by the interrelationship between these processes. Upland lakes are typically characterized by strong but variable meteorological forcing (e.g. George *et al.*, 2001; Bell *et al.*, 2006). This has been documented here through analysis of historical records for the Llyn Conwy area. Wind speed at Llyn Conwy is highly variable ($\sigma \approx 7\ m\ s^{-1}$), especially during winter months when this varies between 0 and 40 $m\ s^{-1}$. The seasonal temperature is also large with monthly average air temperature of over 25^oC in June and below 4^oC in December. Incoming solar radiation, which is a key variable influencing the lake stratification behaviour, varies between nearly 100 $W\ m^{-2}$ in winter up to 1000 $W\ m^{-2}$ in summer.

Bathymetry exerts a major control on both hydrodynamics and sediment dynamics. In tidal systems, the velocity field may be more sensitive to changes in the bathymetry than to the bottom roughness (Cea & French, 2012). In lakes with highly complex bathymetry, the pycnocline turbulence transport varies with bottom slope. About 80% is dissipated where bottom slopes are up to 10%, 60% where bottom slopes are 3%, and less than 7% where bottom slopes are about 0.1% (MacIntyre *et al.*, 2009). The highly irregular bathymetry of Llyn Conwy is comprised of an extended shallow ($h \approx 3\ m$) region in the south and the west where bottom slopes are $< 5\%$, and a deeper

sector ($h \approx 20\ m$) towards the centre, where slopes can be up to 22%. The slightly convex hypsographic area-depth curve indicates a potentially significant exposure of the lake bottom to wind-wave sediment resuspension.

The study of hydrodynamics and sediment dynamics in upland lakes has been approached in this thesis by the implementation of computational models. The main model used is a 3D ocean community code, *FVCOM*, which has been improved and adapted for lake problems by the creation of a graphical user interface, *FVCOM-GUI* and by the addition of a new wind wave model (*UCL-SWM*). A new 1D dynamic model (*UCLAKE*), has also been programmed as a pre-cursor to studies using the 3D model, to investigate the thermal structure at multiple timescales.

The numerical modelling approach provides new insights into the hydrodynamics and sediment dynamics, and their relationships, in upland lakes. Such understanding is crucial in order to provide a scientifically informed context for the coring and analysis of lake sediments for environmental reconstruction (Håkanson, 1984; Rowan *et al.*, 1995). The following sections disccuss the key results emerging from the modelling of hydrodynamics and sediment dynamics in Llyn Conwy and their implications for the applicability of the sediment focusing theory. Finally, some guidelines for the optimal acquision of sediment cores are provided in order to improve the robustness of palaeolimnological studies based on upland lakes.

7.2 Modelling of Upland Lake Thermal Structure

A first step towards the understanding of lake hydrodynamics is the investigation of the thermal structure, particularly the behaviour of the mixed layer (Imberger, 1985; Spigel *et al.*, 1986). Knowledge of the time-variation in stratification allows inferences regarding lake sensitivity to meteorological conditions and, in particular, the intensity of turbulent mixing through the water column and how frequently the mixed layer is depened.

A new 1D dynamic eddy-difusivity lake model (e.g. Riley & Stefan, 1988; Hondzo & Stefan, 1993), *UCLAKE*, has been implemented and calibrated for Llyn Conwy in order to investigate the thermal structure over inter-seasonal periods, at daily and subdaily time scales. A key feature of the model is its ability to dynamically adapt the numerical timestep to guarantee the good computational performance required for long-term studies of thermal structure (e.g. Hondzo & Stefan, 1991). The model is

used to analyse the sensitivity of thermal structure to the important parameters in the advection-diffusion model of water temperature incorporated into the higher dimension *FVCOM* model.

The calibration of *UCLAKE* was achieved with respect to three parameters: Kz_{max}, C and η; commonly subjected to calibration in other eddy difusivity models such as *MINLAKE* (Riley & Stefan, 1988). In some similar models (e.g. Hondzo & Stefan, 1993) the calibration procedure is simpler because the highly sensitive Kz_{max} is estimated as a function of the lake surface area and the buoyancy frequency (N). Other models (e.g. Henderson-Sellers, 1984) have estimated η as an exponential function of the secchi-disk depth, but the accuracy of such a function is highly dependent on the availability of observed data needed to estimate it.

Whilst most 1D lake dynamic models are calibrated and validated against depth-averaged water temperature time series (e.g. Hondzo & Stefan, 1993; Gal *et al.*, 2003), calibration of *UCLAKE* was based on the most appropriate specific temperature information dimensions (time series or water depth profiles). Following the common practice, calibration by comparing water temperature time series was initially chosen. The calibration and sensitivity analysis was carried out at three different depth levels: surface, middle and bottom, for which different sets of parameter values were obtained. The results indicate that Kz_{max} and C decrease in the upper half layer, whereas η increases. The sensitivity analysis shows that, at the water surface layer between March and April, the model is quite sensitive to changes in any of the three parameters. This is because, during these months, the lake undergoes a transition from a long period of overturn to a period of stratification facilitated by a decline in wind speed and the rapid increase in solar radiation. In the middle layer, from April to December, the model is very sensitive to changes of Kz_{max} and η, whereas for C the model is sensitive only during March and April. In general, the sensitivity of Kz_{max} and η seems to increase with depth, especially for summer and autum months, whereas C is only significantly sensitive between March and April.

An alternative calibration procedure (not reported in detail here) using hourly temperature profiles yielded different and heterogenous sets of parameters at each time. Despite this, parameters show certain homegenity by grouping them by months or seasons. Since this approach was not considered practical because of the difficulties in grouping parameters (which also affects the parsimony of the model), a calibration procedure based on water temperature time series was adopted in order to obtain an

unique value for each unconstrained parameter. The model calibration results indicate a generally excellent performance with NSE = 0.97 and RMSE = 0.71 ^oC for $Kz_{max} = 8.90\times10^{-5}$, $C = 0.2$ and $\eta = 2.0$ out of 80 model simulations. Similar procedures applied by Hondzo & Stefan, 1993 to calibrate a 1D dynamic lake model to a wide range of small lakes, yielded an RMSE of 1.1 ^oC. In another example, trial and error calibration of a 1D dynamic lake model of a reservoir by Bonnet *et al.*, 2000, where the parameters were divided into three different groups: heat exchange, dispersion processes and inflow and outflows discharges, yielded an RMSE of 0.57 ^oC.

The performance of *UCLAKE* is also very good for the validation period, which lends confidence to the calibrated parameter set values. The model performance yielded NSE > 0.95 for surface, mid-depth and bottom layer water temperature time series. The comparisons between observed and simulated water temperature profiles in the validation period yield an average RMAE of 8.1%, and RMAEs $< 10\%$ for 77% of the validation period. A high RMAE of 50% was found for some short periods in February and March when the lake is well-mixed and the water temperature falls to $\approx 4^oC$. To deal with low water temperature, some models (e.g. Hondzo & Stefan, 1991) include a threshold under which the model is not able to make any temperature estimation. In other energy-budget models (Imberger & Patterson, 1981; Spigel *et al.*, 1986) the time-step is adaptated within a range from 0 to 24 h as a function of subdaily water-surface energy balance, and the temperature of inflow and outflow. Other sources of discrepancies between observed and simulated temperatures especially at the epilimnetic layers are probably due to the sensitivity of changes in meteorological information such as air and dew point temperature (Hondzo & Stefan, 1992). Unreliable wind forcing information is another source of temperature errors, because most of the components of the heat energy balance at the water surface depend of this variable (Gal *et al.*, 2003).

The analysis of the thermal structure indicates that the mixed layer only persists for short continuous periods (< 20 days) in May, June and July. The mixed layer is quite unstable because of persistent disrruptions of the thermal stratification by the action of high sustained wind speeds during short periods facilitated by a weak thermocline (maximun ΔT 6 ^oC); this allows the continuos stirring of the water column. These periods are also characterized by having a typical thickness (h_e) between 2 and 2.5 m, which can increase up to $\sim$15 m when sudden increments of wind speed occur. On the other hand, in autumn, the lake is weakly and intermittent stratified about 30% of the time because of the low shortwave solar radiation and energetic wind forcing conditions

(averaged $Ws = 14.7\ m\ s^{-1}$). At the end of spring, the lake is predominantly stratified ($> 70\%$ of the time), facilitated by the relatively low wind speed ($< 9\ m\ s^{-1}$) and the rapid increase in shortwave solar radiation. In contrast, during winter the lake is well mixed nearly 100% of the time because of the low incoming solar radiation and the high wind speeds.

UCLAKE constitutes a robust and computationally efficient tool for prediction of lake thermal structure and the behaviour of the mixed layer at sub-daily and daily scales. The active variations of the mixed layer thickness indicate a rapid lake response to changes of the meteorological conditions and this implies that such changes may be potentially important for the resuspension of bottom sediments. Such a response is not only translated into a mixing mechanism that erodes the thermocline, but also into the production of complex patterns of internal waves that are not considered explicitly in 1D modelling. The implementation of *UCLAKE* in Llyn Conwy has served not only to understand its thermal structure, but also provides insights into the hydrodynamics and sediment dynamics. The 1D model approach thus serves as a preparatory stage to a more extensive three-dimensional study of the hydrodynamics and sediment transport in upland lakes.

7.3 3D Hydrodynamic Modelling

3D hydrodynamic models developed primarily for ocean study cases has been widely implemented in large lakes (e.g. Jin *et al.*, 2000; Chen *et al.*, 2004b), but their use in small lakes has been very limited. The use of the 3D hydrodynamic and sediment dynamic model *FVCOM* in the upland Llyn Conwy has introduced some new challenges, such as the design of a computational mesh based on an adequate resolution and configuration, and an appropriate definition of the bathymetry that minimises the model uncertainty and improves its performance (e.g Legrand *et al.*, 2006). A key issue is the mitigation of numerical instabilities caused by the interaction between high wind speeds and the water body at this exposed upland location. *FVCOM* has also been improved by the designing and programming of a graphical user interface, *FVCOM-GUI*, to pre- and post-process model information. This makes it much more comparable with leasing commercial hydrodynamic models such as *Delf 3D* and *MIKE 3D*. In addition, a semi-empirical linear wave model, *UCL-SWM*, has been successfully

incorporated into *FVCOM*. This is of crucial importance for studies of lake sedimentation since it represents the effects of wind-wave generated stresses on bottom sediment resuspension.

The *FVCOM* hydrodynamics model was calibrated for Llyn Conwy by fitting the bottom roughness coefficient (z_0). This yielded an optimum $z_0 = 0.0227\ m$ and a remarkable model performance of NSE = 0.84 with respect to the velocity field. The relatively high value of z_0 is explained by the fact that the lake bed is highly irregular and the sediment bottom composition is quite heterogeneous as was shown by the bottom sediment survey carried out in April 2011. High values of z_0 were also obtained by Gross *et al.*, 1999 in their calibration of a 3D hydrodynamic model of the San Francisco Bay, US, and were attributed to the presence of a rough bed in shallower areas, which served to dampen wind-wave propagation.

Despite the generally good *FVCOM* model performance, the model underestimates the flow velocity by nearly 25% in the middle and near the end of the calibration period when the velocity reaches peak values. These discrepancies might be associated with errors in the recording of wind forcing and/or the measuring of flow velocity profiles, and the asumption of a homogenous bottom sediment composition. According to the sensitivity analysis, the model underestimation for high flow speed $> 0.05\ m\ s^{-1}$ can be overcome if z_0 is $\sim$0.005 m, which demonstrates the dependence of the roughness parameter from the flow velocity magnitude. Similar dependence has been noted in the calibration of 1D/2D river hydrodynamic models, where the bottom roughness represented by the Manning coefficient often exerts a large influence on changes in water discharge (Horritt & Bates, 2002; Pappenberger *et al.*, 2005).

Two major aspects of the hydrodynamics, gross circulation and seiches, were analysed after model calibration and validation. Flow circulation is characterized by the existence of two different gyres which extend throughout the upper half of the water-depth layer. Analysis of persistence of this typical two-gyre circulation pattern using Empirical Orthogonal Functions (EOFS) (Emery & Thomson, 2001; Ji & Jin, 2006) indicates that EOFS mode 1 accounts for more than 85% of the variance of the circulation. This implies that the flow circulation pattern is driven mainly by the predominant south-westerly wind forcing. Observing the anti-cyclonic gyre, this covers the centre-north of the lake and flows intensively along the north shore. The cyclonic gyre located towards the east of the lake flows faster along the east shore and returns toward the centre with great intensity. There, it merges with the anti-cyclonic gyre and flows

smoothly toward the west of the lake. This western flow is completely developed at the lower water-depth layers, where return currents from the north to the centre of the lake are also apparent. The circulation patterns are therefore mainly produced by the interaction of wind forcing, the water body and the bathymetry. The effect of the coriolis force and the vorcity induced by spatially distributed wind forcing fields appear to be negligible.

Vorticity analysis in lakes has concluded that bottom stresses and advection-diffusion of flow act as sinks of vorticity, whereas wind stress gradients, internal pressure gradients (including temperature gradients) and Coriolis force can be regarded as sources of vorticity (Strub & Powell, 1986; Schwab & Beletsky, 2003; Laval *et al.*, 2003; Rueda *et al.*, 2005). The balance of these sources and sinks, as determined by weather conditions, lake catchment topography and the bathymetry, define the vorticity or circulation patterns in the lake. For example, Schwab & Beletsky, 2003 found that, in Lake Michigan, a cyclonic circulation occur in winter periods (unstratified period) caused by a wind stress curl. Similarly, in summer, the cyclonicity was maintained but with slight variations due to non-linearities introduced by the baroclinicity. In Lakes Ontario and Erie, Beletsky *et al.*, 1999 observed two cyclonic gyres during winter, which were triggered by a non-uniform wind field. In Lake Erie, which is shallower than Ontario, anticyclonic circulation was observed due to an anticyclonic wind stress curl induced by a meso-scale high pressure gradient over the lake. Studies conducted to characterise the vorticity in Lake Kinneret and Lake Constance (Serruya *et al.*, 1984), and Lake Geneva (Lemmin & D'Adamo, 1997), show that their circulation patterns are driven by wind stress curls.

In small lakes, it has been demonstrated that the circulation patterns can be strongly affected by topographic sheltering. A study by Podsetchine & Schernewski, 1999 of Lake Belau, a small lake (A = 1.1 km^2) in Northern Germany, compared the circulation patterns triggered by uniform and non-uniform wind stress fields. The non-uniform field was interpolated using data from two meteorological stations located at the lake centre and on the shore. The interpolation assumed a zero stress along the upwind shores and a downwind linear growth of the wind stress along the fetch. The results indicated that local topography and sheltering from surrounding forest creates persistent patterns of non-uniform wind field, resulting in a single gyre pattern in the flow. In contrast, the assumption of uniform wind field yields a two-gyre pattern.

Topographic sheltering is probably relatively unimportant at Llyn Conwy. Moreover, other factors such as the lake shape (Laird *et al.*, 2003), surface roughness heterogeneity and differential wind acceleration along the fetch (Young & Verhagen, 1996a) can create inhomogeneous wind fields over a lake basin. To examine the homogenity of the wind field a comparison between the wind forcing series recorded at the CEH data buoy and at the shore-based automatic weather station between 10 November and 7 December 2006 (Figure 7.1 a)) has been undertaken. The results indicate a systematic average difference of ∼40% between the records, with higher wind speed at the buoy station (see Figure 7.1 c)). Additionally, a linear correlation coefficient of $r^2 = 0.70$ (see Figure 7.1 b)) between both wind speed record indicate that both measurements have the similar growing trend (see Figure 7.1 a)). Comparisons of the wind direction records at both stations reveals that a predominant southwesterly wind is recorded at the shore weather station, whereas a southerly wind was more frequent at the data buoy. There is thus some evidence for non-uniform wind forcing even in a small catchment and lake such as this.

A preliminary study was therefore carried out to analyse the differences between the circulation patterns driven by a uniform and a non-uniform wind forcing field in Llyn Conwy. The first scenario assumes a uniform wind stress field driven by $W_s = 12\ m\ s^{-1}$ and $W_d = 210^o$. The second scenario considers a non-uniform wind stress field based on the assumption that the wind speed grows linearly along the southeasterly wind track from an initial value set along the western shores (upwind side) as a percentage of the value measured at the buoy. The two wind forcing scenarios were then used to force *FVCOM* in steady-state mode.

The model results for the uniform wind field scenario (see Figure 7.2a) show strong bottom current patterns over approximately the whole bottom lake, whereas for the non-uniform wind field scenario (see Figure 7.2b) strong bottom currents are only generated on the east and northeast sectors of the lake. Noticeable differences between both scenarios are detected (see Figure 7.2c) in short-fetch shallower regions in the western and the southern parts of the lake bottom. Circulation patterns are also different in that only one return flow originates from the northeast under the uniform wind field scenario, whereas two return flows emanate from the northeast under the non-uniform scenario. The northern and western flow patterns given in both scenarios would explain the distribution of areas free of lake deposits in the north. However, toward the shallower western and southern sectors, the slower flow patterns given by

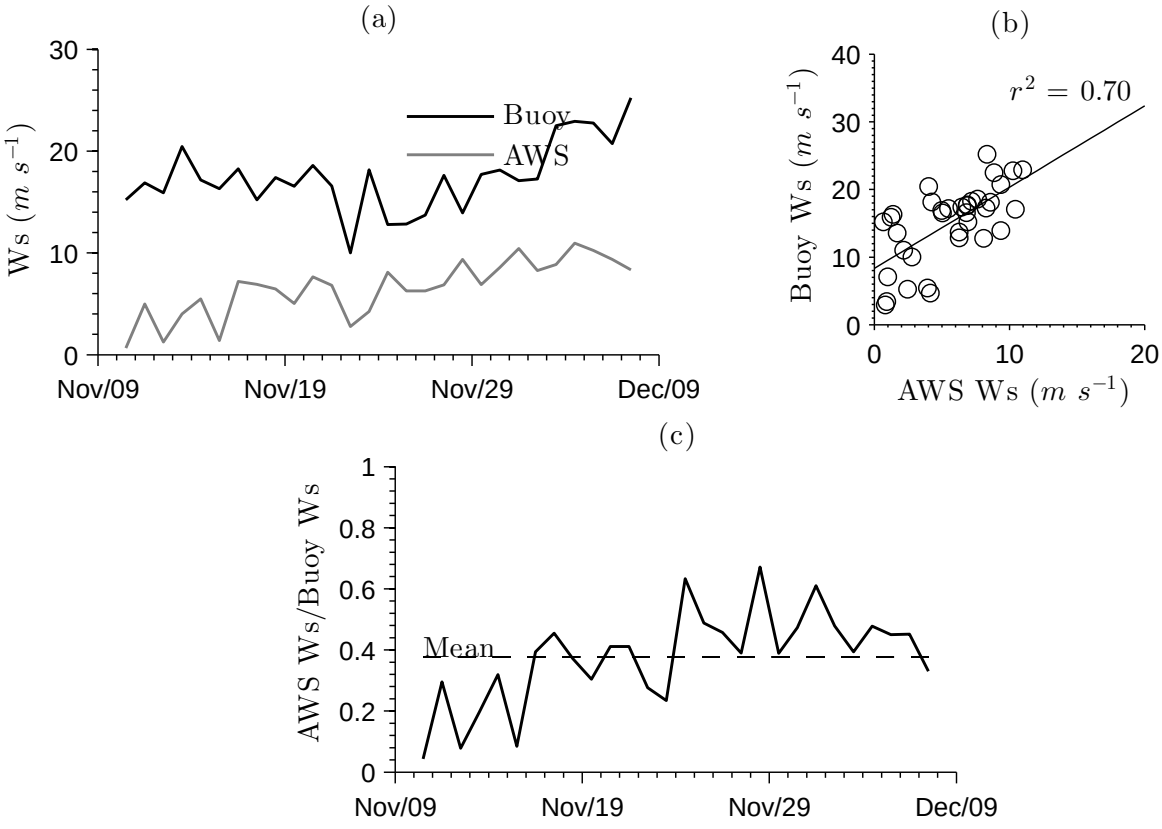

Figure 7.1: Wind speed forcing data recorded from 10-Nov-06 to 07-Dec-06 at the CEH data buoy and shore-based automatic weather station (AWS). a) Wind speeds. b) Linear correlation between the wind speed recorded at both stations. c) Ratio between wind speed records.

non-uniform wind field match the bottom sediment composition rather better (this would facilitate the deposition of sediments in these areas). A interesting aspect is the coincidence between the two return flows from the northeast (see Figure 7.2b) given by the non-uniform wind forcing scenario and the two bottom corridors (see Figure 6.1) where the bed is composed of pre-Holocene sediments and a thin lay deposit of peat pebbles presumably transported by these currents. Despite the apparently better correspondence between the field velocity given by non-uniform wind field and the bottom sediment composition, longer and well distributed records of wind data are needed at different points around the Llyn Conwy basin (e.g. Nuss & Titley, 1994; Rueda *et al.*, 2005), to get a more reliable spatial representation of wind forcing. Further studies might include the use of mesoescale models (e.g. Penn State/NCAR Mesoescale Model (MM5), Kelley *et al.*, 1998; Zhong & Fast, 2003) to simulate the 2D/3D wind field in a spatial grid over Llyn Conwy catchment, which then would serve to force *FVCOM*.

Basin-scale oscillatory motions constitute another important feature of lake hydrodynamics. The spectral analysis of spatially distributed water level records in Llyn Conwy yields a characteristic predominant seiche period of $\sim$12 *min* in the main basin. In sheltered areas such as the northeast bay, the seiche is slightly damped, increasing its frequency. Over the southern basin the $\sim$12 *min* seiche alternates with a more dominant seiche period of $\sim$5 *min* excited by wind forcing acting along a shorter west-to-east fetch and in shallower water. Oscillatory motions were also detected internally through analysis of isotherms during a short stratified period. The analysis of the 12.5^oC isotherm at the bottom of the metalimnion reveals the existence of internal waves oscillating at 24 h driven by diel wind forcing. Vertical mode 1 internal waves with a period of 7 h were also detected at the interface between the epilimnion and metalimnion excited by rapid fluctuations in wind forcing. An 18 h period vertical mode 2 internal wave was also detected by comparing the metalimnetic and top hypolimnetic isotherms. The vertical mode 2 might be associated with higher horizontal modes driven by a combination of bathymetry irregularities and wind direction changes (e.f. Lemmin, 1987; Roget *et al.*, 1997).

Despite the lack of longer water level series and spatially distributed temperature water-depth profiles for longer stratified periods (needed to fully investigate the existence of higher horizontal modes), the approximate characterisation of oscillatory motions in Llyn Conwy has indicated the likely existence of a complex family of waves.

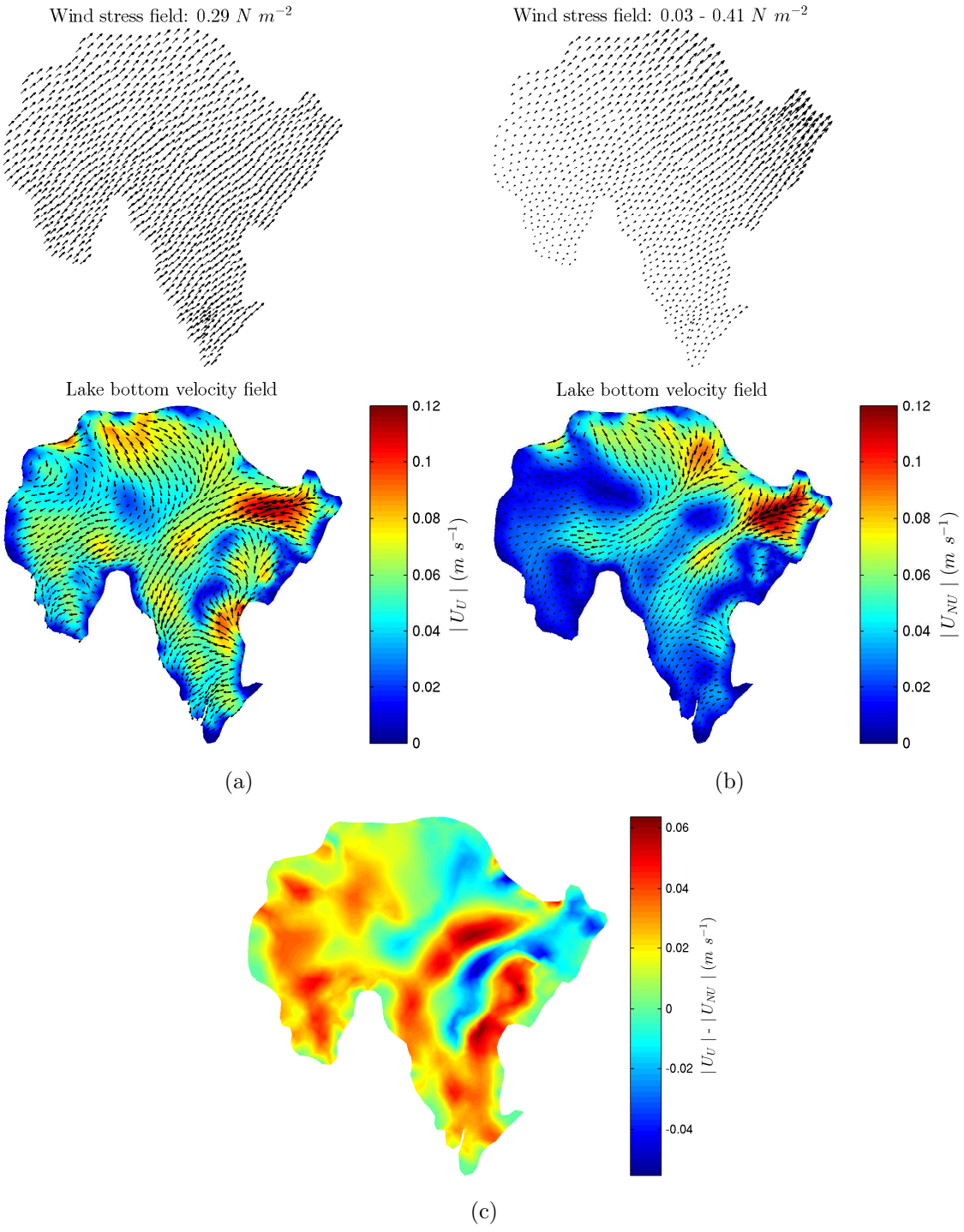

Figure 7.2: Comparison between bottom field velocities generated by uniform and non uniform wind stress fields for $W_s = 12\ m\ s^{-1}$ and $W_d = 225^o$. a) Bottom velocity field for uniform wind stress distribution; b) bottom velocity field for non-uniform wind stress distribution; c) differences between flow speeds for uniform and non-uniform wind stress field.

The importance of such oscillatory motions is twofold. First, they transport turbulent kinetic energy across the unstable thermocline (e.g. Kelvin-Helmholz instability, Thorpe, 1977) to erode the hypolimnion. Second, a portion of their energy is eventually dissipated in the resuspension and redistribution of sediments (Bloesch, 1995; Horppila & Niemisto, 2008).

7.4 Sediment Dynamics in Upland Lakes: Test of the Sediment Focusing Hypothesis

The Llyn Conwy sediment deposits are mainly comprised of allochtonous material derived from the catchment while the production of autochthonous matter is limited by the oligothropic condition. Inflowing sediments are predominantly comprised of organic peat fragments with a variable inclusion of clastic silt-sized material derived from the weathering and breakdown of catchment rocks. The dominant pathways from catchment to lake are unclear. Two small streams in the northeast and southeast corners of the lake have minor accumulations of sediment in their vicinity but have not formed major deltaic deposits. Drainage of the upland peat bogs in the 1930s undoubtedly increased sediment input due to the excavation of multiple drainage channels, especially in the eastern part of the catchment (Patrick & Stevenson, 1986). This conclusion is supported by historical sediment rates inferred from the dated cores (especially CON4), which peak in this period. Most of these drainage channels have since been blocked. A more diffuse pathway in the form of seepage and minor outflows around much of the shoreline at the interface between peat and bedrock may be equally important, although it is hard to estimate its role in the absence of any monitoring data. Finally, direct erosion of the shoreline is evident, especially along eastern shores. This may contribute larger fragments of peat as well as clastic material. The origin of the peat pebbles, found at depth at certain locations, is not entirely clear. These appear to have been transported either from the shoreline, down the steeper slopes, under the action of return wind-driven flow currents. Where recovered in the grab samples, they probably represent a lag deposit that is too coarse for further entrainment.

The Llyn Conwy bed sediments are mostly eroded by the action of shear stresses caused by individual or combined action of wind-waves and currents over the bottom (Grant & Madsen, 1979; Zhang *et al.*, 2004). The transport of sediment is due to the action of currents which mobilize suspended particles mainly via the general circulation

and much less through oscillatory motions. Sediments might be transported short distances by the action of wind-waves that are able to drag sediments inshore, which are then quickly deposited. In relatively quiescent waters sediment deposition depends basically on the grain size (the suspended sediment concentrations here are never likely to be high enought to affect settling velocity). In moving waters, the viscous shear stresses can inhibit sediment deposition such that particles are transported greater distances. The distribution of sediment on the bottom depends of the lake bathymetry. In deeper places, more continuous sediment deposits might be expected to form based on the assumption of sediment focusing (e.g Hilton, 1985; Rowan *et al.*, 1995; Blais & Kalff, 1995), whereas in shallow places, deposits are due to distribution by the circulation currents that weaken in this locations.

In Llyn Conwy the magnitude and patterns of distribution of erosion are dictated by wind forcing conditions and much less by water level variation. Under the predominant wind forcing conditions ($W_s = 12\ m\ s^{-1}$ and $W_d = 210^o$) erosion occurs mostly over small regions along the northern and the eastern shores, which represent $\sim 2.8\%$ of the bottom area. Such erosion is exclusively due to the action of wind-wave bottom stresses (τ_w), since current bottom stresses (τ_c) are weak and only significant for $W_s > 20\ m\ s^{-1}$. This is consistent with the existence of consolidated pre-Holocene deposits (some with a peat pebble lag) that remain after the regular removal of any accumulated sediments.

The wind speed scenarios indicate that, in general, the bottom stresses and the % of bottom areas resuspended (BAR) increase with wind speed. The increment in the magnitude of the stresses is much more rapid in current-induced bottom stresses, τ_c, than in τ_w because of the non-linear behaviour of the flow hydrodynamics. Such rapid increment of τ_c ensures that the stress ratio (τ_w/τ_c) become close to 1 for higher wind speeds. Bottom areas resuspended by τ_c increase more quickly than the areas due to τ_w as wind speed increases, so for the maximun wind speed registered ($W_s = 40\ m\ s^{-1}$) the BAR due to τ_c it is $\sim 80\%$ whereas for τ_c is $\sim 12\%$. The distribution of BAR for τ_w is quite predictable since this grows along the fetch and is therefore located along the downwind shore, limiting it to relatively shallow places. In contrast, the distribution of BAR for τ_c is quite heterogenous and it is found at any range of bottom depth owing to the more complex and non-linear 3D current behaviour. This is why, despite the lower probability of occurrence of $W_s \geq 30\ m\ s^{-1}$, only wind-induced currents are able to resuspend sediments in the deepest sector of the lake.

The analysis of bottom stresses in different bottom depth ranges allows the differentiation of bottom sectors that are potentially affected by each type of bottom stress. The BAR due to τ_w shows a logarithmic behaviour, decreasing rapidly toward almost 0% above 6.6 m depth. Water depths within the range 0 to 6.6 m are located along the shore and more central sectors in the southern part of the lake. Interestingly, the BAR due to τ_c shows a gaussian behaviour, so the maximun BAR would be expected at intermediate depths (6.6-11.0 m) and the minimum BAR would occur at the shallower and deepest sectors. As is intuitively predicted, the combination of both bottom stresses means that the BAR decreases logarithmically from shallower to the deepest sectors, with the major contribution being from τ_w and τ_c in shallow and deep waters respectively.

7.5 Implications for Environmental Reconstruction Based on Lake Sediment Cores

The successful reconstruction of environmental change from lake sediment sequences depends on the acquisition and analysis of one or more core samples from locations of continuous sediment accumulation (Håkanson & Jansson, 1983). The basic sediment focusing model (Lehman, 1975; Blais & Kalff, 1995) provides one means of, a priori, selecting suitable locations based on bathymetric data alone. Such work has been extended in two main directions. First, various workers have attempted to improve the statistical basis for core sampling by considering the number of cores necessary to provide an acceptable level of precision in the estimation of whole lake sedimentation rates (e.g. Håkanson, 1984; Baudo *et al.*, 1989; Floderus, 1989). Second, various attempts have been made to improve the dynamic basis of the sediment focusing model. These have mostly involved modelling of wave-driven redistribution of sediment from shallow to deeper water (e.g. Sheng & Lick, 1979; Bengtsson & Hellström, 1992; Lövstedt & Bengtsson, 2008). Rowan *et al.*, 1992 thus attempted to quantify the mud deposition boundary depth (mud DBD) and subsequently used this to derive the location of suitably representative sedimentary records and optimise the number of cores needed to estimate mean sedimentation rates (Rowan *et al.*, 1995). Other works have attempted to evaluate not only the effects of wind-waves on sediment distribution, but also the effects of bed slopes and wind-induced currents to explain the heterogeneity

of carbon and phosphorus depositional patterns in small lakes (e.g. Mackay *et al.*, 2011).

While wave-driven resuspension is clearly a major factor driving sediment dynamics in shallow lakes, many lakes are deep enough to have significant areas that lie below wave base. The intensive study of Llyn Conwy has revealed a patchy distribution of lake sediments even within these deeper waters that is controlled not only by wave-driven transfer from shallow to deep water but also by wind-driven currents that can re-suspend deep water sediments and even preclude deposition in certain areas. A priori prediction of these zones is more difficult since the wind-driven circulation is governed by complex non-linear interactions between meteorological forcing and lake basin geometry. These can only be understood and predicted through physically-based modelling.

Lessons from the model-based study of Llyn Conwy have been formalized into a set of guidelines for lake sediment coring informed by modelling. These are summarized below and in the workflow presented in Figure 7.3.

1. Bathymetry: A high resolution bathymetry must be surveyed that resolves the steep bottom slopes as well as shallower sectors to allow the effective application of physically based hydrodynamics and sediment transport models. Old bathymetries can usually be supplemented with more recent bottom surveys both to ascertain their accuracy and also to improve their resolution. High resolution bathymetry itself may also allow preliminary inferences about the location of lake sediment deposits (e.g. Lehman, 1975; Blais & Kalff, 1995). Hypsographic curves derived from the bathymetry can be used to classify the lake basin in a way that can also help predict likely areas of erosion, resuspension and deposition (Håkanson, 1977a).

2. Meteorological information: Meteorological forcing records should ideally be for multiple locations around the lake basin in order to resolve spatial variability that can be particularly important in the wind field. The number of weather stations deployed will depend on the area, planform geometry, and degree of topographical sheltering experienced by the lake. It is also appropriate to obtain meteorological series extending over at least two years at a hourly timestep. This allows the definition of probable scenarios to make inferences about further sectors subjected to wind-wave erosion.

3. Computational mesh: Physically-based modelling is performed on a computational mesh that discretizes the model domain. Unstructured meshes are more suitable for irregular lake geometries and provide a better domain resolution than regular grids. Irregular meshes are also more typically implemented by more complex finite element and finite volumes schemes. Model resolution depends also on the available computational resources. High resolution models are increasingly compiled and run using parallel processing libraries to distribute computation across multiple cpus.

4. Hydrodynamic model setup: A basic simplified hydrodynamic model setup requires the input of constant meteorological forcing values (either the most frequent or those considered to dominate the process regime) to run the model in steady-state mode. This simplified setup can be considered as an initial aproximation and serves to characterize typical horizontal and vertical circulation patterns. Steady-state model simulations can be very useful in an exploratory sense to identify zones where higher wind-waves and stronger currents occur and sedimentation is likely to be impeded or affected by resuspension events. For a fuller picture, and as demonstrated in this study, more complex time-dependent simulations are required. These models are sensitive to initial conditions of velocity and temperature that must be introduced from observations or model results from steady-state simulations. They also require time-series for the main meteorological forcing variables. One of the challenges with unsteady models is to ensure numerical stability, and a care is needed to simulate extreme meteorological conditions.

5. Sediment dynamic model setup: The key requirements here are a realistic representation of the sediment particle characteristics and a specification of the bed. Sediment properties such as density, porosity and grain size can be obtained routinely via standard laboratory procedures. However, characteristics such as critical shear stresses for deposition and erosion, erosion rate and settling velocity are more difficult to measure directly and so are typically based on a review of the literature.

   Despite lake bottoms being composed by multiple sediment classes heterogenously distributed, sediment dynamics modelling is, in most of the cases, realized for the most representative sediment class. The modelling with multiple classes

would imply the supply of physical sediment properties for each sediment class and the management of multiple output results increasing the complexity of the model setup and results interpretation. Additionally, for enclosed basin with no tributaries (e.g. rivers and streams) the source of sediments is provided by a thickness limited bottom layer, the modelling of multiple sediment classes will require a delimitation of the bottom according to the cover of each class.

6. Analysis of sediment dynamics model results: Interpretation and analysis of the hydrodynamics and sediment dynamics model results provide the means to quantify zones of erosion, transport and deposition. The model provides the temporal evolution of the bottom at each node from where it is possible to discerns between erosion and deposition. The analysis of erosion, transport and deposition of sediments at sequential bottom depth ranges aids the delimitation of the bottom area at which each of these processes take place. The spatial analysis of the sediment rates serves to indentify these places where accumulation occurs rapidly, with the aim of identifying suitable sediment deposits for sediment sampling works.

The physically-based numerical modelling approach implemented in this work has attempted to understand the key hydrodynamic features and their effects on sediment transport in Llyn Conwy. The results presented here demonstrated the potential of a 3D numerical model to describe the linkages between lake meteorological conditions, hydrodynamics and sediment transport. The approximate erosional and depositional patterns predicted by the model can constitute a tool for guiding sampling and coring works in environmental reconstruction analysis. Therefore, the numerical modelling approach implemented here can be extended to other lakes with the aim of improving the understanding of hydrodynamics and sedimentation processes and to continue the testing of the sediment focusing hypothesis in upland lakes.

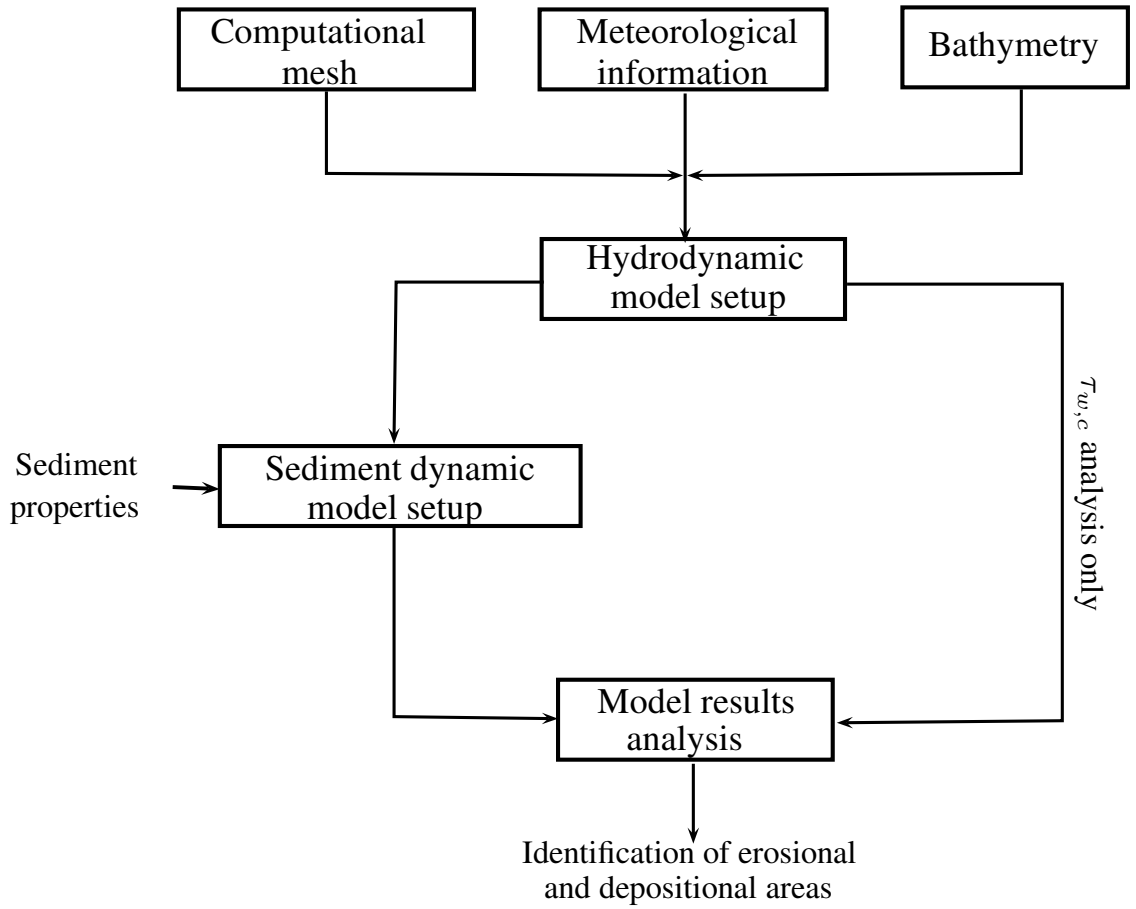

Figure 7.3: Workflow for model-based analysis of lake sediment distribution.

Chapter 8

Conclusions and Recommendations

8.1 Conclusions

This thesis has approached the hydrodynamics and sediment dynamics in upland lakes using computational models to critically evaluate the widely accepted sediment focusing theory. The findings provide a potentially valuable framework for future studies related to environmental reconstruction that places the selection of sediment core sites and their interpretation in the context of physical process that drive sedimentation.

A new 1D model,*UCLAKE*, has been developed to simulate the thermal structure in lakes over multiple scales at daily and sub-daily time resolution. The model is specifically designed for application to exposed upland lakes in that it adapts the time step to guarantee numerical stability under strong wind forcing conditions. Its modular structure allows easy enhancement with the addition of new subroutines (e.g. sediment and oxygen vertical concentration). Calibration of the model for Llyn Conwy yields NSE > 0.95 for all the model parameters, and also shows that that thermal structure is more sensitive to parameters such as K_z during stratified periods. The analysis of the mixed layer shows that the lake is weakly stratified in summer for nearly 80% of the time with an averaged mixed layer thickness of 2 m. The mixed layer thickness behaviour indicates that bottom areas shallower than 2 m are likely to experience resuspension during summer, whereas during winter and autumn deeper areas are commonly affected when the lake is overturned by stronger winds. *UCLAKE* is being made available via GNU open source licence to the limnological community.

An existing community hydrodynamic model, *FVCOM*, has been used as a platform for 3D modelling of hydrodynamics and sediment transport. *FVCOM* has been

enhanced through the providing of a new GUI. This supports a wide range of pre- and post-processing tasks. The *FVCOM-GUI* is also being made freely available to the modelling community.

A linear wave generator model, *UCL-SWM*, was designed and programmed as a stand-alone software and as a library incorporated into *FVCOM* to account for the effects of wind-waves. *UCL-SWM* includes efficient algorithms to estimate wave parameters (significant wave height, wave period and wave length), and to compute wave-induced shear stresses over the lake bottom. A key feature of the model is an algorithm to estimate the fetch at any point in the basin using wind direction and basin geometry only. Benchmarking against a full spectral wave model, *SWAN*, shows that discrepancies between models are below 10%. However, *UCL-SWM* is about 10 times faster than *SWAN*. Calibration and validation against wave measurements at multiple locations shows a generally excellent performance. The new *UCL-SWM* model is thus a useful in its own right to estimate wind-wave parameters in highly irregular hydrosystems (e.g. lakes and estuaries), and it could potentially be used to pre-identify locations of sediment resuspension.

The improved 3D *FVCOM* model has been used to extend the understanding of hydrodynamics and sediment dynamics in upland lake systems. The model was calibrated against measured velocity profiles for Llyn Conwy via adjustment of the bottom roughness coefficient, z_0. Sensitivity analysis indicates a rapid response of the flow velocity field to changes in the wind forcing conditions, and predicts the occurrence of seiches when the wind speed drops substantially. The analysis of flow circulation reveals a persistent two-gyre circulation pattern in the upper half layer of the lake driven by the interaction of a predominant southwesterly wind and the irregular lake bathymetry. At the lake bottom, the flow is characterised by locally strong currents. Analysis of vertical circulation over short time scales shows strong currents in the deepest sectors and, also, the responsiveness of the water column to changes in wind speed and direction. Analysis of secondary hydrodynamic features, such as seiches and internal waves, indicates weak free back-and-forth oscillatory motions for average wind forcing conditions. During stratified periods, a vertical mode 1 internal wave is driven by strong wind forcing fluctuations, and a less frequent and weak vertical mode 2 internal waves may also exist.

As a prelude to a full sediment dynamics modelling, *FVCOM* and *UCL-SWM* were set up independently to analyse current and wind-wave bottom stresses for different

wind and water level scenarios. The results indicate in general, the dominance of wind-wave stresses over flow current stresses for $W_s \leq 12\ m\ s^{-1}$, but the ratio between both bottom stresses become close to unity as wind speed increases above this threshold. The results for wind direction scenarios under typical wind speed conditions indicate that wind waves would resuspend sediments over narrow downwind zones along the shore. The largest bottom area resuspended (BAR) occurs when W_d is equal to 0^o and 225^o, and the smallest when W_d is between 45^o and 180^o. The wind speed scenarios for the predominant southwesterly wind direction, show that BAR due to τ_w is mostly concentrated in northern and eastern areas and extends progressively inshore as wind speed increases. In contrast, the BAR due to τ_c is much larger, reaching $\sim$80% of bottom area for $W_s = 40\ m\ s^{-1}$. It also grows less uniformly due to the non-linearity of flow circulation. Further analysis of bottom shear stresses for a period of extreme forcing conditions indicates that sediment erosion over the northern and eastern sectors is persistent. The analysis of BAR at different depth ranges indicate that wind-waves are only able to resuspend sediments in areas less than about $\sim 5\ m$ in depth, whereas for current-induced stresses, the BAR is more extensive for intermediate depths.

Modelling of sediment dynamics for highly idealized sediment supply and bed configuration scenarios yields simulated bottom sediment distribution that broadly coincide with the surveyed bottom composition. Such distribution patterns reflect a complex interaction between wind forcing, the water body and the basin morphology. The erosional areas delimited by the model coincide with areas of pre-Holocene sediments. Depositional areas located toward the central basin and the southern and the western sectors are also broadly predicted by the model. Sediment transport model results show that sediments are not simply deposited in the deepest places, but are focused towards intermediate depths under the influence of a strongly 3D circulation pattern. A comparative evaluation of the mechanisms involved in the sediment focusing shows that intermittent complete mixing and peripheral wave action are the most important factors. Although there is no direct evidence of sliding and slumping events, the actual bottom slope configuration in Llyn Conwy indicates that this factor may also play a role in sediment focusing in areas of high bottom gradient.

8.2 Recommendations for Future Research

Future research in upland lake hydrodynamics and sediment dynamics should focus on a number of areas that emerge from the present work. These include:

- Further work to extend the modelling approach developed here and to generalize the analysis to a wider range of upland lakes with contrasting size, geometry and exposure. This might also include simulation of idealized geometries.

- Further work using 3D Lagrangian sediment transport models coupled to a hydrodynamic model in order to study more fully the main mechanisms involved in lake sediment focusing (e.g. Niño & García, 1998). This should ideally extend to field validation via bottom sediment surveys deployments of sediment traps.

- More detailed studies of wind forcing heterogeneity in upland lake catchments and its effects on lake circulation and sediment transport. Such work should also consider the effects of topography sheltering, hitherto investigated only for a few lakes (e.g. Rueda *et al.*, 2005).

- Analysis of internal waves in upland lakes by the installation of spatially distributed high resolution thermistor chains to identify oscillatory wave modes and their implications for the erosion and transport of sediments (e.g. Gloor *et al.*, 1994).

References

Abbott, M.B. (1991). *Hydroinformatics: information technology and the aquatic environment*. Avebury Technical, Aldershot; Brookfield, USA. 145 pp. 46, 50

Akiyama, J. & Stefan, H.G. (1984). Plunging flow into a reservoir: Theory. *Journal of Hydraulic Engineering*, **110**, 484–499. 55

Algan, O., Balkis, N., Çağatay, M.N. & Sari, E. (2004). The sources of metal contents in the shelf sediments from the Marmara Sea, Turkey. *Environmental Geology*, **46**, 932–950. 31

Anderson, N., Odgaard, B., Segerström, U. & Renberg, I. (1996). Climate-lake interactions recorded in varved sediments from a Swedish boreal forest lake. *Global Change Biology*, **2**, 399–403. 41

Andrén, H. (1994). *Development of the Laitaure Delta, Swedish Lappland: A Study of Growth, Distributary Forms and Processes*. UNGI Rapport, Uppsala Universitet, Institutionen för Geovetenskap, Naturgeografi. 188 pp. 31

Antonopoulos, V. & Gianniou, S. (2003). Simulation of water temperature and dissolved oxygen distribution in Lake Vegoritis, Greece. *Ecological Modelling*, **160**, 39–53. 55, 56

Appleby, P., Nolan, P., Gifford, D., Godfrey, M., Oldfield, F., Anderson, N. & Battarbee, R. (1986). ^{210}Pb dating by low background gamma counting. *Hydrobiologia*, **143**, 21–27. 93

Appleby, P., Richardson, N. & Nolan, P. (1991). ^{241}Am dating of lake sediments. *Hydrobiologia*, **214**, 35–42. 245

Appleby, P., Richardson, N. & Nolan, P. (1992). Self-absorption corrections for well-type germanium detectors. *Nuclear Instruments and Methods in Physics Research Section B: Beam Interactions with Materials and Atoms*, **71**, 228–233. 94

Austnes, K., Evans, C., Eliot-Laze, C., Naden, P. & Old, G. (2010). Effects of storm events on mobilisation and in-stream processing of dissolved organic matter (DOM) in a Welsh peatland catchment. *Biogeochemistry*, **99**, 157–173. 84

Baba, J. & Komar, P. (1981). Measurements and analysis of setting velocities of natural quartz sand grains. *Journal of Sedimentary Research*, **51**, 631–640. 36, 236

Bailey, M. & Hamilton, D. (1997). Wind induced sediment resuspension: a lake-wide model. *Ecological Modelling*, **99**, 217–228. 28, 75, 251

Battarbee, R. (1978). Observations on the recent history of Lough Neagh and its drainage basin. *Philosophical Transactions of the Royal Society of London. Series B, Biological Sciences*, **281**, 303–345. 39

Battarbee, R. (2000). Palaeolimnological approaches to climate change, with special regard to the biological record. *Quaternary Science Reviews*, **19**, 107–124. 39

Battarbee, R., Anderson, N., Bennion, H. & Simpson, G. (2012). Combining limnological and palaeolimnological data to disentangle the effects of nutrient pollution and climate change on lake ecosystems: problems and potential. *Freshwater Biology*, **57**, 2091–2106. 39

Baudo, R., Amantini, L., Bo, F., Cenci, R., Hannaert, P., Lattanzio, A., Marengo, G. & Muntau, H. (1989). Spatial distribution patterns of metals in the surface sediments of Lake Orta (Italy). *Science of the Total Environment*, **87**, 117–128. 293

Beletsky, D., Saylor, J. & Schwab, D. (1999). Mean circulation in the Great Lakes. *Journal of Great Lakes Research*, **25**, 78–93. 286

Bell, V., George, D., Moore, R. & Parker, J. (2006). Using a 1-D mixing model to simulate the vertical flux of heat and oxygen in a lake subject to episodic mixing. *Ecological Modelling*, **190**, 41–54. 51, 56, 280

Bengtsson, L. & Hellström, T. (1992). Wind-induced resuspension in a small shallow lake. *Hydrobiologia*, **241**, 163–172. 75, 200, 206, 231, 251, 293

Bengtsson, L., Hellström, T. & Rakoczi, L. (1990). Redistribution of sediments in three Swedish lakes. *Hydrobiologia*, **192**, 167–181. 36

Beven, K. & Freer, J. (2001). Equifinality, data assimilation, and uncertainty estimation in mechanistic modelling of complex environmental systems using the GLUE methodology. *Journal of Hydrology*, **249**, 11–29. 103

Blais, J.M. & Kalff, J. (1995). The influence of lake morphometry on sediment focusing. *Limnology and Oceanography*, **40**, 582–588. 265, 292, 293, 294

Blenckner, T., Omstedt, A. & Rummukainen, M. (2002). A Swedish case study of contemporary and possible future consequences of climate change on lake function. *Aquatic Sciences-Research Across Boundaries*, **64**, 171–184. 45

Bloesch, J. (1982). Inshore-offshore sedimentation differences resulting from resuspension in the eastern basin of Lake Erie. *Canadian Journal of Fisheries and Aquatic Sciences*, **39**, 748–759. 31, 36, 37

Bloesch, J. (1994). Editorial: Sediment resuspension in lakes. *Hydrobiologia*, **284**, 1–3. 35

Bloesch, J. (1995). Mechanisms, measurement and importance of sediment resuspension in lakes. *Marine and Freshwater Research*, **46**, 295–304. 291

Bloesch, J. & Uehlinger, U. (1986). Horizontal sedimentation differences in a eutrophic Swiss lake. *Limnology and Oceanography*, **31**, 1094–1109. 37, 42, 44

Bloesch, J., Stadelmann, P. & Buhrer, H. (1977). Primary production, mineralization, and sedimentation in the euphotic zone of two Swiss lakes. *Limnology and Oceanography*, **22**, 511–526. 32, 36, 37

Bloesch, J., Bossard, P., Bührer, H., Bürgi, H. & Müller, R. (1997). Lake oligotrophication due to external phosphorus load reduction in Swiss Lakes. In *Proceedings of 6th International Conference on the Conservation and Management of Lakes, Kasumigaura. Lakes and Reservoirs: Research and Management*, vol. 4, 738–742. 31

Blom, G. & Toet, C. (1993). Modelling sediment transport and sediment quality in a shallow Dutch lake (Lake Ketel). *Water Science & Technology*, **28**, 79–90. 51, 231

Blom, G., Duin, E., Aalderink, R., Lijklema, L. & Toet, C. (1992). Modelling sediment transport in shallow lakes - interactions between sediment transport and sediment composition. *Hydrobiologia*, **235**, 153–166. 31, 51, 231

Blom, G., van Duin, E. & Lijklema, L. (1994). Sediment resuspension and light conditions in some shallow Dutch lakes. *Water Science and Technology*, **30**, 243–252. 47

Blott, S. & Pye, K. (2001). GRADISTAT: a grain size distribution and statistics package for the analysis of unconsolidated sediments. *Earth Surface Processes and Landforms*, **26**, 1237–1248. 236

Blumberg, A.F. (1991). A primer for ECOM-si. *Technique Report of HydroQual, Inc.* 63, 70

Blumberg, A.F. & Mellor, G.L. (1987). A description of a three-dimensional coastal ocean circulation model. *Coastal and Estuarine Sciences*, **4**, 1–16. 47, 51, 65

Blumberg, A.F., Herring, H.J. *et al.* (1987). Circulation modeling using orthogonal curvilinear coordinates. *Three-dimensional models of marine and estuarine dynamics. Elsevier Oceanography Series*, **45**, 55–88. 46

Bonnet, M., Poulin, M. & Devaux, J. (2000). Numerical modeling of thermal stratification in a lake reservoir. methodology and case study. *Aquatic Sciences-Research Across Boundaries*, **62**, 105–124. 60, 100, 102, 283

Booij, N., Holthuijsen, L. & Ris, R. (1996). The SWAN wave model for shallow water. In *Proceedings of the 25th International Conference on Coastal Engineering ASCE*, vol. 1, 668–676. 52, 74

Booij, N., Ris, R. & Holthuijsen, L. (1999). A third-generation wave model for coastal regions. I- Model description and validation. *Journal of Geophysical Research*, **104**, 7649–7666. 52, 74, 78, 194

Bretschneider, C. (1957). Revisions in wave forecasting: deep and shallow water. In *Proceedings of the Sixth Conference on Coastal Engineering*, vol. 1. 78

Brönmark, C. & Hansson, L.A. (2005). *The biology of lakes and ponds*. Oxford University Press, Oxford. 285 pp. 30, 32

Brooks, S. & Birks, H. (2000). Chironomid-inferred late-glacial and early-Holocene mean July air temperatures for Kråkenes Lake, western Norway. *Journal of Paleolimnology*, **23**, 77–89. 39

Brydsten, L. (1992). Wave-induced sediment resuspension in the Öre estuary, northern Sweden. *Hydrobiologia*, **235**, 71–83. 35

Bunge, W. & Bryson, R.A. (1956). Ice on Wisconsin lakes. Tech. rep., University of Wisconsin, Department of Meteorology, Madison. 43, 278

Carpenter, S. (1983). Lake geometry: implications for production and sediment accretion rates. *Journal of Theoretical Biology*, **105**, 273–286. 44

Carpenter, S., Ludwig, D. & Brock, W. (1999). Management of eutrophication for lakes subject to potentially irreversible change. *Ecological Applications*, **9**, 751–771. 38

Cea, L. & French, J. (2012). Bathymetric error estimation for the calibration and validation of estuarine hydrodynamic models. *Estuarine Coastal and Shelf Science*, **100**, 124–132. 47, 53, 94, 280

Cea, L., French, J. & Vázquez-Cendón, M. (2006). Numerical modelling of tidal flows in complex estuaries including turbulence: an unstructured finite volume solver and experimental validation. *International Journal for Numerical Methods in Engineering*, **67**, 1909–1932. 51

Cerco, C. & Cole, T. (1994). Three-dimensional eutrophication model of Chesapeake Bay: Volume 1. Tech. rep., EL-94-4, US Army Engineer Waterways Experiment Station, Vicksburg, MS. 48

Chambers, J. & Cameron, N. (2001). A rod-less piston corer for lake sediments; an improved, rope-operated percussion corer. *Journal of Paleolimnology*, **25**, 117–122. 44, 90, 93

Chao, X., Jia, Y., Shields, F., Wang, S. & Cooper, C. (2008). Three-dimensional numerical modeling of cohesive sediment transport and wind wave impact in a shallow oxbow lake. *Advances in Water Resources*, **31**, 1004–1014. 45, 52, 200, 221, 231, 251

Chao, X., Jia, Y., Shields Jr, F., Wang, S. & Cooper, C. (2009). Numerical simulation of sediment-associated water quality processes for a Mississippi delta lake. *Ecohydrology*, **2**, 350–359. 30, 45

Chen, C., Liu, H. & Beardsley, R. (2003). An unstructured grid, finite-volume, three-dimensional, primitive equations ocean model: application to coastal ocean and estuaries. *Journal of Atmospheric and Oceanic Technology*, **20**, 159–186. 46, 47, 51, 52, 64

Chen, C., Cowles, G. & Beardsley, R. (2004a). An unstructured grid, finite-volume coastal ocean model: FVCOM User Manual. Tech. rep., 04-0601, pp183, School of Marine Science and Technology, University of Massachusetts, Dartmouth. 9, 49, 52, 63, 64, 68, 249

Chen, C., Wang, L., Ji, R., Budd, J.W., Schwab, D.J., Beletsky, D., Fahnenstiel, G.L., Vanderploeg, H., Eadie, B. & Cotner, J. (2004b). Impacts of suspended sediment on the ecosystem in Lake Michigan: A comparison between the 1998 and 1999 plume events. *Journal of Geophysical Research: Oceans*, **109**, n/a–n/a. 65, 284

Chen, C., Zhu, J., Zheng, L., Ralph, E. & Budd, J. (2004c). A non-orthogonal primitive equation coastal ocean circulation model: application to Lake Superior. *Journal of Great Lakes Research*, **30**, 41–54. 52

Christensen, D., Herwig, B., Schindler, D. & Carpenter, S. (1996). Impacts of lakeshore residential development on coarse woody debris in north temperate lakes. *Ecological Applications*, **6**, 1143–1149. 32

Chung, E., Bombardelli, F. & Schladow, S. (2009). Sediment resuspension in a shallow lake. *Water Resources Research*, **45**, n/a–n/a. 34

Cockburn, B., Hou, S. & Shu, C. (1990). The Runge-Kutta local projection discontinuous Galerkin finite element method for conservation laws. IV: The multidimensional case. *Mathematics of Computation*, **54**, 545–581. 46

Cornett, R., Chant, L. & Link, D. (1984). Sedimentation of ^{210}Pb in Laurentian Shield lakes. *Water Pollution Journal of Canada*, **19**, 97–109. 44

Corps, U.S.A. & Center, C.E.R. (1984). Shore Protection Manual. Tech. Rep. 1, United States Army Corps of Engineers, Coastal Engineering Research Center, Vicksburg, MS. 78

Covelli, P., Marsili-Libelli, S. & Pacini, G. (2002). SWAMP: A two-dimensional hydrodynamic and quality modeling platform for shallow waters. *Numerical Methods for Partial Differential Equations*, **18**, 663–687. 129

Cowles, G.W. (2008). Parallelization of the FVCOM coastal ocean model. *International Journal of High Performance Computing Applications*, **22**, 177–193. 64

Cózar, A., Gálvez, J., Hull, V., García, C. & Loiselle, S. (2005). Sediment resuspension by wind in a shallow lake of Esteros del Ibera (Argentina): a model based on turbidimetry. *Ecological Modelling*, **186**, 63–76. 28, 34, 75

Cronin, S., Lamb, H. & Whittington, R. (1993). Seismic reflection and sonar survey as an aid to the investigation of lake sediment stratigraphy: a case study from upland wales. In J. McManus & R. Duck, eds., *Geomorphology and Sedimentology of Lakes and Reservoirs*, 181–203, John Wiley. 276

Csanady, G. (1967). Large-scale motion in the great lakes. *Journal of Geophysical Research*, **72**, 4151–4162. 82

Csanady, G. (1975). Hydrodynamics of large lakes. *Annual Review of Fluid Mechanics*, **7**, 357–386. 82, 153

Csanady, G. (1978). Water circulation and dispersal mechanisms. In A. Lerman, ed., *Lakes*, 21–64, Springer New York. 35

Czuczwa, J. & Hites, R. (1986). Airborne dioxins and dibenzofurans: sources and fates. *Environmental Science & Technology*, **20**, 195–200. 32

Czuczwa, J., Niessen, F. & Hites, R. (1985). Historical record of polychlorinated dibenzo–dioxins and dibenzofurans in Swiss lake sediments. *Chemosphere*, **14**, 1175–1179. 32

Dake, J.M. & Harleman, D.R. (1969). Thermal stratification in lakes: analytical and laboratory studies. *Water Resources Research*, **5**, 484–495. 27, 28

Davis, M. (1969). Climatic changes in southern Connecticut recorded by pollen deposition at Rogers Lake. *Ecology*, **50**, 409–422. 39, 41

Davis, M. (1973). Redeposition of pollen grains in lake sediment. *Limnology and Oceanography*, **18**, 44–52. 43

Davis, M. (1982). Sediment focusing in Mirror Lake, New Hampshire. *Limnology and Oceanography*, **27**, 137–150. 39, 41

Davis, M. & Brubaker, L. (1973). Differential sedimentation of pollen grains in lakes. *Limnology and Oceanography*, **18**, 635–646. 43

Dearing, J. (1986). Core correlation and total sediment influx. In *B.E. Berlund (Ed), Handbook of Holocene Palaeoecology and Palaeohydrology, Wiley*, 247–270. 41

Dearing, J. (1997). Sedimentary indicators of lake-level changes in the humid temperate zone: a critical review. *Journal of Paleolimnology*, **18**, 1–14. 40

Dearing, J., Elner, J. & Happey-Wood, C. (1981). Recent sediment flux and erosional processes in a Welsh upland lake-catchment based on magnetic susceptibility measurements. *Quaternary Research*, **16**, 356–372. 39

Deevey, E. (1955). The obliteration of the hypolimnion. Mem. 1st. *Ital. Idrobiol*, **8**, 9–38. 44

Digerfeldt, G. (1988). Reconstruction and regional correlation of Holocene lake-level fluctuations in Lake Bysjön, South Sweden. *Boreas*, **17**, 165–182. 40

Downing, J.A., Prairie, Y., Cole, J., Duarte, C., Tranvik, L., Striegl, R., McDowell, W., Kortelainen, P., Caraco, N., Melack, J. & Middelburg, J. (2006). The global abundance and size distribution of lakes, ponds, and impoundments. *Limnology and Oceanography*, **51**, 2388–2397. 24

Dyer, K. (1986). *Coastal and estuarine sediment dynamics*. Wiley-Interscience publication, Wiley. 342 pp. 79

Eicher, U. & Siegenthaler, U. (1976). Palynological and oxygen isotope investigations on Late-Glacial sediment cores from Swiss lakes. *Boreas*, **5**, 109–117. 40

Eisenreich, S., Looney, B. & Thornton, J. (1981). Airborne organic contaminants in the Great Lakes ecosystem. *Environmental Science and Technology*, **15**, 30–8. 32

Elliott, J., Persson, I., Thackeray, S. & Blenckner, T. (2007). Phytoplankton modelling of Lake Erken, Sweden by linking the models PROBE and PROTECH. *Ecological Modelling*, **202**, 421–426. 32, 37, 46

Emery, W. & Thomson, R. (2001). *Data analysis methods in physical oceanography*. Elsevier Science & Technology Books. 638 pp. 165, 285

Evans, R. (1994). Empirical evidence of the importance of sediment resuspension in lakes. *Hydrobiologia*, **284**, 5–12. 41

Evans, R. & Rigler, F. (1983). A test of lead-210 dating for the measurement of whole lake soft sediment accumulation. *Canadian Journal of Fisheries and Aquatic Sciences*, **40**, 506–515. 44

Fagherazzi, S. & Wiberg, P.L. (2009). Importance of wind conditions, fetch, and water levels on wave-generated shear stresses in shallow intertidal basins. *Journal of Geophysical Research: Earth Surface*, **114**, n/a–n/a. 35, 78

Fang, X. & Stefan, H. (1996). Long-term lake water temperature and ice cover simulations/measurements. *Cold Regions Science and Technology*, **24**, 289–304. 51

Filstrup, C. & Lind, O. (2010). Sediment transport mechanisms influencing spatiotemporal resuspension patterns in a shallow, polymictic reservoir. *Lake and Reservoir Management*, **26**, 85–94. 34

Fischer, H. (1979). *Mixing in inland and coastal waters*. Academic Press Inc. 483 pp. 33, 35, 50, 51

Floderus, S. (1989). Sediment sampling evaluated with a new weighting function and index of reliability. *Hydrobiologia*, **176**, 451–464. 293

Flower, R., Dearing, J. & Nawas, R. (1984). Sediment supply and accumulation in a small Moroccan lake: an historical perspective. *Hydrobiologia*, **112**, 81–92. 39

Folk, R. & Ward, W. (1957). Brazos river bar: a study in the significance of grain size parameters. *Journal of Sedimentary Petrology*, **27**, 3–26. 236

Ford, D. & Stefan, H. (1980). Thermal predictions using integral energy model. *Journal of the Hydraulics Division*, **106**, 39–55. 52, 59

Foster I.D., J..G.R., Dearing (1988). Lake-catchments: a evaluation of their contribution to studies of sediment yield and delivery processes. *IAHS*, 413–424. 39

Fragoso, C., Motta Marques, D., Collischonn, W., Tucci, C. & van Nes, E. (2008). Modelling spatial heterogeneity of phytoplankton in lake mangueira, a large shallow subtropical lake in south brazil. *Ecological Modelling*, **219**, 125–137. 46, 51

French, C.E., French, J.R., Clifford, N.J. & Watson, C.J. (2000). Sedimentation–erosion dynamics of abandoned reclamations: the role of waves and tides. *Continental Shelf Research*, **20**, 1711–1733. 200

French, J. (2010). Critical perspectives on the evaluation and optimization of complex numerical models of estuary hydrodynamics and sediment dynamics. *Earth Surface Processes and Landforms*, **35**, 174–189. 53, 54

French, J. & Clifford, N. (2000). Hydrodynamic modelling as a basis for explaining estuarine environmental dynamics: some computational and methodological issues. *Hydrological Processes*, **14**, 2089–2108. 129

Fritz, S. (1990). Twentieth-century salinity and water-level fluctuations in Devils Lake, North Dakota: Test of a diatom-based transfer function. *Limnology and Oceanography*, **35**, 1771–1781. 40

Fukushima, T., Kamiya, K., Onda, Y., Imai, A. & Matsushige, K. (2010). Long-term changes in lake sediments and their influences on lake water quality in Japanese shallow lakes. *Fundamental and Applied Limnology/Archiv für Hydrobiologie*, **177**, 177–188. 30

Gabrielson, J. & Lukatelich, R. (1985). Wind-related resuspension of sediments in the Peel-Harvey estuarine system. *Estuarine, Coastal and Shelf Sciences*, **20**, 135–145. 35, 36, 37

Gajewski, K., Hamilton, P. & McNeely, R. (1997). A high resolution proxy-climate record from an arctic lake with annually-laminated sediments on Devon Island, Nunavut, Canada. *Journal of Paleolimnology*, **17**, 215–225. 39

Gal, G., Imberger, J., Zohary, T., Antenucci, J., Anis, A. & Rosenberg, T. (2003). Simulating the thermal dynamics of Lake Kinneret. *Ecological Modelling*, **162**, 69–86. 100, 282, 283

Galperin, B., Kantha, L., Hassid, S. & Rosati, A. (1988). A quasi-equilibrium turbulent energy model for geophysical flows. *Journal of the Atmospheric Sciences*, **45**, 55–62. 66

Garcia-Martinez, R. & Rodriguez-Molina, J. (1998). A visual tool to simulate hydrodynamics, pollutant and suspended sediment transport in rivers and coastal regions. In *Proceedings 3rd International Conference on Hydroinformatics, Copenhagen, Denmark*, 583–589. 130

Gee, D., Anderson, M. & Baird, L. (1990). Large-scale floodplain modelling. *Earth Surface Processes and Landforms*, **15**, 513–523. 51

George, D., Talling, J. & Rigg, E. (2001). Factors influencing the temporal coherence of five lakes in the english lake district. *Freshwater Biology*, **43**, 449–461. 280

George, G. (2010). The impact of climate change on european lakes. In G. George, ed., *The Impact of Climate Change on European Lakes*, vol. 4 of *Aquatic Ecology Series*, 1–13, Springer Netherlands. 24

Gilbert, R. (2003). Spatially irregular sedimentation in a small, morphologically complex lake: implications for paleoenvironmental studies. *Journal of Paleolimnology*, **29**, 209–220. 41, 44

Glanz, D., Orlob, G. & Young, G. (1973). *Ecologic simulation : Tocks Island Lake*. Water Resources Engineers, Inc. 144 pp. 58

Gloor, M., Wüest, A. & Münnich, M. (1994). Benthic boundary mixing and resuspension induced by internal seiches. *Hydrobiologia*, **284**, 59–68. 83, 301

Gould, H. & Budinger, T. (1958). Control of sedimentation and bottom configuration by convection currents, Lake Washington, Washington. *Journal Of Marine Research*, **17**, 183–198. 43

Grafenstein, U., Erlenkeuser, H., Kleinmann, A., Müller, J. & Trimborn, P. (1994). High-frequency climatic oscillations during the last deglaciation as revealed by oxygen-isotope records of benthic organisms (Ammersee, southern Germany). *Journal of Paleolimnology*, **11**, 349–357. 40

Grant, W.D. & Madsen, O.S. (1979). Combined wave and current interaction with a rough bottom. *Journal of Geophysical Research: Oceans*, **84**, 1797–1808. 291

Gross, E., Koseff, J. & Monismith, S. (1999). Three-dimensional salinity simulations of south san francisco bay. *Journal of Hydraulic Engineering*, **125**, 1199–1209. 154, 285

Gu, B., Mehlhorn, T., Liang, L. & McCarthy, J. (1996). Competitive adsorption, displacement, and transport of organic matter on iron oxide: I. Competitive adsorption. *Geochimica et Cosmochimica Acta*, **60**, 1943–1950. 31

Håkanson, L. (1977a). On lake form, lake volume and lake hypsographic survey. *Geografiska Annaler*, **59**, 1–29. 100, 294

Håkanson, L. (1977b). The influence of wind, fetch, and water depth on the distribution of sediments in Lake Vänern, Sweden. *Canadian Journal of Earth Sciences*, **14**, 397–412. 20, 41, 43, 78, 275, 277

Håkanson, L. (1981). *A manual of lake morphometry*. Springer Verlag. 78 pp. 30, 37

Håkanson, L. (1984). On the relationship between lake trophic level and lake sediments. *Water Research*, **18**, 303–314. 30, 44, 59, 226, 281, 293

Håkanson, L. (1992). Sediment variability. *In: Sediment Toxicity Assessment. Lewis Publishers, Boca Raton, Florida.*, 19–35. 44

Håkanson, L. & Jansson, M. (1983). *Principles of lake sedimentology*. Springer. 332 pp. 9, 32, 33, 44, 235, 293

Håkanson, L. & Karlsson, B. (1984). On the Relationship between Regional Geomorphology and Lake Morphometry. A Swedish Example. *Geografiska Annaler. Series A. Physical Geography*, **66**, 103–119. 25

Håkanson, L., Floderus, S. & Wallin, M. (1989). Sediment trap assemblages-a methodological description. *Hydrobiologia*, **176**, 481–490. 37

Hallermeier, R. (1981). Terminal settling velocity of commonly occurring sand grains. *Sedimentology*, **28**, 859–865. 236

Hamilton, D. & Mitchell, S. (1996). An empirical model for sediment resuspension in shallow lakes. *Hydrobiologia*, **317**, 209–220. 34, 52

Hamilton, D. & Schladow, S. (1997). Prediction of water quality in lakes and reservoirs. Part I–Model description. *Ecological Modelling*, **96**, 91–110. 50, 51

Hanson, P., Carpenter, S., Cardille, J., Coe, M. & Winslow, L. (2007). Small lakes dominate a random sample of regional lake characteristics. *Freshwater Biology*, **52**, 814–822. 25

Harmon, M. & Hua, C. (1991). Coarse woody debris dynamics in two old-growth ecosystems. *BioScience*, **41**, 604–610. 32

Harris, C. & Wiberg, P. (1997). Approaches to quantifying long-term continental shelf sediment transport with an example from the Northern California STRESS mid-shelf site. *Continental Shelf Research*, **17**, 1389–1418. 70, 74

Hasselmann, K. (1973). *Measurements of Wind-wave Growth and Swell Decay During the Joint North Sea Wave Project (JONSWAP)*. Ergänzungsheft. Reihe A, Deutsches Hydrographisches Institut. 95 pp. 78

Hatfield, R. & Maher, B. (2009). Fingerprinting upland sediment sources: particle size-specific magnetic linkages between soils, lake sediments and suspended sediments. *Earth Surface Processes and Landforms*, **34**, 1359–1373. 31

Havens, K.E., Aumen, N.G., James, R.T. & Smith, V.H. (1996). Rapid ecological changes in a large subtropical lake undergoing cultural eutrophication. *Ambio. Stockholm*, **25**, 150–155. 48

Havnø, K., Madsen, M., Dørge, J. & Singh, V. (1995). MIKE 11-a generalized river modelling package. *Computer Models of Watershed Hydrology*, 733–782. 130

Hawley, N., Lesht, B.M. & Schwab, D.J. (2004). A comparison of observed and modeled surface waves in southern Lake Michigan and the implications for models of sediment resuspension. *Journal of Geophysical Research: Oceans*, **109**, n/a–n/a. 194

Hearn, C. (2008). *The dynamics of coastal models*. Cambridge University Press. 488 pp. 47

Henderson-Sellers, B. (1984). *Engineering limnology*. Pitman Advanced Pub., Boston. 356 pp. 55, 58, 59, 60, 102, 103, 110, 282

Henderson-Sellers, B. (1985). New formulation of eddy diffusion thermocline models. *Applied Mathematical Modelling*, **9**, 441–446. 60, 61, 102

Henriksen, H., Troldborg, L., Nyegaard, P., Sonnenborg, T., Resgaard, J. & Madsen, B. (2003). Methodology for construction, calibration and validation of a national hydrological model for Denmark. *Journal of Hydrology*, **280**, 52–71. 54

Herb, W.R. & Stefan, H.G. (2005). Dynamics of vertical mixing in a shallow lake with submersed macrophytes. *Water Resources Research*, **41**, n/a–n/a. 38

Herdendorf, C. (1990). Distribution of the Worlds Large Lakes. In M. Tilzer & C. Serruya, eds., *Large Lakes*, Brock/Springer Series in Contemporary Bioscience, 3–38, Springer Berlin Heidelberg. 24

Hilton, J. (1985). A conceptual framework for predicting the occurrence of sediment focusing and sediment redistribution in small lakes. *Limnology and Oceanography*, **30**, 1131–1143. 42, 44, 279, 292

Hilton, J., Lishman, J. & Allen, P. (1986a). The dominant processes of sediment distribution and focusing in a small, eutrophic, monomictic lake. *Limnology and Oceanography*, **31**, 125–133. 42, 44, 275, 276, 279

Hilton, J., Lishman, J. & Millington, A. (1986b). A comparison of some rapid techniques for the measurement of density in soft sediments. *Sedimentology*, **33**, 777–781. 236

Hodges, B., Imberger, J., Saggio, A. & Winters, K. (2000). Modeling basin-scale internal waves in a stratified lake. *Limnology and Oceanography*, **45**, 1603–1620. 82, 94, 153

Holland, J., Dortch, M. & Smith, D. (1982). Norfork Lake, Arkansas, temperature analysis; mathematical model investigation. Tech. rep., Army Engineer Waterways Experiment Station, Vicksburg, MS (USA). Hydraulics Lab. 55

Hondzo, M. & Stefan, H. (1991). Three case studies of lake temperature and stratification response to warmer climate. *Water Resources Research*, **27**, 1837–1846. 281, 283

Hondzo, M. & Stefan, H. (1992). Propagation of uncertainty due to variable meteorological forcing in lake temperature models. *Water Resources Research*, **28**, 2629–2638. 283

Hondzo, M. & Stefan, H. (1993). Lake water temperature simulation model. *Journal of Hydraulic Engineering*, **119**, 1251–1273. 27, 28, 60, 100, 102, 103, 109, 110, 281, 282, 283

Horppila, J. & Niemisto, J. (2008). Horizontal and vertical variations in sedimentation and resuspension rates in a stratifying lake-effects of internal seiches. *Sedimentology*, **55**, 1135–1144. 34, 291

Horppila, J. & Nurminen, L. (2003). Effects of submerged macrophytes on sediment resuspension and internal phosphorus loading in Lake Hiidenvesi (southern Finland). *Water Research*, **37**, 4468–4474. 38

Horritt, M. & Bates, P. (2002). Evaluation of 1D and 2D numerical models for predicting river flood inundation. *Journal of Hydrology*, **268**, 87–99. 51, 285

Huber, W. & Harleman, D. (1968). *Laboratory and analytical studies of the thermal stratification of reservoirs*. Massachusetts Institute of Technology, Hydrodynamics Laboratory. 58

Hutchinson, G. (1957). A treatise on limnology. Vol. 1. Geography. *Physics, and Chemistry. Wiley, New York*. 21, 25, 26, 28

Hutchinson, G. & Löffler, H. (1956). The thermal classification of lakes. *Proceedings of the National Academy of Sciences of the United States of America*, **42**, 84. 28

Imberger, J. (1985). The diurnal mixed layer. *Limnology and Oceanography*, **30**, 737–770. 281

Imberger, J. (1998). *Physical Processes in Lakes and Oceans*. Coastal and estuarine studies, 54, American Geophysical Union. 668 pp. 25, 28, 30, 33, 35, 50

Imberger, J. & Hamblin, P. (1982). Dynamics of lakes, reservoirs, and cooling ponds. *Annual Review of Fluid Mechanics*, **14**, 153–187. 25, 28, 82, 153, 175

Imberger, J. & Patterson, J. (1981). A dynamic reservoir simulation model-DYRESM: 5. In *Transport Models for Inland and Coastal Waters: Symposium Proceedings. Academic Press Inc*, 310–361. 55, 102, 283

Imberger, J., Loh, I., Hebbert, B. & Patterson, J. (1978). Dynamics of reservoir of medium size. *Journal of the Hydraulics Division*, **104**, 725–743. 50

Itkonen, A. & Salonen, V. (1994). The response of sedimentation in three varved lacustrine sequences to air temperature, precipitation and human impact. *Journal of Paleolimnology*, **11**, 323–332. 39

James, W., Best, E. & Barko, J. (2004). Sediment resuspension and light attenuation in Peoria Lake: can macrophytes improve water quality in this shallow system? *Hydrobiologia*, **515**, 193–201. 38

Jassby, A. & Powell, T. (1975). Vertical patterns of eddy diffusion during stratification in Castle Lake, California. *Limnology and Oceanography*, **20**, 530–543. 60

Jeppesen, E. (1998). *The structuring role of submerged macrophytes in lakes*. Ecological Studies, Springer Verlag. 423 pp. 37

Ji, Z. (2008). *Hydrodynamics and Water Quality: Modeling Rivers, Lakes, and Estuaries*. Wiley. 624 pp. 25, 33, 46, 47, 50, 79, 83, 154

Ji, Z. & Jin, K. (2006). Gyres and seiches in a large and shallow lake. *Journal of Great Lakes Research*, **32**, 764–775. 82, 165, 285

Ji, Z., Morton, M. & Hamrick, J. (2001). Wetting and drying simulation of estuarine processes. *Estuarine, Coastal and Shelf Science*, **53**, 683–700. 51

Jin, K. & Ji, Z. (2001). Calibration and verification of a spectral wind-wave model for Lake Okeechobee. *Ocean Engineering*, **28**, 571–584. 52

Jin, K., Hamrick, J. & Tisdale, T. (2000). Application of three-dimensional hydrodynamic model for lake okeechobee. *Journal of Hydraulic Engineering*, **126**, 758. 52, 154, 284

Jin, K.R. & Ji, Z.G. (2004). Case study: modeling of sediment transport and wind-wave impact in Lake Okeechobee. *Journal of hydraulic engineering*, **130**, 1055–1067. 28, 32, 47, 75, 231, 251

Jin, K.R. & Ji, Z.G. (2005). Application and validation of three-dimensional model in a shallow lake. *Journal of Waterway, Port, Coastal, and Ocean Engineering*, **131**, 213–225. 46, 48

Julien, P. (1998). *Erosion and sedimentation*. Cambridge University Press. 280 pp. 36, 38

Justus, C. & Mikhail, A. (1976). Height variation of wind speed and wind distributions statistics. *Geophysical Research Letters*, **3**, 261–264. 196

Kang, S., Sheng, Y. & Lick, W. (1982). Wave action and bottom shear stresses in lake erie. *Journal of Great Lakes Research*, **8**, 482–494. 206, 251

Kazanci, N., Leroy, S., Ileri, Ö., Emre, Ö., Kibar, M. & Öncel, S. (2004). Late Holocene erosion in NW Anatolia from sediments of Lake Manyas, Lake Ulubat and the southern shelf of the Marmara Sea, Turkey. *Catena*, **57**, 277–308. 31

Kazanci, N., Leroy, S., Öncel, S., İleri, Ö., Toprak, Ö., Costa, P., Sayili, S., Turgut, C. & Kibar, M. (2010). Wind control on the accumulation of heavy metals in sediment of Lake Ulubat, Anatolia, Turkey. *Journal of Paleolimnology*, **43**, 89–110. 31, 35

Kelley, J.G., Hobgood, J.S., Bedford, K.W. & Schwab, D.J. (1998). Generation of three-dimensional lake model forecasts for Lake Erie. *Weather and Forecasting*, **13**, 659–687. 289

Kelts, K. & Hsü, K. (1978). Freshwater carbonate sedimentation. *Lakes: Chemistry, Geology, Physics*, 295–323. 32

Kirillin, G., Engelhardt, C. & Golosov, S. (2008). A mesoscale vortex in a small stratified lake. *Environmental Fluid Mechanics*, **8**, 349–366. 162

Kobayashi, M., Pereira, J. & Pereira, J. (1999). A conservative finite-volume second-order-accurate projection method on hybrid unstructured grids. *Journal of Computational Physics*, **150**, 40–75. 70

Komar, P.D. & Reimers, C. (1978). Grain shape effects on settling rates. *The Journal of Geology*, **86**, 193–209. 36

Krauskopf, K. (1979). *Introduction to geochemistry*. McGraw-Hill, New York. 617 pp. 31

Kristensen, P., Søndergaard, M. & Jeppesen, E. (1992). Resuspension in a shallow eutrophic lake. *Hydrobiologia*, **228**, 101–109. 47, 231

Kuusisto, E. & Hyvarinen, V. (2000). Hydrology of Lakes. *Hydrological and limnological aspects of lake monitoring*, 1. 23

Laird, N.F., Walsh, J.E. & Kristovich, D.A.R. (2003). Model simulations examining the relationship of lake-effect morphology to lake shape, wind direction, and wind speed. *Monthly Weather Review*, **131**, 2102–2111. 287

Lam, D., Leon, L., Hamilton, S., Crookshank, N., Bonin, D. & Swayne, D. (2004). Multi-model integration in a decision support system: a technical user interface approach for watershed and lake management scenarios. *Environmental Modelling & Software*, **19**, 317–324. 51

Lambert, A. (1982). Turbidity currents from the Rhine River on the bottom of Lake Constance. *Wasserwirtschaft*, **72**, 1–4. 31

Lambert, A. & Giovanoli, F. (1988). Records of riverborne turbidity currents and indications of slope failures in the Rhone delta of Lake Geneva. *Limnology and Oceanography*, **33**, 458–468. 31

Langmuir, D. (1997). *Aqueous environmental geochemistry*. Prentice Hall. 600 pp. 31

Larsen, J., Appleby, P., Christensen, G., Berg, T. & Eide, I. (2010). Historical and geographical trends in sediment chronology from lakes and marine sites along the Norwegian coast. *Water, Air, & Soil Pollution*, **206**, 237–250. 42

Last, W., Smol, J. & Birks, H. (2001). *Tracking Environmental Change Using Lake Sediments: Volume 1: Basin Analysis, Coring, and Chronological Techniques*. Kluwer. 576 pp. 31

Laval, B., Imberger, J., Hodges, B. & Stocker, R. (2003). Modeling circulation in lakes: Spatial and temporal variations. *Limnology and Oceanography*, **48**, 983–994. 35, 36, 162, 286

Lee, C., Schwab, D.J. & Hawley, N. (2005). Sensitivity analysis of sediment resuspension parameters in coastal area of southern Lake Michigan. *Journal of Geophysical Research: Oceans*, **110**, n/a–n/a. 231, 251

Lee, C., Schwab, D.J., Beletsky, D., Stroud, J. & Lesht, B. (2007). Numerical modeling of mixed sediment resuspension, transport, and deposition during the March 1998 episodic events in southern Lake Michigan. *Journal of Geophysical Research: Oceans*, **112**, n/a–n/a. 45, 231, 252

Lee, D.Y. & Wang, H. (1984). Measurement of surface waves from subsurface gage. In *Proceedings of the 19th International Conference on Coastal Engineering*, vol. 1, 271–286. 93, 185

Leeder, M. (1982). *Sedimentology: Process and Product*. Chapman & Hall. 344 pp. 30, 39

Legates, D. & McCabe, G. (1999). Evaluating the use of 'goodness-of-fit' measures in hydrologic and hydroclimatic model validation. *Water Resources Research*, **35**, 233–241. 54

Legrand, S., Deleersnijder, E., Hanert, E., Legat, V. & Wolanski, E. (2006). High-resolution, unstructured meshes for hydrodynamic models of the Great Barrier Reef, Australia. *Estuarine, Coastal and Shelf Science*, **68**, 36–46. 284

Lehman, J.T. (1975). Reconstructing the rate of accumulation of lake sediment: the effect of sediment focusing. *Quaternary Research*, **5**, 541–550. 41, 293, 294

Lemmin, U. (1987). The structure and dynamics of internal waves in Baldeggersee. *Limnology and Oceanography*, **32**, 43–61. 182, 289

Lemmin, U. & D'Adamo, N. (1997). Summertime winds and direct cyclonic circulation: observations from Lake Geneva. In *Annales Geophysicae*, vol. 14, 1207–1220, Springer. 36, 198, 286

León, L., Lam, D., Schertzer, W., Swayne, D. & Imberger, J. (2007). Towards coupling a 3D hydrodynamic lake model with the Canadian regional climate model: simulation on Great Slave Lake. *Environmental Modelling & Software*, **22**, 787–796. 52

Lesser, G., Roelvink, J., Van Kester, J. & Stelling, G. (2004). Development and validation of a three-dimensional morphological model. *Coastal Engineering*, **51**, 883–915. 47, 51

LeVeque, R. (2002). *Finite Volume Methods for Hyperbolic Problems*. Cambridge Texts in Applied Mathematics, Cambridge University Press. 578 pp. 46

Lewis Jr, W. (1983). Temperature, heat, and mixing in Lake Valencia, Venezuela. *Limnology and Oceanography*, **28**, 273–286. 103

Likens, G. (1985). *An Ecosystem Approach to Aquatic Ecology: Mirror Lake and its Environment*. Springer-Verlag. 516 pp. 31, 38

Likens, G. & Davis, M. (1975). Post-Glacial History of Mirror Lake and Its Watershed In New Hampshire, U. S. A.: An Initial Report. *Verhandlungen Internationale Vereinigung Limnologie*, **19**, 982–993. 41, 262

Lin, B. & Chandler-Wilde, S. (1996). A depth-integrated 2D coastal and estuarine model with conformal boundary-fitted mesh generation. *International Journal for Numerical Methods in Fluids*, **23**, 819–846. 46

Lindell, T. (1980). Hydrographic characteristics. *Welch EB, Ecological effects of waste water. Cambridge Univ Press, Cambridge*, 17–47. 21, 28, 29

Livingstone, D. & Lotter, A. (1998). The relationship between air and water temperatures in lakes of the Swiss Plateau: a case study with palaeolimnological implications. *Journal of Paleolimnology*, **19**, 181–198. 40

Lou, J., Schwab, D., Beletsky, D. & Hawley, N. (2000). A model of sediment resuspension and transport dynamics in southern Lake Michigan. *Journal of Geophysical Research*, **105**, 6591–6610. 206, 251

Lövstedt, C.B. & Bengtsson, L. (2008). The role of non-prevailing wind direction on resuspension and redistribution of sediments in a shallow lake. *Aquatic Sciences*, **70**, 304–313. 35, 78, 293

Luettich Jr, R., Harleman, D. & Somlyody, L. (1990). Dynamic behavior of suspended sediment concentrations in a shallow lake perturbed by episodic wind events. *Limnology and Oceanography*, **35**, 1050–1067. 34, 35, 79, 200, 221, 231, 251

MacIntyre, S., Clark, J.F., Jellison, R. & Fram, J.P. (2009). Turbulent mixing induced by nonlinear internal waves in Mono Lake, California. *Limnology and Oceanography*, **54**, 2255–2272. 280

Mackay, E.B., Jones, I.D., Folkard, A.M. & Barker, P. (2011). Contribution of sediment focussing to heterogeneity of organic carbon and phosphorus burial in small lakes. *Freshwater Biology*, **57**, 290–304. 294

Maday, Y. & Patera, A. (1989). Spectral element methods for the incompressible Navier-Stokes equations. In *State-of-the-art surveys on computational mechanics. American Society of Mechanical Engineers. Research supported by DARPA.*, 71–143. 46

Margalef, R. (1994). *Limnology now: a paradigm of planetary problems*. Elsevier. 553 pp. 24, 30

McMahon, T. & Mein, R. (1978). *Reservoir capacity and yield*. Elsevier Science & Technology. 213 pp. 38

McWilliams, J., Sullivan, P. & Moeng, C. (1997). Langmuir turbulence in the ocean. *Journal of Fluid Mechanics*, **334**, 1–30. 35

Mehta, A.J. (1996). Interaction between fluid mud and water waves. *Water Science and Technology Library*, **19**, 153–188. 47

Mellor, G. & Yamada, T. (1982). Development of a turbulence closure model for geophysical fluid problems. *Reviews of Geophysics*, **20**, 851–875. 66

Mellor, G., in Atmostpheric, P.U.P. & Sciences, O. (1993). *Users guide for a three dimensional, primitive equation, numerical ocean model*. Atmospheric and Oceanic Sciences Program, Princeton University. 56 pp. 63

Meybeck, M. (1995). Global distribution of lakes. In A. Lerman, D. Imboden & J. Gat, eds., *Physics and chemistry of lakes*, 1–35, Springer-Verlag. 24

Mohanty, P. (2008). *Monitoring and modelling lakes and coastal environments*. Springer London, Limited. 247 pp. 25, 50

Moore, A., Arango, H., Di Lorenzo, E., Cornuelle, B., Miller, A. & Neilson, D. (2004). A comprehensive ocean prediction and analysis system based on the tangent linear and adjoint of a regional ocean model. *Ocean Modelling*, **7**, 227–258. 74

Morales, L., French, J. & Burningham, H. (2011-Unpublished). UCLAKE V1.0: An One-Dimensional Dynamic Model. Tech. rep., Costals and Estuaries Research Unit, Deparment of Geography, University College London (UCL). 55, 56, 58

Moriasi, D., Arnold, J., Van Liew, M., Bingner, R., Harmel, R. & Veith, T. (2007). Model evaluation guidelines for systematic quantification of accuracy in watershed simulations. *Transactions of the American Society of Agricultural Engineers*, **50**, 885–900. 53, 54

Morris, G.L. & Fan, J. (1998). *Reservoir sedimentation handbook: design and management of dams, reservoirs, and watersheds for sustainable use*, vol. 9. McGraw-Hill New York. 736 pp. 38

Moustafa, M. & Hamrick, J. (2000). Calibration of the wetland hydrodynamic model to the Everglades Nutrient Removal Project. *Water Quality and Ecosystems Modeling*, **1**, 141–167. 51

Munk, W. & Anderson, E. (1948). Notes on a theory of the thermocline. *Journal of Marine Research*, **7**, 276–295. 61

Nakamura, Y. & Hayakawa, N. (1991). Modelling of thermal stratification in lakes and coastal seas. *20 th General Assembly of the International Union of Geodesy and Geophysics, Vienna, Austria, 08/11-24/91*, 227–236. 102

Nash, J. & Sutcliffe, J. (1970). River flow forecasting through conceptual models part I–A discussion of principles. *Journal of Hydrology*, **10**, 282–290. 54

Nicholas, A. & Walling, D. (1997). Modelling flood hydraulics and overbank deposition on river floodplains. *Earth Surface Processes and Landforms*, **22**, 59–77. 51

Niño, Y. & García, M. (1998). Using Lagrangian particle saltation observations for bedload sediment transport modelling. *Hydrological Processes*, **12**, 1197–1218. 301

Novak, P., Moffat, A., Nalluri, C. & Narayanan, R. (2007). *Hydraulic Structures*. Taylor & Francis. 736 pp. 38

Nuhfer, E. & Anderson, R. (1984). Changes in sediment composition during seasonal resuspension in small shallow dimictic inland lakes. *Sedimentary Geology*, **41**, 131–158. 39

Nürnberg, G. (1995). Quantifying anoxia in lakes. *Limnology and Oceanography*, **40**, 1100–1111. 38

Nuss, W. & Titley, D. (1994). Use of multiquadric interpolation for meteorological objective analysis. *Monthly Weather Review*, **122**, 1611–1631. 289

Oldfield, F. (1977). Lakes and their drainage basins as units of sediment-based ecological study. *Progress in Physical Geography*, **1**, 460–504. 39

O'Reilly, C., Alin, S., Plisnier, P., Cohen, A. & McKee, B. (2003). Climate change decreases aquatic ecosystem productivity of Lake Tanganyika, Africa. *Nature*, **424**, 766–768. 40

Orlob, G. & Selna, L. (1970). Temperature variations in deep reservoirs. *Journal of the Hydraulics Division*, **96**, 391–410. 55

O'Sullivan, P. (1983). Annually-laminated lake sediments and the study of Quaternary environmental changes–a review. *Quaternary Science Reviews*, **1**, 245–313. 39

O'Sullivan, P. & Reynolds, C. (2005). *The Lakes Handbook: Limnology and Limnetic Ecology*. No. v. 1 in Limnology and limnetic ecology, Wiley. 708 pp. 23, 24

Pan, H., Avissar, R. & Haidvogel, D. (2002). Summer circulation and temperature structure of Lake Kinneret. *Journal of Physical Oceanography*, **32**, 295–313. 35, 198

Pannard, A., Beisner, B., Bird, D., Braun, J., Planas, D. & Bormans, M. (2011). Recurrent internal waves in a small lake: Potential ecological consequences for metalimnetic phytoplankton populations. *Limnology & Oceanography: Fluids & Environments*, **1**, 91–109. 184

Pappenberger, F., Beven, K., Horritt, M. & Blazkova, S. (2005). Uncertainty in the calibration of effective roughness parameters in HEC-RAS using inundation and downstream level observations. *Journal of Hydrology*, **302**, 46–69. 285

Park, K. (1995). *A Three-dimensional Hydrodynamic-eutrophication Model (HEM-3D): Description of Water Quality and Sediment Process Submodels*. Special report in applied marine science and ocean engineering, Virginia Institute of Marine Science. 204 pp. 47

Patrick, S. & Stevenson, A. (1986). Palaeoecological evaluation of the recent acidification of Welsh lakes Part 3; Llyns Conwy and Gamallt, Gwynedd (site descriptions, fishing and land use/management histories). Tech. Rep. 19, University College London, Department of Geography. 9, 10, 83, 85, 92, 94, 95, 245, 252, 291

Patten, B., Egloff, D. & Richardson, T. (1975). *Total Ecosystem Model for a Cove in Lake Texoma*. University of Georgia. Contributions in systems ecology, Academic Press. 217 pp. 102

Pennington, W. & Tutin, T. (1974). Seston and sediment formation in five Lake District lakes. *The Journal of Ecology*, **62**, 215–251. 42, 43

Pharo, C. & Carmack, E.C. (1979). Sedimentation processes in a short residence-time intermontane lake, Kamloops Lake, British Columbia. *Sedimentology*, **26**, 523–541. 42

Pickrill, R. & Irwin, J. (1983). Sedimentation in a deep glacier-fed lake–Lake Tekapo, New Zealand. *Sedimentology*, **30**, 63–75. 42

Podsetchine, V. & Schernewski, G. (1999). The influence of spatial wind inhomogeneity on flow patterns in a small lake. *Water Research*, **33**, 3348–3356. 286

Power, M. (1993). The predictive validation of ecological and environmental models. *Ecological Modelling*, **68**, 33–50. 53

Punning, J., Koff, T., Kadastik, E. & Mikomägi, A. (2005). Holocene lake level fluctuations recorded in the sediment composition of Lake Juusa, Southeastern Estonia. *Journal of Paleolimnology*, **34**, 377–390. 40

Quinlan, R., Smol, J. & Hall, R. (1998). Quantitative inferences of past hypolimnetic anoxia in south-central Ontario lakes using fossil midges (Diptera: Chironomidae). *Canadian Journal of Fisheries and Aquatic Sciences*, **55**, 587–596. 38

Rajar, R. & Cetina, M. (1997). Hydrodynamic and water quality modelling: an experience. *Ecological Modelling*, **101**, 195–207. 47

Reed, W. & Hill, T. (1973). Triangular mesh methods for the neutron transport equation. Tech. Rep. LA-UR-73-479, Los Alamos Scientific Laboratory, Los Alamos, NM. 46

Rew, R. & Davis, G. (2002). NetCDF: an interface for scientific data access. *Computer Graphics and Applications, IEEE*, **10**, 76–82. 82, 130, 133

Rew, R., Davis, G., Emmerson, S. & Davies, H. (1997). NetCDF users guide for C: An access interface for self-describing, portable data, version 3. *Unidata Program Center, University Corporation for Atmospheric Research, Boulder, Colorado*. 130

Reynolds, C. (1979). Seston sedimentation. *Freshwater Biology*, **9**, 55–76. 43

Riley, M. & Stefan, H. (1988). MINLAKE: A dynamic lake water quality simulation model. *Ecological modelling*, **43**, 155–182. 27, 50, 55, 56, 281, 282

Roget, E., Salvadé, G. & Zamboni, F. (1997). Internal seiche climatology in a small lake where transversal and second vertical modes are usually observed. *Limnology and Oceanography*, **42**, 663–673. 289

Rose, N. (2002). Fly-Ash Particles. In W. Last & J. Smol, eds., *Tracking Environmental Change Using Lake Sediments*, vol. 2 of *Developments in Paleoenvironmental Research*, 319–349, Springer Netherlands. 32

Rouse, H. (1937). Modern conceptions of the mechanics or fluid turbulence. *Transactions of the American Society of Civil Engineers*, **102**, 463–505. 253

Rowan, D., Kalff, J. & Rasmussen, J. (1992). Estimating the mud deposition boundary depth in lakes from wave theory. *Canadian Journal of Fisheries and Aquatic Sciences*, **49**, 2490–2497. 45, 293

Rowan, D., Cornett, R., King, K. & Risto, B. (1995). Sediment focusing and ^{210}Pb dating: a new approach. *Journal of Paleolimnology*, **13**, 107–118. 45, 281, 292, 293

Rueda, F., Schladow, S., Monismith, S. & Stacey, M. (2003). Dynamics of large polymictic lake. I: Field observations. *Journal of Hydraulic Engineering*, **129**, 82. 45, 47, 154

Rueda, F., Schladow, S., Monismith, S. & Stacey, M. (2005). On the effects of topography on wind and the generation of currents in a large multi-basin lake. *Hydrobiologia*, **532**, 139–151. 78, 286, 289, 301

Rusu, E., Conley, D. & Ferreira-Coelho, E. (2008). A hybrid framework for predicting waves and longshore currents. *Journal of Marine Systems*, **69**, 59–73. 130

Ryan, P. & Harleman, D. (1973). *An analytical and experimental study of transient cooling pond behavior*. Volume 161 of Report (Ralph M. Parsons Laboratory for Water Resources and Hydrodynamics), Dept. of Civil Engineering, Massachusetts Institute of Technology. 439 pp. 123

Saloranta, T. & Andersen, T. (2007). MyLake–A multi-year lake simulation model code suitable for uncertainty and sensitivity analysis simulations. *Ecological Modelling*, **207**, 45–60. 46

Santhi, C., Arnold, J., Williams, J., Dugas, W., Srinivasan, R. & Hauck, L. (2001). Validation of the SWAT model on a large river basin with point and nonpoint sources. *Journal of the American Water Resources Association*, **37**, 1169–1188. 54

Scheffer, M. (1998). *Ecology of Shallow Lakes*. Chapman & Hall, London. 357 pp. 37

Schiefer, E. (2006). Depositional regimes and areal continuity of sedimentation in a montane lake basin, British Columbia, Canada. *Journal of Paleolimnology*, **35**, 617–628. 42, 44

Schindler, D., Bayley, S., Parker, B., Beaty, K., Cruikshank, D., Fee, E., Schindler, E. & Stainton, M. (1996). The effects of climatic warming on the properties of boreal lakes and streams at the Experimental Lakes Area, northwestern Ontario. *Limnology and Oceanography*, **41**, 1004–1017. 41

Schoellhamer, D. (2002). Variability of suspended-sediment concentration at tidal to annual time scales in San Francisco Bay, USA. *Continental Shelf Research*, **22**, 1857–1866. 176

Schwab, D.J. & Beletsky, D. (2003). Relative effects of wind stress curl, topography, and stratification on large-scale circulation in Lake Michigan. *Journal of Geophysical Research: Oceans*, **108**, n/a–n/a. 35, 162, 286

Schwab, D.J., Bennett, J.R., Liu, P.C. & Donelan, M.A. (1984). Application of a simple numerical wave prediction model to Lake Erie. *Journal of Geophysical Research: Oceans*, **89**, 3586–3592. 194

Serruya, S., Hollan, E. & Bitsch, B. (1984). Steady winter circulations in Lakes Constance and Kinneret driven by wind and main tributaries. *Archiv fur Hydrobiologie Supplement 70*, 33–110. 286

Sheng, Y. & Lick, W. (1979). The transport and resuspension of sediments in a shallow lake. *Journal of Geophysical Research*, **84**, 1809–1826. 34, 206, 251, 293

Simons, T. (1980). *Circulation Models of Lakes and Inland Seas*. Canadian bulletin of fisheries and aquatic sciences, Dept. of Fisheries and Oceans. 146 pp. 60

Simpson, J. & Dickey, T. (1981). The relationship between downward irradiance and upper ocean structure. *Journal of Physical Oceanography*, **11**, 309–323. 67

Singh, J., Knapp, H.V., Arnold, J. & Demissie, M. (2005). Hydrological modeling of the iroquois river watershed using HSPF and SWAT1. *Journal of the American Water Resources Association*, **41**, 343–360. 54

Sly, P. (1978). Sedimentary processes in lakes. In A. Lerman, ed., *Lakes: Chemistry, Geology, Physics*, 65–89, Spring-Verlag, New York. 37

Smagorinsky, J. (1963). General circulation experiments with the primitive equations. *Monthly Weather Review*, **91**, 99–164. 66

Smith, S., Renwick, W., Bartley, J. & Buddemeier, R. (2002). Distribution and significance of small, artificial water bodies across the united states landscape. *Science of the Total Environment*, **299**, 21–36. 24

Smol, J. (1992). Paleolimnology: an important tool for effective ecosystem management. *Journal of Aquatic Ecosystem Stress and Recovery*, **1**, 49–58. 39

Smol, J., Walker, I. & Leavitt, P. (1991). Paleolimnology and hindcasting climatic trends. *Internationale Vereinigung fuer Theoretische und Angewandte Limnologie. Verhandlungen*, **24**, 1240–1246. 39

Solovieva, N., Jones, V., Nazarova, L., Brooks, S., Birks, H., Grytnes, J.A., Appleby, P., Kauppila, T., Kondratenok, B., Renberg, I. & Ponomarev, V. (2005). Palaeolimnological evidence for recent climatic change in lakes from the northern Urals, arctic Russia. *Journal of Paleolimnology*, **33**, 463–482. 39

Spigel, R. & Imberger, J. (1980). The classification of mixed-layer dynamics of lakes of small to medium size. *Journal of Physical Oceanography*, **10**, 1104–1121. 28, 175

Spigel, R.H., Imberger, J. & Rayner, K.N. (1986). Modeling the diurnal mixed layer. *Limnology and Oceanography*, **31**, 533–556. 281, 283

Stansby, P. (1997). Semi-implicit finite volume shallow-water flow and solute transport solver with k–ε turbulence model. *International Journal for Numerical Methods in Fluids*, **25**, 285–313. 46

Stern, G., Braekevelt, E., Helm, P., Bidleman, T., Outridge, P., Lockhart, W., McNeeley, R., Rosenberg, B., Ikonomou, M., Hamilton, P., Tomy, G. & Wilkinson, P. (2005). Modern and historical fluxes of halogenated organic contaminants to a lake in the Canadian arctic, as determined from annually laminated sediment cores. *Science of the Total Environment*, **342**, 223–243. 39

Stocker, R. & Imberger, J. (2003). Horizontal transport and dispersion in the surface layer of a medium-sized lake. *Limnology and Oceanography*, **48**, 971–982. 35, 36

Stoermer, E. & Smol, J. (2001). *The Diatoms: Applications for the Environmental and Earth Sciences*. Cambridge University Press, Cambridge. 469 pp. 39

Street-Perrott, F. & Harrison, S. (1985). Lake levels and climate reconstruction. In A.D. Hecht, ed., *Paleoclimate Analysis and Modeling*, 291–340, Wiley, New York. 40

Strub, P. & Powell, T. (1986). Wind-driven surface transport in stratified closed basins: Direct versus residual circulations. *Journal of Geophysical Research: Oceans*, **91**, 8497–8508. 36, 286

Stuiver, M. (1970). Oxygen and carbon isotope ratios of fresh-water carbonates as climatic indicators. *Journal of Geophysical Research*, **75**, 5247–5257. 40

Stumm, W. (1985). *Chemical Processes in Lakes*. John Wiley & Sons, New York. 435 pp. 30, 32

Sturm, M. & Matter, A. (1978). Turbidites and varves in Lake Brienz (Switzerland): deposition of clastic detritus by density currents. *Modern and Ancient Lake Sediments*, **2**, 147–168. 31

Sutherland, J., Walstra, D., Chesher, T., Van Rijn, L. & Southgate, H. (2004). Evaluation of coastal area modelling systems at an estuary mouth. *Coastal Engineering*, **51**, 119–142. 53, 54

Svensson, U. (1998). PROBE: program for boundary layers in the environment: system description and manual. Tech. Rep. 24, SMHI, Oceanography. 45

Sverdrup, H. & Munk, W. (1947). Wind, sea, and swell: theory of relations for forecasting. Tech. rep., Hydrographic Office, Washington. 78

Szesztay, K. (1974). Water balance and water level fluctuations of lakes. *Hydrological Sciences Journal*, **19**, 73–84. 27

Taguchi, K. & Nakata, K. (1998). Analysis of water quality in Lake Hamana using a coupled physical and biochemical model. *Journal of Marine Systems*, **16**, 107–132. 47

Talbot, M. (1990). A review of the palaeohydrological interpretation of carbon and oxygen isotopic ratios in primary lacustrine carbonates. *Chemical Geology: Isotope Geoscience section*, **80**, 261–279. 39

Tan, W. (1992). *Shallow Water Hydrodynamics: Mathematical Theory and Numerical Solution for a Two-dimensional System of Shallow-water Equations*. Elsevier Oceanography Series, Elsevier Science. 434 pp. 46

Te Chow, V., Maidment, D.R. & Mays, L.W. (1988). *Applied hydrology*. Tata McGraw-Hill Education. 572 pp. 50

Terasmaa, J. & Punning, J. (2006). Sedimentation dynamics in a small dimictic lake in northern Estonia. *Proc Estonian Acad Sci Biol Ecol*, **55**, 228–242. 37

Thompson, J., SøRENSON, H., Gavin, H. & Refsgaard, A. (2004). Application of the coupled MIKE SHE/MIKE 11 modelling system to a lowland wet grassland in southeast England. *Journal of Hydrology*, **293**, 151–179. 130

Thorpe, S. (1977). Turbulence and mixing in a scottish loch. *Philosophical Transactions for the Royal Society of London. Series A, Mathematical and Physical Sciences*, 125–181. 291

Timms, B. (1992). *Lake Geomorphology*. Gleneagles Pub., Adelaide. 180 pp. 23

Trauth, M., Deino, A. & Strecker, M. (2001). Response of the East African climate to orbital forcing during the last interglacial (130-117 ka) and the early last glacial (117-60 ka). *Geology*, **29**, 499. 39

Triska, F. & Cromack Jr, K. (1980). The role of wood debris in forests and streams. In *Proceedings of the annual biology colloquium (Oregon State University)*, vol. 40, 171–190. 32

Tsanis, I., Wu, J., Shen, H. & Valeo, C. (2007). *Environmental Hydraulics: Hydrodynamic and Pollutant Transport Models of Lakes and Coastal Waters*. Developments in Water Science, Elsevier Science. 368 pp. 25, 46

Udall, S. (1968). *Design of Small Dams*. Oxford & IBH Publishing Company. 611 pp. 38

Versteeg, H. & Malalasekera, W. (1995). *An Introduction to Computational Fluid Dynamics*. Longman Scientific & Technical. 520 pp. 46, 50

Walker, I., Smol, J., Engstrom, D. & Birks, H. (1991). An assessment of Chironomidae as quantitative indicators of past climatic change. *Canadian Journal of Fisheries and Aquatic Sciences*, **48**, 975–987. 40

Walker, I., Levesque, A., Cwynar, L. & Lotter, A. (1997). An expanded surface-water palaeotemperature inference model for use with fossil midges from eastern Canada. *Journal of Paleolimnology*, **18**, 165–178. 40

Walters, R., Carey, G. & Winter, D. (1978). Temperature computation for temperate lakes. *Applied Mathematical Modelling*, **2**, 41–48. 60

Wang, H., Holmes, J., Street-Perrott, F., Waller, M. & Perrott, R. (2008). Holocene environmental change in the West African Sahel: sedimentological and mineral-magnetic analyses of lake sediments from Jikariya Lake, northeastern Nigeria. *Journal of Quaternary Science*, **23**, 449–460. 39

Wang, J., Zhu, L., Nishimura, M., Nakamura, T., Ju, J., Xie, M., Takahiro, W. & Testsuya, M. (2009). Spatial variability and correlation of environmental proxies during the past 18,000 years among multiple cores from Lake Pumoyum Co, Tibet, China. *Journal of Paleolimnology*, **42**, 303–315. 44

Warner, J., Sherwood, C., Signell, R., Harris, C. & Arango, H. (2008). Development of a three-dimensional, regional, coupled wave, current, and sediment-transport model. *Computers and Geosciences*, **34**, 1284–1306. 68, 69, 73, 194

Welch, P. (1963). *Limnology*. McGraw-Hill publications in the zoological sciences, McGraw-Hill. 538 pp. 23

Wetzel, R. (1975). *Limnology*. Saunders, Philadelphia. 860 pp. 25

Wetzel, R. & Manny, B. (1978). Postglacial rates of sedimentation, nutrient and fossil pigment deposition in a hardwater marl lake of Michigan. *Polskie Archiwum Hydrobiologii*, **25**, 453–469. 44

Weyhenmeyer, G., Håkanson, L. & Meili, M. (1997). A validated model for daily variations in the flux, origin, and distribution of settling particles within lakes. *Limnology and Oceanography*, **42**, 1517–1529. 37, 265

White, W. (2001). *Evacuation of Sediments from Reservoirs*. Thomas Telford Limited. 260 pp. 38

Wieland, E., Lienemann, P., Bollhalder, S., Lück, A. & Santschi, P. (2001). Composition and transport of settling particles in Lake Zurich: Relative importance of vertical and lateral pathways. *Aquatic Sciences-Research Across Boundaries*, **63**, 123–149. 42

Winter, T. (1981). Uncertainties in estimating the water balance of lakes. *Journal of the American Water Resources Association*, **17**, 82–115. 25, 27, 28

Winter, T. & Woo, M. (1990). Hydrology of lakes and wetlands. In *Surface Water Hydrology*, 159–187, Geological Society of America, Boulder, Colorado. 25, 27, 28

Wu, J. (1982). Wind-stress coefficients over sea surface from breeze to hurricane. *Journal of Geophysical Research: Oceans*, **87**, 9704–9706. 59

Wünnemann, B., Mischke, S. & Chen, F. (2006). A Holocene sedimentary record from Bosten lake, China. *Palaeogeography, Palaeoclimatology, Palaeoecology*, **234**, 223–238. 40

Young, I. & Verhagen, L. (1996a). The growth of fetch limited waves in water of finite depth. Part 1. Total energy and peak frequency. *Coastal Engineering*, **29**, 47–78. 35, 78, 110, 185, 186, 287

Young, I. & Verhagen, L. (1996b). The growth of fetch limited waves in water of finite depth. Part 2. Spectral evolution. *Coastal Engineering*, **29**, 79–99. 35

Young, I., Verhagen, L. & Khatri, S. (1996). The growth of fetch limited waves in water of finite depth. Part 3. Directional spectra. *Coastal Engineering*, **29**, 101–121. 35

Zaharescu, D., Hooda, P., Soler, A., Fernandez, J. & Burghelea, C. (2009). Trace metals and their source in the catchment of the high altitude Lake Respomuso, Central Pyrenees. *Science of the Total Environment*, **407**, 3546–3553. 31

Zhai, Q., Guo, Z., Li, Y. & Li, R. (2006). Annually laminated lake sediments and environmental changes in Bashang Plateau, North China. *Palaeogeography, Palaeoclimatology, Palaeoecology*, **241**, 95–102. 39

Zhang, H., Madsen, O., Sannasiraj, S. & Soon Chan, E. (2004). Hydrodynamic model with wave–current interaction in coastal regions. *Estuarine, Coastal and Shelf Science*, **61**, 317–324. 291

Zhang, M. & Li, Y. (1997). The dynamic coupling of a third-generation wave model and a 3D hydrodynamic model through boundary layers. *Continental Shelf Research*, **17**, 1141–1170. 73, 194

Zhiliang, H. (1986). Preliminary approach of the classification of lake basin deltas. *Oil & Gas Geology*, **4**, 1–13. 31

Zhong, S. & Fast, J. (2003). An evaluation of the MM5, RAMS, and Meso-Eta models at subkilometer resolution using VTMX field campaign data in the Salt Lake Valley. *Monthly Weather Review*, **131**, 1301–1322. 289

Zundel, A. (2005). Surface-water Modeling System reference manual–Version 9.0. *Brigham Young University Environmental Modeling Research Laboratory*. 130